SISSA
Scuola
Internazionale
Superiore di
Studi Avanzati

Physics Area - PhD course in
Theory and Numerical Simulation
of Condensed Matter Physics

STUDIES ON IMPURITIES MOVING IN TOMONAGA–LUTTINGER LIQUIDS

CANDIDATE:
Martino Stefanini

ADVISORS:
Prof. Alessandro Silva
Prof. Massimo Capone

Academic Year 2021-2022

Ad hoc, ad loc and quid pro quo
So little time, so *much* to know!

Jeremy Hillary Boob, PhD
Yellow Submarine

CONTENTS

1 INTRODUCTION

This thesis deals with the physics of impurities in a host system. The term "impurity" is here used in a broad sense to identify a "simple" system, such as a particle, that is distinguishable from the environment in which it is embedded. Impurity problems have been a workhorse of condensed matter physics since its early decades, because they involve very general questions of both conceptual and practical importance. They also played a pivotal role in one of the major developments of the discipline, namely the first application of renormalisation group ideas by P.W. Anderson [2] to the Kondo model.

A very natural question one can ask about an impurity is how its properties (e.g. mass) are modified by the interaction with the environment. This is, for instance, the core of the very prolific field of polarons [22, 66], which aims to describe the electric transport properties of polar crystals. In these systems, it is argued that the interaction of the electrons with the dynamic polarisation of the ionic lattice (described in terms of its quantised vibrations—phonons), gives rise to a new quasiparticle, the above-mentioned polaron, which is actual the carrier of electric charge. This topic has had a long and successful history, dating back to the work of L.D. Landau [57] and of Landau and S.I. Pekar [56], and then developed by many others. The relevant feature of polaron theory is that it deals with impurities that are allowed to move within their environment. This is a situation that is frequently encountered in disparate physical systems, from the above-mentioned ionic solids to ^{3}He atoms in liquid ^{4}He and to diffusion of fast particles in metals [79]. A long-debated question for these systems is whether the polaron can become localised (i.e. with a diverging effective mass) for a sufficiently strong coupling [25, 30, 90].

A second line of research analyses the properties of systems hosting immobile impurities, often endowed with some kind of internal degree of freedom (e.g. spin). For this second kind of impurities, the most frequent kind of investigation takes the opposite perspective: how does the presence of impurities affect the properties of the host system, that is, the environment[1]? This is a very practical question, since most[2] system samples naturally and unavoidably host foreign atomic species, i.e the impurities. In this scenario, the basic focus is on the transport properties of the environment. While the obvious effect of impurities is to hinder transport, i.e. augmenting the resistance of the environment, there may be unexpected effects, as in what is arguably the most famous impurity problem in condensed matter physics—the Kondo problem [1, 43, 66]. This problem emerged in the 1930's with

1 Nonetheless, the enquiry about the modification of the properties of fixed impurity can be a very active line of research, as in spin-boson models and the like [61].

2 There are nowadays exceptionally clean systems, both solid-state [32] but especially in the field of ultracold atoms [9, 62].

the experimental study of the resistance properties of nonmagnetic metals doped with magnetic impurities [43], in which it was found that below a certain temperature the electric resistance unexpectedly increased with decreasing temperature. This unusual behaviour was explained by J. Kondo [52] with a model that featured a gas of noninteracting fermions (the conduction electrons) scattering off a single spinful, immobile impurity because of an antiferromagnetic interaction. The peculiar properties of this model, and the theoretical challenges that it posed, stimulated many other studies, including the above-mentioned paper by Anderson [2].

Another aspect of impurity problems which is relevant for this work is the so-called orthogonality catastrophe (OC). This phenomenon was first noticed by P.W. Anderson [3], in an immobile-impurity setting. He pointed out that if a fixed scattering centre is introduced within a metal (such as a positively charged ion created by an X-ray), the new ground state of the conduction sea is orthogonal to the one without the scattering centre when the thermodynamic limit is taken. In particular, the overlap between the two decreases as a power-law $N^{-\beta/2}$ of the number of electrons N. This is a genuinely many-body phenomenon: the wave function of each electron is subjected only to a small modification, but the cumulative effect is a vanishing overlap between the many body states. It is also quite general, occurring both in fermionic and bosonic systems (see, for instance, refs. [24, 40, 76]), albeit it is much more commonly analysed in the former case. Of course, the functional form of the decay of the overlap for a growing number of particles depends on the type of system, impurity and interactions—the power law being the most common case for fermions.

The OC plays a central role in another area of impurity problems which is of interest here, namely the physics of absorption spectra of X-rays [31, 33, 66], in which the scattering centre is the immobile hole in a core atomic state that is left after the ionisation caused by the absorption of an X-ray photon. It is in this context that the name "catastrophe" emerged (also in the alternative name of X-ray catastrophe), because the naive expectation was that the amplitude for the absorption should have been the overlap between the ground states before and after the creation of the hole, which is vanishing, however—hence, the transition should be forbidden. The resolution of the paradox lies in the observation that in this context the OC has to be seen as a dynamical phenomenon: the impurity (the hole) is suddenly injected into the environment (the conduction electrons), and the subsequent excitation of particle-hole pairs allows the conduction sea to relax. However, the orthogonality of the two ground states (before and after) is manifested in the very slow relaxation, which actually takes place only in an infinite amount of time.

A convenient quantity to measure this effect is the return amplitude[3] [31, 33, 51, 66]

$$\mathcal{L}(t) = \langle \Omega | d e^{-i\mathcal{H}_V t} d^\dagger | \Omega \rangle \ , \tag{1.0.1}$$

in which d, $d^\dagger$ are the annihilation and creation operators of the impurity, $|\Omega\rangle$ is the ground state of the system without the impurity, and $\mathcal{H}_V$ is the

3 Throughout this thesis we will set the reduced Planck's constant to one, $\hbar = 1$, unless noted otherwise.

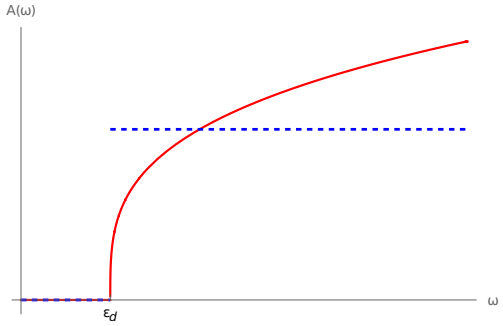

Figure 1.1: Schematic depiction of the effect of the orthogonality catastrophe on the X-ray absorption spectrum $A(\omega)$: the naive prediction of a step function (dashed, blue) is suppressed in a power-law fashion near to the threshold ε_d (continuous red line).

Hamiltonian of the system in the presence of the hole. We assume is has the form $\mathcal{H}_V = \mathcal{H}_0 + d^\dagger dV$, where $\mathcal{H}_0$ is the Hamiltonian of the system without the impurity and V is the operator describing the scattering of the environment states off the hole. The squared absolute value of $\mathcal{L}(t)$ is the fidelity of the initial state, namely the probability of returning to the initial state at a time t after the creation of the hole, which is assumed to happen at $t = 0$. For brevity, we will also call $\mathcal{L}(t)$ the fidelity. For the problem at hand, this quantity coincides, up to a global phase, with the Loschmidt echo[4] [35]

$$L(t) \equiv \langle \Omega | d e^{i\mathcal{H}_0 t} e^{-i\mathcal{H}_V t} d^\dagger | \Omega \rangle \tag{1.0.2}$$

and to the retarded Green's function [1, 42, 66]

$$G(t) \equiv -i\theta(t) \langle \Omega | d(t) d^\dagger | \Omega \rangle \tag{1.0.3}$$

for $t > 0$. In the above equations, $d(t)$ is the time-evolved annihilation operator in the Heisenberg picture, and $\theta(t)$ is the Heaviside step function. The two quantities (1.0.2) and (1.0.3) correspond to two conceptually different ways to assess the time evolution of the system, which in the present case give the same object. The Loschmidt echo compares [35] the interacting time-evolved state $e^{-i\mathcal{H}_V t} d^\dagger |\Omega\rangle$ with the evolved state in the absence of the interaction with the hole[5], $e^{-i\mathcal{H}_0 t} d^\dagger |\Omega\rangle$. The Green's function is a fundamental object for perturbation theory, and corresponds to the hypothetical procedure of probing the system by introducing the hole and removing it at a later time.

Whatever the quantity one chooses to measure, the main result is that at a sufficiently long time [31, 33, 66, 86]

$$|\mathcal{L}(t)| \sim t^{-\beta} \ , \tag{1.0.4}$$

where β is related to the scattering phase against the impurity, and it is the same exponent regulating the decay of the overlap of the ground states with the system size. The equation above shows the dynamical manifestation of

4 As with the fidelity, the actual Loschmidt echo is the squared absolute value of the quantity reported.

5 Of course, the hole creation operator has to be present in order for the overlap ti be nonzero, but it has no effect on the evolution induced by $\mathcal{H}_0$.

the OC: the system relaxes very slowly to the introduction of the impurity, without an intrinsic timescale. As the X-ray absorption spectrum is related to the Fourier transform of $\mathcal{L}(t)$, the effect of the dynamical OC is that the spectrum amplitude close to the threshold for absorption becomes rounded to a power-law behaviour in frequency, growing from zero instead of jumping to a finite value[6] [66]. In other words, the OC inhibits the absorption. This is illustrated schematically in figure 1.1.

In general, the existence of the OC depends both on the environment and on the impurity. It is typical of gapless environments, in which there is plenty of low-energy modes to be excited. In particular, the phase space for scattering with the impurity must allow for a significant density of states at low energy, i.e. the number of available states should not decrease too fast with energy. This has the interesting consequence that mobile impurities in two or more dimensions show no OC, in the sense that the overlap of the ground states does not vanish in the thermodynamic limit and that the Green's function tends to a finite constant, $\lim_{t\to+\infty}|G(t)| \neq 0$ [79]. This is because [79, 84] the finite mass of a mobile impurity introduces a non-vanishing recoil energy $p_R^2/(2M)$ that limits the available phase space. Here, p_R is a relevant exchanged momentum, such as the momentum of the particle-hole pairs excited in a fermionic environment.

However, even this limitation of phase space is not sufficient to suppress the OC if the impurity is confined to move in one dimension (1D). Actually, also the usual OC for fixed impurities in higher-dimensional metals is a "disguised" 1D problem. In intuitive terms, within each angular momentum channel, the scattering of the bath particles off the impurity involves only the radial motion, that is, 1D motion on a half-line [31, 33, 66, 86].

The connection of the OC to 1D physics is only a facet of the rich phenomenology emerging from constrained geometry. Impurities interacting with 1D baths have enjoyed a prolonged theoretical interest, because the restricted motion allows for a conceptual simplification of the problem, and for the use of theoretical tools that are essentially unique to 1D. The most renowned of these techniques is bosonisation [1, 12, 31, 33, 41], which is a nonlinear mapping from chiral massless (i.e. linearly dispersing) fermions to bosons. In many cases, such mapping allows to transform interacting fermionic Hamiltonians to solvable, quadratic bosonic models. Bosonisation is an exact correspondence, albeit it can be applied only for states close to the Fermi surface, whose dispersion can be linearised[7]. It is thus convenient for extracting universal, low-energy properties of 1D systems. Indeed, many 1D fermionic and bosonic systems with short-range interactions fall in the universality class known as Tomonaga-Luttinger Liquid (TLL), which describes a gapless state with critical (i.e. power-law) correlation function. In more physical terms, bosonisation works because the only possible low-energy excitations allowed by the 1D geometry are collective density fluctuations, namely acoustic phonons—which are bosons.

6 It is also possible to observe a divergent power law behaviour, caused by exciton effects [66]. The final sign of the exponent depends on the competition between these effects and the OC.

7 A systematic inclusion of nonlinearities in the dispersion can be built on bosonisation: see [45].

The conclusion from the discussion in the previous paragraph is that an advantage of working with impurities in 1D is that we have a good description of the baths, even in the case they are interacting. Moreover, the analytic techniques provided by bosonisation can be harnessed to analyse the properties of systems including impurities. For instance, this is the case for static impurities, beginning from simple scattering centres immersed in the TLL, whose effect on the transport properties of 1D systems has been assessed with the language of bosonisation and renormalisation group in [48, 49] (also discussed in more didactic terms in [31, 33]). The outcome of these studies is that even a single impurity can completely suppress conduction if the interactions within the bath are repulsive. Also problems related to the X-ray response have been analysed, both for TLL themselves [59, 72] and exploiting the mapping of three-dimensional metals to 1D [86]. Analogous considerations apply to the bosonisation treatment of the Kondo model [31, 33].

Models featuring mobile impurities embedded within TLLs have been analysed with these techniques, from weak to strong impurity-bath coupling and focusing either on mobility [14, 16, 55], or on the spectral properties [47, 50, 54]. Besides bosonisation, the kinematic constraints coming from the restricted 1D motion has allowed theoreticians to tackle impurity problems with a huge variety of techniques, among which we recall Feynman-Vernon influence functional [11, 15, 36], approaches based on Schwinger-Keldysh formalism and hydrodynamics [4, 28, 82], ingenious applications of semiclassical solutions at strong coupling [13], direct integration of the equations of motion [10], and effective field theories [79, 80]. Moreover, various insights have come from a number of solvable impurity models [59, 69] and related 1D models [29, 64] that are integrable via Bethe Ansatz. These exact solutions have been leveraged to compute both static and dynamical properties of impurities [68, 95], and to benchmark some of the approximate methods listed above. In addition to the mainly analytic approaches mentioned above, various flavours of Monte Carlo have been applied [38, 75]. Together with bosonisation, another set of numerical techniques that are particularly successful in 1D are the ones based on matrix-product states (MPS). The MPS representation can be applied both to determine ground-state properties (through the density-matrix renormalisation group [85]) and to simulate the dynamics [73], and has been applied to mobile impurities in 1D [46, 47, 50].

The interest in impurity problems originated in experimental solid-state physics, and has been fuelled by the conceptual challenges they posed to the theory. The appeal of these problems has seen a reinvigoration since the advent of ultracold atom technologies [9, 62, 77]. These technologies allow a high degree of control over the characteristics of the physical systems that can be realised, and this allowed to study impurities, from different perspectives, beyond those offered by traditional solid-state experiments. On the one hand, a large set of interaction regimes can be explored even in a single experimental setup. On the other hand, the exceptionally low temperature and low density of ultracold gases implies that the timescales for the dynamics are greatly dilated, hence the time evolution can be observed. These new experimental possibilities have stimulated a great deal of studies on

polarons [81], both immersed in Bose-Einstein condensates (Bose polarons) [39, 87] and in degenerate Fermi gases (Fermi polarons) [67]. The issue of OC has seen a revived interest, as well, both in the usual fermionic setting [51, 84] and in the bosonic one [24, 40]. In the next chapter we will provide more details on the experimental techniques that have been used to produce, manipulate and measure ultracold atomic systems with impurities.

The present thesis work takes inspiration from these theoretical and experimental studies. It aims to contribute to the ongoing research on impurity problems with some perspectives on a little-explored model. As we remarked above, polaron problems in 1D have been investigated in quite a detail in theory, albeit we will see in the next chapter that they are far less explored in experiments. We will also see that in general, experiments deal with systems composed of many 1D baths, each one endowed with its own impurity. Each of the latter propagates within its own bath, so that these real systems are made of many copies of the impurity-bath system meant to be studied. The model we analyse in this thesis takes a first step towards a multi-bath scenario in which the impurity can actually access more than one bath: it considers two independent 1D baths coupled to the impurity, so that the latter can propagate along each bath but also hop from one to the other. We will describe this model in full detail in section 2.2, and we will also consider a more general many-baths setup in section 4.2. The model we are proposing is thus a rather natural generalisation of the usual scenario of a single bath, and within the reach of present experiments. Its main point of interest concerns the dynamics of the impurity, namely the interplay between longitudinal (i.e. within one bath) and transverse motion (i.e. from one bath to the other), the former being continuous while the latter oscillatory in nature. Moreover, it raises the question on the effect on the extra degree of freedom on the usual OC that characterises the 1D motion. A similar model has been addressed in ref. [47], but in a complementary setting in which the impurity is confined to one of the baths, while the baths themselves are coupled with each other by exchange of particles. A generalisation of the spin-boson model including two different baths has been proposed in the literature, as in ref. [71], for instance. As we will see, this extended spin-boson model is a close relative of the static-impurity limit of our model. During our work, we became aware that the same two-bath model we are proposing was also considered in [46], with a similar analysis of the impurity Green's function.

In this thesis, we considered several aspects of the impurity-baths system. A first important point was to understand the OC in the system, and in general the behaviour of the impurity Green's function (1.0.3), which is experimentally relevant. The following step had a twofold purpose: we aimed to get a picture of the dynamics of the impurity, and to obtain a more complete view on its observables. As a byproduct of this effort, we were able to look at the dynamics of the baths themselves, which is seldom done in polaron studies, but that is worth looking at in the context of ultracold atoms. In our theoretical approach we tried to obtain a simple view on the very demanding problem of simulating the dynamics of quantum systems, keeping the numerical efforts as low as possible. Therefore, we mainly employed various flavours of perturbation theory, which allowed us to work close to the

continuum limit (which is crucial for a correct description of the OC) and to access the time evolution of impurity wave packets.

This thesis is organised as follows. In the following chapter 2 we will describe some experimental setups and techniques for the realisation of impurity systems with ultracold atoms in section 2.1, then we will introduce our model in section 2.2, along with all the approximations and simplification involved, and finally in section 2.3 we perform a warm-up calculation with an integrable model, that already contains much of the physics involved in the full model. In chapter 3 we present our results for the impurity Green's function, obtained with the Linked Cluster Expansion (LCE). After introducing this perturbative technique, in section 3.1 we perform a detailed asymptotic analysis of the LCE result, in order to elucidate the physics of the system. This analytic discussion is complemented in section 3.2 by a study of the results obtained by numerical computation of the LCE formulae. In section 3.3, we employ both analytic and numerical insights to investigate the effect of the OC on the impurity spectral function. We end the chapter with section 3.4, in which we extend the previous LCE results to baths possessing a finite temperature, which is relevant to actual experiments.

In chapter 4 we develop a perturbative approach that allows us to have a more comprehensive view of the impurity-baths system. We employ this results to take the unusual perspective of looking to the time evolution of observables describing the baths. After introducing a useful unitary transformation in 4.0.1, in section 4.1 we describe the techniques and its results. The technical details are reported in 4.1.2, while in the following two parts we describe analytic and numeric results for the impurity 4.1.3 and for the baths 4.1.4. In section 4.2 we extend the same approach to explore a general model with an arbitrary number of baths. We also included some ongoing research in appendix B, where we introduce a unitary transformation that completely decouples the impurity from the baths, and sketch how to employ it in a simple mean-field approach. Finally, in 5 we provide some conclusions and outlook.

List of publications

This thesis is based on the original results presented in the following publications:

- M. Stefanini, M. Capone, and A. Silva
  Motion of an impurity in a two-leg ladder
  Phys. Rev. B **103** 094310 (2021),

- M. Stefanini, M. Capone, and A. Silva
  (Forthcoming, 2022),

and on some unpublished work that is still under development. The author also collaborated to

- F. Caleffi, M. Stefanini, M. F. Ludovico
  (Forthcoming, 2022),

whose topics will not be discussed in the present thesis.

2 MODEL AND EXPERIMENTS

In this chapter, we make some preliminary steps before describing our work. First, we will give a brief introduction to the experimental realisation of impurity models with ultracold atoms. This description serves to motivate the model that we will study, and it gives an idea on what observables can be measured. Then, we will introduce the model that we are going to analyse in the following chapters, and discuss the assumptions it rests on. Finally, we will do a warm-up calculation on a solvable impurity model, that will illustrate some important physical points.

2.1 EXPERIMENTAL REALISATION

In this work, we explored a number of theoretical and conceptual issues, but we also tried to keep in mind the possibility of realising our model in an experiment. In fact, the model itself has been partially inspired by experiments done with ultracold atoms. In this section, we give a brief account on the experimental realisation of 1D systems with mobile and immobile impurities. The author is not an experimentalist, so the account will be mostly qualitative in nature.

Ultracold atoms have emerged as an unrivalled platform for the study and simulation of quantum many-body physics, besides a growing number of technological applications. As the topic has been much better detailed in reviews [9] and books [62, 77], we will not describe the fundamental aspects of these experimental techniques. Rather, we will concentrate on experiments more relevant to impurity problems in one dimension. References [17, 74] and [70] provide paradigmatic examples on the actual realisation of this kind of systems. In all three cases, a cloud of $\mathcal{O}(10^5)$ bosonic atoms (^{87}Rb for the first two refs., ^{133}Cs for the last one) is first trapped and cooled to a few hundreds of nK. Then, the three-dimensional cloud is adiabatically immersed in a two-dimensional optical lattice created by two (or four) crossed laser beams. The result is that the cloud becomes partitioned into a 2D lattice of elongated clouds, as depicted in figure 2.1. Besides the overall, harmonic 3D confinement of the whole system, the potential provided by the optical lattice around each site can be considered to be harmonic as well. If this potential has oscillator frequencies in the transverse directions that are large enough with respect to the temperature and chemical potential of each cloud, then the atoms in the latter are actually confined to 1D. Each cloud contains from a few tens to a few hundred atoms, depending on its position in the 2D lattice. These atoms constitute the bath, or environment, for the impurities. Impurity atoms can be introduced in the system in two different ways. The first is to perform the above procedure in presence a small concentration of another kind of atoms (^{41}K in the case of [17], with a concentration of about

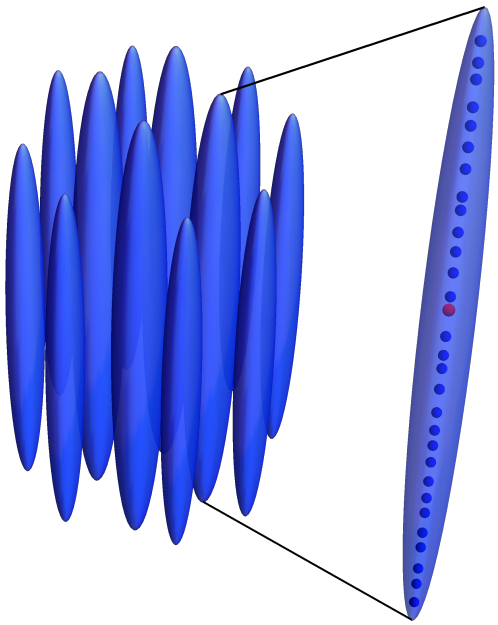

Figure 2.1: Typical appearance of a cold atom setup for an impurity in a 1D bath: a 2D lattice of elongated clouds of atoms. The magnification of one cloud shows the atoms constituting the bath as blue spheres and one impurity atom in red.

3%) already present in the system. This setup needs some care because of the different confining potentials seen by the two species. The whole setup can nonetheless be adjusted so that on average there is about one impurity atom per 1D cloud. The impurities can be addressed and manipulated by a species-selective dipole potential, namely a laser beam that acts on the impurity atoms only, that is used in [17] to prepare the potassium atoms in the centres of the baths. An important point is that during the preparation of the system the inter-species interaction is held at a vanishing value with the help of a magnetic field at a suitable intensity (by the well-known phenomenon of Feschbach resonance [9, 21, 62, 77]). The system dynamics is initiated by ramping up the magnetic field to the value corresponding to the desired scattering strength between the two species.

In [74] and [70], the impurity atoms are introduced by an entirely different method. In cold-atom experiments, usually the atoms are prepared in a known hyperfine level, in order to control their response properties to external magnetic fields. In [70, 74], impurities are simply a small subset of the bath atoms driven to a different hyperfine level by a radio-frequency pulse with frequency, size and duration suitably chosen so that only a few impurities per bath are generated in the desired positions. Hence, this method provides impurities whose individual properties (such as the mass) are identical to the bath atoms, and this is relevant because in this case there can be interesting kinematic effects (e.g. see [28]) and exactly solvable models are available [29]. Moreover, the different hyperfine level implies that impurities respond differently to the confining fields, a fact is exploited in [70] and [74] to let the impurities accelerate freely in the gravitational field.

For either scenario of impurity creation, the impurities effectively appear to be suddenly injected in the systems. It is possible to reconstruct the subsequent time evolution of both impurities and bath atoms by various imaging techniques. The creation of a whole lattice of baths, each with its own impurity, means that during each run the experiments are actually observing the dynamics of many copies of the same system in parallel, with obvious advantages in terms of statistical analysis and increased signal-to-noise ratio with respect to a single 1D subsystem. On the other hand, the various "copies" of the subsystem are actually not perfectly identical with each other, because of the inhomogeneous density of the initial atom cloud and of the non-deterministic number of impurities in each bath. This is a source of statistical uncertainty in the data.

We also mention the setup on ref. [26], in which the starting point is a gas of $\mathcal{O}(10^2)$ ^{87}Rb atoms confined to form a 2D system, which is then partitioned into a collection of parallel 1D system of $\mathcal{O}(10)$ atoms by turning on a 2D optical lattice. The impurities are created by changing the hyperfine state of a fraction of the atoms, and then they are imaged individually to follow their time evolution. An important difference with respect to the three references reported in the previous paragraphs is that in this experiment both the impurity and the bath atoms move in a 1D lattice, instead of being only subjected to the shallow confinement in the longitudinal direction.

The experimental examples presented so far all have baths composed of bosons[1]. Indeed, it appears that the subject of impurities moving in 1D fermionic baths is under-explored in experiments. For instance, the authors of ref. [94] developed a system of an impurity and other few fermions in an elongated trap, but their intent was to investigate the approach to the thermodynamic limit as the number of atoms increased, rather than observing any impurity physics. There is nevertheless a burgeoning field devoted to the understanding of Fermi polarons [67, 83], which studies the properties of mixtures of fermionic species in which one is significantly more diluted than the other. These studies, however, mainly deal with 2D or 3D systems, in which definite polaron quasiparticles exist. The experimental investigation of fermionic systems displaying the OC is even more recent [18], but only at the level of fixed impurities in higher-dimensional baths, which are simpler to analyse theoretically [51]. The reason for the different levels of development of experiments for boson and fermion 1D systems is not entirely clear, it may be historical (as the field of Bose-Einstein condensation developed earlier than degenerate Fermi systems [9, 62]), but nowadays we are not aware of any strong technical hindrance to the extension of the above-mentioned techniques to fermionic systems. In any case, from a conceptual point of view, there is little difference between bosonic and fermionic 1D systems at low energy, as both kind of systems can be described as TLLs [31, 33]. For instance, the discrepancies emerge only in certain correlation functions [31]. In the next section we will build the model we will use throughout this work, and we will retain only the lowest-momentum contribution to the bath density, that does not distinguish between a fermionic or bosonic

1 Also the impurities are bosonic, but as long as their mutual interactions can be neglected, their statistics is irrelevant for the "single-particle" polaronic properties.

bath. Therefore, the results we will obtain are equally applicable to bosonic or fermionic baths.

In chapter 1 we introduced one of the main characters of the present work, namely the OC. Besides its conceptual importance in fermionic systems, it can be experimentally characterised by measuring either one of the equivalent quantities (1.0.1), (1.0.2), (1.0.3) in real time or in frequency (i.e. their Fourier transform). In both cases, the measurement relies on the possibility to tune the impurity-bath interaction, and in particular on the possibility to tune it to zero.

Let us begin with the measurement in the frequency domain, which is performed via the so-called radio-frequency (RF) spectroscopy [51, 84]. Let us name $|0\rangle$ the state of the impurity corresponding to zero coupling with the bath, and $|1\rangle$ the state in which the coupling is finite[2]. The RF spectroscopy is then a standard linear-response measurement, in which the system is subjected to a weak RF field capable of switching the impurity state from $|0\rangle$ to $|1\rangle$ and vice-versa, and the absorption amplitude of the RF signal is measured. At lowest order in the perturbing field, the absorption amplitude for a monochromatic RF probe of frequency ω can be calculated through Fermi's Golden Rule [84]:

$$A(\omega) = 2\pi\Omega_R^2 \sum_{f,i} p_i |\langle f|F|i\rangle|^2 \delta(\omega - E_f + E_i) \,, \tag{2.1.1}$$

where Ω_R is the Rabi frequency that quantifies the intensity of the incoming field, whereas $F = |0\rangle\langle 1| + |1\rangle\langle 0|$ is the operator corresponding to the perturbation. As usual in Fermi's Golden Rule calculations, the sum in the above equation runs on the initial $|i\rangle$ and final $|f\rangle$ many-body eigenstates of the Hamiltonian describing the whole impurity-bath system, having energies E_i and E_f, respectively, with the initial states weighted by their occupation probability $p_i \equiv \langle i|\rho_{in}|i\rangle$ in the initial density matrix ρ_{in}. Calling $\mathcal{H}_{in}$ and $\mathcal{H}_{fin}$ the initial and final Hamiltonian, and assuming that ρ_{in} commutes with $\mathcal{H}_{in}$ (it could be its ground state, for instance), we can re-write equation (2.1.1) as

$$\begin{aligned} A(\omega) &= \Omega_R^2 \int_{\mathbb{R}} dt\, e^{i\omega t} \operatorname{Tr}\left[e^{i\mathcal{H}_{in}t} e^{-i\mathcal{H}_{fin}t} \rho_{in}\right] = \\ &= 2\Omega_R^2 \operatorname{Re} \int_0^{+\infty} dt\, e^{i\omega t} \operatorname{Tr}\left[e^{i\mathcal{H}_{in}t} e^{-i\mathcal{H}_{fin}t} \rho_{in}\right] \end{aligned} \tag{2.1.2}$$

If we start with the impurity in its interacting state $|1\rangle$, then we obtain the standard (or ejection) RF absorption spectrum. On the other hand, we can start from the impurity in the noninteracting state $|0\rangle$ and perform the so-called reverse (or injection) RF spectroscopy. If the bath in its ground state $|\Omega\rangle$, then in the notation of the previous section $\mathcal{H}_{in} = \mathcal{H}_0$ and $\mathcal{H}_{fin} = \mathcal{H}_V$, so that

$$A(\omega) \propto \operatorname{Re} \int_0^{+\infty} dt\, e^{i\omega t} \mathcal{L}(t) \tag{2.1.3}$$

precisely corresponds to the Fourier transform of the return amplitude. In terms of the Green's function (1.0.3), $A(\omega) \propto -\operatorname{Im} \int_0^{+\infty} dt\, e^{i\omega t} G(t)$, which is nothing but the spectral function of the impurity [42, 66].

2 Refs. [51, 84] deal with immobile impurities, whose only degree of freedom is whether they are present or absent in the system. We are following their presentation, keeping in mind that the generalisation to mobile impurities gives the same results. See [87], for instance.

The RF spectroscopy described in the previous paragraphs is a standard linear response measurement, in the spirit of traditional solid state physics. The ultracold atom setup allows for a different approach, known as Ramsey interferometry, that is able to track $\mathcal{L}(t)$ in real time. Conceptually, it works as follows [34, 51, 84]. We prepare the impurity in its noninteracting state $|0\rangle$, while the bath is in its ground state $|\Omega\rangle$. We begin the dynamics by applying a $\pi/2$ pulse that rotates[3] the impurity state $|0,1\rangle \to |\pm\rangle = (|0\rangle \pm |1\rangle)/2^{1/2}$, so that at $t = 0$ we have the state $(|0\rangle \pm |1\rangle)/2^{1/2}\,|\Omega\rangle$. The subsequent time evolution reads

$$|\Psi(t)\rangle = \tfrac{1}{2^{1/2}}\,|0\rangle\, e^{-i\mathcal{H}_0 t}\,|\Omega\rangle + \tfrac{1}{2^{1/2}}\,|1\rangle\, e^{-i\mathcal{H}_V t}\,|\Omega\rangle \ . \tag{2.1.4}$$

After waiting the desired evolution time, a second $\pi/2$ pulse is applied, and the expectation value of $\sigma^z \equiv |0\rangle\langle 0| - |1\rangle\langle 1|$ is measured, yielding

$$\langle \sigma^z \rangle = \mathrm{Re}\ \langle \Omega | e^{i\mathcal{H}_0 t} e^{-i\mathcal{H}_V t} | \Omega \rangle = \mathrm{Re}\,\mathcal{L}(t)\ . \tag{2.1.5}$$

Alternatively, the same information can be extracted from the probability of finding the impurity in the $|0\rangle$ [$|1\rangle$] state, which is $(1 + \mathrm{Re}\,\mathcal{L}(t))/2$ [$(1 - \mathrm{Re}\,\mathcal{L}(t))/2$]. If the second $\pi/2$ pulse also adds a known phase $|0,1\rangle \to |\pm\rangle = (|0\rangle \pm e^{i\varphi}\,|1\rangle)/2^{1/2}$, then $\langle \sigma^z \rangle = \mathrm{Re}[e^{i\varphi}\mathcal{L}(t)]$ and the whole complex $\mathcal{L}(t)$ can be measured.

The use of these two techniques (RF spectroscopy and Ramsey interference) for the characterisation of the OC in fermionic systems have been experimentally demonstrated in ref. [18] for the case of ^{40}K impurities immersed in a cloud of ^{6}Li. This setup is an example in which the both the particles of the bath and the impurities are fermions. However, the large mass ratio between the two species was chosen so that the impurities could be considered immobile, and the whole system was three-dimensional.

2.2 DEFINITION OF THE MODEL

In this section we define our model and the main assumptions and approximations behind it.

Figure 2.2 illustrates the system we want to analyse. We consider a pair of parallel, one-dimensional (1D) wires, or baths, made of spinless fermions (or bosons). These particles interact among themselves within each bath, but otherwise the two subsystems are independent of each other[4]. Then, we consider a spinless impurity that interacts locally with the particles of the baths, and that is allowed to move within the wires, or to tunnel from one to the other. As we remarked in the introduction, this model represents a generalisation of the well-studied single-bath problem. From the perspective of experiments with ultracold atoms, it can be seen as a "building block" for the many-baths setup, but it can also be realised directly by confining the atoms in a double-well potential [37, 44].

3 For the procedure to give clean results, the $\pi/2$ pulse should be fast enough so that the bath state is not affected by it, a requirement that may be not trivial in an actual experiment.

4 This model is thus complementary to the ones analysed in refs. [47] and [46], where the baths can exchange particles.

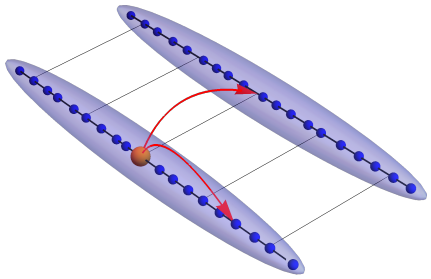

Figure 2.2: The system under analysis is composed of a particle (an impurity) which is able to move through a ladder, whose legs host two independent fermion baths inter-acting with the impurity

The Hamiltonian has the generic form

$$\mathcal{H} = \mathcal{H}_{\text{imp}} + \mathcal{H}_{\text{bath}} + \mathcal{H}_{\text{c}} \,, \tag{2.2.1}$$

where the three terms describe the free impurity, the baths and the impurity-bath coupling, respectively. The impurity motion can be thought of as taking place on a ladder, with a free Hamiltonian

$$\mathcal{H}_{\text{imp}} = 2J_{\parallel} \sum_{j\sigma} d^{\dagger}_{j\sigma} d_{j\sigma} - J_{\parallel} \sum_{j\sigma} (d^{\dagger}_{j+1,\sigma} d_{j,\sigma} + \text{h.c.}) - J_{\perp} \sum_{j\sigma} d^{\dagger}_{j\bar{\sigma}} d_{j\sigma} \,, \tag{2.2.2}$$

where $d_{j\sigma}$ is the annihilation operator for a fermion at site j along the bath $\sigma \in \{\uparrow, \downarrow\}$:

$$\{d_{j\sigma}, d_{j'\sigma'}\} = \{d^{\dagger}_{j\sigma}, d^{\dagger}_{j'\sigma'}\} = 0, \quad \{d_{j\sigma}, d^{\dagger}_{j'\sigma'}\} = \delta_{j\sigma,j'\sigma'} \tag{2.2.3}$$

We choose the impurity to be a fermion, but all subsequent results equally apply to a bosonic impurity, because statistics is irrelevant for a single particle. The matrix elements $J_{\parallel}$ and $J_{\perp}$ are the hopping amplitudes along and between the chains, respectively. We will assume that the inter-bath hopping $J_{\perp}$ is (much) smaller than the intra-bath one $J_{\parallel}$, but this is not a crucial assumption. We take the length of the system to be $L = Na$ (a being the lattice spacing), and we work in periodic boundary conditions (pbc), both for the impurity and the baths. The choice of working on a lattice is only a matter of theoretical convenience. Indeed, we will consider the low-momentum behaviour of the system, for which a continuum description applies. Hence, our conclusions are not altered by the presence of a lattice. In the long-wavelength limit the impurity dispersion is parabolic[5]:

$$E(p) = \frac{p^2}{2M} \,, \tag{2.2.4}$$

of course, with a mass $M = 1/(2J_{\parallel}a^2)$. We can write a continuum Hamiltonian

$$\mathcal{H}_{\text{imp}} = \sum_{\sigma} \int dx \, [d^{\dagger}_{\sigma}(x) E(-i\, d/dx) d_{\sigma}(x) - J_{\perp} d^{\dagger}_{\bar{\sigma}}(x) d_{\sigma}(x)] \,, \tag{2.2.5}$$

5 We use units such that $\hbar = 1$

where $d_\sigma(x) \equiv d_{j\sigma}/a^{1/2}$, $x = ja$. The impurity Hamiltonian (2.2.2) can be diagonalised by going to the momentum space,

$$d_{j\sigma} = \frac{1}{N^{1/2}} \sum_p e^{ipaj} d_{p\sigma} \,, \tag{2.2.6}$$

and then forming the even (e) and odd (o) modes

$$d_{p,\mu=e/o} \equiv \tfrac{1}{2^{1/2}}(d_{p\uparrow} \pm d_{p\downarrow}) \quad \Rightarrow \quad \mathcal{H}_{\rm imp} = \sum_{p\mu} \lambda_{p\mu} d^\dagger_{p\mu} d_{p\mu} \,, \tag{2.2.7}$$

(which is nothing but a Fourier transform in the transverse direction), where the labelling refers to the parity of the corresponding impurity states with respect to the exchange of the bath index. Thus, the noninteracting impurity has two bands (even and odd, or bonding and anti-bonding)

$$\lambda_{p\mu} = E(p) - \mu J_\perp \,, \tag{2.2.8}$$

separated by a gap $2J_\perp$. We introduce the shorthand notation for which $\mu = e(o)$ corresponds to $+1(-1)$ when it is used as a multiplicative factor in expressions. We will always work in a subspace of the fermionic Fock space that can have either one or zero particles, where either

$$\sum_{j\sigma} d^\dagger_{j\sigma} d_{j\sigma} = \mathbb{1} \tag{2.2.9}$$

or

$$|0\rangle\langle 0| + \sum_{j\sigma} d^\dagger_{j\sigma} d_{j\sigma} = \mathbb{1} \tag{2.2.10}$$

hold true, $|0\rangle$ being the fermion vacuum.

At long wavelength and low energy, the baths can be described[6] by two independent Tomonaga-Luttinger Liquid (TLL) Hamiltonians [31]

$$\mathcal{H}_{\rm bath} = \sum_\sigma v_\sigma \int \frac{dx}{2\pi} \left[K_\sigma \left(\frac{d\theta_\sigma}{dx} \right)^2 + \frac{1}{K_\sigma} \left(\frac{d\phi_\sigma}{dx} \right)^2 \right] \,, \tag{2.2.11}$$

where v_σ is the speed of sound in bath σ, while the dimensionless Luttinger parameter K_σ measures the interaction of the particles constituting the bath. In particular, for a fermionic bath, $K_\sigma < 1$ ($K_\sigma > 1$) for repulsive (attractive) interactions. For a bosonic bath, typically $K_\sigma > 1$ [31].

Finally, in the spirit of ultracold atom physics, the bath-impurity coupling is described as a contact density-density interaction

$$\mathcal{H}_c = \sum_\sigma g_\sigma \int dx \, d^\dagger_\sigma(x) d_\sigma(x) \rho_\sigma(x) \,, \tag{2.2.12}$$

with $\rho_\sigma(x)$ being the particle density of the bath σ and g_σ is the coupling constant. The chosen form of the interaction corresponds to the situation in

6 We are using *equilibrium* bosonization. While the operator identities are true independently of the state of the system, the translation of generic initial conditions from the fermionic to the bosonic description generally leads to a non-quadratic theory for the bosons out of equilibrium [12, 41]. As the baths will always start in a thermal state (the ground state), this subtleties will not be an issue.

real experiments, in which the dilution of the system and the low temperatures make s-wave scattering dominant. The coupling constant is usually expressed as[7] [9, 62, 67, 77, 81] $g_\sigma = 2\pi a_\sigma / m_{r\sigma}$ in terms of the scattering length a_σ between impurity and σ bath atoms, and their reduced mass $m_{r\sigma}$. At the level of our treatment (long wavelength, weak coupling), this interaction can be either repulsive or attractive (i.e. $g_\sigma > 0$ or < 0), as it will enter in most quantities only as g_σ^2. We will generally take $g_\sigma > 0$ for concreteness[8].

In the following, we will refer to the case of *symmetric* baths whenever their properties, namely the sound velocities v_σ, the Luttinger parameters K_σ and the couplings g_σ are the same, independently of the bath index σ. Most of the results that will be presented will be referred to this condition. If any of the parameters of the system depends on the bath being considered, we will refer to the setup as being asymmetric.

Bosonization [31] provides a link between density fluctuations and the boson field ϕ:

$$\rho_\sigma(x) = \bar{\rho}_\sigma - \frac{1}{\pi}\frac{d}{dx}\phi_\sigma(x) + \bar{\rho}_\sigma \sum_{n\neq 0} A^\sigma_{|n|} e^{2ni(\pi\bar{\rho}_\sigma x - \phi_\sigma(x))} , \tag{2.2.13}$$

where $\bar{\rho}_\sigma$ is the average density of the bath σ, and $A^\sigma_{|n|}$ are nonuniversal coefficients. The third term describes backscattering, that is, fluctuations with large wavenumbers $2n\pi\bar{\rho}_\sigma$ in which bath fermions can be exchanged between the two Fermi points $\pm k_F = \pm\pi\bar{\rho}_\sigma$. If we assume that the impurity momenta are always much smaller than this momentum, then we keep only the first two. The discarded terms are important only in case we want to describe fast impurities, where they give rise to effects like the pseudo-Bloch oscillations. The constant term can be adsorbed in ϕ_σ by a canonical transformation, hence the final expression of the coupling Hamiltonian is

$$\mathcal{H}_c = -\sum_\sigma \frac{g_\sigma}{\pi}\int dx\, d^\dagger_\sigma(x) d_\sigma(x) \frac{d}{dx}\phi_\sigma(x) . \tag{2.2.14}$$

Following ref. [31], we can diagonalise $\mathcal{H}_{\text{bath}}$ by expressing $\phi_\sigma(x)$, $\theta_\sigma(x)$ in terms of the phonon modes $b_{q\sigma}$ according to[9]:

$$\phi_\sigma(x) = -i\pi\frac{K_\sigma^{1/2}}{L^{1/2}}\sum_{p\neq 0}\frac{V(p)}{p} e^{-ipx}(b^\dagger_{p\sigma} + b_{-p\sigma}) , \tag{2.2.15a}$$

$$\theta_\sigma(x) = +i\pi\frac{1}{L^{1/2}K_\sigma^{1/2}}\sum_{p\neq 0}\frac{V(p)}{|p|} e^{-ipx}(b^\dagger_{p\sigma} - b_{-p\sigma}) . \tag{2.2.15b}$$

7 We are neglecting the issue of UV regularisation: g_σ depends on the momentum cutoff, whereas a_σ is a physical quantity.

8 Of course, in presence of an attraction between the impurity and the particles making up the baths there will be the possibility of formation of bound states, which cannot be captured by the approaches we use in this work.

9 We are implicitly dropping terms of $\mathcal{O}(1/L)$, that give vanishing contributions in the thermodynamic limit. These terms should be kept if we were including also backscattering in the interaction.

The Hamiltonian in momentum space reads:

$$\mathcal{H}_{\text{imp}} = \sum_{p\sigma} \left(E(p) d^\dagger_{p\sigma} d_{p\sigma} - J_\perp d^\dagger_{p\bar{\sigma}} d_{p\sigma} \right) , \tag{2.2.16a}$$

$$\mathcal{H}_{\text{bath}} = \sum_{p\neq 0,\sigma} v_\sigma |p| b^\dagger_{p\sigma} b_{p\sigma} , \tag{2.2.16b}$$

$$\mathcal{H}_c = \sum_\sigma \frac{g_\sigma K_\sigma^{1/2}}{L^{1/2}} \sum_{p\neq 0} V(p) N_\sigma(p) (b^\dagger_{p\sigma} + b_{-p\sigma}) . \tag{2.2.16c}$$

In the above formulae, $N_\sigma(p) = \sum_k d^\dagger_{k-p,\sigma} d_{k\sigma}$ is the Fourier transform of the impurity density, and

$$V(p) = \left(\frac{|p|}{2\pi} \right)^{1/2} e^{-\frac{\alpha|p|}{2}} ,$$

where α is a small length providing an ultraviolet momentum cutoff (it can be loosely identified with the underlying lattice spacing). This cutoff is needed because the TLL description of the baths is an effective theory, valid only for small energies and momenta [31, 33, 66]. The choice of the shape of the cutoff function is rather arbitrary. The above one is best suited for TLL calculations. In the following, for mathematical convenience, we will often switch to a cutoff in energy $\Lambda^{-1} \sim M\alpha^2$, rather than momentum. Most of the interesting quantities that we will compute will be independent of the cutoff scheme.

We can see that the role of Luttinger parameters K_σ is to rescale the bare interaction to

$$\tilde{g}_\sigma = g_\sigma K_\sigma^{1/2} . \tag{2.2.17}$$

This implies that baths with attractive interactions ($K_\sigma > 1$) are coupled more strongly to the impurity than baths whose particles repel each other ($K_\sigma < 1$).

It has to be pointed out that the validity of the model holds under various restrictions. First of all, we neglected the $\sim \cos(2n\bar{\rho}_\sigma x - 2n\phi_\sigma(x))$ terms [31] in the long-wavelength expansion of the bosonized bath density. These terms would allow the bath fermions to jump between the two Fermi points, exchanging a multiple of momentum $2\pi\bar{\rho}_\sigma = 2k_{F\sigma}$ with the impurity, thus we are excluding the possibility to observe pseudo-Bloch oscillations [70]. This, however, should be a good approximation as long as the impurity momentum is much smaller than $2\pi\bar{\rho}_\sigma$. Moreover, this cosine term is less relevant than $-1/\pi\, d\phi_\sigma(x)/dx$ in a renormalization-group sense whenever $K_\sigma > 1$, i.e. for an attractive interaction between the fermions in the baths (see [31]).

The calculations described in this thesis are non-perturbative in $J_\perp$, thus in principle the inter-chain hopping could take any value. However, we will see that the coupling to the baths causes the odd mode to decay, with emission of phonons of energy $\approx 2J_\perp$. Then, this energy (or, equivalently, the wave number $q \sim 2J_\perp/v_\sigma$) must be small enough so that the bosonized description of the baths in terms of sound modes applies. Therefore, we take $2J_\perp \ll \Lambda$, where Λ is a suitable energy cutoff for the TLL. Moreover, we must also have $2J_\perp \ll 2k_{F\sigma}v_\sigma$ in order to ensure that we can neglect the above-mentioned cosine term in the bosonized density.

2.3 AN INSTRUCTIVE WARM-UP: STATIC IMPURITY

In this section we will study a simple integrable model that features some of the core elements of the treatments that we will perform later on. In particular, we will show how the OC and its dynamical counterpart emerge.

Let us suppose that we have one TLL in its ground state and that a static fermionic impurity is suddenly introduced in it [59, 66]. The low-energy bosonized Hamiltonian is

$$\mathcal{H} = \varepsilon_d d^\dagger d + \sum_{q\neq 0} v|q| b_q^\dagger b_q + g d^\dagger d \frac{K^{1/2}}{L^{1/2}} \sum_{q\neq 0} V_q (b_q + b_q^\dagger) \,, \tag{2.3.1}$$

where $x = 0$ is the position the impurity (its position is arbitrary, as any possible complex phase of V_q will not enter in the final result). Again, to keep the physics simple, we discarded the backscattering term $\sim \cos(2\pi\bar{\rho}x - 2\phi(x))$. This is legitimate as long as $K > 1$, otherwise backscattering is relevant in a renormalisation group sense [31, 33] and has to be included. The Hamiltonian above is similar to the ones analysed for the X-ray edge problem [31, 66], where the impurity d would play the role of a static hole suddenly created in a metal by the absorption of an X-ray photon. Real metals are of course three-dimensional, but it turns out that the fermionic bath surrounding the impurity can be bosonised, by considering that within each angular momentum sector of the impurity potential the relevant motion is only radial, i.e. 1D (with a boundary) [31, 33]. The resulting physics is consequently also similar to our toy model above, and goes under the name of X-ray or orthogonality catastrophe (OC) [66].

The word "catastrophe" refers to the fact that the ground state of equation (2.3.1) after the introduction of the impurity is orthogonal to the one before. When no impurity is present, the ground state of $\mathcal{H}(d^\dagger d = 0) = \sum_{q\neq 0} v|q| b_q^\dagger b_q$ is of course $|\omega\rangle$, namely the ground state of the TLL. After the impurity is introduced, we have

$$\mathcal{H}(d^\dagger d = 1) = \varepsilon_d + \sum_{q\neq 0} v|q| b_q^\dagger b_q + g \frac{K^{1/2}}{L^{1/2}} \sum_{q\neq 0} V_q (b_q + b_q^\dagger) \,, \tag{2.3.2}$$

which can be diagonalised by a suitable displacement of the bosonic oscillators $D^\dagger[-f_q] b_q D[-f_q] = b_q - f_q$, where

$$D[\alpha_q] \equiv e^{\sum_{q\neq 0} (\alpha_q b_q^\dagger - \text{h.c.})} \tag{2.3.3}$$

is the displacement operator, and $f_q \equiv \frac{g K^{1/2} V_q}{\varepsilon_q L^{1/2}}$. The result is

$$D^\dagger[-f_q]\mathcal{H}(d^\dagger d = 1) D[-f_q] = \varepsilon_d - \frac{g^2 K}{L} \sum_{q\neq 0} \frac{V_q^2}{\varepsilon_q} + \sum_{q\neq 0} v|q| b_q^\dagger b_q \equiv \mathcal{H}_D \,, \tag{2.3.4}$$

where $\varepsilon_q \equiv v|q|$. Hence, the new eigenstates[10] are of the form $D[-f_q]|\mathbf{n}\rangle$, where $\mathbf{n}$ is a vector whose components n_q specify the number of bosons

10 One may notice that the second term of the shifted Hamiltonian (2.3.4) is divergent. However, this is a harmless ultraviolet divergence, that merely signals that the overall energy shift is too sensitive to the precise form of the underlying model to be predicted with accuracy by the effective model (2.3.1).

populating the state at momentum q. In particular, the new ground state $|\omega_1\rangle$ is a coherent state:

$$|\omega_1\rangle = D[-f_q]\,|\omega\rangle \equiv |\mathrm{coh}[-f_q]\rangle \ . \tag{2.3.5}$$

The overlap with the initial state is

$$\langle\omega|\omega_1\rangle = \langle\omega|D[-f_q]|\omega\rangle = e^{-\frac{1}{2}\sum_{q\neq 0} f_q^2} \ .$$

The exponent is

$$\begin{aligned} -\frac{1}{2}\sum_{q\neq 0} f_q^2 &= -\frac{g^2K}{2L}\sum_{q\neq 0}\frac{V_q^2}{\varepsilon_q^2} \approx -\frac{g^2K}{(2\pi v)^2}\int_{2\pi/L}^{+\infty}\frac{e^{-\alpha q}}{q} = \\ &= -\frac{g^2K}{(2\pi v)^2}E_1\left(\tfrac{2\pi\alpha}{L}\right) \sim -\frac{g^2K}{(2\pi v)^2}\ln\left(\frac{L}{2\pi e^{\gamma}\alpha}\right) , \end{aligned}$$

where we used the momentum $2\pi/L$ as an infrared cutoff, and used the definition and properties of the exponential integral function $E_1(x)$ (γ is the Euler-Mascheroni constant; see [23]). The overall result is that the overlap decreases as a power-law in the size of the system:

$$\langle\omega|\omega_1\rangle = \left(\frac{L}{2\pi e^{\gamma}\alpha}\right)^{-\beta_{OC}/2}, \quad \beta_{OC} = \frac{g^2K}{2(\pi v)^2} \ . \tag{2.3.6}$$

As advertised earlier, the two ground states are orthogonal in the thermodynamic limit. Physically, this occurs because the host system is characterised by gapless excitations (the phonons, i.e. the particle-hole pairs in the fermionic languages), which can be generated in large numbers at a very low energy cost by the introduction of a scattering centre (the static impurity). In fact,

$$\langle\omega_1|b_q^\dagger b_q|\omega_1\rangle = f_q^2 = \frac{g^2K}{L}\frac{V_q^2}{\varepsilon_q^2} \sim \frac{1}{|q|} \text{ for } |q|\to 0 \tag{2.3.7}$$

diverges in the long-wavelength limit, and as a consequence the total number of phonons $N_b \equiv \sum_{q\neq 0} b_q^\dagger b_q$ diverges in the thermodynamic limit [11]. The scaling with the system size (i.e, with the number of modes available to the system) shows that the OC is also a genuine many-body effect. As we are dealing with an independent particle model (the phonons are not coupled), we can also rephrase the vanishing of the overlap as the cumulative effect of many small changes in the state of each mode.

The OC phenomenon has also a dynamic analogue. We can ask ourselves: how fast does the system departs from the initial state after the introduction of the impurity? As mentioned in 1, the relevant quantity is the fidelity

$$\mathcal{L}(t) \equiv \langle\Omega|de^{-i\mathcal{H}t}d^\dagger|\Omega\rangle = \langle\Omega|d(t)d^\dagger|\Omega\rangle = iG(t), \ t>0 \ , \tag{2.3.8}$$

where $|\Omega\rangle \equiv |0\rangle\,|\omega\rangle$ is the product of the fermionic and bosonic vacua. In the second equality we introduced the impurity time-ordered Green's function

$$G(t) \equiv -i\,\langle\Omega|\mathcal{T}d(t)d^\dagger|\Omega\rangle = -i\theta(t)\,\langle\Omega|d(t)d^\dagger|\Omega\rangle \ , \tag{2.3.9}$$

11 One immediately sees that $\langle\omega|\omega_1\rangle = \exp(-\langle N_b\rangle/2)$, so that the vanishing of the overlap and the divergence of the number of excitations are actually two faces of the same coin.

where $d(t) \equiv e^{i\mathcal{H}t} d\, e^{-i\mathcal{H}t}$ is the Heinsenberg evolution of the impurity annihilation operator and $\mathcal{T}$ is the time-ordering symbol. In this case, where the average is on the fermionic vacuum, there is no difference between the time-ordered Green's function and the retarded one. The fidelity is easily computed, with the help of equation (2.3.4):

$$\begin{aligned}\mathcal{L}(t) = \langle\Omega|d\, d^\dagger e^{-i\mathcal{H}(d^\dagger d=1)t}|\Omega\rangle = \langle 0|d\, d^\dagger|0\rangle\ \langle\omega|e^{-i\mathcal{H}(d^\dagger d=1)t}|\omega\rangle = \\ = \langle\omega|D[-f_q]e^{-i\mathcal{H}_D t}D^\dagger[-f_q]|\omega\rangle = \\ = e^{-i(\varepsilon_d+\Delta E_0)t}\,\langle coh[f_q]|e^{-it\sum_{q\neq 0}\varepsilon_q b_q^\dagger b_q}|coh[f_q]\rangle = \\ = e^{-i(\varepsilon_d+\Delta E_0)t}\,\big\langle coh[f_q]\big|coh[e^{-it\varepsilon_q}f_q]\big\rangle = \\ = e^{-i(\varepsilon_d+\Delta E_0)t-\sum_{q\neq 0}f_q^2(1-e^{-i\varepsilon_q t})}\,.\end{aligned}$$

In the manipulations above, we defined $\Delta E_0 \equiv -\frac{g^2K}{L}\sum_{q\neq 0}\frac{V_q^2}{\varepsilon_q}$ and we used a couple of useful properties of coherent states:

$$e^{i\sum_q h_q b_q^\dagger b_q}\,|coh[f_q]\rangle = \big|coh[e^{ih_q}f_q]\big\rangle\ , \tag{2.3.10a}$$

$$\langle coh[\alpha_q]|coh[\beta_q]\rangle = e^{-\frac{1}{2}\sum_{q\neq 0}(|\alpha_q|^2+|\beta_q|^2-2\alpha_q^*\beta_q)}\,. \tag{2.3.10b}$$

Summing up, the fidelity can be written as

$$\mathcal{L}(t) = e^{-i\varepsilon_d t+F(t)}\ , \tag{2.3.11}$$

where

$$F(t) = -i\Delta E_0 t - \sum_{q\neq 0} f_q^2(1-e^{-i\varepsilon_q t}) = -\frac{g^2K}{L}\sum_{q\neq 0}V_q^2\frac{1-it\varepsilon_q-e^{-i\varepsilon_q t}}{\varepsilon_q^2}\,. \tag{2.3.12}$$

This function can be calculated in the continuum limit $L\to\infty$ by introducing the density:

$$R(\varepsilon) \equiv \frac{g^2K}{L}\sum_{q\neq 0}V_q^2\delta(\varepsilon-\varepsilon_q) = \beta_{OC}\theta(\varepsilon)\varepsilon e^{-\varepsilon/\Lambda},\ \Lambda\equiv\frac{\nu}{\alpha}\,, \tag{2.3.13}$$

from which

$$\begin{aligned}F(t) = -\int_{-\infty}^{+\infty}d\varepsilon\, R(\varepsilon)\frac{1-i\varepsilon t-e^{-i\varepsilon t}}{\varepsilon^2} = \\ = -\beta_{OC}\int_0^{+\infty}d\varepsilon\, e^{-\varepsilon/\Lambda}\frac{1-i\varepsilon t-e^{-i\varepsilon t}}{\varepsilon} = \\ = -\beta_{OC}\Big[-i\Lambda t+\ln(1+i\Lambda t)\Big] \sim \\ \sim -\beta_{OC}\left[-i\Big(\Lambda-\frac{\pi}{2}\Big)t+\ln(\Lambda t)+\mathcal{O}\Big(\frac{1}{\Lambda t}\Big)\right],\end{aligned}$$

where the last (asymptotic) equality is valid for times larger than the inverse energy cutoff, i.e for $\nu t \gg \alpha$ (for shorter times the effective Hamiltonian is not reliable, anyway). Thus, we find

$$\begin{aligned}\mathcal{L}(t) = e^{-i(\varepsilon_d-\beta_{OC}\Lambda)t}(1+i\Lambda t)^{-\beta_{OC}} = \\ \sim e^{-i(\varepsilon_d-\beta_{OC}\Lambda+\pi\beta_{OC}/2)t}(\Lambda t)^{-\beta_{OC}}\left[1+\mathcal{O}\big((\Lambda t)^{-1}\big)\right]\end{aligned} \tag{2.3.14}$$

As in the static version of the OC, we find a power-law decrease, but in time in this case, and the scaling exponent is the same[12] we found when varying the size, equation (2.3.6). This is the typical dynamical equivalent of the OC: the fidelity decays as a power law, without a timescale. Physically, this means that the bath relaxes very slowly to the introduction of the impurity.

Once again, we find that an equivalent signature of the OC is the excitation of many low-energy phonons,

$$\langle\Omega|de^{i\mathcal{H}t}b_q^\dagger b_q e^{-i\mathcal{H}t}d^\dagger|\Omega\rangle = 2\frac{g^2K}{L}\frac{1-\cos(\varepsilon_q t)}{\varepsilon_q^2} \sim t^2 \text{ as } |q|\to 0\,, \quad (2.3.15)$$

and the consequent divergence of their total number, as time goes on:

$$\langle N_b\rangle(t) = -2\,\mathrm{Re}\,F(t) \sim 2\beta_{OC}\ln\Lambda t + \mathcal{O}\big((\Lambda t)^{-1}\big)\,. \quad (2.3.16)$$

As in the static case, the link between these two perspectives on the OC is confirmed by a relation between the fidelity and the number of excited phonons:

$$|\mathcal{L}(t)| = e^{-\langle N_b\rangle(t)/2}\,. \quad (2.3.17)$$

Another quantity that is useful to calculate is the impurity spectral function

$$A(\omega) \equiv -2\,\mathrm{Im}\,G(\omega)\,, \quad (2.3.18)$$

where $G(\omega)$ is the Fourier transform of the impurity retarded Green's function,

$$G(\omega) \equiv \int_0^\infty dt\, e^{i\omega^+ t}G(t)\,.$$

In the equation above, we used $G(t) \propto \theta(t)$ and we defined $\omega^+ \equiv \omega + i0^+$, in order to ensure convergence. The above time integral can be performed exactly by deforming the integration path on the branch cut on the positive imaginary semi-axis (see also [66]), yielding

$$G(\omega) = e^{-i\beta_{OC}\pi}\Lambda^{-\beta_{OC}}e^{-(\omega-\tilde{\varepsilon}_d)/\Lambda}\frac{\Gamma(1-\beta_{OC},-(\omega-\tilde{\varepsilon}_d)/\Lambda)}{(\omega^+-\tilde{\varepsilon}_d)^{1-\beta_{OC}}}\,, \quad (2.3.19)$$

where we defined $\tilde{\varepsilon}_d = \varepsilon_d - \beta_{OC}\Lambda + \pi\beta_{OC}/2$, and $\Gamma(a,z)$ is the incomplete Gamma function [23]. We find that the Green's function has a power law behaviour for $\omega \to \tilde{\varepsilon}_d$[13]. This could be easily be guessed by a simple rescaling argument from the definition of $G(\omega)$. Neglecting the frequency dependence of the incomplete Gamma function, we get the spectral function

$$A(\omega) = 2\theta(\omega-\tilde{\varepsilon}_d)\Lambda^{-\beta_{OC}}e^{-(\omega-\tilde{\varepsilon}_d)/\Lambda}\frac{\Gamma(1-\beta_{OC})\sin\beta_{OC}\pi}{(\omega-\tilde{\varepsilon}_d)^{1-\beta_{OC}}}\,. \quad (2.3.20)$$

This *threshold* behaviour is the hallmark of the OC in the frequency domain [31, 33, 45, 66], and it is widely known in the X-ray problem. If $\beta_{OC} \leqslant 1$, the

12 The identity of the exponent can be explained as a light-cone effect: if we assume that $|L(t)| \sim |\langle\omega|\omega_1(L(t))\rangle|^2 \sim [L(t)]^{-\beta_{OC}}$ converges to the square of the static ground state overlap (i.e. the quasiparticle residue [79]), but only involving the portion of the bath that has been able to feel the presence of the impurity, then the finite speed of sound in the bath implies that $N(t) \sim vt$, and we obtain the power law in time.

13 This is true only for $\beta_{OC} \neq 1$. If $\beta_{OC} = 1$, the result is a milder logarithmic divergence.

singular part is divergent at the threshold, unlike the regular part, so that $A_{\text{sing}}(\omega)$ gives the dominant contribution. This behaviour is in stark contrast with the fairly common situation of quasiparticles, whose spectral function has a Lorentzian shape centred on the renormalised energy [1, 66]. In this problem, we recover a delta peak only in the limit in which the impurity is not interacting with the bath.

In concluding this chapter, we notice that equation (2.3.11) for the fidelity implies an interesting form of the impurity Green's function:

$$G(t) = G_0(t)e^{F(t)} , \tag{2.3.21}$$

where $G_0(t) \equiv -i\theta(t)e^{-i\varepsilon_d t}$ is the noninteracting impurity Green's function. We will see that this will provide the basis for the perturbative calculation that we will develop in the following chapter.

3 LINKED CLUSTER EXPANSION

In this chapter[1], we take a first look at the dynamics of the impurity by employing a technique known as Linked Cluster Expansion (LCE) to calculate its Green's function. From the numerical evaluation of the latter, and from its asymptotic expansion we infer a number of properties of the interacting impurity.

Let us imagine the following setup: we have prepared the baths in their respective ground state, $|\omega\rangle \equiv |\omega\rangle_\uparrow |\omega\rangle_\downarrow$, and at time $t = 0$ we inject the impurity in the bath labelled σ with a given momentum p.[2] We want to characterise the subsequent evolution of the whole system. As discussed in 1 and 2, a basic quantity to observe is the overlap between the initial state $d^\dagger_p |0\rangle_d |\omega\rangle_b$, and its evolved counterpart $e^{-i\mathcal{H}t} d^\dagger_p |0\rangle_d |\omega\rangle_b$, a quantity whose squared norm yields the fidelity. As in the case of the static impurity in section 2.3, this overlap is related to the Green's function

$$G_{\sigma'\sigma}(p', p; t) \equiv -i \langle \Omega | \mathcal{T} d_{p'\sigma'}(t) d^\dagger_{p\sigma} | \Omega \rangle = -i\theta(t) \langle \Omega | d_{p'\sigma'}(t) d^\dagger_{p\sigma} | \Omega \rangle \ , \quad (3.0.1)$$

where we defined $|\Omega\rangle = |0\rangle_d |\omega\rangle_b$ as the product of the impurity vacuum $|0\rangle_d$ and the (interacting) ground state of the baths, $|\omega\rangle_b$. The above Green's function also measures the amplitude for elastic scattering, namely the amplitude for the initial state to end up in any other impurity state without exciting any phonon in the bath. Moreover, we remind the reader that in ultracold atomic experiments the return amplitude, $iG_{\sigma\sigma}(p, p; t)$, is a measurable quantity, both in real time and in frequency (see section 2.1 and references therein).

The choice of the Green's function (3.0.1) has the advantage that we can compute it with the usual zero-temperature perturbative technique, despite that it is meant to describe a nonequilibrium situation. This is because $|\Omega\rangle$ is the ground state of the full $\mathcal{H}$ in the Hilbert space sector with no impurities present ($\mathcal{H}$ conserves the number of impurities, hence the dynamics cannot bring the state outside a given sector): $\mathcal{H}|\Omega\rangle = 0$, and coincides with the noninteracting ground state in the same sector. This fact allows us to use Gell-Mann-Low theorem to compute (3.0.1) within the standard zero-temperature perturbation theory.

3.0.1 The perturbative series

We will construct a perturbation series for the impurity Green's function using $\mathcal{H}_{imp} + \mathcal{H}_{bath}$ as the unperturbed Hamiltonian and expanding in the effective coupling $g_\sigma K_\sigma^{1/2}$. Strictly speaking, g_σ has dimensions [Energy·Length],

1 This chapter is based on the paper [92].

2 The sudden introduction of an impurity in a system is actually a common procedure with ultracold atoms, see chapter 2.1.

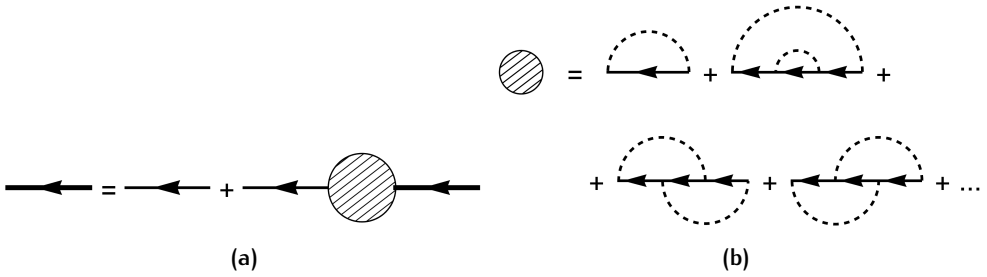

Figure 3.1: Perturbative series for the impurity Green's function. (a) Dyson equation. Thin lines indicate $\hat{G}_0$, thick lines the interacting $\hat{G}$ and the hatched circle is the self-energy. (b) the expansion of the self-energy up to fourth order. The dashed lines are the bosonic propagators.

i.e. a velocity, as [Energy] = [Time^{-1}] with $\hbar = 1$. The natural speed characterising the noninteracting dynamics is the sound speed v_σ, so that the perturbation series is actually an expansion in the dimensionless coupling[3] $g_\sigma K_\sigma^{1/2}/v_\sigma$. As the system has translational invariance, it is useful to go to momentum space. However, for the present chapter we will work in real time instead of frequency.

The basic ingredients of the perturbative series are the noninteracting impurity Green's function,

$$G^0_\mu(p,t) = -i\theta(t)e^{-i\lambda_{p\mu}t} \iff G^0_{\sigma\sigma'}(p,t) = -\frac{i}{2}\theta(t)(e^{-i\lambda_{pe}t} + \sigma\sigma' e^{-i\lambda_{po}t}) , \tag{3.0.2a}$$

and the bosonic propagator

$$\begin{aligned} D^0_\sigma(p,t) &\equiv -i\,\langle\Omega|\mathcal{T}(b^\dagger_{p\sigma}e^{iv_\sigma|p|t} + b_{-p\sigma}e^{-iv_\sigma|p|t})(b^\dagger_{-p\sigma} + b_{p\sigma})|\Omega\rangle_0 = \\ &= -i\theta(t)e^{-iv_\sigma|p|t} - i\theta(-t)e^{iv_\sigma|p|t} . \end{aligned} \tag{3.0.2b}$$

In the σ basis the vertices and phonon lines conserve the bath index, whereas the free propagation G_0 changes it. In the rotated (e,o) basis the free propagation conserves the band index, while only interactions may change it.

The perturbation series is described pictorially in figure 3.1, namely it is made of a sequence of free impurity lines to which any number of (possibly interlaced) phonons "arcs" are attached. There are no tadpole diagrams, because:

- there are no zero momentum phonons;
- the impurity loops give a vanishing density $-i(G_0)_{\sigma\sigma}(p, t = 0^-) = \langle\Omega|d^\dagger_{p\sigma}d_{p\sigma}|\Omega\rangle = 0$.

Analogously, $\hat{G}_0(p, t < 0) = 0$ forbids the existence of any loop made of impurity lines. This is consistent with the property that the theory conserves the number of impurities: there is only one of them, and so no particle-hole pairs can be generated.

3 If the impurity were static, $g_\sigma K^{1/2}/v_\sigma$ would be the low-energy, 1D scattering phase of the bath fermions on the impurity.

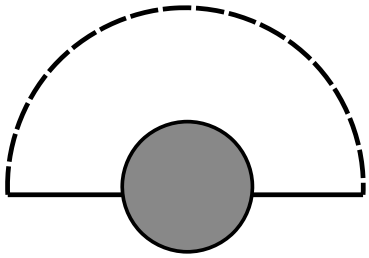

Figure 3.2: All self-energy diagrams with the "Non Crossing Approximation" structure are diagonal in bath index.

The momentum index is conserved, because all phonon lines begin and end on the continuous sequence of impurity free propagators, therefore

$$\hat{G}(p', p;, t) = \delta_{p'p}\hat{G}(p, t)\ , \tag{3.0.3}$$

where we use a hat $\hat{}$ to indicate matrices in bath index space. The bare Green's function equation (3.0.2a) is symmetric in this index, while in general the interaction with the baths could alter the symmetry. All self-energy diagrams in the "Non-Crossing Approximation" form (figure 3.2), including the lowest-order one, are diagonal in bath index and thus they yield a symmetric Green's function. The lowest-order diagrams which may be not diagonal are the fourth-order crossed diagram, namely the last two terms in figure 3.1b. However, if the two sound speeds are identical these are still diagonal in bath index space. In appendix B we will show that $\hat{G}$ must be symmetric if the baths are symmetric, but we do not know if the same is true in the asymmetric case.

The lowest-order contribution to the self-energy is at the second order:

$$\hat{\Sigma}^{(2)}(p, t) = \begin{pmatrix} \Sigma_\uparrow(p, t) & 0 \\ 0 & \Sigma_\downarrow(p, t) \end{pmatrix}, \tag{3.0.4a}$$

where

$$\begin{aligned} \Sigma_\sigma(p, t) &= ig_\sigma^2 K_\sigma \frac{1}{L}\sum_{q\neq 0} V^2(q)(G_0)_{\sigma\sigma}(p-q, t)D_\sigma^0(q, t) = \\ &= -i\tilde{g}_\sigma^2\theta(t)\cos J_\perp t \int \frac{dq}{2\pi} V^2(q)\, e^{-i(E_{p-q}+v_\sigma|q|)t}\ , \end{aligned} \tag{3.0.4b}$$

and we defined a renormalised coupling

$$\tilde{g}_\sigma = g_\sigma K_\sigma^{1/2} \tag{3.0.5}$$

It is possible to perform the momentum integral to obtain $\hat{\Sigma}^{(2)}$ in closed form, but in later calculations it turns out that it is more useful to keep it in this form.

3.0.2 The Linked Cluster Expansion (LCE)

The Linked Cluster Expansion is a resummation scheme for the Green's function perturbative expansion, which has been historically successful in the

treatment of impurities from weak up to intermediate coupling. See [66], for instance. It amounts to a cumulant expansion of the Green's function or, equivalently, to making the Ansatz:

$$\hat{G}(p,t) = \hat{G}_0(p,t)e^{\hat{F}(p,t)} \tag{3.0.6}$$

where $\hat{F}(p,t)$ has to be determined as a perturbative expansion $\hat{F}(p,t) = \sum_{n=1}^{\infty} \hat{F}_n(p,t)$, $\hat{F}_n = \mathcal{O}(\tilde{g}_\sigma^n/\nu_\sigma^n)$. Then, we expand $e^{\hat{F}(p,t)}$ and match its terms with the ordinary perturbation series, order by order:

$$\begin{aligned}\hat{G}_0(p,t)\big(\hat{\mathbb{1}} + \hat{F}_1(p,t) + \tfrac{1}{2}\hat{F}_1^2(p,t) + \hat{F}_2(p,t) + \dots\big) = \\ = \hat{G}_0(p,t) + (\hat{G}_0 * \hat{\Sigma}^{(2)} * \hat{G}_0)(p,t) + \dots ,\end{aligned} \tag{3.0.7}$$

where $*$ stands for time convolution and $\Sigma^{(n)}$ is the impurity self-energy at order n. There are only even orders, so $\hat{F}_{2n+1} = 0$, $\forall n \geqslant 0$. The lowest-order F_ns are determined by

$$\hat{G}_0(p,t)\cdot\hat{F}_2(p,t) = (\hat{G}_0 * \hat{\Sigma}^{(2)} * \hat{G}_0)(p,t) , \tag{3.0.8a}$$

$$\begin{aligned}\hat{G}_0(p,t)\cdot\hat{F}_4(p,t) = (\hat{G}_0 * \hat{\Sigma}^{(4)} * \hat{G}_0)(p,t) + \\ + (\hat{G}_0 * \hat{\Sigma}^{(2)} * \hat{G}_0 * \hat{\Sigma}^{(2)} * \hat{G}_0)(p,t) - \frac{1}{2}\hat{F}_2^2(p,t) ,\end{aligned} \tag{3.0.8b}$$

$$\dots$$

We will stop at the lowest nontrivial order, namely the second-order expression

$$\hat{F}_2(p,t) = \hat{G}_0^{-1}(p,t)\int_{\mathbb{R}^2} dt_1\, dt_2\, \hat{G}_0(p,t-t_1)\hat{\Sigma}^{(2)}(p,t_1-t_2)\hat{G}_0(p,t_2) , \tag{3.0.9}$$

where $\hat{G}_0^{-1}(p,t)$ means an inverse in bath index space.

Before proceeding with the calculation, we notice that the LCE Ansatz (3) is remarkably similar to equation (2.3.21). In fact, the latter equation implies that for a static impurity (i.e. infinitely massive) the second-order LCE actually gives the exact result. In our opinion, this could be a justification for the reliability of the LCE in impurity problems, and points to the possibility that it may become less so if the impurity mass is too low.

To compute $\hat{F}_2$ from equation (3.0.9), it is convenient to first switch to the parity basis in which $\hat{G}_0(p,t)$ is diagonal. Most importantly, it is advantageous to perform the momentum integration in the self-energy equation .(3.0.4b) after the time convolution. To obtain the LCE Green's function, we have to take the exponential of $\hat{F}_2$, and this is simpler if we decompose it in the Pauli matrices basis $\hat{\boldsymbol{\sigma}} \equiv (\sigma_1, \sigma_2, \sigma_3)$, along with the 2×2 identity matrix $\mathbb{1}$

$$\hat{F}_2(p,t) = A(p,t)\mathbb{1} + (B(p,t), C(p,t), D(p,t))\cdot\hat{\boldsymbol{\sigma}} , \tag{3.0.10}$$

where A, B, C, D are complex functions which will be defined shortly. The exponential is now easily computed (omitting the (p,t) arguments):

$$e^{\hat{F}_2(p,t)} = e^A\left(\cosh\lambda\,\mathbb{1} + \frac{\sinh\lambda}{\lambda}(B,C,D)\cdot\hat{\boldsymbol{\sigma}}\right) , \tag{3.0.11}$$

where

$$\lambda(p,t) \equiv \sqrt{B^2(p,t) + C^2(p,t) + D^2(p,t)} \tag{3.0.12}$$

(any of the two complex roots can be chosen).

The meaning and physical role of the above functions will become clear in the next paragraphs, but for now we point out that the the $C(p,t)$ and $D(p,t)$ functions are nonzero only if there is an asymmetry between the baths (in any of the v_σ, K_σ or in g_σ). The other $A(p,t)$ and $B(p,t)$ functions are less sensitive to asymmetries, and will be shown to encapsulate most of the physics of the problem.

Putting together equation (3.0.11) and equation (3.0.2a) we obtain the full expression for the Green's function:

$$\begin{aligned} G_{\sigma\sigma}(p,t) &= -i\theta(t)e^{-iE(p)t+A(p,t)}\Big[\cosh\lambda\cos(J_\perp t) + i\tfrac{\sinh\lambda}{\lambda}B\sin(J_\perp t) + \\ &\quad + \sigma\tfrac{\sinh\lambda}{\lambda}(D\cos(J_\perp t) - C\sin(J_\perp t))\Big]\,, \qquad (3.0.13a) \\ G_{\sigma\bar\sigma}(p,t) &= -i\theta(t)e^{-iE(p)t+A(p,t)}\Big[i\cosh\lambda\sin(J_\perp t) + \tfrac{\sinh\lambda}{\lambda}B\cos(J_\perp t)\Big]\,. \qquad (3.0.13b) \end{aligned}$$

In writing the second of these equations, we have anticipated that the $C(p,t)$ and $D(p,t)$ functions satisfy the relation $C(p,t)\cos J_\perp t + D(p,t)\sin J_\perp t = 0$, which makes the off-diagonal elements of $\hat G(p,t)$ equal, just as in the non-interacting case. This relation is specific to the second order in perturbation theory, because it ultimately depends on the self-energy being diagonal in bath index space [see equation (3.0.4a)]. Going to the next perturbative order (the fourth) allows for the inclusions of vertex corrections, which generally provide[4] the self-energy $\hat\Sigma$ with off-diagonal elements. In appendix B, we will prove that if the baths are symmetric, then the exact Green's function is indeed symmetric in the bath indices.

The four components of $\hat F_2(p,t)$ have the expressions

$$\begin{aligned} A(p,t) &= F_p(0,t) + \frac{1}{2}(F_p(J_\perp,t) + F_p(-J_\perp,t))\,, \qquad (3.0.14a) \\ B(p,t) &= \frac{1}{2}(F_p(-J_\perp,t) - F_p(J_\perp,t))\,, \qquad (3.0.14b) \\ C(p,t) &= i\frac{1-\cos 2J_\perp t}{J_\perp}H_p(0,t) + \\ &\quad + \frac{\sin J_\perp t}{J_\perp}\left[-e^{-iJ_\perp t}H_p(J_\perp,t) + e^{iJ_\perp t}H_p(-J_\perp,t)\right]\,, \qquad (3.0.14c) \\ D(p,t) &= -i\frac{\sin 2J_\perp t}{J_\perp}H_p(0,t) + \\ &\quad + \frac{\cos J_\perp t}{J_\perp}\left[e^{-iJ_\perp t}H_p(J_\perp,t) - e^{iJ_\perp t}H_p(-J_\perp,t)\right]\,, \qquad (3.0.14d) \end{aligned}$$

in terms of the functions

$$\begin{aligned} F_p(J,t) &\equiv \sum_\sigma F_{p\sigma}(J,t)\,, \qquad (3.0.15a) \\ H_p(J,t) &\equiv \sum_\sigma H_{p\sigma}(J,t)\,, \qquad (3.0.15b) \end{aligned}$$

4 However, this may not happen if $\tilde g_\uparrow \neq \tilde g_\downarrow$, but the sound speeds v_σ are the same.

defined as

$$F_{p\sigma}(J,t) \equiv -\frac{1}{4}\int_{\mathbb{R}} d\varepsilon\, \frac{1-i\varepsilon t-e^{-i\varepsilon t}}{\varepsilon^2} R_{p\sigma}(\varepsilon+2J)\,, \tag{3.0.16a}$$

$$H_{p\sigma}(J,t) \equiv \sigma\frac{1}{8}\int_{\mathbb{R}} d\varepsilon\, \frac{1-e^{-i\varepsilon t}}{\varepsilon} R_{p\sigma}(\varepsilon+2J) \equiv i\frac{\sigma}{2}\frac{\partial F_{p\sigma}(J,t)}{\partial t}\,, \tag{3.0.16b}$$

for $J = \pm J_\perp$ or 0. The function $R_{p\sigma}(\varepsilon)$ is defined as:

$$R_{p\sigma}(\varepsilon) \equiv \tilde{g}_\sigma^2 \int_{\mathbb{R}} \frac{dq}{2\pi} V^2(q)\delta(E(p-q)+v_\sigma|q|-E(p)-\varepsilon)\,. \tag{3.0.17}$$

The latter expression can be interpreted as the density of states available for scattering between the impurity and the phonons. Expressions like equation (3.0.16) and equation (3.0.17) are recurrent when dealing with the OC [66, 86]. It also coincides with the "spectral function" of the baths that is frequently encountered in the literature regarding the spin-boson model [61].

Recalling that the noninteracting impurity dispersion is given by two bands $\lambda_{e,op} = E(p) \mp J_\perp$, it can be seen that for $\varepsilon \to 0$ $R_{p\sigma}(\varepsilon)$ depends on intra-band processes, while $R_{p\sigma}(\varepsilon \pm 2J_\perp)$ give the effect of inter-band transitions.

Notice that all the results above hold for a generic bare impurity dispersion $E(p)$, as long as it is independent of the bath index.

Now we can take advantage of the quadratic dispersion $E(p) = p^2/2M$, which allows us to explicitly compute $R_{p\sigma}(\varepsilon)$. In the subsonic regime $|p| < M\max\{v_\uparrow, v_\downarrow\}$ it reads:

$$R_{p\sigma}(\varepsilon) = \tilde{g}_\sigma^2 \frac{M}{(2\pi)^2}\left[2 - \sum_{s=\pm}\frac{1}{\sqrt{1+\varepsilon/k_{s\sigma}(p)}}\right] e^{-|\varepsilon|/\Lambda}\theta(\varepsilon)\,, \tag{3.0.18}$$

where

$$k_{s\sigma}(p) \equiv \frac{(Mv_\sigma + sp)^2}{2M},\ s = \pm 1\,. \tag{3.0.19}$$

In obtaining equation (3.0.18), we have traded the momentum cutoff α^{-1} with an energy cutoff $\Lambda^{-1} \sim M\alpha^2$, which is easier to handle analytically. The low-energy physics should not be sensitive to the cutoff scheme used.

At small energies $\varepsilon \ll Mv_\sigma^2$, $R(\varepsilon)$ is linear, so that the Luttinger-liquid baths are classified as ohmic:

$$R_{p\sigma}(\varepsilon) = \theta(\varepsilon)\varepsilon e^{-\frac{\varepsilon}{\Lambda}}\frac{\tilde{g}_\sigma^2}{2\pi^2 v_\sigma^2}\frac{1+(p/Mv_\sigma)^2}{(1-(p/Mv_\sigma)^2)^2} + \mathcal{O}\left(\tfrac{\varepsilon^2}{M^2v_\sigma^4}\right) = \tag{3.0.20}$$

$$= \theta(\varepsilon)\varepsilon e^{-\frac{\varepsilon}{\Lambda}}\beta_\sigma^{sb}(p) + \mathcal{O}\left(\tfrac{\varepsilon^2}{M^2v_\sigma^4}\right)\,. \tag{3.0.21}$$

The quantity

$$\beta_\sigma^{sb}(p) \equiv \frac{\tilde{g}_\sigma^2}{2\pi^2 v_\sigma^2}\frac{1+(p/Mv_\sigma)^2}{(1-(p/Mv_\sigma)^2)^2} \tag{3.0.22}$$

is the single-bath OC exponent [47, 50].

For supersonic momenta, the density of states has an additional term

$$\Delta R_\sigma^{super}(\varepsilon) = \tilde{g}_\sigma^2\frac{2M}{(2\pi)^2}e^{-|\varepsilon|/\Lambda}\theta(-\varepsilon)\sum_{s=\pm 1}\theta(\varepsilon+k_{s\sigma}(p))\frac{1}{\sqrt{1+\varepsilon/k_{s\sigma}(p)}}\,. \tag{3.0.23}$$

Before embarking in the calculation of the various components of $\hat{F}_2$, we wish to comment on the physical content of the LCE Ansatz. In fact, the behaviour of the impurity depends on the long-time asymptotic form of $\hat{F}_2(p,t)$, that generally has the structure

$$\hat{F}_2(p,t) \sim \hat{X}(p)t + \hat{Y}(p) + \hat{\phi}_{nl}(p,t) + \mathcal{O}\left(\frac{1}{t}\right) \tag{3.0.24}$$

for $t \to \infty$. The first two terms on the right-hand side of this equation describe quasiparticle physics: the imaginary part of the $\hat{X}(p)$ matrix renormalises the single-particle properties (i.e. the mass and inter-bath hopping $J_\perp$), while its (negative) real part endows the momentum state with a finite lifetime. The $\hat{Y}(p)$ matrix quantifies the quasiparticle residue through $\hat{Z} = \exp\hat{Y}$. If only these two terms are present, the Green's function describes the propagation of a so-called quasiparticle, which is analogous to a free particle, except for a possible finite lifetime. However, it is possible that the asymptotic expansion of $\hat{F}_2(p,t)$ contains a growing—yet subleading—nonlinear function of time, indicated by the third term. If any of such terms is present, it causes the Green's function to depart from the quasiparticle picture. In two and three dimensions the asymptotic expansion of $\hat{F}_2$ does not contain any nonlinearity, and the impurity behaves as a quasiparticle, the polaron [66, 79]. In one dimension and with one bath, it was shown [50, 79] that there is a logarithmic term, which causes the Green's function to acquire a power-law decay at long times. This is related to the orthogonality catastrophe [3, 31, 33, 51, 54, 66]. In the following, we will see that in our double-bath scenario there is an analogous power-law behaviour. The considerations above may become clearer if we specialise the LCE to the symmetric case, in which

$$G_{\sigma'\sigma}(p,t) = -\frac{i}{2}\theta(t)\left(e^{-i\lambda_{pe}t+F_p(0,t)+F_p(-J_\perp,t)} + \sigma'\sigma e^{-i\lambda_{po}t+F_p(0,t)+F_p(J_\perp,t)}\right), \tag{3.0.25a}$$

or

$$G_{\mu\mu}(p,t) = -i\theta(t)e^{-i\lambda_{pe}t+F_p(0,t)+F_p(-\mu J_\perp,t)}. \tag{3.0.25b}$$

This form is actually valid to all orders for the LCE, one just substitutes $F_p(0,t) + F_p(-\mu J_\perp, t)$ with the generic component $F_{\mu\mu}(p,t)$ in the parity basis (in the symmetric case, $\hat{F}(p,t)$ is diagonal in this basis). Therefore, we see that the F functions "renormalise" the phases and amplitudes of the Green's function.

We point out that the Green's function is invariant under momentum inversion $p \to -p$. It can be observed either because of the invariance of $\hat{G}_0(p,t)$ and $\hat{\Sigma}^{(2)}(p,t)$ or by inspecting the parity of the density $R_{p\sigma}(\varepsilon)$. This invariance is valid at all orders, because it can be seen as a consequence of the time-reversal symmetry or of the space inversion symmetry enjoyed by the Hamiltonian. Thanks to this symmetry, we will usually present the results for positive momenta, with the understanding that they represent equally the negative momenta.

3.1 ASYMPTOTIC EXPANSIONS

This section is heavily mathematical in nature. We derive detailed expressions for the asymptotic expansions of the F and H functions in the long-time limit. As a byproduct, we also find a way to efficiently compute their full expressions by numerical integration, avoiding the unstable oscillatory integrals involved in their definitions equations (3.0.16).

3.1.1 $F_{p\sigma}$ functions

The full expression for the $F_{p\sigma}(p,t)$ function is

$$F_{p\sigma}(J,t) = -\frac{M\tilde{g}_\sigma^2}{(4\pi)^2}\int_{-2J}^{\infty} d\varepsilon\, \frac{1-i\varepsilon t - e^{-i\varepsilon t}}{\varepsilon^2} e^{-|\varepsilon|/\Lambda} \times \\ \times \left[2 - \sum_{s=\pm} \frac{1}{\sqrt{1+(2J+\varepsilon)/k_{s\sigma}(p)}}\right], \quad (3.1.1)$$

It is useful to separate the cases $J \neq 0$ from $J = 0$.

$J \neq 0$ *case*

Omitting the prefactor, the integral in equation (3.1.1) can be naturally split into two addends, and the first one can be calculated analytically:

$$f(J,t) \equiv 2\int_{-2J}^{\infty} d\varepsilon\, \frac{1-i\varepsilon t - e^{-i\varepsilon t}}{\varepsilon^2} e^{-|\varepsilon|/\Lambda} = \\ = \pi t + 2t\,\mathrm{Si}(2Jt) - \frac{1-\cos 2Jt}{J} + 2it\left[\ln\frac{2|J|}{\Lambda e^{-\gamma}} + \mathrm{Re}\,E_1(2i|J|t) + \frac{\sin 2Jt}{2Jt}\right], \quad (3.1.2)$$

where $\mathrm{Si}(z)$ is the sine integral function, and $E_1(z)$ is the exponential integral function [23]. The symbol $\gamma = 0.57721\ldots$ denotes the Euler-Mascheroni constant. In the above equation (3.1.2) we have performed the limit $\Lambda \to \infty$ whenever this did not cause divergences. It can be seen that the only the imaginary part of $f(J,t)$ is (weakly) dependent on Λ.

When[5] $J_\perp t \gg 1$ equation (3.1.2) has the asymptotic expansion (putting $J = \pm J_\perp$)

$$f(J_\perp,t) = 2\left(\pi + i\ln\frac{2J_\perp}{\Lambda e^{-\gamma}}\right)t - \frac{1}{J_\perp} + i\frac{e^{2iJ_\perp t}}{2J_\perp^2 t} + \mathcal{O}\left(\frac{1}{(J_\perp t)^2}\right), \quad (3.1.3a)$$

$$f(-J_\perp,t) = 2i\ln\frac{2J_\perp}{\Lambda e^{-\gamma}}\,t + \frac{1}{J_\perp} + i\frac{e^{-2iJ_\perp t}}{2J_\perp^2 t} + \mathcal{O}\left(\frac{1}{(J_\perp t)^2}\right). \quad (3.1.3b)$$

These expressions have been found using the large-z expansions for $\mathrm{Si}(z)$ and $E_1(z)$, and the property $\mathrm{Si}(z)$ is odd [23].

5 Notice that there are two timescales in our problem, namely the inter-bath tunnelling amplitude $J_\perp$ and the intra-bath one, $k_{s\sigma}(p) \sim Mv_\sigma^2/2$. We expect the realistic case to be the one in which the former is far smaller than the latter, and so we will often assume that $1/J_\perp$ is the longest timescale in the problem. However, this assumption is violated for p close to Mv_σ.

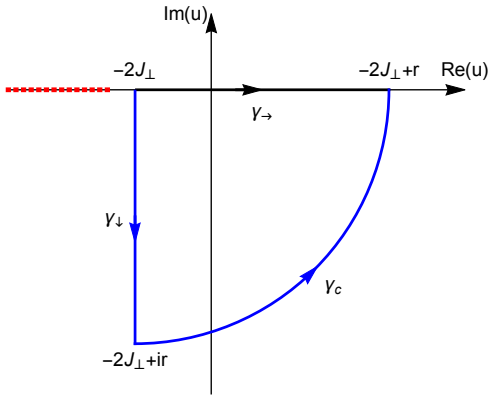

Figure 3.3: Paths of integration in the complex plane. Black: original path. Blue: deformed path. Dotted red: branch cut. It has been chosen to show the $J > 0$ case, the $J \leqslant 0$ ones are analogous.

The remaining part of the integral is in the form

$$\int_{-2J}^{\infty} d\varepsilon \, \frac{1 - i\varepsilon t - e^{-i\varepsilon t}}{\varepsilon^2} \frac{1}{\sqrt{1 + (2J + \varepsilon)/k}} \,,$$

which is finite when the cutoff is removed. The above equation can be simplified by doing the integral in the complex plane. The main idea is to integrate parallel to the imaginary axis, i.e. $\varepsilon \to iu$, so that the integrand changes from oscillatory to exponentially damped and the numerical integration can be tackled more efficiently. As a byproduct, some pieces of the final expression can be computed analytically. Moreover, this procedure provides a shorter route to obtaining the asymptotic form when $t \to \infty$.

The first step is a deformation of the integration path, as depicted in figure 3.3. The path goes from a segment on the real axis to a contour made of a vertical segment, followed by a quarter of circumference of radius r. The only singularity of the integrand is the branch cut of the square root, which is chosen to lie on the real axis, to the left of $-k - 2J$, so this manipulation does not alter the value of the integral. Moreover, it is easy to see that the integral on the quarter of circumference vanishes as $1/\sqrt{r}$ when $r \to \infty$, and we obtain:

$$\begin{aligned}
\int_{-2J}^{\infty} d\varepsilon \, \frac{1 - i\varepsilon t - e^{-i\varepsilon t}}{\varepsilon^2} \frac{1}{\sqrt{1 + (\varepsilon + 2J)/k}} &= \\
&= -i \int_0^{\infty} du \, \frac{1 + i(iu + 2J)t - e^{2iJt - ut}}{(iu + 2J)^2} \frac{1}{\sqrt{1 - iu/k}} = \\
&= -i \frac{1}{k} \phi_1\left(\tfrac{2J}{k}\right) + t\phi_2\left(\tfrac{2J}{k}\right) - ie^{2iJt} \int_0^{\infty} du \, \frac{e^{-ut}}{(iu + 2J)^2} \frac{1}{\sqrt{1 - iu/k}} \,, \qquad (3.1.4)
\end{aligned}$$

where

$$\phi_1(x) \equiv \int_0^{\infty} du \, \frac{1}{(iu + x)^2} \frac{1}{\sqrt{1 - iu}} \qquad (3.1.5a)$$

$$\phi_2(x) \equiv \int_0^{\infty} du \, \frac{1}{iu + x} \frac{1}{\sqrt{1 - iu}} \qquad (3.1.5b)$$

This is the sought-for expression. The two functions (3.1.5) can be computed exactly by going back to the real axis[6]:

$$\phi_1(x) = \begin{cases} \frac{1}{2x(1+x)^{3/2}}\left[\pi x - 2i\left(\sqrt{x+1} + x\,\mathrm{arcsinh}(\frac{1}{\sqrt{x}})\right)\right], & x > 0 \\ \frac{i}{|x|(1-|x|)} - \frac{i}{(1-|x|)^{3/2}}\mathrm{arccosh}(\frac{1}{\sqrt{|x|}}) & x < 0 \end{cases}, \tag{3.1.6}$$

$$\phi_2(x) = \begin{cases} \frac{1}{\sqrt{1+x}}\left[\pi - 2i\,\mathrm{arcsinh}(\frac{1}{\sqrt{x}})\right], & x > 0 \\ -\frac{2i}{\sqrt{1-|x|}}\mathrm{arccosh}(\frac{1}{\sqrt{|x|}}) & x < 0 \end{cases}, \tag{3.1.7}$$

in which it is understood that

$$\mathrm{arccosh}(x) = i\arccos x \quad \text{for} \quad |x| < 1\,.$$

The numerical evaluation of the last integral in equation (3.1.4) is rapidly converging.

When $J_\perp t \gg 1$ one can easily find an asymptotic approximation of this term, using the general expansion [23]

$$\int_a^\infty du\, e^{-tu} q(u) \sim e^{-at} \sum_{n=0}^{\infty} \frac{q^{(n)}(0)}{t^{n+1}}\,, \tag{3.1.8}$$

which is valid when the function $q(u)$ is infinitely differentiable around $u = a$. Applying this relation to the last integral in equation (3.1.4) we obtain:

$$\int_0^\infty du\, \frac{e^{-ut}}{(iu+2J)^2} \frac{1}{\sqrt{1-iu/k}} \sim \frac{1}{(2J)^2 t} + \mathcal{O}\left(\frac{1}{(Jt)^2}\right).$$

Therefore, the contribution of this term to the integral becomes small quite rapidly in the long-time limit.

Summing up, we can write

$$\int_{-2J}^\infty d\varepsilon\, \frac{1 - i\varepsilon t - e^{-i\varepsilon t}}{\varepsilon^2} \frac{1}{\sqrt{1+(\varepsilon+2J)/k}} \sim \\ \sim t\phi_2(\tfrac{2J}{k}) - i\frac{1}{k}\phi_1(\tfrac{2J}{k}) - i\frac{e^{2iJt}}{(2J)^2 t} + \mathcal{O}\left(\frac{1}{(2Jt)^2}\right), \tag{3.1.9}$$

6 One may exploit the observation that $\phi_1(x) = -\frac{d\phi_2}{dx}$.

and inserting this into equation (3.1.2), we find the desired asymptotic approximation:

$$\begin{aligned} F_{p\sigma}(J_\perp, t) \sim -\tilde{g}_\sigma^2 \frac{M}{(4\pi)^2} \Bigg[& -\frac{1}{J_\perp} + i \sum_{s=\pm 1} \frac{1}{k_{s\sigma}(p)} \phi_1\left(\tfrac{2J_\perp}{k_{s\sigma}(p)}\right) + \\ & + \left(2\pi + 2i \ln \tfrac{2J_\perp}{\Lambda e^{-\gamma}} - \sum_{s=\pm 1} \phi_2\left(\tfrac{2J_\perp}{k_{s\sigma}(p)}\right)\right) t + \\ & + i \frac{e^{2iJ_\perp t}}{J_\perp^2 t} + \mathcal{O}\left(\frac{1}{(J_\perp t)^2}\right) \Bigg] \end{aligned} \tag{3.1.10a}$$

$$\begin{aligned} F_{p\sigma}(-J_\perp, t) \sim -\tilde{g}_\sigma^2 \frac{M}{(4\pi)^2} \Bigg[& \frac{1}{J_\perp} + i \sum_{s=\pm 1} \frac{1}{k_{s\sigma}(p)} \phi_1\left(-\tfrac{2J_\perp}{k_{s\sigma}(p)}\right) + \\ & + \left(2i \ln \tfrac{2J_\perp}{\Lambda e^{-\gamma}} - \sum_{s=\pm 1} \phi_2\left(-\tfrac{2J_\perp}{k_{s\sigma}(p)}\right)\right) t + \\ & + i \frac{e^{-2iJ_\perp t}}{J_\perp^2 t} + \mathcal{O}\left(\frac{1}{(J_\perp t)^2}\right) \Bigg] . \end{aligned} \tag{3.1.10b}$$

$J = 0$ ***case***

As in the previous case, the first part of equation (3.1.1) can be calculated exactly:

$$f(0, t) \equiv 2 \int_0^\infty d\varepsilon \, \frac{1 - i\varepsilon t - e^{-i\varepsilon t}}{\varepsilon^2} e^{-|\varepsilon|/\Lambda} = \pi t - 2it \ln \tfrac{\Lambda t}{e} . \tag{3.1.11}$$

The remaining integrals can again be converted from oscillatory to exponentially damped by deformation of the integration contour,

$$\begin{aligned} \int_0^\infty d\varepsilon \, \frac{1 + i\varepsilon t - e^{-i\varepsilon t}}{\varepsilon^2} \frac{1}{\sqrt{1 + \varepsilon/k}} = \\ = i \int_0^\infty du \, \frac{1 - ut - e^{-ut}}{u^2} \frac{1}{\sqrt{1 - iu/k}} , \end{aligned} \tag{3.1.12}$$

and this can be helpful for their numerical evaluation. However, on the analytical side, they cannot be separated into three components as in the $J \neq 0$ case, because we have to treat the "kernel" $(1 - ut - e^{-ut})/u^2$ carefully at the $u = 0$ integration limit. We can do the following:

$$\begin{aligned} & \int_0^\infty d\varepsilon \, \frac{1 - i\varepsilon t - e^{-i\varepsilon t}}{\varepsilon^2} \frac{1}{\sqrt{1 + \varepsilon/k}} = \\ & = t \Bigg[\underbrace{\int_0^{\bar{\varepsilon}} d\varepsilon \, \frac{1 - i\varepsilon - e^{-i\varepsilon}}{\varepsilon^2} \frac{1}{\sqrt{1 + \varepsilon/\bar{\varepsilon}}}}_{\mathrm{I}} + \underbrace{\int_{\bar{\varepsilon}}^\infty d\varepsilon \, \frac{1 - i\varepsilon - e^{-i\varepsilon}}{\varepsilon^2} \frac{1}{\sqrt{1 + \varepsilon/\bar{\varepsilon}}}}_{\mathrm{II}} \Bigg] , \end{aligned} \tag{3.1.13}$$

where we performed the substitution $\varepsilon \to \varepsilon/t$ and we introduced the notation $\bar{\varepsilon} \equiv kt$. The first integral can be estimated for large t, i.e. for large $\bar{\varepsilon}$, by expanding the square root in powers of $\varepsilon/\bar{\varepsilon}$:

$$I \sim \sum_{n=0}^{\infty} \binom{-1/2}{n} \frac{1}{\bar{\varepsilon}^n} \int_0^{\bar{\varepsilon}} d\varepsilon \, \frac{1 - i\varepsilon - e^{-i\varepsilon}}{\varepsilon^2} \varepsilon^n =$$
$$= \frac{\pi}{2} - \Big(1 + \frac{\gamma}{2} - c_1\Big)\frac{1}{\bar{\varepsilon}} - \frac{\ln \bar{\varepsilon}}{\bar{\varepsilon}} + i\Big(1 - \gamma - c_0 - \ln \bar{\varepsilon} - \frac{\pi}{4\bar{\varepsilon}}\Big) + \mathcal{O}\big(\tfrac{1}{\bar{\varepsilon}^2}\big) \,, \quad (3.1.14)$$

where

$$c_0 \equiv \sum_{n \geqslant 1} \binom{-1/2}{n} \frac{1}{n} = \ln 4 - 2\operatorname{arcsinh}(1) \,, \quad (3.1.15a)$$

$$c_1 \equiv \sum_{n \geqslant 2} \binom{-1/2}{n} \frac{1}{n-1} = \frac{3 - 2\sqrt{2}}{2} - \ln 2 + \operatorname{arcsinh}(1) \,. \quad (3.1.15b)$$

These results were obtained by explicitly integrating all terms in the series, and expanding them up to $\mathcal{O}(\bar{\varepsilon}^{-2})$. As we can see, a real term containing $\ln \bar{\varepsilon} \sim \ln t$ has appeared. This originates from the structure of the kernel $(1 + i\varepsilon - e^{i\varepsilon})/\varepsilon^2$ for $\varepsilon \sim 0$.

The second integral, II, avoids the neighbourhood of $\varepsilon = 0$ and therefore it can be computed straightforwardly by evaluating each piece separately:

$$II = \underbrace{\int_{\bar{\varepsilon}}^{\infty} d\varepsilon \, \frac{1}{\varepsilon^2 \sqrt{1 + \varepsilon/\bar{\varepsilon}}}}_{II_a} \underbrace{- i \int_{\bar{\varepsilon}}^{\infty} d\varepsilon \, \frac{1}{\varepsilon \sqrt{1 + \varepsilon/\bar{\varepsilon}}}}_{II_b} \underbrace{- \int_{\bar{\varepsilon}}^{\infty} d\varepsilon \, \frac{e^{-i\varepsilon}}{\varepsilon^2 \sqrt{1 + \varepsilon/\bar{\varepsilon}}}}_{II_c} \,, \quad (3.1.16)$$

yielding

$$II_a = \frac{1}{\bar{\varepsilon}} \int_1^{\infty} d\varepsilon \, \frac{1}{\varepsilon^2 \sqrt{1 + \varepsilon}} = \frac{\sqrt{2} - \operatorname{arcsinh}(1)}{\bar{\varepsilon}} \,,$$
$$II_b = -i \int_1^{\infty} d\varepsilon \, \frac{1}{\varepsilon \sqrt{1 + \varepsilon}} = -2i \operatorname{arcsinh}(1) \,,$$
$$II_c = -\int_{\bar{\varepsilon}}^{\infty} d\varepsilon \, \frac{e^{-i\varepsilon}}{\varepsilon^2 \sqrt{1 + \varepsilon/\bar{\varepsilon}}} \sim \frac{i e^{-i\bar{\varepsilon}}}{\sqrt{2}\bar{\varepsilon}^2} + \mathcal{O}\big(\tfrac{1}{\bar{\varepsilon}^3}\big), \; \bar{\varepsilon} \gg 1 \,,$$

where for the last estimate we used the analogous of equation (3.1.8) [23]:

$$\int_a^{\infty} d\varepsilon \, e^{ix\varepsilon} q(\varepsilon) \sim e^{iax} \sum_{n=0}^{\infty} q^{(n)}(a) \big(\tfrac{i}{x}\big)^{n+1}, \quad x \gg 1 \,. \quad (3.1.17)$$

Therefore,

$$II \sim -2i \operatorname{arcsinh}(1) + \frac{\sqrt{2} - \operatorname{arcsinh}(1)}{\bar{\varepsilon}} + \frac{i e^{-i\bar{\varepsilon}}}{\sqrt{2}\bar{\varepsilon}^2} + \mathcal{O}\big(\tfrac{1}{\bar{\varepsilon}^3}\big) \,.$$

Unlike the I integral, this one does not contain any term depending logarithmically on $\bar{\varepsilon}$.

The final estimate is

$$\int_0^{\infty} d\varepsilon \, \frac{1 + i\varepsilon t - e^{i\varepsilon t}}{\varepsilon^2} \frac{1}{\sqrt{1 + \varepsilon/k}} = t(I + II) \sim$$
$$\sim -\frac{a_1}{k} - \frac{\ln kt}{2k} + \frac{\pi}{2} t + i\Big[-\frac{\pi}{4k} - t \ln kt + (1 - \gamma - \ln 4)t\Big] + \mathcal{O}\big(\tfrac{1}{t}\big) \,, \quad (3.1.18)$$

where

$$a_1 \equiv \ln 2 - \frac{1-\gamma}{2} = 0.481755\ldots\ . \tag{3.1.19}$$

Gathering all terms together, we obtain the asymptotic approximation

$$\begin{aligned} F_{p\sigma}(0,t) \sim -\tilde{g}_\sigma^2 \frac{M}{(4\pi)^2}\Big[(2a_1 + i\frac{\pi}{2}) \sum_{s=\pm 1} \frac{M}{(Mv_\sigma + sp)^2} + \\ + \sum_{s=\pm 1} \frac{M}{(Mv_\sigma + sp)^2} \ln \frac{(Mv_\sigma + sp)^2 t}{2M} + \\ + 2it \ln \frac{2\left|M^2 v_\sigma^2 - p^2\right|}{M\Lambda e^{-\gamma}} + \mathcal{O}\Big(\tfrac{2M}{(Mv_\sigma \pm p)^2 t}\Big)\Big], \\ \text{for} \quad \frac{(Mv_\sigma \pm p)^2 t}{2M} \gg 1\ . \end{aligned} \tag{3.1.20}$$

3.1.2 $H_{p\sigma}$ functions

The $H_{p\sigma}$ functions are obtained from the $F_{p\sigma}$ ones by differentiation

$$H_{p\sigma}(J,t) = i\frac{\sigma}{2}\frac{\partial F_{p\sigma}(J,t)}{\partial t}\ .$$

Their fast-converging integral expression is

$$\begin{aligned} H_{p\sigma}(J,t) = \sigma \frac{\tilde{g}_\sigma^2 M}{2(4\pi)^2}\Big[h(J,t) + i\sum_{s=\pm 1}\Big(\phi_2(\tfrac{2J}{k_{s\sigma}(p)}) + \\ - \int_0^\infty d\varepsilon\, \frac{e^{2iJt - t\varepsilon}}{i\varepsilon + 2J} \frac{1}{\sqrt{1 - i\varepsilon/k_{s\sigma}(p)}}\Big)\Big]\ , \end{aligned} \tag{3.1.21}$$

where

$$\begin{aligned} h(\pm J_\perp, t) &= 2\ln\tfrac{2J_\perp}{\Lambda e^{-\gamma}} + 2\,\mathrm{Re}\,E_1(2iJ_\perp t) - i\big(\pi \pm 2\mathrm{Si}(2J_\perp t)\big) \sim \\ &\sim 2\ln\tfrac{2J_\perp}{\Lambda e^{-\gamma}} - i(1\pm 1)\pi \pm i\frac{e^{\pm 2iJ_\perp t}}{J_\perp t} + \mathcal{O}\Big(\tfrac{1}{(J_\perp t)^2}\Big)\ , \qquad (3.1.22a) \\ h(0,t) &= -2\ln \Lambda t - i\pi\ . \qquad (3.1.22b) \end{aligned}$$

The asymptotic expansions are

$$\begin{aligned} H_{p\sigma}(J_\perp, t) = \sigma\frac{\tilde{g}_\sigma^2 M}{2(4\pi)^2}\Big[2\ln\tfrac{2J_\perp}{\Lambda e^{-\gamma}} - 2i\pi + \\ + i\sum_{s=\pm 1}\phi_2\big(\tfrac{2J_\perp}{k_{s\sigma}(p)}\big) - 2i\frac{e^{2iJ_\perp t}}{J_\perp t} + \mathcal{O}\Big(\tfrac{1}{(J_\perp t)^2}\Big)\Big]\ , \end{aligned} \tag{3.1.23a}$$

$$\begin{aligned} H_{p\sigma}(-J_\perp, t) = \sigma\frac{\tilde{g}_\sigma^2 M}{2(4\pi)^2}\Big[2\ln\tfrac{2J_\perp}{\Lambda e^{-\gamma}} + \\ + i\sum_{s=\pm 1}\phi_2\big(-\tfrac{2J_\perp}{k_{s\sigma}(p)}\big) + 2i\frac{e^{-2iJ_\perp t}}{J_\perp t} + \mathcal{O}\Big(\tfrac{1}{(J_\perp t)^2}\Big)\Big]\ , \end{aligned} \tag{3.1.23b}$$

$$H_{p\sigma}(0,t) = \sigma\frac{\tilde{g}_\sigma^2 M}{2(4\pi)^2}\Big[2\ln\tfrac{2|p^2 - M^2 v_\sigma^2|}{M\Lambda e^{-\gamma}} + i\sum_{s=\pm 1}\frac{1}{2k_{s\sigma}(p)t} + \mathcal{O}\Big(\tfrac{1}{(J_\perp t)^2}\Big)\Big]\ . \tag{3.1.23c}$$

All these functions tend to a constant at $t \to \infty$. In fact, they are the derivatives of asymptotically linear functions $F_{p\sigma}(p,t)$.

3.1.3 Results: asymptotic expansion of the Green's function.

In the previous section we found the necessary ingredients to compute the leading asymptotic behaviour of the $\hat{F}_2(p,t)$ function.

We can introduce the asymptotic expressions for $\tilde{F}_{p\sigma}$ and $\tilde{H}_{p\sigma}$ into equations (3.0.14) to obtain:

$$A(p,t) \sim -\gamma(p)t - i\Delta E(p)t - \beta(p)\ln t/t_0 + c_A(p,t_0) + \mathcal{O}\left(\tfrac{1}{t}\right), \tag{3.1.24a}$$

$$B(p,t) \sim \gamma(p)t + i\Delta J_\perp(p)t + c_B(p) + \mathcal{O}\left(\tfrac{1}{t}\right), \tag{3.1.24b}$$

$$C(p,t) \sim i\frac{1-\cos 2J_\perp t}{J_\perp}c_H^{(0)} + \frac{\sin J_\perp t}{J_\perp}\left(c_H^{(-)}e^{iJ_\perp t} - c_H^{(+)}e^{-iJ_\perp t}\right) + \mathcal{O}\left(\tfrac{1}{t}\right), \tag{3.1.24c}$$

$$D(p,t) \sim -i\frac{\sin 2J_\perp t}{J_\perp}c_H^{(0)} + \frac{\cos J_\perp t}{J_\perp}\left(c_H^{(+)}e^{-iJ_\perp t} - c_H^{(-)}e^{iJ_\perp t}\right) + \mathcal{O}\left(\tfrac{1}{t}\right), \tag{3.1.24d}$$

where the coefficients are

$$\beta(p) = \frac{M}{2(4\pi)^2}\sum_{s,\sigma}\frac{\tilde{g}_\sigma^2}{k_{s\sigma}(p)}, \tag{3.1.25a}$$

$$\gamma(p) = \frac{M}{32\pi}\sum_{s,\sigma}\tilde{g}_\sigma^2\left(1 - \frac{1}{\sqrt{1+2J_\perp/k_{s\sigma}(p)}}\right), \tag{3.1.25b}$$

$$c_A(p,t_0) = -\frac{M}{2(4\pi)^2}\sum_{s,\sigma}\frac{\tilde{g}_\sigma^2}{k_{s\sigma}(p)}\Big[2a_1 + \ln k_{s\sigma}(p)t_0 + i\Big(\phi_1\big(\tfrac{2J_\perp}{k_{s\sigma}(p)}\big) + \phi_1\big(-\tfrac{2J_\perp}{k_{s\sigma}(p)}\big) + \tfrac{\pi}{2}\Big)\Big], \tag{3.1.25c}$$

$$c_B(p) = -\frac{M}{2(4\pi)^2}\sum_{s,\sigma}\frac{\tilde{g}_\sigma^2}{k_{s\sigma}(p)}\left[\frac{k_{s\sigma}(p)}{J_\perp} + i\Big(\phi_1\big(\tfrac{-2J_\perp}{k_{s\sigma}(p)}\big) - \phi_1\big(\tfrac{2J_\perp}{k_{s\sigma}(p)}\big)\Big)\right], \tag{3.1.25d}$$

$$\Delta E(p) = \frac{M}{(4\pi)^2}\sum_{s,\sigma}\tilde{g}_\sigma^2\left[\ln\left(\frac{4J_\perp}{\Lambda e^{-\gamma}}\frac{|M^2\nu_\sigma^2 - p^2|}{M\Lambda e^{-\gamma}}\right) + \frac{\operatorname{arcsinh}\left(\sqrt{k_{s\sigma}(p)/2J_\perp}\right)}{\sqrt{1+2J_\perp/k_{s\sigma}(p)}} + \frac{\operatorname{arccosh}\left(\sqrt{k_{s\sigma}(p)/2J_\perp}\right)}{\sqrt{1-2J_\perp/k_{s\sigma}(p)}}\right], \tag{3.1.25e}$$

$$\Delta J_\perp(p) = -\frac{M}{(4\pi)^2}\sum_{s,\sigma}\tilde{g}_\sigma^2\left[\frac{\operatorname{arccosh}\left(\sqrt{k_{s\sigma}(p)/2J_\perp}\right)}{\sqrt{1-2J_\perp/k_{s\sigma}(p)}} - \frac{\operatorname{arcsinh}\left(\sqrt{k_{s\sigma}(p)/2J_\perp}\right)}{\sqrt{1+2J_\perp/k_{s\sigma}(p)}}\right], \tag{3.1.25f}$$

and

$$c_H^{(+)}(p) = \frac{M}{2(4\pi)^2}\sum_{s,\sigma}\sigma\tilde{g}_\sigma^2\Big(\ln\tfrac{2J_\perp}{\Lambda e^{-\gamma}} - i\pi + i\phi_2\big(\tfrac{2J_\perp}{k_{s\sigma}(p)}\big)\Big), \tag{3.1.26a}$$

$$c_H^{(-)}(p) = \frac{M}{2(4\pi)^2}\sum_{s,\sigma}\sigma\tilde{g}_\sigma^2\Big(\ln\tfrac{2J_\perp}{\Lambda e^{-\gamma}} + i\phi_2\big(-\tfrac{2J_\perp}{k_{s\sigma}(p)}\big)\Big), \tag{3.1.26b}$$

$$c_H^{(0)}(p) = \frac{M}{(4\pi)^2}\sum_{\sigma}\sigma\tilde{g}_\sigma^2\ln\tfrac{2|M^2\nu_\sigma^2 - p^2|}{M\Lambda e^{-\gamma}}. \tag{3.1.26c}$$

We also introduced an arbitrary timescale t_0, so that the physical dimensions are consistent.

At this point, we can finally put everything together and state our main result, namely the asymptotic form of the Green's function. From equations (3.1.24), we see that the leading behaviour of the $A(p,t)$ and $B(p,t)$ functions is linear in time, while the $C(p,t)$ and $D(p,t)$ functions are purely oscillating. This is in accord with our general discussion on the physical content of the LCE Ansatz: $\hat{F}_2(p,t)$ has the structure advertised in equation (3.0.24), with $A(p,t)$ and $B(p,t)$ making most of the linear and constant contributions, while $C(p,t)$ and $D(p,t)$ give only an oscillatory part to $\hat{\phi}_{nl}(t)$. The most important term of this function is given by the logarithmic term in $A(p,t)$. This is the hallmark of the breakdown of the quasiparticle description. To see the consequences of this term, we approximate equation (3.0.12) with

$$\lambda(p,t) = \sqrt{B^2(p,t) + C^2(p,t) + D^2(p,t)} = B(p,t) + \mathcal{O}\left(\tfrac{1}{t}\right) ,$$

because at sufficiently large times $B(p,t)$ is much larger than $C(p,t)$ and $D(p,t)$. We can finally write a relatively simple asymptotic expression for the Green's function, which represents our first important result:

$$\begin{aligned} G_{\sigma\sigma'}(p,t) \sim -\tfrac{i}{2}\left(\tfrac{t_0}{t}\right)^{\beta(p)} \Big[& Z_e(p,t_0) e^{-i\tilde{\lambda}_e(p)t} + \\ & + \sigma\sigma' Z_o(p,t_0) e^{-2\gamma(p)t - i\tilde{\lambda}_o(p)t} \Big] \left(1 + \mathcal{O}\left(\tfrac{1}{t}\right)\right) . \end{aligned} \tag{3.1.27}$$

In writing the above equation, we introduced the complex "quasiparticle weights"

$$Z_{e,o}(p,t_0) \equiv e^{c_A(p,t_0) \pm c_B(p)} \tag{3.1.28}$$

and the renormalised bands

$$\tilde{\lambda}_{e,o}(p) \equiv E(p) + \Delta E(p) \mp (J_\perp + \Delta J_\perp(p)) \equiv \tilde{E}(p) \mp \tilde{J}_\perp(p) . \tag{3.1.29}$$

Transforming to the (e,o) basis, the Green's function reads

$$\begin{aligned} G_{ee}(p,t) &\sim -iZ_e(p,t_0)\left(\tfrac{t_0}{t}\right)^{\beta(p)} e^{-i\tilde{\lambda}_e(p)t} , \\ G_{oo}(p,t) &\sim -iZ_o(p,t_0)\left(\tfrac{t_0}{t}\right)^{\beta(p)} e^{-2\gamma(p)t - i\tilde{\lambda}_o(p)t} , \\ G_{\bar{\mu}\mu}(p,t) &\sim \mathcal{O}\left(\tfrac{1}{t}\right) . \end{aligned} \tag{3.1.30}$$

The equations above have a suggestive structure, namely a renormalised version of the noninteracting Green's function [cfr. equation (3.0.2a)] multiplied by a decreasing power-law $\sim t^{-\beta(p)}$. This is the distinctive signature of the OC (compare with the results in 2.3), which "spoils" what would be a quasiparticle behaviour.

One should notice that only $\Delta E(p)$ and the three $c_H(p)$s bear a (logarithmic) dependence on the cutoff Λ. The former is an energy shift, so it is reasonable that it depends sensitively on the behaviour of the theory at high energy. Conversely, measurable quantities like $\tilde{J}_\perp \equiv J_\perp + \Delta J_\perp$ and $\beta(p)$ are cutoff-independent and thus proper low-energy properties.

Before analysing the properties of the asymptotic Green's function, we would like to make some remarks about the region of validity of the asymptotic expansions equation (3.1.24). Figures 3.4 shows the comparison of the Green's function calculated with the approximation equation (3.1.24) with

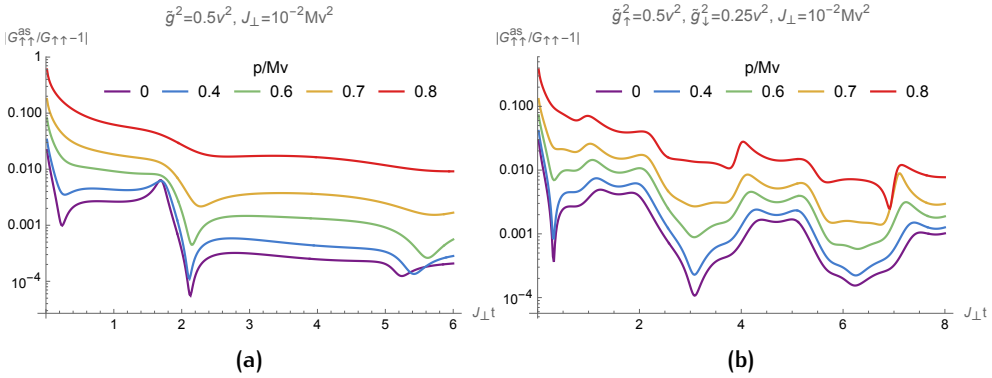

Figure 3.4: Relative accuracy of the asymptotic expansions (3.1.24) for the Green's function. Figure (a) refers to a symmetric case with $\tilde{g}^2 = 0.5v^2$ and $J_\perp = 0.01Mv^2$. Figure (b) refers to an asymmetric coupling $\tilde{g}^2_\uparrow = 0.5v^2$, $\tilde{g}^2_\downarrow = 0.25v^2$, while $J_\perp = 0.01Mv^2$ and $\Lambda = 10^3 Mv^2$.

the one obtained by the numerical evaluation of the $F(p,t)$ and $H(p,t)$ integrals. It can be appreciated that the asymptotic expansion gives rather accurate results for $G_{\sigma,\sigma'}(p,t)$ even for times as low as $J_\perp t \approx 0.1$ if the momentum is sufficiently close to zero. Under this condition, equation (3.1.24) is a good approximation for practically any relevant time. Increasing the impurity momentum causes one of the $k_{s\sigma}(p)$ to become small, and hence the asymptotic expressions retain their reliability only at larger times $t \gg \max\{1/J_\perp, 1/k_{s\sigma}(p)\}$. For symmetric baths this is equivalent to say that equation (3.1.27) at small momentum is a good approximation at almost any time. This is not true for asymmetric baths. While equation (3.1.24) still yield a reliable approximation, equation (3.1.27) turns out to be valid only at exceedingly large times. Notice that we have chosen to show the relative accuracy of the approximation for $G_{\uparrow\uparrow}(p,t)$ and for a fixed $J_\perp$, but the plots are qualitatively the same also for the off-diagonal components $G_{\bar{\sigma}\sigma}(p,t)$ and for various choices of the parameters.

Now we turn to the discussion of the properties of the impurity Green's function equation (3.1.27).

ORTHOGONALITY CATASTROPHE The first thing we want to point out is that the Green's function (3.1.27) is characterised by a *single* OC exponent $\beta(p)$ for all components. Explicitly, it has the expression:

$$\begin{aligned}\beta(p) &= \frac{1}{8\pi^2}\sum_\sigma \frac{g_\sigma^2 K_\sigma}{v_\sigma^2}\frac{1+(p/Mv_\sigma)^2}{(1-(p/Mv_\sigma)^2)^2} = \\ &= \frac{1}{2}\sum_\sigma \frac{g_\sigma^2 K_\sigma}{(2\pi v_\sigma)^2}\left[1+3\left(\frac{p}{Mv_\sigma}\right)^2+\mathcal{O}\left(\left(\frac{p}{Mv_\sigma}\right)^4\right)\right]. \end{aligned} \tag{3.1.31}$$

A comparison with ref. [50] shows that it is proportional to the sum of the analogous single-bath exponents $\beta^{sb}_\sigma(p)$,

$$\beta(p) = \tfrac{1}{4}(\beta^{sb}_\uparrow(p)+\beta^{sb}_\downarrow(p)), \tag{3.1.32}$$

or half the average of the two single-chain ones. For instance, if the baths have identical properties then the OC exponent is halved by the presence of

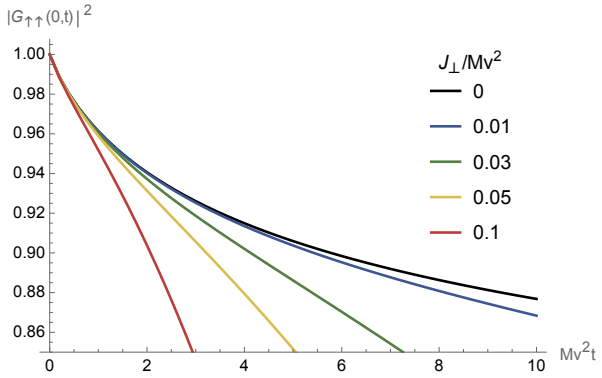

Figure 3.5: Typical appearance of the short-time Green's function compared to its single-bath counterpart (the upper curve, in black), showing the dimensional crossover. The parameters used are $p = 0$ and $\tilde{g}^2 = 0.5v^2$, in the symmetric case.

a second bath: $\beta(p) = \beta^{sb}(p)/2$. This happens irrespective of the magnitude of the inter-chain hopping $J_\perp$. We want to stress that the above results are non-perturbative in $J_\perp$. We are lead to the conclusion that the addition of the bath degree of freedom is able to weaken the orthogonality catastrophe, but not to destroy it.

The existence of a single OC exponent characterising both baths is simply explained by noticing that this phenomenon is observed in the limit $J_\perp t \gg 1$, namely when the impurity has had enough time to repeatedly interact with each bath. In fact, the numeric evaluation of the Green's function shows that for short times $J_\perp t \ll 1$ there is a "dimensional crossover". Its typical appearance is depicted in figure 3.5. From $t = 0$, $G_{\sigma\sigma}(p,t)$ evolves close to the single-bath $G^{sb}_\sigma(p,t)$, with its characteristic power-law β^{sb}_σ rapidly established. Then, the impurity starts to populate the other bath and the Green's function acquires the two-bath shape. This qualitative behaviour is the same for any momentum and also for the asymmetric case. We found numerically that the time at which the two-bath curve departs from the single-bath one by more than a few percent scales as $J_\perp^{-1}$.

Our explanation for $\beta(p)$ being less than the average of the single-bath exponents is based on the observation at weak coupling the impurity is able to spread across both baths. As a hand-waving argument, we may think that each bath effectively sees only "half" of the impurity, so that the actual couplings become $\tilde{g}_\sigma/2$. In this picture, equation (3.1.32) would only state that $\beta(p)$ is the sum of the single-bath exponents computed with $\tilde{g}_\sigma/2$ instead of $\tilde{g}_\sigma$, because all of these quantities are proportional to $\tilde{g}^2_\sigma$. This line of reasoning will be supported by the extension of our model to the case of N baths, which we will present in section 4.2. Within our present hand-waving reasoning, in the case of N_b baths we would predict that $\beta^{N_b}(p) = \sum_i \beta^{sb}_i/N^2_b$. Indeed, we will see that this expression is essentially correct (albeit it misses a factor that has interesting consequences). This relation implies that the exponent vanishes in the $N_b \to \infty$ limit. This is the natural expectation simply because in this limit the impurity moves in an effectively two-dimensional *bosonic* bath. Such a system does not display any OC [88]. Of course, despite the expectation is completely generic, our results are limited to the second-

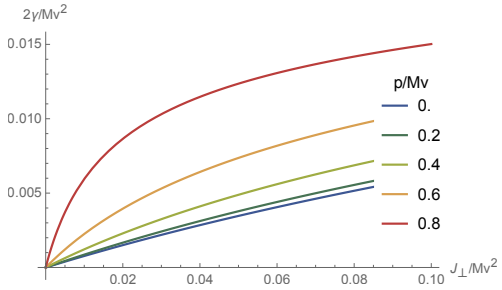

Figure 3.6: Behaviour of the decay rate for $\tilde{g}^2_{\uparrow,\downarrow} = 0.5v^2$ as a function of inter-bath hopping amplitude and longitudinal momentum.

order of perturbation theory and we can not assume that the exact value of β^{N_b} vanishes following the same functional behaviour $\beta^{N_b} \propto 1/N_b$ as a function of N_b.

Let us also comment on the noticeable divergence of $\beta(p)$ close to the threshold for phonon emission $p = Mv_\sigma$. In fact, many quantities in equations (3.1.25) and (3.1.26) have a singular behaviour at this threshold. Although intriguing, this behaviour is in a range of momenta were the long-wavelength approximation for the impurity dispersion and for the bosonised density are likely to be poor. Their validity depends on the (possible) lattice constant and how the Fermi wave vector of the baths compares with $Mv_\sigma/2$. Besides, we stopped the LCE at second perturbative order, hence it may deemed reliable only if the predicted $\hat{F}_2(p,t)$ is "small" in some sense, e.g. if $\beta(p)$ is small. Therefore, we cannot claim that the LCE is valid when $\hat{F}_2(p,t)$ diverges.

"QUASIPARTICLE" PROPERTIES Now we proceed to analyse the would-be quasiparticle properties exhibited by equation (3.1.27). Ignoring the power-law behaviour, the interaction with the bath natural has the two effects: the even and odd bands (hence, the hopping rate $J_\perp$) become renormalised, and the upper band becomes unstable. Its decay rate $2\gamma(p)$ is given by

$$2\gamma(p) = \frac{M}{16\pi} \sum_{\sigma,s=\pm 1} g_\sigma^2 K_\sigma \left(1 - \frac{1}{\sqrt{1 + 2J_\perp/k_{s\sigma}(p)}}\right). \tag{3.1.33}$$

For $J_\perp = 0$ this expression vanishes, and this is consistent with the observation that in the absence of inter-bath tunnelling there cannot be emission of phonons by an impurity with subsonic speed, because momentum and energy conservation cannot be simultaneously satisfied. This simple kinematic constraint hinders any decay in the symmetric, low energy band, while inter-band decay of the anti-symmetric one can be accompanied by the emission of phonons, causing the finite relaxation rate.

The typical behaviour of $2\gamma(p)$ is depicted in figure 3.6 for symmetric baths. The decay rate is a monotonically increasing function of both momentum and inter-bath hopping, upper bounded by $M\sum_\sigma \tilde{g}_\sigma^2/(8\pi)$ for either $J_\perp \to +\infty$ or $p \to Mv_\sigma$. Both these limits, however, lie beyond the regime of

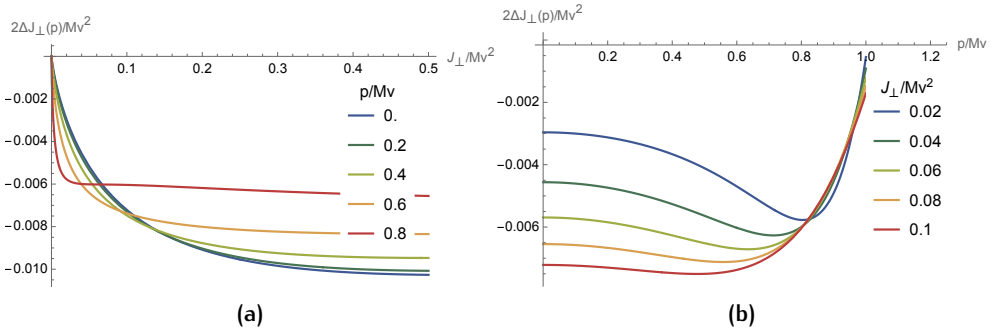

Figure 3.7: Behaviour of the inter-bath hopping frequency correction for (a) varying $J_\perp$ and (b) varying momentum p. The impurity-bath coupling is $\tilde{g}^2_{\uparrow,\downarrow} = 0.5v^2$, and the baths are symmetric.

validity of our low-energy model. In the long-wavelength limit in which it is reliable, a humbler expression for $2\gamma(p)$ is

$$2\gamma(p) = \frac{M}{8\pi}\sum_\sigma g_\sigma^2 K_\sigma\left(1-\frac{1}{\sqrt{1+\mu_\sigma}}\right)+ \\ +\frac{3}{8\pi}\sum_\sigma\left(\frac{\tilde{g}_\sigma}{v_\sigma}\right)^2\frac{\mu_\sigma}{(1+\mu_\sigma)^2}\frac{p^2}{2M}+\mathcal{O}\left(\left(\tfrac{p}{Mv_\sigma}\right)^4\right) \tag{3.1.34}$$

where

$$\mu_\sigma \equiv \frac{4J_\perp}{Mv_\sigma^2} \tag{3.1.35}$$

quantifies the relevance of transverse hopping with respect to the longitudinal one.

At small inter-bath hopping, the decay rate is approximately linear in $J_\perp$:

$$2\gamma(p) = 2\pi\beta(p)J_\perp + \mathcal{O}\left(J_\perp^2\right) . \tag{3.1.36}$$

This is an unexpected link between the decay rate and the OC exponent, namely that $\beta(p)$ is nothing but the derivative of $\gamma(p)$ with respect to $J_\perp$, $\beta(p) = 1/\pi\ \partial\gamma(p, J_\perp = 0)/\partial J_\perp$. From a more physical perspective, this means that the number of free oscillation periods $2\pi/J_\perp$ it takes to the odd mode to decay of a factor e is $1/(4\pi^2\beta(p))$ in the $J_\perp \to 0$ limit. We find the above equation particularly noteworthy, because $\gamma(p)$ is "easy" to compute by a straightforward Fermi Golden Rule calculation, while $\beta(p)$ can be calculated only by summing infinite subdiagrams in perturbation theory (which is precisely what the LCE does). Unfortunately, we could not rationalise this result in simple terms and, for the same reason, we do not have arguments about its validity beyond second-order perturbation theory.

Now we focus on the renormalised energy bands, equation (3.1.29). In the present model, the presence of the power-law behaviour of the Green's function prevents us from a straightforward interpretation of these expressions as actual dispersions of some excitation within the system. Their role will be clearer in section 3.3, when we will discuss the spectral function of the impurity. This will clarify that these bands are the locations of the only two sharp features in the spectrum. The even band represents the lower threshold of the energy spectrum of the whole system (hence, $\lambda_e(p = 0)$ is the

ground-state energy), while the odd band corresponds to a higher-energy peak.

In more detail, the bands are rigidly shifted by the same function $\Delta E(p)$, while their energy difference is increased by $2\Delta J_\perp(p)$. The energy shift is always negative, and it contains a logarithmic divergence as a function of the TLL cutoff Λ (of course, this divergence is harmless because it is the same for all momenta). The renormalised gap $2\tilde{J}_\perp(p) = 2(J_\perp + \Delta J_\perp(p))$ is always lesser than the bare gap, and it is explicitly momentum-dependent. In more practical terms, this means that the modulus of the Green's function will oscillate with a reduced frequency with respect to the free impurity, with each momentum having its own renormalised frequency. In the next chapter we will see that this oscillation reflects the actual oscillation of the impurity between the two baths. The typical behaviour of the correction to the gap is shown in figures 3.7. For a given momentum (figure 3.7a), its absolute value grows while increasing $J_\perp$, reaches its maximum, then slowly decreases. The $J_\perp$ yielding the maximum absolute is of the order of Mv^2, which is quite large. Notice that $\Delta J_\perp(p)$ is not analytic as $J_\perp \to 0$, where it behaves as $J_\perp \ln J_\perp$. As a function of momentum, figure 3.7b, the inter-bath hopping renormalisation is slightly increasing in modulus, before turning abruptly to zero as $|p|$ approaches the threshold Mv. In the small-coupling regime, $|\Delta J_\perp(p)| \ll J_\perp$, unless $J_\perp$ is exponentially small in $\tilde{g}$.

The overall shape modification of the two bands is rather minimal in the perturbative regime, except from a logarithmic divergence for $|p| \to Mv_\sigma$, coming from $\Delta E(p)$. Once again, this momentum region is likely to be outside of the region of validity of our model.

It is interesting to look at the effective dispersion of the two bands in the low-momentum regime:

$$\tilde{\lambda}_{e,o}(p) = \Delta E_0 + \frac{p^2}{2M_{e,o}} \mp (J_\perp + \Delta J_{\perp 0}) + \mathcal{O}\left(\left(\frac{p}{Mv_\sigma}\right)^4\right), \tag{3.1.37}$$

where the new band curvatures define two "effective masses"

$$\frac{M}{M_e} = 1 - \sum_\sigma \left(\frac{\tilde{g}_\sigma}{2\pi v_\sigma}\right)^2 \left[\frac{\mu_\sigma^2+2}{(1-\mu_\sigma)^2} - \frac{3\mu_\sigma}{(1-\mu_\sigma)^{5/2}} \operatorname{arccosh}\left(\tfrac{1}{\sqrt{\mu_\sigma}}\right)\right], \tag{3.1.38a}$$

$$\frac{M}{M_o} = 1 - \sum_\sigma \left(\frac{\tilde{g}_\sigma}{2\pi v_\sigma}\right)^2 \left[\frac{\mu_\sigma^2+2}{(1+\mu_\sigma)^2} + \frac{3\mu_\sigma}{(1+\mu_\sigma)^{5/2}} \operatorname{arcsinh}\left(\tfrac{1}{\sqrt{\mu_\sigma}}\right)\right]. \tag{3.1.38b}$$

We also introduced the constants

$$\Delta E_0 = \frac{M}{2(2\pi)^2} \sum_\sigma \tilde{g}_\sigma^2 \left[\ln \tfrac{4J_\perp}{\Lambda e^{-\gamma}} \tfrac{Mv_\sigma^2}{\Lambda e^{-\gamma}} + \tfrac{\operatorname{arcsinh}(1/\sqrt{\mu_\sigma})}{\sqrt{1+\mu_\sigma}} + \tfrac{\operatorname{arccosh}(1/\sqrt{\mu_\sigma})}{\sqrt{1-\mu_\sigma}}\right], \tag{3.1.39a}$$

$$\Delta J_{\perp,0} = \frac{M}{2(2\pi)^2} \sum_\sigma \tilde{g}_\sigma^2 \left[\tfrac{\operatorname{arcsinh}(1/\sqrt{\mu_\sigma})}{\sqrt{1+\mu_\sigma}} - \tfrac{\operatorname{arccosh}(1/\sqrt{\mu_\sigma})}{\sqrt{1-\mu_\sigma}}\right]. \tag{3.1.39b}$$

The first, ΔE_0, is just a UV-divergent overall energy shift, while ΔJ_0 is the constant part of the renormalisation of the gap between the bands. The behaviour of the two masses as a function of $J_\perp$ is shown in figure 3.8. They are always larger than the bare mass, but the two behave quite differently.

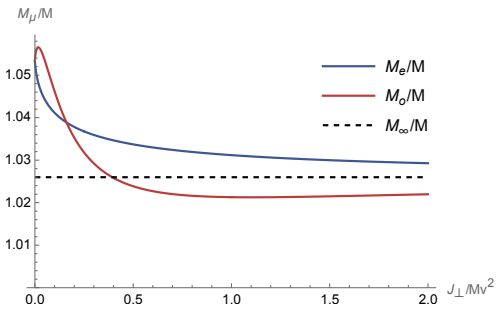

Figure 3.8: "Effective masses" of the even and odd mode [equations (3.1.38)] for the symmetric case, at a coupling $\tilde{g}^2 = 0.5v^2$. The dashed line shows the limiting value of both masses.

Both functions start with the same value $[1-2\sum_\sigma(\tilde{g}_\sigma/(2\pi v_\sigma))^2]^{-1}$ at $J_\perp = 0$ (as they should, because at $J_\perp = 0$ the impurity dispersion has only one band), but while the even mass decreases monotonically, the odd band mass first reaches a maximum[7], then decreases below the even mass and forms a very broad minimum. Eventually, the two masses converge to the same limit, $[1-\sum_\sigma(\tilde{g}_\sigma/(2\pi v_\sigma))^2]^{-1}$. Of course, the limit $J_\perp \to +\infty$ lies beyond the region of validity of our bosonised model.

We end this section by commenting about the physical interpretation of the effective masses we just computed, beyond the obvious definition of being the curvatures of the bands. This uncertainty arises because our 1D "polaron" is not a quasiparticle in the usual sense, because of the power-law decay of its Green's function. In the case of the even band, it is possible that effective mass defined above may actually have a dynamical meaning. This is because there are no states with energy below $\tilde{\lambda}_e(p)$, so we could imagine that the impurity prepared in the $p = 0$ ground state may follow the even band dispersion when adiabatically dragged by a very small constant force. However, this band is the lower edge of a continuum of states (whose density is actually diverging close to the threshold-see section 3.3), and thus there is no guarantee that adiabaticity will not break down as soon as the force is nonzero. For the upper band, the situation is even worse, as it is immersed in a continuum of states, and has a finite lifetime.

CUTOFF DEPENDENCE It is worth discussing the cutoff dependence of our results, both the general formulae (3.0.13) and the asymptotic ones (3.1.27). Relevant measurable quantities, like $\beta(p)$ and $\gamma(p)$, are independent of the high-energy physics of the baths. The same does not hold for the whole Green's function. The TLL cutoff Λ is involved only in two terms, through $\ln\Lambda$ in both cases. The first occurrence is within $\Delta E(p)$. This is perfectly reasonable, and this cutoff dependence enters simply as an overall energy shift. The second dependence is within the $C(p,t)$ and $D(p,t)$ functions, and it can be found also in their asymptotic coefficients $c_H^{0,\pm}$. These functions contribute with oscillating factors [see equation (3.0.14)] which cannot be accounted for by simple overall phases of the Green's function. Therefore, while in the case of equal baths $G_{\sigma',\sigma}(p,t)$ is well-defined except for an overall phase, when the baths are different the Green's function is cutoff-

7 When the speeds of sound of the baths are equal, this maximum occurs at $J_\perp \approx 0.016912 Mv^2$.

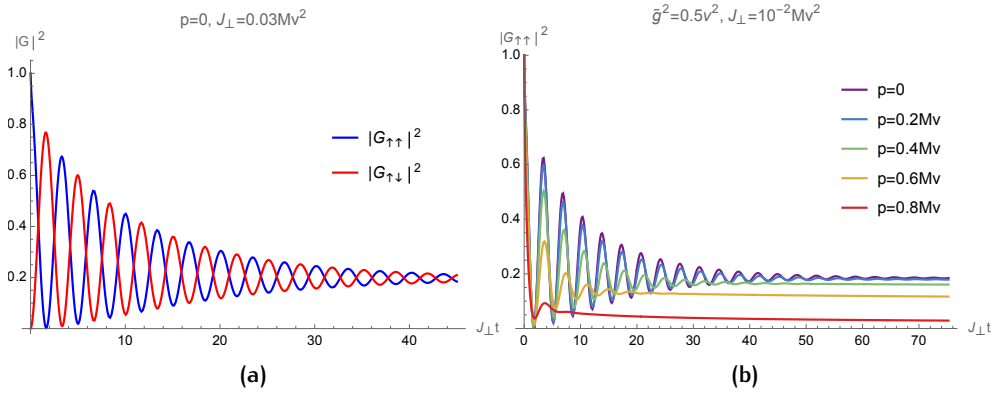

Figure 3.9: Green's function for symmetric baths, obtained numerically. (a) $G_{\uparrow\uparrow}$ and $G_{\uparrow\downarrow}$ have similar shapes, but they oscillate out of phase. (b) Coherence is lost at higher p. These plots allow to observe the relation between the oscillating and power-law regimes.

dependent.[8] The asymptotic expression equation (3.1.27) assures that even in the asymmetric case the cutoff dependence must be washed out for very long times, but the numerical results of section 3.2 show that this regime may require exceedingly long times.

3.2 NUMERICAL RESULTS FOR THE GREEN'S FUNCTION

In this section we analyse the behaviour of the full Green's function (3.0.13) obtained by direct numerical integration of equation (3.0.16), after the simplifications explained in the previous section. It thus complements the analytical results discussed so far.

The simplest case of symmetric baths is shown in figures 3.9 and 3.10b. We choose to display the quantity $|G_{\sigma\sigma'}|^2$, because it is easier to interpret, and also because for $\sigma = \sigma'$ it has the intuitive meaning of the probability of return to the initial state. The Green's function generally looks as follows: initially, $|G_{\sigma\sigma'}|^2$ oscillates at the renormalised frequency $2\tilde{J}_\perp(p)$ and with an amplitude that decays exponentially as $e^{-2\gamma(p)t}$. After a variable number of periods, the oscillations essentially disappear, and the absolute value of both $G_\parallel \equiv G_{\sigma\sigma}$ and of $G_\perp \equiv G_{\sigma\bar{\sigma}}$ become equal. In this regime, they decay as the very weak[9] power law $t^{-2\beta(p)}$. The diagonal $G_{\uparrow\uparrow} = G_{\downarrow\downarrow}$ and off-diagonal components share the same overall shape, with the only difference that their oscillations are out of phase (just as in the noninteracting case, equation (3.0.2a)). This is shown in figure 3.9a.

The asymptotic expression equation (3.1.27) is able to account for all these features. In fact, as we already pointed out before, for symmetric baths the equation (3.1.27) gives an excellent approximation of the full Green's function equation (3.0.13) basically for all times (except for $J_\perp t \lesssim 0.1$) when

8 The disappearance of the cutoff in the symmetric case requires that the two baths have the same value of Λ. We always assume that this is true, even for dissimilar baths.

9 Indeed, in the perturbative, low-momentum regime we are working in, $\beta(p)$ is a rather small number. From equation (3.1.31) it is easy to see that even for the possibly large value $\tilde{g}_\sigma = 1$, $\beta(0)$ is of the order of $1/(2\pi)^2 \approx 0.025$.

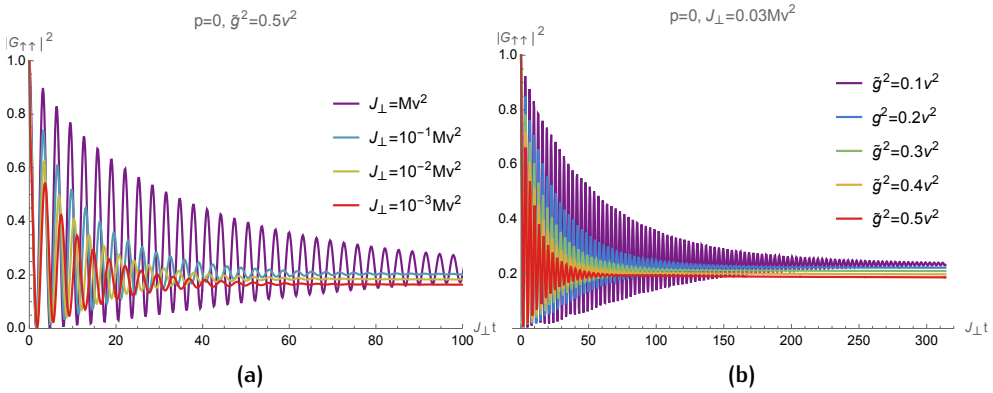

Figure 3.10: (a) Increasing $J_\perp$ causes the oscillations to live relatively longer (please notice that the timescale is $J_\perp t$). (b) Green's function for increasing strength of the impurity-bath interaction, showing how larger couplings quench the oscillations and decrease $|G|^2$.

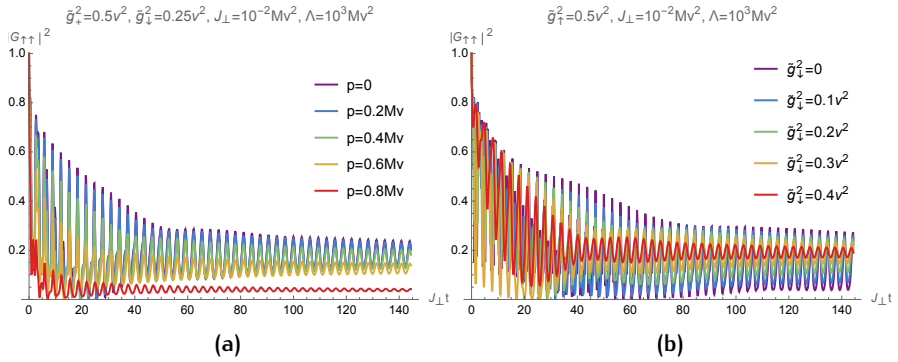

Figure 3.11: Numerically obtained $\left|G_{\uparrow\uparrow}(p,t)\right|^2$ when $\tilde{g}_\downarrow/v$ is lower than the fixed $\tilde{g}_\uparrow/v$. (a) The Green's function decreases faster at higher momenta. Inset: $|G_{\sigma\sigma}|^2$ is larger on the more interacting bath, although the difference decreases with time. (b) The amplitude of the oscillations increases the more different the baths are.

p is not too large. From equation (3.1.27), we can see that the oscillations of $|G(p,t)|^2$ are easily interpreted as a consequence of the interference between the even and odd contributions. As the antisymmetric mode decays, the oscillations disappear, and this is a manifestation of decoherence.

In figures 3.9b, 3.10a and 3.10b we show how the Green's function changes quantitatively as we vary various parameters and momentum. It can be observed that the number of oscillations before the power-law regime sets in decreases as p or $\tilde{g}_\sigma$ increase, or as $J_\perp$ tends to 0 (consistently with the observation that for $J_\perp = 0$ there cannot be any oscillation, obviously). This behaviour is in agreement with the property that the decay constant of the antisymmetric mode, $2\gamma(p)$, is an increasing function of p, $\tilde{g}_\sigma$ and $J_\perp$ (see its expression in equation (3.1.33)). Moreover, it can be noticed that a decrease in the number of oscillations is concomitant with a suppression the overall value of the Green's function. This can be traced back, at least partially, to the increase of $\beta(p)$ for larger momentum and/or coupling.

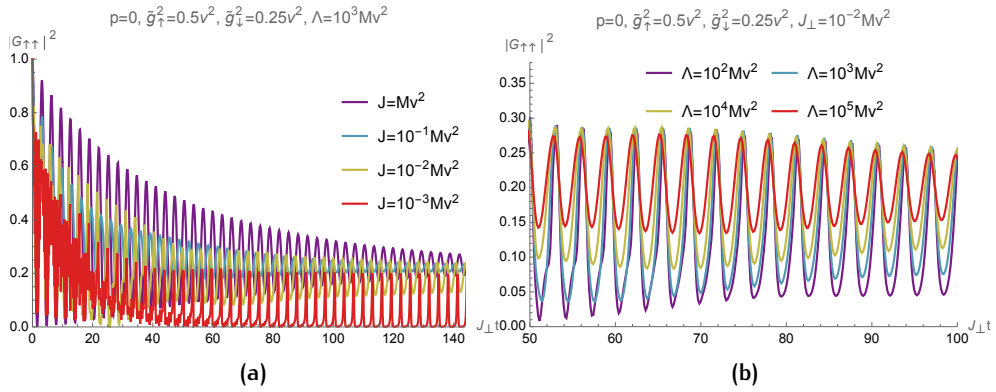

Figure 3.12: Plots of the Green's function for asymmetric baths as the inter-chain hopping is lowered. (a): a smaller $J_\perp$ causes $|G|^2$ to become noisier at early times and characteristically "spiked" at later times. (b) shows that a larger cutoff favours wider oscillations at late times.

When we introduce an asymmetry between the baths the Green's function changes rather drastically. The breaking of symmetry can be caused by either different bath parameters v_σ, K_σ or by different couplings g_σ.[10] Within our low-momentum approximation, g_σ and K_σ always appear together as the effective coupling $\tilde{g}_\sigma = g_\sigma K_\sigma^{1/2}$, but the actual dimensionless coupling constants are $\tilde{g}_\sigma/v_\sigma$. Therefore, we can choose to vary $\tilde{g}_\sigma$ only while keeping the sound speeds constant, because the following qualitative remarks are equally valid if $v_\uparrow \neq v_\downarrow$.

figures 3.11 and 3.12 show some examples of the Green's function for asymmetric baths. Comparing these plots with the corresponding ones in the symmetric case reveals that $|G(p,t)|^2$ increases or decreases when the parameters are varied in the same fashion. Apart from these large-scale qualitative tendencies, the plots are starkly different from the symmetric case. The most prominent feature is that the Green's function generally shows wider and more persisting oscillations.

Also in this case, we can distinguish two different regimes, namely short and longer times. The first few oscillation cycles are distinctly noisy, with peaks and valleys whose shapes become increasingly irregular for higher momenta and (overall) couplings (see figures 3.11a and 3.11b), and especially for the lowest $J_\perp$s (figure 3.12). We have observed that the detailed behaviour in this region depends strongly on the cutoff. This dependence suggests that this regime is dominated by the interference between the various terms of equation (3.0.13), each one quite sensitive to the value of Λ through the $C(p,t)$ and $D(p,t)$ functions.

At longer times the oscillations acquire a more regular shape, with a frequency $2\tilde{J}_\perp(p)$, and a slowly decreasing amplitude. These oscillations seem to be more persistent than in the symmetric scenario, so the power-law decline can be explicitly seen only by looking at the average (unless we go to extremely long times,). The variation of $\gamma(p)$ as $\tilde{g}_\sigma$ are changed does not appear to be responsible for this behaviour. In fact, we get the same results as

10 Strictly speaking, one could allow also for different cutoffs Λ_σ. We preferred to avoid this complication.

figure 3.11b even if we vary the couplings in a way to keep $\gamma(p)$ fixed. Moreover, this phenomenon is rather sharp, as a few percent difference between $\tilde{g}_\uparrow$ and $\tilde{g}_\downarrow$ is sufficient to observe it. Its root lies in the UV logarithmic divergence of the $C(p,t)$ and $D(p,t)$ functions, and this is confirmed by varying Λ, as we show int the inset in figure 3.12: a larger cutoff increases the depth of the oscillations (but leaves the maxima unchanged).

The above discussion implies that even for large times the $C(p,t)$ and $D(p,t)$ functions still have a relevant role in determining the Green's function, despite being asymptotically sub-leading. This is true in particular when $J_\perp$ is very small, as we show in figure 3.12. In this interesting parameter regime, the long-time oscillations have a distinctive "spiked" shape, which is keenly different from all the other cases discussed so far. We can hypotesise that the cutoff-dependence allows the coherence between the symmetric and antisymmetric modes to be retained longer, as soon as the two baths are made unequal. However, this can only be a qualitative explanation, because the explicit dependence of the Green's function on the cutoff means that its actual behaviour is sensitive to the details of the microscopic Hamiltonian of the baths, beyond the universal description provided by the TLL theory.

3.3 THE IMPURITY SPECTRAL FUNCTION

In this section, we compute and analyse the spectral function obtained from the LCE Green's function.

The spectral function

$$\hat{A}(p,\omega) \equiv -2\,\mathrm{Im}\,\hat{G}(p,\omega) \tag{3.3.1}$$

yields information about the energy spectrum of the theory [66], and in general it is a measurable quantity by means of radio-frequency spectroscopy [87]. In analogy with the calculation at the end of 2.3, we can have an analytical insight on the behaviour of $\hat{A}(p,\omega)$ from the asymptotic expansion, equation (3.1.27). We can already anticipate that we will find a power-law also in the frequency domain.

As $\hat{G}(p,t) \propto \theta(t)$, we have

$$\hat{G}(p,\omega) = \int_0^\infty dt\, e^{i\omega^+ t}\hat{G}(p,t) = \underbrace{\int_0^{\bar{t}} dt\, e^{i\omega^+ t}\hat{G}(p,t)}_{\hat{G}^{\mathrm{reg}}} + \underbrace{\int_{\bar{t}}^\infty dt\, e^{i\omega^+ t}\hat{G}(p,t)}_{\hat{G}^{\mathrm{as}}},$$

where $\omega^+ \equiv \omega + i0^+$ and $\bar{t}$ is an arbitrary time. We choose it to be large enough so that for later times we can well approximate the Green's function by its asymptotic expression (3.1.27). Then, the integral for $\hat{G}^{\mathrm{as}}$ is made of terms of the form

$$\int_{\bar{t}}^\infty dt\, \frac{e^{izt}}{t^\beta} = \begin{cases} \frac{\Gamma(1-\beta,-iz\bar{t})}{(-iz)^{1-\beta}}, & \text{if } \beta \neq 1\,, \\ E_1(-iz\bar{t}) & \text{if } \beta = 1\,, \end{cases}$$

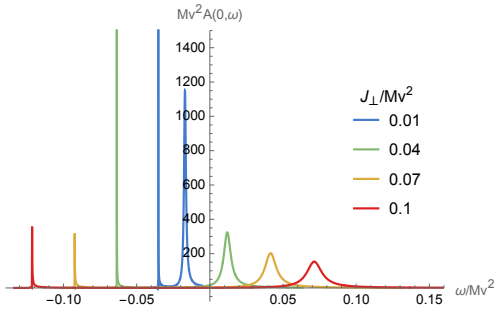

Figure 3.13: Numerically computed spectral function in the symmetric case, for $g^2K = 0.5v^2$, $p = 0$. At each value of $J_\perp$ the double-peak structure can be appreciated. The frequencies are measured with respect to the noninteracting impurity ground-state energy $E(p = 0)$.

where $\Gamma(a, z)$ is the incomplete Gamma function (see [23]). We are working in the regime of weak coupling and small impurity momentum, so we expect that $\beta(p) < 1$. The result is

$$G^{as}_{\sigma\sigma'}(p,\omega) \approx -\frac{i}{2} t_0^{\beta_p} \left\{ Z_e(p,t_0) \frac{\Gamma(1-\beta_p, -i(\omega^+ - \tilde{\lambda}_{pe})\bar{t})}{[-i(\omega^+ - \tilde{\lambda}_{pe})]^{1-\beta_p}} + \right.$$
$$\left. + \sigma\cdot\sigma' \, Z_o(p,t_0) \frac{\Gamma(1-\beta_p, -i(\omega - \tilde{\lambda}_{po} + 2i\gamma_p)\bar{t})}{[-i(\omega - \tilde{\lambda}_{po} + 2i\gamma_p)]^{1-\beta_p}} \right\},$$

where most of the momentum arguments have been transformed into subscripts to improve readability.

As we anticipated, the power-law decay at long times is mirrored by a power-law *divergence* at the frequencies of the renormalized bands.[11] On the contrary, $\hat{G}^{reg}$ is the integral of a regular function over a finite domain, so it yields a non-singular contribution to the Green's function. We can conclude that for $\beta(p) \leqslant 1$, and frequencies around $\tilde{\lambda}_e(p)$ (possibly, also around $\tilde{\lambda}_o(p)$), $\hat{G}^{as}$ is the dominant contribution:

$$G_{\sigma\sigma'}(p,\omega) \approx -\frac{i}{2} t_0^{\beta_p} \left\{ Z_e(p,t_0) \frac{\Gamma(1-\beta_p, -i(\omega^+ - \tilde{\lambda}_{pe})\bar{t})}{[-i(\omega^+ - \tilde{\lambda}_{pe})]^{1-\beta_p}} + \right.$$
$$\left. + \sigma\cdot\sigma' \, Z_o(p,t_0) \frac{\Gamma(1-\beta_p, -i(\omega - \tilde{\lambda}_{po} + 2i\gamma_p)\bar{t})}{[-i(\omega - \tilde{\lambda}_{po} + 2i\gamma_p)]^{1-\beta_p}} \right\} +$$
$$+ \text{ regular terms for } \omega \to \tilde{\lambda}_{e,o} \quad (3.3.2)$$

The imaginary part of the above expression features a threshold-like sharper peak at $\omega = \tilde{\lambda}_e(p)$ and a broadened one around $\omega = \tilde{\lambda}_o(p)$. These are, of course, the remnants of the original noninteracting bands, "dressed" by the phonons in the baths. This structure can be clearly appreciated in figure 3.13, which shows the result of the direct computation of $A_{\sigma\sigma}(p,\omega)$ from the numerical Fourier transform of the Green's function.

11 $\Gamma(a,z) = \Gamma(a) + \mathcal{O}(z)$ for $z \to 0$, so the singular behaviour does not change as long as $a \neq 0$, i.e. $\beta(p) \neq 1$. For $\beta(p) = 1$ one has a weaker logarithmic divergence.

We can also evaluate the analytical expression of the spectral function very close to $\tilde{\lambda}_e(p)$. In this region, we can further simplify the Green's function (3.3.2) to

$$G_{\sigma\sigma}(p,\omega) \sim -\frac{i}{2} t_0^{\beta_p} |Z_e(p,t_0)| \Gamma(1-\beta_p) \frac{e^{i\delta_e(p)}}{[-i(\omega^+ - \tilde{\lambda}_{pe})]^{1-\beta_p}} ,$$

where $\delta_e(p) \equiv \arg Z_e(p) = \mathrm{Im}(c_A(p,t_0) + c_B(p))$. Substituting $c_A(p)$ and $c_B(p)$ from equation (3.1.25) we obtain the interesting relation

$$\delta_e(p) = \mathrm{Im}(c_A(p,t_0) + c_B(p)) = -\frac{\pi}{2}\beta(p) .$$

Then

$$\begin{aligned} A_{\sigma\sigma}(p,\omega) &\equiv -2\,\mathrm{Im}(G_{\sigma\sigma}(p,\omega)) \sim \\ &\sim -t_0^{\beta_p} |Z_e(p,t_0)| \Gamma(1-\beta_p)\, \mathrm{Im}\left(\frac{-ie^{i\delta_e}}{[-i(\omega^+ - \tilde{\lambda}_{pe})]^{1-\beta_p}}\right) = \\ &= -t_0^{\beta_p} |Z_e(p,t_0)| \Gamma(1-\beta_p)\, \mathrm{Im}\left(\frac{(-i)^{2\beta_p}}{e^{i\pi(1-\beta_p)\theta(\tilde{\lambda}_{pe}-\omega)}}\right) = \\ &= -\frac{t_0^{\beta_p} |Z_e(p,t_0)| \Gamma(1-\beta_p)}{|\omega - \tilde{\lambda}_{pe}|^{1-\beta_p}}\, \mathrm{Im}\; e^{-i\pi((1-\beta_p)\theta(\tilde{\lambda}_{pe}-\omega)+\beta_p)} \end{aligned}$$

and finally[12]

$$A_{\sigma\sigma}(p,\omega) \sim \theta(\omega - \tilde{\lambda}_{pe}) t_0^{\beta_p} |Z_e(p,t_0)| \frac{\Gamma(1-\beta_p)\sin\beta_p\pi}{(\omega - \tilde{\lambda}_{pe})^{1-\beta_p}} . \tag{3.3.3}$$

The above equation clearly indicates that there is a threshold singularity at $\omega = \tilde{\lambda}_e(p)$: there are no eigenstates with energies below $\tilde{\lambda}_e(p)$, while immediately above it there is a (integrable) divergence of the density of states. This can be interpreted as the impurity becoming "dressed" with an arbitrarily large number of very low-energy phonons. This edge singularity is an a well-known feature of impurities in 1D [45, 50, 54, 66], and it is related to the well-known X-ray threshold problem. In fact, equation (3.3.3) shows a remarkable resemblance to the spectral function of the X-ray edge problem [66].

The higher-energy peak corresponds to an unstable state and has a width of order $2\gamma(p)$, but the shape is only approximately Lorentzian. If we assume that the expression (3.3.2) is the most relevant contribution also around the odd mode energy $\tilde{\lambda}_o(p)$, we can repeat a calculation similar to the one reported above to find that for $\omega \to \tilde{\lambda}_o(p)$

$$\begin{aligned} A_{\sigma\sigma}(p,\omega) \sim t_0^{\beta_p} |Z_o(p,t_0)| &\frac{\Gamma(1-\beta(p))}{\left[(\omega - \tilde{\lambda}_{po})^2 + 4\gamma_p^2\right]^{\frac{1-\beta_p}{2}}} \times \\ &\times \sin\left[\beta_p\pi - \delta_o(p) + (1-\beta_p)\arg(\omega - \tilde{\lambda}_{po} + 2i\gamma_p)\right] , \end{aligned} \tag{3.3.4}$$

where

$$\delta_o(p) \equiv \mathrm{Im}(c_A(p) - c_B(p)) + \frac{\pi}{2}\beta(p) = -\frac{M}{32\pi}\sum_{s,\sigma} \frac{\tilde{g}_\sigma^2}{k_{s\sigma}(p)\left(1 + \frac{2J_\perp}{k_{s\sigma}(p)}\right)^{3/2}} , \tag{3.3.5}$$

12 We notice, en passant, that $\Gamma(1-\beta_p)\sin\beta_p\pi = \pi/\Gamma(\beta_p)$ by a well-known relation of the Gamma function [23].

$\arg(\omega - \tilde{\lambda}_{po} + 2i\gamma_p) = \pi\theta(-\omega + \tilde{\lambda}_{po}) + \arctan\big(2\gamma_p/(\omega - \tilde{\lambda}_{po})\big)$ and we have approximated $\Gamma(1-\beta_p, -i(\omega - \tilde{\lambda}_{po} + 2i\gamma_p)\bar{t}) \approx \Gamma(1-\beta_p)$, which is accurate as long as $2\gamma_p\bar{t}$ and β_p are small. We can emphasise the difference with a usual quasiparticle peak by expanding the sine function in equation (3.3.4):

$$\begin{aligned} A_{\sigma\sigma}(p,\omega) \sim t_0^{\beta_p} |Z_o(p,t_0)| \frac{\Gamma(1-\beta(p))}{\left[(\omega - \tilde{\lambda}_{po})^2 + 4\gamma_p^2\right]^{1-\frac{\beta_p}{2}}} \times \\ \times \left\{ 2\gamma_p \cos\left[\beta_p(\arg(-\omega + \tilde{\lambda}_{po} + 2i\gamma_p)) - \delta_o(p)\right] + \right. \\ \left. + \omega \sin\left[\beta_p(\arg(-\omega + \tilde{\lambda}_{po} + 2i\gamma_p)) - \delta_o(p)\right] \right\} . \end{aligned} \tag{3.3.6}$$

In this expression, we can see two effects of the OC on the spectral function. The first is that the would-be Lorentzian peak $\left[(\omega - \tilde{\lambda}_{po})^2 + 4\gamma_p^2\right]^{-1}$ that is usually encountered in quasiparticle states is actually raised to the power $1 - \beta_p/2$, which means that its width is slightly enlarged. The second is caused by the terms in curly braces, which make the spectral function asymmetric around $\tilde{\lambda}_{po}$, increasing the spectral weight above the band with respect to below it. In the perturbative regime, the smallness of the OC exponent β_p implies that both effects are rather small (indeed, the terms in curly braces approximate to $2\gamma_p + \mathcal{O}(\tilde{g}^2/\nu^2)$), so these deviations are difficult to observe (see figure 3.13). Even with such a small β_p, the asymmetry of the peak would be visible if γ_p were sufficiently small, but this does not seem to be the case in the parameter regime we have investigated. However, it could still occur happen for the even mode in cases when it is endowed with a finite lifetime, such as in the case of a finite baths temperature (as considered in the next section) or in presence of external reservoirs of impurities [42].

3.4 LCE AT FINITE TEMPERATURE

In actual experiments, the temperature of the baths is always different from zero, and it can be significant for fermionic baths [9, 18, 51, 62]. Therefore, it is important to assess its effects on the Green's function computed in the previous section. In particular, it may affect the visibility of the initial oscillations (i.e increase decoherence) and the ease of observation of the power-law decay at longer times. In this section, we lay the foundations for this analysis.

Following [53], we can easily incorporate a finite temperature by extending the LCE to the nonequilibrium Green's function formalism [42], that allows us to work in real time.[13] Out of equilibrium, we have to consider (at least) two different Green's functions (for instance, the greater and the lesser), but the presence of only one impurity in the system implies that there is only one independent impurity Green's function:

$$\begin{aligned} G^{<}_{\sigma'\sigma}(p,t) &= 0 & G^{R}_{\sigma'\sigma}(p,t) &= \theta(t) G^{>}_{\sigma'\sigma}(p,t) \\ G^{>}_{\sigma'\sigma}(p,t) &\equiv -i\left\langle d_{p\sigma'}(t) d^{\dagger}_{p\sigma} \right\rangle & G^{A}_{\sigma'\sigma}(p,t) &= -\theta(-t) G^{>}_{\sigma'\sigma}(p,t) \end{aligned} . \tag{3.4.1}$$

13 Performing the LCE in the imaginary time formalism and then making the analytic extension to real time appears to yield the same results.

These relations are valid also for the free one, $(G_0)_{\sigma'\sigma}(p,t)$. Here, we are anticipating that, in analogy with the zero-temperature case, the interacting Green's function is diagonal in the momentum label p. The average $\langle\mathcal{O}\rangle = \mathrm{Tr}(\mathcal{O}\rho_0)$ is taken on the mixed state

$$\rho_0 \equiv |0\rangle\langle 0| \otimes \frac{e^{-\mathcal{H}_{\mathrm{bath}}/T}}{Z(T)}, \qquad Z(T) \equiv \mathrm{Tr}_{\mathrm{bath}}\, e^{-\mathcal{H}_{\mathrm{bath}}/T} \tag{3.4.2}$$

which is the thermal state of the baths[14] at temperature T (setting Boltzmann's constant $k_B = 1$) in the absence of the impurity. Because of equations (3.4.1) above we can make the LCE Ansatz either on the retarded (or advanced) or the greater component, as one necessarily implies the other. As usual with nonequilibrium Green's functions, the perturbative series is formally identical with the equilibrium one, the only difference being that the time convolutions run on the Keldysh contour, and we have to use Langreth rules [42] to go back on the real time axis. The Dyson equation for the retarded component coincides with the equilibrium one,

$$\hat{G}^R(p,t) = \hat{G}_0^R(p,t) + (\hat{G}_0^R * \hat{\Sigma}_2^R * \hat{G}_0^R)(p,t) + \dots\,, \tag{3.4.3}$$

with the usual hat notation for matrices in bath index space. Assuming the LCE Ansatz $\hat{G}^R(p,t) = \hat{G}_0^R(p,t)e^{\hat{F}_2(p,t)}$, we find that $\hat{F}_2(p,t)$ is determined by

$$\hat{G}_0^R(p,t)\hat{F}_2(p,t) = (\hat{G}_0^R * \hat{\Sigma}_2^R * \hat{G}_0^R)(p,t)\,, \tag{3.4.4}$$

in perfect correspondence with the zero-temperature scenario. The second-order self-energy defined on the Keldysh contour $\tau \in \mathcal{C}$ is formally identical with equation (3.0.4b):

$$\Sigma_{2\sigma}(p,\tau) = ig_\sigma^2 K_\sigma \frac{1}{L}\sum_{q\neq 0} V^2(q)(G_0)_{\sigma\sigma}(p-q,\tau)D_\sigma^0(q,\tau)\,. \tag{3.4.5}$$

Its retarded component is

$$\begin{aligned}\Sigma_{2\sigma}^R(p,t) = ig_\sigma^2 K_\sigma \frac{1}{L}\sum_{q\neq 0} V^2(q)\Big[&(G_0^R)_{\sigma\sigma}(p-q,t)D_\sigma^{0,<}(q,t) + \\ &+ (G_0^<)_{\sigma\sigma}(p-q,t)D_\sigma^{0,R}(q,t) + (G_0^R)_{\sigma\sigma}(p-q,t)D_\sigma^{0,R}(q,t)\Big] = \\ &= ig_\sigma^2 K_\sigma \frac{1}{L}\sum_{q\neq 0} V^2(q)(G_0^R)_{\sigma\sigma}(p-q,t)\Big[D_\sigma^{0,<}(q,t) + D_\sigma^{0,R}(q,t)\Big]\,.\end{aligned}$$

Since there is an overall $\theta(t)$ factor coming from G_0^R, we have $D_\sigma^{0,<}(q,t) + D_\sigma^{0,R}(q,t) = D_\sigma^{0,<}(q,t) + D_\sigma^{0,>}(q,t) - D_\sigma^{0,<}(q,t) = D_\sigma^{0,>}(q,t)$, from which we find

$$\begin{aligned}\Sigma_{2\sigma}^R(p,t) &= ig_\sigma^2 K_\sigma \frac{1}{L}\sum_{q\neq 0} V^2(q)(G_0^R)_{\sigma\sigma}(p-q,t)D_\sigma^{>,0}(q,t) = \\ &= ig_\sigma^2 K_\sigma \theta(t)\frac{1}{L}\sum_{q\neq 0} V^2(q)(G_0^>)_{\sigma\sigma}(p-q,t)D_\sigma^{>,0}(q,t)\,,\end{aligned} \tag{3.4.6}$$

14 The extension to different temperatures of the baths is straightforward, amounting to a mere substitution $T \to T_\sigma$ in the following formulae, and $B(\varepsilon,T) \to (B(\varepsilon,T_\uparrow) + B(\varepsilon,T_\downarrow))/2$ in the final results, $B(\varepsilon,T)$ being the Bose distribution.

which is noting but $\theta(t)\Sigma^{>}_{2\sigma}(p,t)$, as it could have been determined directly by taking the greater component of the self-energy. The retarded Green's function for the noninteracting impurity is the same as at zero temperature, equation (3.0.2), whereas

$$\begin{aligned} D^{0,>}_{\sigma}(q,t) &\equiv -i\left\langle (b^{\dagger}_{q\sigma}e^{i\nu_{\sigma}|q|t} + b_{-q\sigma}e^{-i\nu_{\sigma}|q|t})(b^{\dagger}_{-q\sigma} + b_{q\sigma})\right\rangle = \\ &= -i\big[1 + B(\nu_{\sigma}|q|)\big]e^{-i\nu_{\sigma}|q|t} - iB(\nu_{\sigma}|q|)e^{i\nu_{\sigma}|q|t}\ , \end{aligned} \tag{3.4.7}$$

where $B(\varepsilon) \equiv (e^{\varepsilon/T} - 1)^{-1}$ is the Bose distribution.

From now on, we will restrict ourselves to the symmetric case. For this setup it is convenient to work in the parity basis, in which $\hat{G}_0$ (and hence the LCE approximation of $\hat{G}$) is diagonal, and it turns out that $\hat{\tilde{F}}_2 = \hat{W}\hat{F}_2\hat{W}$ is diagonal, too. Here,

$$\hat{W} = \hat{W}^{\dagger} \equiv \frac{1}{2^{1/2}}\begin{pmatrix} 1 & 1 \\ 1 & -1 \end{pmatrix} \tag{3.4.8}$$

is the matrix that administers the change of basis from the bath index to the parity bands. The diagonal components of $\hat{\tilde{F}}_2$ are

$$\begin{aligned} (\tilde{F}_2)_{\mu\mu}(p,t) = -\sum_q \frac{W_q^2}{2L}\Big\{ & B(\nu|q|)\,\frac{1+i(\nu|q|+E(q)-E(p-q))t-e^{i(\nu|q|+E(q)-E(p-q))t}}{(\nu|q|+E(p)-E(p-q))^2} + \\ & + B(\nu|q|)\,\frac{1+i(\nu|q|+E(p)-E(p-q)-2\mu J_{\perp})t-e^{i(\nu|q|+E(p)-E(p-q)-2\mu J_{\perp})t}}{(\nu|q|+E(p)-E(p-q)-2\mu J_{\perp})^2} + \\ & + \big[1+B(\nu|q|)\big]\,\frac{1-i(\nu|q|+E(p-q)-E(p))t-e^{-i(\nu|q|+E(p-q)-E(p))t}}{(\nu|q|+E(p-q)-E(p))^2} + \\ & + \big[1+B(\nu|q|)\big]\,\frac{1-i(\nu|q|+E(p-q)-E(p)-2\mu J_{\perp})t-e^{-i(\nu|q|+E(p-q)-E(p)+2\mu J_{\perp})t}}{(\nu|q|+E(p-q)-E(p)+2\mu J_{\perp})^2}\Big\}\ , \end{aligned} \tag{3.4.9}$$

where $W_q \equiv gK^{1/2}V(q)$. Introducing the kernel

$$K_t(\varepsilon) \equiv \frac{1 - i\varepsilon t - e^{-i\varepsilon t}}{\varepsilon^2} \tag{3.4.10}$$

and going from momentum summations to integration in energy, we can write

$$(\tilde{F}_2)_{\mu\mu}(p,t) = -\tfrac{1}{2}\int d\varepsilon\,\Big[R^{abs}_p(\varepsilon) + R^{em}_p(\varepsilon)\Big]\,[K_t(\varepsilon) + K_t(\varepsilon + 2\mu J_{\perp})]\ , \tag{3.4.11}$$

where

$$R^{abs}_p(\varepsilon) \equiv \tfrac{1}{L}\sum_q W_q^2 B(\nu|q|)\delta(\nu|q| + E(p) - E(p-q) + \varepsilon) \tag{3.4.12}$$

is the density of states for absorption of thermally excited phonons, and

$$R^{em}_p(\varepsilon) \equiv \tfrac{1}{L}\sum_q W_q^2\big[B(\nu|q|) + 1\big]\delta(\nu|q| - E(p) + E(p-q) - \varepsilon) \tag{3.4.13}$$

is the density of states for emission of phonons. The latter can be separated into a stimulated and spontaneous emission part:

$$\begin{aligned} R^{em}_p(\varepsilon) &= \tfrac{1}{L}\sum_q W_q^2 B(\nu|q|)\delta(\nu|q| - E(p) + E(p-q) - \varepsilon) + \\ &\quad + \tfrac{1}{L}\sum_q W_q^2\delta(\nu|q| - E(p) + E(p-q) - \varepsilon) \equiv \\ &\equiv \Delta R^{em}_p(\varepsilon) + R_0(\varepsilon)\ . \end{aligned} \tag{3.4.14}$$

It is easy to recognise $R_0(\varepsilon)$ as equation (3.0.17). This means that the $\tilde{F}_2$ function can be split into a thermal contribution, and a zero-temperature contribution, which we already calculated in the previous section:

$$(\tilde{F}_2)_{\mu\mu}(p,t) = (\Delta\tilde{F}_2)_{\mu\mu}(p,t) + F_p(0,t) + F_p(-\mu J_\perp, t)\,. \tag{3.4.15}$$

Therefore, all the results obtained so far at zero temperature form part of the solution also at finite temperature, and we only need to assess the behaviour of the thermal contribution. We expect to find that the latter induces a thermal lifetime for both the even and the odd states of the impurity, and so we will focus on calculating it.

The absorption density of states for subsonic momentum $|p| < Mv$ reads

$$\begin{aligned} R_p^{\rm abs}(\varepsilon) = \tfrac{\tilde{g}^2}{(2\pi)^2}\Big\{ \tfrac{\theta(\varepsilon+k_+)}{(1+\varepsilon/k_+)^{1/2}} \Big[\tfrac{q_+^>(\varepsilon)}{v_+} B\left(vq_+^>(\varepsilon)\right) + \theta(-\varepsilon)\tfrac{q_-^>(\varepsilon)}{v_+} B\left(vq_-^>(\varepsilon)\right)\Big] + \\ + \tfrac{\theta(\varepsilon+k_-)}{(1+\varepsilon/k_-)^{1/2}} \Big[\tfrac{|q_-^<(\varepsilon)|}{v_+} B\left(v|q_-^<(\varepsilon)|\right) + \theta(-\varepsilon)\tfrac{|q_+^<(\varepsilon)|}{v_+} B\left(v|q_+^<(\varepsilon)|\right)\Big] \Big\}\,, \end{aligned} \tag{3.4.16}$$

where we recall that $v_\pm = v_\pm(p) \equiv v \pm p/M$ and $k_\pm = k_\pm(p) \equiv Mv_\pm^2/2 = (Mv \pm p)^2/(2M)$, while

$$q_\pm^>(\varepsilon) \equiv Mv_+ \left[1 \pm \left(1 + \tfrac{\varepsilon}{k_+(p)}\right)^{1/2}\right]\,, \tag{3.4.17a}$$

$$q_\pm^<(\varepsilon) \equiv Mv_- \left[-1 \pm \left(1 + \tfrac{\varepsilon}{k_-(p)}\right)^{1/2}\right]\,, \tag{3.4.17b}$$

are the positive and negative solutions to $v|q| + E(p) - E(p-q) + \varepsilon = 0$, respectively. Namely, $q_\pm^> \geqslant 0$ and $q_\pm^< \leqslant 0$, when they are real. For $\varepsilon > 0$ there are only two real solutions, whereas for $\min\{-k_+(p), -k_-(p)\} \leqslant \varepsilon \leqslant 0$ there are four. This means that $R_p^{\rm abs}(\varepsilon)$ has a jump discontinuity at $\varepsilon = 0$:

$$\begin{aligned} R_p^{\rm abs}(0^-) = \tfrac{\tilde{g}^2}{(2\pi)^2}\Big\{ \tfrac{1}{v_+}\left[q_+^>(0) B\left(vq_+^>(0)\right) + \tfrac{T}{v}\right] + \\ + \tfrac{1}{v_-}\left[|q_-^<(0)| B\left(v|q_-^<(0)|\right) + \tfrac{T}{v}\right]\Big\}\,, \end{aligned} \tag{3.4.18a}$$

$$R_p^{\rm abs}(0^+) = \tfrac{\tilde{g}^2}{(2\pi)^2}\Big\{ \tfrac{q_+^>(0)}{v_+} B\left(vq_+^>(0)\right) + \tfrac{|q_-^<(0)|}{v_-} B\left(v|q_-^<(0)|\right)\Big\}\,. \tag{3.4.18b}$$

More explicitly, in the above formulae $q_+^>(0) = 2Mv_+$ and $q_-^<(0) = -2Mv_-$, which means that the leading contribution to $R_p^{\rm abs}(0+\pm)$ is linear in temperature, for $T \ll Mv^2$.

For the stimulated emission part we have

$$\Delta R_p^{\rm em}(\varepsilon) = \tfrac{\tilde{g}^2}{(2\pi)^2}\theta(\varepsilon)\left[\tfrac{q_e^>(\varepsilon)}{v_-}\tfrac{B(vq_e^>(\varepsilon))}{(1+\varepsilon/k_-)^{1/2}} + \tfrac{|q_e^<(\varepsilon)|}{v_+}\tfrac{B(v|q_e^<(\varepsilon)|)}{(1+\varepsilon/k_+)^{1/2}}\right]\,, \tag{3.4.19}$$

where

$$q_e^>(\varepsilon) = Mv_-\Big[-1 + \left(1 + \tfrac{\varepsilon}{k_-(p)}\right)^{1/2}\Big] \geqslant 0\,, \tag{3.4.20a}$$

$$q_e^<(\varepsilon) = Mv_+\Big[1 - \left(1 + \tfrac{\varepsilon}{k_+(p)}\right)^{1/2}\Big] \leqslant 0 \tag{3.4.20b}$$

are the positive and negative solutions of $v|q| + E(p-q) - E(p) - \varepsilon = 0$, which exist only for $\varepsilon \geqslant 0$. This density of states has a finite limit for $\varepsilon \to 0^+$:

$$\Delta R_p^{\rm em}(0^+) = \tfrac{\tilde{g}^2}{(2\pi)^2}\left(\tfrac{1}{v_-} + \tfrac{1}{v_+}\right)\tfrac{T}{v}\,. \tag{3.4.21}$$

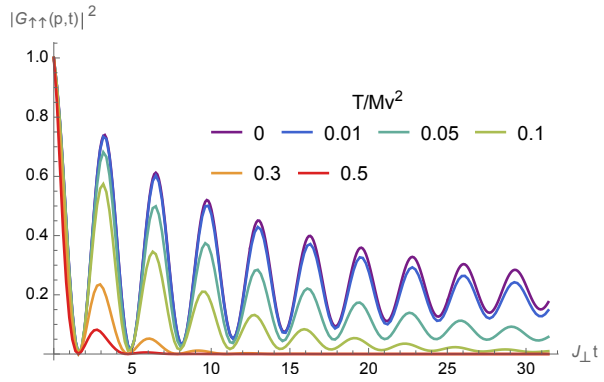

Figure 3.14: Effect of the temperature on the LCE Green's function, showing the increasing rate of decoherence as the temperature grows. The parameters are $g^2K = 0.5v^2$, $J_\perp = 0.1Mv^2$ and $p = 0$, for symmetric baths.

In general, both $R_p^{abs}(\varepsilon)$ and $\Delta R_p^{em}(\varepsilon)$ decrease exponentially for $\varepsilon \to +\infty$ and $T \to 0$, because of the presence of the Bose distributions.

Figure 3.14 shows the square modulus of the LCE Green's function, calculated numerically using equation (3.4.11). We can see that the main effect of temperature is to decrease its magnitude, and that the rate of decrease is particularly strong when $2J_\perp \lesssim T$, when only the very first oscillations can be clearly observed. This increased decay is of course to be expected on physical grounds, as the presence of thermally excited phonons in the baths can only increase the number of available decay channels. As the possibility of observing the coherent oscillations, and possibly measuring the the OC exponent, is limited by the enhanced decay rate, we now turn to its study.

3.4.1 Analytic results: thermal decay constant

From the discussion of equation (3.0.24) and from section 3.1.3, we know that at long times the imaginary part of $(\tilde{F}_2)_{\mu\mu}(p,t)$ quantifies the renormalisation of the impurity energy bands, whereas its real part contains the Green's function decay, either exponential or power-law. Therefore, we concentrate on the real part:

$$\mathrm{Re}(\Delta\tilde{F}_2)_{\mu\mu}(p,t) = -\frac{1}{2}\int d\varepsilon \left[R_p^{abs}(\varepsilon) + R_p^{em}(\varepsilon) + \right. \\ \left. + R_p^{abs}(\varepsilon - 2\mu J_\perp) + R_p^{em}(\varepsilon - 2\mu J_\perp)\right] \frac{1-\cos\varepsilon t}{\varepsilon^2} \,.$$

For long times, the kernel $(1-\cos\varepsilon t)/\varepsilon^2$ gets narrower and narrower, so that the most relevant contributions will come from $|\varepsilon| \lesssim t^{-1}$. From section 3.1 we know that any correction to the OC exponent, namely a term with a logarithmic dependence on t, would originate from a Ohmic density of states: $R(\varepsilon) \sim \varepsilon$ for $\varepsilon \to 0$. However, we just saw that the thermal contributions to the density of states are finite in this limit, and this rules out the possibility of a thermal correction to the OC exponent. The finite density of states at zero energy allows us to use a simple trick to obtain the thermal contribution

to the decay constant. We notice that the kernel is simply a smeared Dirac delta:

$$\lim_{t\to+\infty} \frac{1}{\pi t}\frac{1-\cos\varepsilon t}{\varepsilon^2} = \delta(\varepsilon)\ . \tag{3.4.22}$$

Then, we can get the leading contribution to $(\Delta\tilde{F}_2)_{\mu\mu}(p,t)$ at long times by simply replacing $(1-\cos\varepsilon t)/\varepsilon^2$ with $\pi t\delta(\varepsilon)$. We should just pay attention to the discontinuity of $R_p^{abs}(\varepsilon)$ at $\varepsilon = 0$, which is easily resolved because $(1-\cos\varepsilon t)/\varepsilon^2$ is an even function of ε, hence the weight of the nascent delta is equally distributed between positive and negative energies, and so we should take the average of the $\varepsilon \to 0^{\pm}$ limits. Analogously, the integral of the stimulated emission part is limited to $\varepsilon \geqslant 0$, and so we should attribute it a weight of $1/2$. The final result is

$$\mathrm{Re}(\Delta\tilde{F}_2)_{\mu\mu}(p,t) \sim -\gamma^{th}_{p\mu}t + \mathcal{O}(t^0)\ , \tag{3.4.23}$$

where

$$\gamma^{th}_{p\mu} \equiv \frac{\pi}{2}\Big[\frac{1}{2}\big(R_p^{abs}(0^-)+R_p^{abs}(0^+)\big)+\frac{1}{2}\Delta R_p^{em}(0^+)+ \\ +R_p^{abs}(-2\mu J_\perp)+\Delta R_p^{em}(-2\mu J_\perp)\Big] \tag{3.4.24}$$

is the sought thermal contribution to the decay constant. More explicitly,

$$\gamma^{th}_{pe} = \frac{\pi}{2}\Big[\frac{1}{2}\big(R_p^{abs}(0^-)+R_p^{abs}(0^+)\big)+\frac{1}{2}\Delta R_p^{em}(0^+)+R_p^{abs}(-2J_\perp)\Big]\ , \tag{3.4.25a}$$

$$\gamma^{th}_{po} \equiv \frac{\pi}{2}\Big[\frac{1}{2}\big(R_p^{abs}(0^-)+R_p^{abs}(0^+)\big)+\frac{1}{2}\Delta R_p^{em}(0^+)+ \\ +R_p^{abs}(2J_\perp)+\Delta R_p^{em}(2J_\perp)\Big]\ , \tag{3.4.25b}$$

where in the first equation $R_p^{abs}(-2J_\perp) \neq 0$ only if $2J_\perp \leqslant \max\{k_-(p), k_+(p)\}$. Therefore, we see that also the even mode acquires a finite lifetime, while the odd mode decay constant increases. Notice that the coherent oscillations of $|G_{\sigma'\sigma}(p,t)|^2 = [\sum_\mu |G_\mu(p,t)|^2 + 2\sigma'\sigma\,\mathrm{Re}(G_e^*(p,t)G_o(p,t))]/4$ arise from the interference term $\mathrm{Re}(G_e^*(p,t)G_o(p,t))$, so their amplitude decays with the constant

$$\gamma_p^{osc} \equiv \gamma^{th}_{pe} + \gamma^{th}_{po} + 2\gamma_p\ . \tag{3.4.26}$$

When $T \ll J_\perp, Mv^2$, namely when the temperature is the smallest energy scale, we can discard all the Bose functions present in the densities of states in equation (3.4.24) and we find that the decay constants of both bands are proportional to T:

$$\gamma^{th}_{p\mu} \approx \frac{\tilde{g}^2}{8\pi}\left(\frac{1}{v_+(p)}+\frac{1}{v_-(p)}\right)\frac{T}{v} = \frac{\tilde{g}^2}{4\pi v^2}\frac{T}{1-\left(\frac{p}{Mv}\right)^2}\ . \tag{3.4.27}$$

This formula is usually quite accurate, as the neglected terms are exponentially small in $v|q^{<>}(\pm 2J_\perp)|/T \sim \max\{Mv^2, 2J_\perp\}/T$. The above result is consistent with the one reported in [84] for an immobile impurity suddenly immersed in a gas of free fermions.[15]

15 In the cited ref., there is more than one contribution to the decay constant, because the full spectrum of free fermions is considered, and not only a low-energy approximation, so that different scattering processes may set in. Our decay constants should be compared with the "Fermi surface contribution" γ_0.

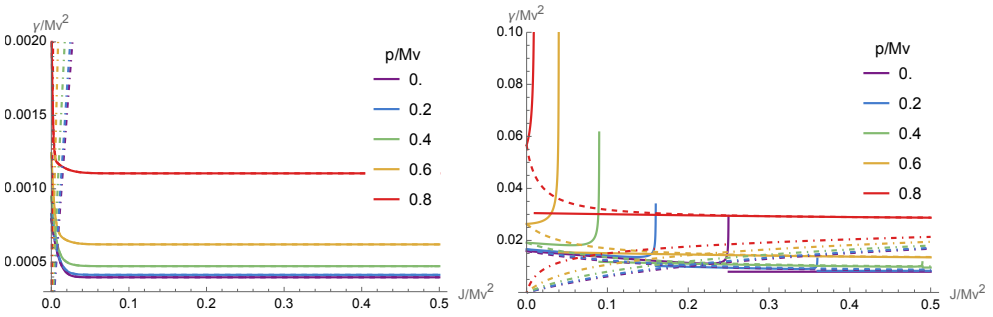

(a) $T = 0.01Mv^2$ **(b)** $T = 0.2Mv^2$

Figure 3.15: Plots of the thermal contributions to the decay constants as functions of $J_\perp$ and for various momenta p. Plot (a) is for low temperature $T = 0.01Mv^2$, while (b) is for the relatively high $T = 0.2Mv^2$. In each one, the continuous lines represent γ^{th}_{pe}, the dashed ones γ^{th}_{po} and the dotted-dashed show the zero-temperature contribution $2\gamma_p$ for comparison. The coupling constant is $g^2K = 0.5v^2$ for both graphs.

There is a case, however, in which the approximation (3.4.27) fails, namely when one of the singularities of $R^{\text{abs}}_p(\varepsilon)$ at $\varepsilon = -k_\pm(p)$ is hit. This condition requires $\varepsilon < 0$, so the singular behaviour affects only γ^{th}_{pe}, when the condition $2J_\perp \approx k_\pm(p)$ is satisfied. These divergences have the same origin as the well-known van Hove singularity of the density of states for free particles at zero energy in 1D [66]. Albeit virtually these singularities are always possible to reach, we will see that they can be observed only when some conditions are met: there is either a relatively large $J_\perp$ or a significant momentum p, $2J_\perp$ has to be very close to $k_\pm(p)$ and, moreover, the temperature has to be large enough (i.e. at least comparable to $2J_\perp$) so that the Bose factor does not suppresses the amplitude of the divergence.

We show the typical behaviour of the thermal decay constants (3.4.25) in figures 3.15. Plot 3.15a shows the low-temperature behaviour at $T = 0.01Mv^2$: γ^{th}_{pe} (continuous line) and γ^{th}_{po} (dashed line) are essentially coinciding, and show a steep decrease as $J_\perp$ increases beyond the temperature T. For $2J_\perp \gtrsim T$, both constants converge to the low-temperature limit equation (3.4.27). The plots also show that the decay constants increase with p.[16] They show very little variation until $p \approx 0.5Mv$, and then increase very rapidly as the supersonic threshold $p = Mv$ is approached. The plot also compares the thermal decay constants to the zero-temperature contribution to the decay constant of the odd mode, $2\gamma_p$ [equation (3.1.33)], displayed as a dashed-dotted line. It can be seen that at $T = 0.01Mv^2$, the thermal decay constants are usually only a tiny correction, except for $2J_\perp \lesssim T$, when they are the dominant ones because $\gamma^{\text{th}}_{p\mu}(J_\perp = 0)$ is finite, while $\gamma_p(J_\perp = 0) = 0$. Notice that the two constants always coincide at vanishing inter-bath hopping, $\gamma^{\text{th}}_{pe}(J_\perp = 0) = \gamma^{\text{th}}_{po}(J_\perp = 0) = 2\lim_{J_\perp \to +\infty} \gamma^{\text{th}}_{p\mu}$.

There are qualitatively new features in the second plot, figure 3.15b, which shows the situation for a relatively high temperature of $T = 0.2Mv^2$. The most visible feature is the presence of various divergences in γ^{th}_{pe}, in contrast

16 We recall that all these expressions are invariant under momentum inversion $p \to -p$, because of the time-reversal and inversion symmetry of the model.

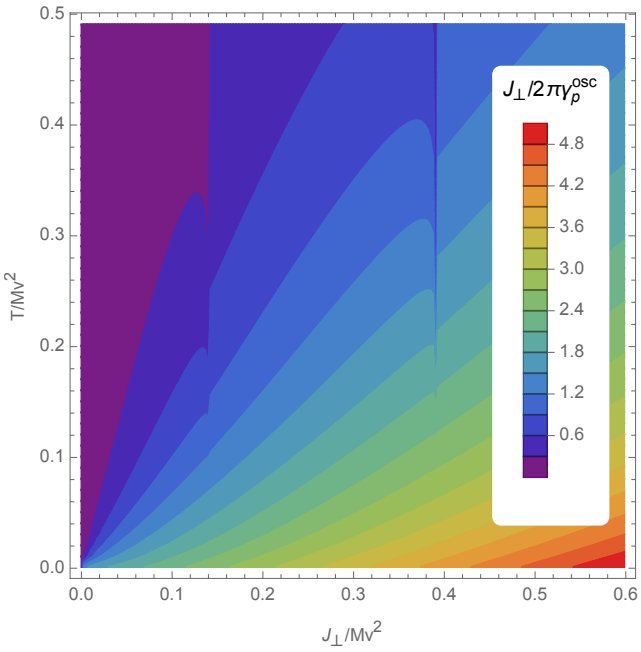

Figure 3.16: The behaviour of the figure of merit of the decoherence $J_\perp/(2\pi\gamma_p^{osc})$ as a function of temperature and inter-bath hopping. The larger the value, the more visible are the oscillations of the Green's function. The best visibility is attained for large $J_\perp$ and small T. The parameters are $g^2K = 0.5v^2$ and $p = 0.25Mv$.

with the smooth appearance of γ_{po}^{th}. As already noticed before, these are always present for $2J_\perp \approx -k_\pm(p)$, but for low temperature the amplitude of their rising part is exponentially reduced and they can be seen only infinitesimally close to the threshold, so that in plot 3.15a they seem to be absent. For $p \neq 0$, there are two of them, and as p increases there is one that comes closer to $J_\perp = 0$, while the other goes towards $J_\perp = Mv^2$. For $p = 0.2Mv$ and $p = 0.4Mv$ both peaks can be observed in figure 3.15b (for larger momentum, they occur beyond the range of $J_\perp$ shown), but the amplitude of the higher peaks is much more suppressed than the lowest ones, so that they are barely visible. Apart from these divergences, figure 3.15b allows us to observe how both decay constants coincide at $J_\perp \to 0$ and $J_\perp \to +\infty$, and that they generally decrease with $J_\perp$ (except for close to the singular points of γ_{pe}^{th}). Also, at this large temperature the thermal contributions to decoherence are comparable, or larger, than the one from the spontaneous decay, even if the latter surpasses the former in magnitude for a sufficiently large $J_\perp$ and low momentum. Notice that both plots in 3.15 would not change qualitatively if the coupling $gK^{1/2}$ were modified, because all decay constants are proportional to its square.

We can assess the influence of the finite temperature on the visibility of the oscillations of the Green's function by plotting the ratio of their characteristic decay time $1/\gamma_p^{osc}$, to the (noninteracting) oscillation period $2\pi/J_\perp$. We plot this figure of merit in figure 3.16. A large value of $J_\perp/(2\pi\gamma_p^{osc})$ means that it takes many oscillations before the Green's function becomes exponentially small. From the contour plot, we can observe that this situation can be ob-

tained by decreasing the temperature or increasing $J_\perp$.[17] If, for instance, we would like to have $J_\perp/(2\pi\gamma_p^{osc})$ larger than 2, we can infer that the temperature should be kept under about $J_\perp$. Of course, the singularities of γ_{pe}^{th} cause an infinitely fast decay (visible in figure 3.16 as two "cuts" in the contours at $J_\perp = 0.14Mv^2$ and $0.39Mv^2$) and should be avoided.

The visibility of the power-law decay at finite temperature depends crucially on keeping the thermal contributions to the decay as small as possible, which again implies small T and large $J_\perp$. As for any $T > 0$ also the even component of the Green's function is subjected to decoherence, there is no parameter regime in which the pure power-law decay can be observed (moreover, $\beta(p)$ cannot altered by neither T, nor $J_\perp$). Hence, in an experiment the value of the OC exponent could be computed only by fitting the data with the asymptotic form of the Green's function. Nevertheless, the clearest view of the would-be power-law regime occurs when the odd mode is completely decayed, while the even mode thermal decay should be as small as possible, so one should try to look into the regime in which $\gamma_{pe}^{th} \ll \gamma_p^{osc}$.

17 With the warning that if $J_\perp$ is too large the bosonisation approach we used for building our model is expected to break down, and so the validity of the plot becomes questionable. The threshold for this breakdown depends on the details of the microscopic Hamiltonian, hence on the experimental implementation of the model.

4 A GLOBAL VIEW

In this chapter[1] we take a more encompassing perspective on the impurity model we are examining. We do so by developing a perturbative expansion for the dynamics of the state of the whole system. We can then access the time evolution of observables both of the impurity and of the baths. At the end of the chapter, we give a first look to the generalisation of our model to more than two baths.

4.0.1 The Lee-Low-Pines transformation

The model considered so far, defined by equations (2.2.16), has translational invariance, thanks to the periodic boundary conditions we chose. This implies that the total system momentum (i.e. what we could call the polaron momentum) $P_{tot} = \sum_{p\sigma} p\, d^\dagger_{p\sigma} d_{p\sigma} + \sum_{q\neq 0,\sigma} q\, b^\dagger_{q\sigma} b_{q\sigma}$ is a conserved quantity. As it is usual in quantum mechanics, changing the basis to the one in which a conserved operator is diagonal allows for a great simplification[2]. In the context of polaron physics, i.e. of mobile impurities, this change of basis is known as the Lee-Low-Pines transformation [60]. Its form can be easily derived by the following argument. Suppose we want to build an eigenstate $|\psi_Q\rangle$ of the total momentum operator with eigenvalue Q. We can always decompose it as

$$|\psi_Q\rangle = \sum_{p,\sigma,\alpha} \psi(p,\sigma,\alpha)\, |p,\sigma\rangle_d\, |P_\alpha\rangle_b \ ,$$

where $|p\sigma\rangle_d$, $|P_\alpha\rangle_b$ are eigenstates of the impurity and baths momenta

$$P_d \equiv \sum_{p\sigma} p\, d^\dagger_{p\sigma} d_{p\sigma} \ ,$$
$$P_b \equiv \sum_{q\neq 0,\sigma} q\, b^\dagger_{q\sigma} b_{q\sigma}$$

with respective eigenvalues p and P_α. In the present model, the label α would be the list of all bosonic occupation numbers in the modes $q\sigma$ of the baths, and the states $|P_\alpha\rangle$ would coincide with the eigenstates of the unperturbed baths. We would like to impose $P_{tot}|\psi_Q\rangle = Q|\psi_Q\rangle$, which is satisfied if the state $|\psi_Q\rangle$ has components only on momentum states respecting the constraint $p + P_\alpha = Q$,

$$|\psi_Q\rangle = \sum_{\sigma,\alpha} \psi(p = Q - P_\alpha, \sigma, \alpha)\, |Q - P_\alpha, \sigma\rangle_d\, |P_\alpha\rangle_b \ .$$

1 This chapter is largely based on [91].

2 In the case of symmetric baths, there is also a conserved quantity for the transverse motion that allows a complete decoupling of the impurity from the baths: see appendix B.

We can re-write this state as follows. Let us define

$$X = a \sum_{j\sigma} j d^\dagger_{j\sigma} d_{j\sigma}$$

to be the impurity position operator.[3] Then, the operator e^{-iqX} (namely the Fourier transform of the impurity density operator) implements translations in momentum space, $e^{-iqX}|p,\sigma\rangle_d = |p-q,\sigma\rangle_d$, and so we can write

$$|\psi_Q\rangle = e^{-iP_b X} \sum_{\sigma,\alpha} \psi'(Q,\sigma,\alpha)\, |Q,\sigma\rangle_d\, |P_\alpha\rangle_b \ ,$$

where $\psi'(Q,\sigma,\alpha) \equiv \psi(p = Q - P_\alpha, \sigma, \alpha)$, which means that the eigenstates of the total momentum are obtained by applying $e^{-iP_b X}$ to states in which the impurity has momentum equal to the total momentum. The operator

$$U_{LLP} = e^{-iP_b X} \tag{4.0.1}$$

is the sought unitary change of basis [60]. This transformation acts on the annihilation operators as

$$U^\dagger_{LLP} d_{j\sigma} U_{LLP} = e^{-iajP_b} d_{j\sigma} \ , \tag{4.0.2a}$$

$$U^\dagger_{LLP} b_{q\sigma} U_{LLP} = e^{-iqX} b_{q\sigma} \ . \tag{4.0.2b}$$

In the single-impurity subspace of the Hilbert space we can use the relation $d^\dagger_{j\sigma} d_{j\sigma} e^{iqX} = e^{iqaj} d^\dagger_{j\sigma} d_{j\sigma}$, and we obtain the transformed Hamiltonian

$$\begin{aligned} \mathcal{H}_{LLP} \equiv U^\dagger_{LLP} \mathcal{H} U_{LLP} = \sum_{p\sigma} E(p - P_b) d^\dagger_{p\sigma} d_{p\sigma} - J_\perp \sum_{p\sigma} d^\dagger_{p\bar{\sigma}} d_{p\sigma} + \\ + \sum_{q\neq 0,\sigma} \varepsilon_{q\sigma} b^\dagger_{q\sigma} b_{q\sigma} + \sum_{q\neq 0,\sigma} \frac{W_{q\sigma}}{L^{1/2}} \sum_j d^\dagger_{j\sigma} d_{j\sigma} (b^\dagger_{q\sigma} + b_{-q\sigma}) \ . \end{aligned} \tag{4.0.3}$$

We can see the effect of the change of basis: the new Hamiltonian is decomposed in a sum over all impurity momentum sectors (recall that $\sum_j d^\dagger_{j\sigma} d_{j\sigma} = \sum_p d^\dagger_{p\sigma} d_{p\sigma}$), which is another way of saying that the impurity momentum P_d is now conserved. This conservation occurs because in the LLP frame P_d equals the total momentum of the system. We can work within a given momentum sector, corresponding with a given momentum eigenvalue p. The only dynamical impurity degree of freedom that is left is the bath index, which is conveniently described by the pseudo-spin variables

$$\sigma_i \equiv \sum_{p,\sigma,\sigma'} (\hat{\sigma}_i)_{\sigma\sigma'} d^\dagger_{p\sigma} d_{p\sigma'} = \sum_{j,\sigma,\sigma'} (\hat{\sigma}_i)_{\sigma\sigma'} d^\dagger_{j\sigma} d_{j\sigma'} \ . \tag{4.0.4}$$

In the above equation, $(\hat{\sigma}_i)_{\sigma\sigma'}$ is the i-th Pauli matrix. Taking into account that $\sum_{p\sigma} d^\dagger_{p\sigma} d_{p\sigma} = \mathbb{1}$ (i.e. there is only one impurity in the system), we can write

$$\begin{aligned} \mathcal{H}_{LLP}(p) = \frac{(p-P_b)^2}{2M} - J_\perp \sigma_1 + \sum_{q\neq 0,\sigma} \nu_\sigma |q| b^\dagger_{q\sigma} b_{q\sigma} + \\ + \sum_{q\neq 0,\sigma} \frac{W_{q\sigma}}{L^{1/2}} \frac{\mathbb{1} + \sigma\sigma_3}{2} (b^\dagger_{q\sigma} + b_{-q\sigma}) \ . \end{aligned} \tag{4.0.5}$$

3 In pbc the position operator is of course ill-defined. However, the operator e^{-iqX} is perfectly defined because all momenta q are quantized in multiples of $2\pi/L$, so that e^{-iqX} is periodic with period L. The same holds true for the LLP operator.

Thus, we end up with a Hamiltonian that is somewhat reminiscent of a spin-boson model [61]. We see that the price for disentangling the impurity momentum degree of freedom from the description is that the bath becomes interacting through the first term of equation (4.0.5). The latter reflects the phenomenon that phonons can indirectly exchange momentum between themselves by being adsorbed and emitted by the impurity. The Hamiltonian (4.0.5) will be the basis of the following analysis.

4.1 TIME-DEPENDENT PERTURBATION THEORY

As in the previous chapter, we assume that the baths have been initially prepared in their ground state $|\omega\rangle$, and that at time $t = 0$ the impurity is suddenly introduced in the system. In general, we allow the impurity to be in an arbitrary[4] wave packet:

$$|\Psi_{\text{lab}}(0)\rangle = \sum_{p\mu} c_{p\mu} |p\mu\rangle_d |\omega\rangle_b \ . \tag{4.1.1}$$

We use the labels lab and LLP to distinguish the state before and after the LLP transformation, respectively. As the baths are in their ground state, the transformation acts as the identity:

$$|\Psi_{\text{LLP}}(0)\rangle = U^\dagger_{\text{LLP}} |\Psi_{\text{lab}}(0)\rangle = \sum_{p\mu} c_{p\mu} |p\mu\rangle_d |\omega\rangle_b \ . \tag{4.1.2}$$

For the sake of readability, from now on we will omit the LLP label on the states, and use the label lab when needed.

4.1.1 Choice of the unperturbed Hamiltonian

We want to set up a perturbative expansion in powers of $g_\sigma K_\sigma^{1/2}/v_\sigma$ that is able to capture the OC. In the usual diagrammatic perturbation theory for the Green's function, this is accomplished by the so-called parquet resummation [33, 66], which is, however, rather unwieldy, especially for mobile impurities. Instead, we will pursue a less technical route by choosing an unperturbed Hamiltonian that already contains this phenomenon. We can better illustrate how such a Hamiltonian can be found in the case of symmetric baths, i.e. for $v_\sigma = v$, $K_\sigma = K$ and $g_\sigma = g$ (hence, $W_{q\sigma} \equiv W_q$). In this situation, it is natural to introduce even and odd bath modes, analogous to the impurity ones,

$$b_{q\mu=e/o} \equiv \tfrac{1}{2^{1/2}}(b_{q\uparrow} \pm b_{q\downarrow}) \ , \tag{4.1.3}$$

4 Almost arbitrary, actually. First, the number of momentum components is limited by the increasing computational cost, depending on the observables we measure. Second, we will always work in the subsonic regime, $|p| < M \min\{v_\uparrow, v_\downarrow\}$, and the validity of the long-wavelength model we are using is restricted to small p. This still leaves room for a large variety of wave packets.

and rewrite the Hamiltonian (4.0.5) as[5]

$$\mathcal{H}_{LLP}(p) = \frac{(p-P_e-P_o)^2}{2M} - J_\perp \sigma_1 + \sum_{q\neq 0} v|q| b^\dagger_{qe} b_{qe} + \sum_{q\neq 0} \frac{W_q}{(2L)^{1/2}}(b_{qe} + b^\dagger_{qe}) + \\ + \sum_{q\neq 0} v|q| b^\dagger_{qo} b_{qo} + \sigma_3 \sum_{q\neq 0} \frac{W_q}{(2L)^{1/2}}(b_{qo} + b^\dagger_{qo}) \,, \quad (4.1.4)$$

where

$$P_\mu \equiv \sum_{q\neq 0} q\, b^\dagger_{q\mu} b_{q\mu} \quad (4.1.5)$$

is the momentum of the μ bath modes. From the above equation (4.1.4) it is evident that the even and odd bath modes become partially independent of each other, and that they have different roles. In fact, the bath degree of freedom of the impurity is coupled only to the odd bath modes, and thus the deexcitation of the odd impurity band will directly generate only odd phonons. The even modes feel the effect of the impurity only indirectly, through the momentum-momentum coupling with the odd modes provided by the first term. If the impurity were fixed, namely for $M \to +\infty$, even and odd phonon modes would be completely decoupled from each other.

With this separation in mind, it is natural to attempt a first approximation in which the bath parity modes evolve independently. This would be exact if the impurity had infinite mass, but we can expect it to be approximately valid for a finite (but possibly large) mass if the coupling to the impurity is small. In this regime, the number of excited phonons should be small, and thus the product $P_e P_o/M$ should be small as well.[6] Moreover, odd phonon modes can be generated only when the impurity transitions between the even and odd bands, exchanging an energy of order $2J_\perp$ with the bath. In a perturbative perspective, this implies that the the number of excited odd phonons will be further suppressed by powers of $2J_\perp$. This hand-waving argument boils down to the following choice for the separation of the Hamiltonian in an unperturbed part $\mathcal{H}_0$ and a perturbation $\Delta\mathcal{H}$:

$$\mathcal{H}_{LLP}(p) = \mathcal{H}_0(p) + \Delta\mathcal{H}(p) \,, \quad (4.1.6a)$$

$$\mathcal{H}_0(p) \equiv E(p) - J_\perp \sigma_1 + \sum_{q\neq 0} \left[\Omega_q(p) b^\dagger_{qe} b_{qe} + \frac{W_q}{(2L)^{1/2}}(b_{qe} + b^\dagger_{qe})\right] + \\ + \sum_{q\neq 0} \Omega_q(p) b^\dagger_{qo} b_{qo} \,, \quad (4.1.6b)$$

$$\Delta\mathcal{H}(p) \equiv \sigma_3 \sum_{q\neq 0} \frac{W_q}{(2L)^{1/2}}(b_{qo} + b^\dagger_{qo}) + \frac{P_e P_o}{M} + \sum_\mu \frac{:P_\mu^2:}{2M} \,, \quad (4.1.6c)$$

where

$$\Omega_q(p) \equiv v|q| - \frac{qp}{M} + \frac{q^2}{2M} \quad (4.1.7)$$

5 Notice that we used $W_q = W_{-q}$ to change the sign of the momentum label of the annihilation operators in the coupling terms.

6 This low-density approach is similar to spin-wave theory in spirit [7].

and the colons $:\cdot:$ stand for normal-ordering with respect to the phonon vacuum $|\omega\rangle$. If we now go back to the σ basis for the bath and to the general situation, the separated Hamiltonian reads

$$\mathcal{H}_0(p) \equiv E(p) - J_\perp \sigma_1 + \\ + \sum_{q\neq 0,\sigma} \left[\Omega_{q\sigma}(p) b^\dagger_{q\sigma} b_{q\sigma} + \frac{W_{q\sigma}}{2L^{1/2}}(b^\dagger_{q\sigma} + b_{q\sigma})\right] , \tag{4.1.8a}$$

$$\Delta\mathcal{H}(p) \equiv \sigma_3 V + :\frac{P_b^2}{2M}: , \tag{4.1.8b}$$

$$V \equiv \sum_{q\neq 0,\sigma} \sigma \frac{W_{q\sigma}}{2L^{1/2}}(b^\dagger_{q\sigma} + b_{q\sigma}) , \tag{4.1.8c}$$

and we have introduced the shorthand

$$\Omega_{q\sigma}(p) \equiv v_\sigma |q| - \frac{qp}{M} + \frac{q^2}{2M} . \tag{4.1.9}$$

We also introduce the bath part of the unperturbed Hamiltonian,

$$h_0(p) \equiv \sum_{q\neq 0,\sigma} \left[\Omega_{q\sigma}(p) b^\dagger_{q\sigma} b_{q\sigma} + \frac{W_{q\sigma}}{2L^{1/2}}(b^\dagger_{q\sigma} + b_{q\sigma})\right] . \tag{4.1.10}$$

Notice that we chose to treat $:P_b^2:/2M$ as a perturbation, despite its formal independence of the coupling constant. This is justified when the initial bath state is the vacuum, as then phonons modes will start to be populated only because of the interaction. This is in the spirit of spin-wave theory for magnetic systems [1, 7].

The physical meaning of the particular splitting of the Hamiltonian can be seen from different perspectives. Firstly, we point out that $\mathcal{H}_0$ contains $g_\sigma K_\sigma^{1/2}$, so that the perturbative calculation we are going to describe actually yields an infinite-order result. This is akin to a resummation of the standard perturbative series for the Green's function, and from the previous chapter we know that this is necessary to correctly capture the OC. We can see that $\mathcal{H}_0$ incorporates "half" of the original interaction term, which is easily traced back through equation (4.0.3) to the intra-band processes $d^\dagger_{p-q\mu} d_{p\mu}$ before the LLP transformation. These are the only ones which may involve the exchange of arbitrarily small energies between the bath and the impurity, hence the only ones that can be responsible for the OC.[7] Thus, our choice of $\mathcal{H}_0$ is taking into account these processes in an exact way, and this is made possible only by the LLP transformation. The rest of the impurity-bath interaction is the term proportional to σ_3, which is nothing but the coupling of the phonons to inter-band processes. These processes always involve a finite amount of energy of order $2J_\perp$, and thus cannot modify the OC exponents at low perturbative order.

The take-home message of this hand-waving discussion is that our splitting of the Hamiltonian is equivalent to including intra-band processes exactly, while expanding in the inter-band ones (while assuming that the number of phonons is small, so that also the recoil term $:P_b^2/2M:$ can be considered to be a perturbation).

7 Of course, this is true only at low orders in perturbation theory. We expect the OC to be influenced by higher order processes, namely the absorption or emission of multiple phonons, because the evolution with $\mathcal{H}_0$ is able to provide only the leading-order term of $\beta(p)$.

A third way of rephrasing of the perturbative splitting of the Hamiltonian is that in the bath index basis we are splitting the impurity population in bath σ, $(\mathbb{1} + \sigma\sigma_3)/2$, into $\mathbb{1}/2$ and $\sigma\sigma_3/2$, and including the former into $\mathcal{H}_0$. In intuitive terms, we are choosing to incorporate in the unperturbed dynamics the interaction of the bath with the "averaged" impurity population, $1/2(\sum_j d^\dagger_{j\uparrow} d_{j\uparrow} + \sum_j d^\dagger_{j\downarrow} d_{j\downarrow}) = \mathbb{1}/2$. This choice can be expected to be sensible in the perturbative regime, namely when we are close to the free impurity behaviour, whose eigenstates $|p\mu\rangle$ occupy both baths with equal probability. In this scenario, we can say that $\mathcal{H}_0$ describes the modification of the baths arising from the very "presence" of the impurity in the system.

Apart from the question of how we can rationalise the choice of the unperturbed Hamiltonian, the foremost check of the sensibleness of this choice is that it fulfils the first goal that we stated at the beginning of this section, namely the ability of describing the OC. In fact, the zeroth-order approximation to the state already reproduces the LCE OC exponent, $\beta(p)$. In detail,

$$\left|\psi^{(0)}_{p\sigma}(t)\right\rangle = e^{-i\mathcal{H}_0 t} |p\sigma\rangle_d |\omega\rangle_b = e^{-i(E(p)-J_\perp \sigma_1)t} |p\sigma\rangle_d |\omega_p(t)\rangle_b \ , \quad (4.1.11)$$

where

$$|\omega_p(t)\rangle \equiv e^{-ih_0 t} |\omega\rangle = e^{i\,\mathrm{Im}\,F_p(0,t)} \left|\mathrm{coh}\Big[-\tfrac{W_{q\sigma}}{2L^{1/2}} \tfrac{1-e^{-i\Omega_{q\sigma}(p)t}}{\Omega_{q\sigma}(p)}\Big]\right\rangle \ , \quad (4.1.12)$$

is the zeroth order evolution of the initial bath vacuum state. The notation $|\mathrm{coh}[z_{q\sigma}]\rangle$ stands for a normalised coherent state [1]

$$|\mathrm{coh}[z_{q\sigma}]\rangle \equiv e^{\sum_{q\neq 0,\sigma} (z_{q\sigma} b^\dagger_{q\sigma} - z^*_{q\sigma} b_{q\sigma})} |\omega\rangle \ , \quad (4.1.13)$$

and the phase is written in terms of the $F_p(J=0,t)$ function introduced in the previous chapter. The impurity Green's function is

$$G_{\sigma',\sigma}(p,t) = -i \left\langle \psi^{(0)}_{p\sigma'}(0) \middle| \psi^{(0)}_{p\sigma}(t) \right\rangle = G^0_{\sigma',\sigma}(p,t) \langle\omega|\omega_p(t)\rangle \ , \quad (4.1.14)$$

where $G^0_{\sigma',\sigma}(p,t)$ is the free impurity Green's function, and $\langle\omega|\omega_p(t)\rangle$ is easily calculated using the property $\langle\omega|\mathrm{coh}[z_{q\sigma}]\rangle = \exp\left(-\frac{1}{2}\sum_{q\neq 0,\sigma} |z_{q\sigma}|^2\right)$ of coherent states, from which

$$\begin{aligned} \langle\omega|\omega_p(t)\rangle &= e^{i\,\mathrm{Im}\,F_p(0,t) - \frac{1}{2}\sum_{q\neq 0,\sigma} \frac{W^2_{q\sigma}}{4L} 2 \frac{1-\cos\Omega_{q\sigma}(p)t}{(\Omega_{q\sigma}(p))^2}} = \\ &= e^{F_p(J=0,t)} \sim t^{-\beta_p} \ , \end{aligned} \quad (4.1.15)$$

where $F_p(J,t)$ is the family of functions introduced in the previous chapter. As we claimed, the zeroth order approximation already gives a Green's function reminiscent of the LCE one, with the same OC exponent.

4.1.2 Improved perturbation theory

We are going to describe the technical details of the perturbative calculation of the time-evolved state. We are going to follow the procedure of Ref. [58], that is designed to avoid the appearance of secular terms. These are terms that grow indefinitely in time [8], whose presence invalidates the naive time-dependent perturbation theory.

We begin from the case in which the initial $|\Psi(0)\rangle$ is factorised as $|p\mu\rangle_d |\omega\rangle_b \equiv |p\mu,\omega\rangle \equiv |\Psi_{p\mu}(0)\rangle$. We will be able to reconstruct the general case of a wave packet by superposition of the result. As usual in perturbation theory, the first step is to go to the interaction picture:

$$\begin{aligned} |\Psi_{p\mu}(t)\rangle &= e^{-i\mathcal{H}_0 t} \left|\psi^I_{p\mu}(t)\right\rangle \ , \\ i\frac{d}{dt}\left|\psi^I_{p\mu}(t)\right\rangle &= \Delta\mathcal{H}(t)\left|\psi^I_{p\mu}(t)\right\rangle \ , \end{aligned} \tag{4.1.16}$$

where $\Delta\mathcal{H}(t) \equiv e^{i\mathcal{H}_0 t}\Delta\mathcal{H}e^{-i\mathcal{H}_0 t}$. Then, we split the vector $\left|\psi^I_{p\mu}(t)\right\rangle$ into a complex function $a_\mu(t)$ and a state $|\phi_{p\mu}\rangle$ that in general is not normalised to 1.

$$\left|\psi^I_{p\mu}(t)\right\rangle = a_{p\mu}(t)\,|\phi_{p\mu}(t)\rangle \ . \tag{4.1.17}$$

The arbitrariness of this splitting is removed requiring that

$$\langle p\mu,\omega|\phi_{p\mu}(t)\rangle \equiv 1 \tag{4.1.18}$$

at all times (and order by order in perturbation strength). This condition ensures that secular terms will be resummed to all orders into $a_{p\mu}(t)$. Substituting the equations above into the Schrödinger equation in the interaction picture we obtain a set of two independent equations for $a_{p\mu}(t)$ and $|\phi_{p\mu}(t)\rangle$:

$$i\frac{d}{dt}|\phi_{p\mu}(t)\rangle = (\Delta\mathcal{H}(t) - \Delta E_{p\mu}(t))\,|\phi_{p\mu}(t)\rangle \ , \tag{4.1.19a}$$

$$i\frac{da_{p\mu}}{dt} = \Delta E_{p\mu}(t)a_{p\mu},\ a_{p\mu}(0) = 1 \ , \tag{4.1.19b}$$

where

$$\Delta E_{p\mu}(t) \equiv \langle p\mu,\omega|\Delta\mathcal{H}(t)|\phi_{p\mu}(t)\rangle \ . \tag{4.1.19c}$$

The equation for $a_{p\mu}$ has been obtained by projecting the Schrödinger equation onto $|p\mu,\omega\rangle$. The equation for $a_{p\mu}$ is straightforwardly solved:

$$a_{p\mu}(t) = e^{-i\int_0^t dt' \Delta E_{p\mu}(t')} \ . \tag{4.1.20}$$

Of course, the above set of equations would be equivalent to the original Schrödinger equation if we were able to solve it exactly. Instead, we will solve it in a perturbative fashion, assuming the that the state $|\phi_{p\mu}(t)\rangle$ can be expanded in powers of $g_\sigma K_\sigma^{1/2}/v_\sigma$:

$$|\phi_{p\mu}(t)\rangle = |p\mu,\omega\rangle + \left|\phi^{(1)}_{p\mu}\right\rangle + \left|\phi^{(2)}_{p\mu}\right\rangle + \dots \ , \tag{4.1.21}$$

where $\left|\phi^{(n)}_{p\mu}\right\rangle = \mathcal{O}\left([g_\sigma K_\sigma^{1/2}/v_\sigma]^n\right)$. As the condition equation (4.1.18) must be satisfied order by order, the vectors $\left|\phi^{(n)}_{p\mu}\right\rangle$ are orthogonal to the initial state $|p\mu,\omega\rangle$. Substituting the above expansion in equations (4.1.19a) and (4.1.19c), and matching terms of the same order, we generate a hierarchy of equations for $\left|\phi^{(n)}_{p\mu}(t)\right\rangle$. Owing to equation (4.1.19c), the function $\Delta E_{p\mu}(t)$ is itself a series in powers of the coupling, and the result at a given order is then substituted into equation (4.1.20), namely it appears in the exponent,

yielding a formally infinite-order approximation. In the present case, the matching of powers of $g_\sigma K_\sigma^{1/2}/v_\sigma$ is non-trivial because $\mathcal{H}_0$ already contains the coupling constant, and because the perturbation contains the recoil term $:\frac{P_b^2}{2M}:$, which is formally of order 0. This means that $\Delta\mathcal{H}(t)\left|\phi_{p\mu}^{(n)}\right\rangle$ may give terms of different orders, greater or equal to n.

In more detail, the interaction-picture perturbation Hamiltonian is

$$\begin{aligned}\Delta\mathcal{H}(t) &\equiv e^{i\mathcal{H}_0 t}\big(\sigma_3 V + :\tfrac{P_b^2}{2M}:\big)e^{-i\mathcal{H}_0 t} = \\ &= \sigma_3(t)\big(\hat{V}(t) + \langle V(t)\rangle\big) + :\tfrac{P_b^2}{2M}:(t)\end{aligned} \tag{4.1.22}$$

where[8]

$$\sigma_3(t) = \sum_\mu e^{-2i\mu J_\perp t}\,|p\mu\rangle\langle p\bar{\mu}|\,, \tag{4.1.23a}$$

$$\hat{V}(t) = \sum_{q\neq 0,\sigma} \sigma \tfrac{W_{q\sigma}}{2L^{1/2}}\big(b_{q\sigma}e^{-i\Omega_{q\sigma}t} + b_{q\sigma}^\dagger e^{i\Omega_{q\sigma}t}\big)\,, \tag{4.1.23b}$$

$$\langle V(t)\rangle = -2\sum_{q\neq 0,\sigma} \sigma \tfrac{W_{q\sigma}^2}{4L}\tfrac{1-\cos\Omega_{q\sigma}t}{\Omega_{q\sigma}}\,, \tag{4.1.23c}$$

and for brevity we avoid to expand the last term. In the following, we will use the property

$$\sigma_3(t)\,|p\mu\rangle = e^{2i\mu J_\perp t}\,|p\bar{\mu}\rangle\ . \tag{4.1.24}$$

Now we insert the perturbative expansion of $|\phi_{p\mu}\rangle$ in equation (4.1.19). The initial state generates terms of first to fourth order:

$$\begin{aligned}\Delta\mathcal{H}(t)\,|p\mu,\omega\rangle = \sum_{q\neq 0,\sigma} &\sigma\tfrac{W_{q\sigma}}{2L^{1/2}}e^{i\Omega_{q\sigma}^{+\mu}(p)t}b_{q\sigma}^\dagger\,|p\bar{\mu},\omega\rangle + \\ &+ e^{2i\mu J_\perp t}\,\langle V(t)\rangle\,|p\bar{\mu},\omega\rangle + \tfrac{:P_b^2:}{2M}(t)\,|p\mu,\omega\rangle\ .\end{aligned} \tag{4.1.25}$$

Once more, we have introduced a new shorthand

$$\Omega_{q\sigma}^{\pm\mu}(p) \equiv \Omega_{q\sigma}(p) \pm 2\mu J_\perp\ . \tag{4.1.26}$$

The last term $\frac{:P_b^2:}{2M}(t)\,|p\mu,\omega\rangle$ generates contributions from second to fourth order. If we assume that $\frac{:P_b^2:}{2M}(t)\left|\phi_{p\mu}^{(1)}(t)\right\rangle$ is of second order (to be verified *a posteriori*), then there is no first-order contribution to $\Delta E_{p\mu}(t)$, and the first-order equation is simply

$$i\frac{d}{dt}\left|\phi_{p\mu}^{(1)}(t)\right\rangle = \sigma_3(t)\hat{V}(t)\,|p\mu,\omega\rangle\ , \tag{4.1.27}$$

which is easily integrated:

$$\left|\phi_\mu^{(1)}(t)\right\rangle = \sum_{q\neq 0,\sigma}\sigma\tfrac{W_{q\sigma}}{2L^{1/2}}\tfrac{1-e^{i\Omega_{q\sigma}^{+\mu}t}}{\Omega_{q\sigma}^{+\mu}}b_{q\sigma}^\dagger\,|p\bar{\mu}\omega\rangle\,. \tag{4.1.28}$$

From this result, it is easily verified that $\frac{:P_b^2:}{2M}(t)\left|\phi_{p\mu}^{(1)}(t)\right\rangle$ is of second order, as claimed above. The correct (perturbative) normalisation of the state is guaranteed by computing $\Delta E_{p\mu}(t)$ to the second order:

$$\Delta E_{p\mu}(t) = \Delta E_{p\mu}^{(2)}(t) = \left\langle \mu\omega\middle|\sigma_3(t)\hat{V}(t)\middle|\phi_\mu^{(1)}(t)\right\rangle = -\sum_{q\sigma}\tfrac{W_{q\sigma}^2}{4L}\tfrac{1-e^{-i\Omega_{q\sigma}^{+\mu}t}}{\Omega_{q\sigma}^{+\mu}}\,.$$

8 Notice that $\langle V(t)\rangle$ is logarithmically divergent in the TLL cutoff if the baths are asymmetric.

Then, the normalisation factor is:

$$a_{p\mu}(t) = e^{-i\int_0^t dt_1 \Delta E^{(2)}_{p\mu}(t_1)} = e^{-\sum_{q\sigma} \frac{W_{q\sigma}^2}{4L} \frac{1-i\Omega^{+\mu}_{q\sigma} t - e^{-i\Omega^{+\mu}_{q\sigma} t}}{(\Omega^{+\mu}_{q\sigma})^2}} = e^{F_p(-\mu J_\perp, t)} \ . \tag{4.1.29}$$

For the computation of inter-bath correlation functions we will need also the second-order correction to $|\phi_{p\mu}(t)\rangle$, which is more involved. The perturbative procedure requires that we find the various second-order contributions among all terms in the expansion:

$$\begin{aligned}
&(\Delta\mathcal{H}(t)\,|p\mu,\omega\rangle)^{(2)} = e^{2i\mu J_\perp t}\,\langle V(t)\rangle\,|p\bar{\mu},\omega\rangle + \\
&+ \sum_{q\sigma,q'\sigma'} \frac{q q'}{2M} \frac{W_{q\sigma}W_{q'\sigma'}}{4L} \chi^*_t(\Omega_{q\sigma})\chi^*_t(\Omega_{q'\sigma'}) b^\dagger_{q\sigma} b^\dagger_{q'\sigma'}\,|p\mu,\omega\rangle \ , \qquad (4.1.30a) \\
&\left(\Delta\mathcal{H}(t)\left|\phi^{(1)}_{p\mu}\right\rangle(t)\right)^{(2)} = \Delta E^{(2)}_{p\mu}\,|p\mu,\omega\rangle + \\
&+ \sum_{q\sigma,q'\sigma'} \sigma\sigma' \frac{W_{q\sigma}W_{q'\sigma'}}{4L} \chi^*_t(\Omega^{+\mu}_{q\sigma}(p)) e^{i\Omega^{-\mu}_{q'\sigma'} t} b^\dagger_{q\sigma} b^\dagger_{q'\sigma'}\,|p\mu,\omega\rangle + \\
&+ \sum_{q\sigma,q'\sigma'} \sigma \frac{q q'}{M} \frac{W_{q\sigma}W_{q'\sigma'}}{4L} \chi^*_t(\Omega^{+\mu}_{q\sigma}(p))\chi^*_t(\Omega_{q'\sigma'}(p)) b^\dagger_{q\sigma} b^\dagger_{q'\sigma'}\,|p\bar{\mu},\omega\rangle \ . \qquad (4.1.30b)
\end{aligned}$$

In the above equations we introduced the function

$$\chi_t(\varepsilon) \equiv \frac{1-e^{-i\varepsilon t}}{\varepsilon} \tag{4.1.31}$$

to lighten the formulae. We can see that the second-order terms either involve no phonon creation operators or two of them. The first set comprises the first term on the right-hand side of equation (4.1.30a) and the first term on the right-hand side of equation (4.1.30b). The former yields

$$\begin{aligned}
\left|\delta_1\phi^{(2)}_{p\mu}(t)\right\rangle &= -i\int_0^t dt'\, e^{2i\mu J_\perp t}\,\langle V(t')\rangle\,|p\bar{\mu},\omega\rangle = \\
&= \tfrac{1}{2\mu J_\perp} \sum_{q\neq 0,\sigma} \sigma \tfrac{W^2_{q\sigma}}{4L} \big[e^{2i\mu J_\perp t} 2\,\mathrm{Re}\,\chi_t(\Omega_{q\sigma}(p)) + \\
&\quad - \chi_t(\Omega^{-\mu}_{q\sigma}(p)) - \chi^*_t(\Omega^{+\mu}_{q\sigma}(p))\big]\,|p\bar{\mu},\omega\rangle \equiv \\
&\equiv B_{p\mu}(t)\,|p\bar{\mu},\omega\rangle \ . \qquad (4.1.32)
\end{aligned}$$

The latter would integrate to the secular term $-i\Delta E^{(2)}_{p\mu} t\,|p\mu,\omega\rangle$, but it is exactly cancelled by the perturbative procedure [see equation (4.1.19)].

The remaining contributions involve pairs of bosonic creation operators and, in analogy with the first-order correction equation (4.1.28), we assume that they give rise to a state of the form

$$\left|\delta_2\phi^{(2)}_{p\mu}(t)\right\rangle = \sum_\nu \sum_{q\sigma,q'\sigma'} A^{\mu\nu}_{q\sigma,q'\sigma'}(p,t) b^\dagger_{q\sigma} b^\dagger_{q'\sigma'}\,|p\nu,\omega\rangle \ , \tag{4.1.33}$$

where $A^{\mu\nu}_{q\sigma,q'\sigma'}(p,t)$ is assumed to be of order two in the interaction, and symmetric upon exchange of $q\sigma$ with $q'\sigma'$. Then, we see that the action

of the recoil term $: P_b^2/2M : (t) \left|\delta_2\phi^{(2)}_{p\mu}(t)\right\rangle$ generates a term of the second order:

$$\left(\Delta\mathcal{H}(t)\left|\delta_2\phi^{(2)}_{p\mu}\right\rangle(t)\right)^{(2)} = \tfrac{P_b^2}{2M}\left|\phi^{(2)}_{p\mu}(t)\right\rangle = \\ = \sum_{\nu}\sum_{q\sigma,q'\sigma'} \tfrac{qq'}{M} A^{\mu\nu}_{q\sigma,q'\sigma'}(p,t) b^\dagger_{q\sigma} b^\dagger_{q'\sigma'} |p\nu,\omega\rangle \ . \tag{4.1.34}$$

The second order is the lowest order at which we loose the usual hierarchical structure of perturbative expansions, in which terms of order n are the sources for the next order. Nonetheless, the equation for $A^{\mu\nu}_{q\sigma,q'\sigma'}(t)$ is linear and thus solvable:

$$i\frac{d}{dt}\left|\delta_2\phi^{(2)}_{p\mu}(t)\right\rangle = \sum_{\nu}\sum_{q\sigma,q'\sigma'} i\frac{d}{dt}A^{\mu\nu}_{q\sigma,q'\sigma'}(p,t) b^\dagger_{q\sigma} b^\dagger_{q'\sigma'} |p\nu,\omega\rangle = \\ = \sum_{\nu}\sum_{q\sigma,q'\sigma'} \left(\tfrac{qq'}{M} A^{\mu\nu}_{q\sigma,q'\sigma'}(p,t) + S^{\mu\nu}_{q\sigma,q'\sigma'}(p,t)\right) b^\dagger_{q\sigma} b^\dagger_{q'\sigma'} |p\nu,\omega\rangle \ , \tag{4.1.35}$$

where we merged all terms in equations (4.1.30a) and (4.1.30b) that involve two creation operators into the matrix $S^{\mu\nu}_{q\sigma,q'\sigma'}(p,t)$. If we multiply the above equation by $\langle p\nu,\omega| b_{q'\sigma'} b_{q\sigma}$ to the left, and we take into account that, unlike $A^{\mu\nu}_{q\sigma,q'\sigma'}(p,t)$, $S^{\mu\nu}_{q\sigma,q'\sigma'}(p,t)$ is not symmetric under exchange of $q\sigma$ and $q'\sigma'$, we find

$$i\frac{d}{dt}A^{\mu\nu}_{q\sigma,q'\sigma'}(p,t) = \tfrac{qq'}{M}A^{\mu\nu}_{q\sigma,q'\sigma'}(p,t) + \tfrac{1}{2}\left(S^{\mu\nu}_{q\sigma,q'\sigma'}(p,t) + S^{\mu\nu}_{q'\sigma',q\sigma}(p,t)\right) \ , \tag{4.1.36}$$

which is readily integrated with the initial condition $A^{\mu\nu}_{q\sigma,q'\sigma'}(p,0) = 0$ (because $\left|\phi^{(n)}_{p\mu}(t=0)\right\rangle = 0 \ \forall n \geqslant 1$):

$$A^{\mu\nu}_{q\sigma,q'\sigma'}(p,t) = -\tfrac{i}{2}e^{-i\frac{qq'}{M}t}\int_0^t dt' \, e^{i\frac{qq'}{M}t'}\left(S^{\mu\nu}_{q\sigma,q'\sigma'}(p,t') + S^{\mu\nu}_{q'\sigma',q\sigma}(p,t')\right) \ .$$

The integral yields

$$A^{\mu\mu}_{q\sigma,q'\sigma'}(p,t) = \tfrac{W_{q\sigma}W_{q'\sigma'}}{4L}\Big\{\tfrac{qq'}{2M}\tfrac{1}{\Omega_{q\sigma}\Omega_{q'\sigma'}}\times \\ \times\left[e^{i\Omega_{q\sigma}t}\chi_t(\Omega_{q\sigma}+\tfrac{qq'}{M}) + e^{i\Omega_{q'\sigma'}t}\chi_t(\Omega_{q'\sigma'}+\tfrac{qq'}{M}) + \right. \\ \left. -\chi_t(\tfrac{qq'}{M}) - e^{i(\Omega_{q\sigma}+\Omega_{q'\sigma'})t}\chi_t(\Omega_{q\sigma}+\Omega_{q'\sigma'}+\tfrac{qq'}{M})\right] + \\ + \tfrac{\sigma\sigma'}{2}\Big[\tfrac{1}{\Omega^{+\mu}_{q'\sigma'}}\left(e^{i(\Omega_{q\sigma}+\Omega_{q'\sigma'})t}\chi_t(\Omega_{q\sigma}+\Omega_{q'\sigma'}+\tfrac{qq'}{M}) - e^{i\Omega^{-\mu}_{q\sigma}t}\chi_t(\Omega^{-\mu}_{q\sigma}+\tfrac{qq'}{M})\right) + \\ + \tfrac{1}{\Omega^{+\mu}_{q\sigma}}\left(e^{i(\Omega_{q\sigma}+\Omega_{q'\sigma'})t}\chi_t(\Omega_{q\sigma}+\Omega_{q'\sigma'}+\tfrac{qq'}{M}) - e^{i\Omega^{-\mu}_{q'\sigma'}t}\chi_t(\Omega^{-\mu}_{q'\sigma'}+\tfrac{qq'}{M})\right)\Big]\Big\} \tag{4.1.37}$$

$$A^{\mu\bar{\mu}}_{q\sigma,q'\sigma'}(p,t) = \tfrac{1}{2}\tfrac{W_{q\sigma}W_{q'\sigma'}}{4L}\Big\{\tfrac{\sigma}{\Omega^{+\mu}_{q\sigma}\Omega_{q'\sigma'}}\times \\ \left[e^{i\Omega^{+\mu}_{q\sigma}t}\chi_t(\Omega^{+\mu}_{q\sigma}+\tfrac{qq'}{M}) + e^{i\Omega_{q'\sigma'}t}\chi_t(\Omega_{q'\sigma'}+\tfrac{qq'}{M}) + \right. \\ \left. -\chi_t(\tfrac{qq'}{M}) - e^{i(\Omega^{+\mu}_{q\sigma}+\Omega_{q'\sigma'})t}\chi_t(\Omega^{+\mu}_{q\sigma}+\Omega_{q'\sigma'}+\tfrac{qq'}{M})\right] + \\ + \tfrac{\sigma'}{\Omega^{+\mu}_{q'\sigma'}\Omega_{q\sigma}}\left[e^{i\Omega^{+\mu}_{q'\sigma'}t}\chi_t(\Omega^{+\mu}_{q'\sigma'}+\tfrac{qq'}{M}) + e^{i\Omega_{q\sigma}t}\chi_t(\Omega_{q\sigma}+\tfrac{qq'}{M}) + \right. \\ \left. -\chi_t(\tfrac{qq'}{M}) - e^{i(\Omega_{q\sigma}+\Omega^{+\mu}_{q'\sigma'})t}\chi_t(\Omega_{q\sigma}+\Omega^{+\mu}_{q'\sigma'}+\tfrac{qq'}{M})\right]\Big\} \ . \tag{4.1.38}$$

In the above equations, all $\Omega_{q\sigma}$s and $\Omega^{\pm\mu}_{q\sigma}$s are understood to be evaluated at momentum p, i.e. as $\Omega_{q\sigma}(p)$ and $\Omega^{\pm\mu}_{q\sigma}(p)$.

At this point, we can finally write our second-order approximation to the state. For the initial condition $|\Psi_{p\mu}(0)\rangle = |p\mu,\omega\rangle$, we have

$$\begin{aligned}|\Psi_{p\mu}(t)\rangle = a_{p\mu}(t)e^{-ih_0(p)t}\Big[&e^{-i\lambda_{p\mu}t}|p\mu,\omega\rangle + \\ &+e^{-i\lambda_{p\bar{\mu}}t}\sum_{q\neq 0,\sigma}\sigma\frac{W_{q\sigma}}{2L^{1/2}}\frac{1-e^{i\Omega^{+\mu}_{q\sigma}(p)t}}{\Omega^{+\mu}_{q\sigma}(p)}b^\dagger_{q\sigma}|p\bar{\mu},\omega\rangle + \\ &+e^{-i\lambda_{p\bar{\mu}}t}B_{p\mu}(t)|p\bar{\mu},\omega\rangle + \\ &+\sum_\nu\sum_{q\sigma,q'\sigma'}e^{-i\lambda_{p\nu}t}A^{\mu\nu}_{q\sigma,q'\sigma'}(p,t)b^\dagger_{q\sigma}b^\dagger_{q'\sigma'}|p\nu,\omega\rangle\Big]\,. \quad (4.1.39)\end{aligned}$$

Alternatively, we can let $e^{-ih_0(p)t}$ act on the bath states, to obtain

$$\begin{aligned}|\Psi_{p\mu}(t)\rangle = a_{p\mu}(t)\Big[&e^{-i\lambda_{p\mu}t}|p\mu\rangle|\omega_p(t)\rangle + \\ &-e^{-i(\lambda_{p\bar{\mu}}-2\mu J_\perp)t}\sum_{q\neq 0,\sigma}\sigma\frac{W_{q\sigma}}{2L^{1/2}}\frac{1-e^{-i\Omega^{+\mu}_{q\sigma}(p)t}}{\Omega^{+\mu}_{q\sigma}(p)}b^\dagger_{q\sigma}|p\bar{\mu}\rangle|\omega_p(t)\rangle + \\ &+e^{-i\lambda_{p\bar{\mu}}t}\tilde{B}_{p\mu}(t)|p\bar{\mu}\rangle|\omega_p(t)\rangle + \\ &+\sum_\nu\sum_{q\sigma,q'\sigma'}e^{-i\lambda_{p\nu}t}A^{\mu\nu}_{q\sigma,q'\sigma'}(p,t)e^{-i(\Omega_{q\sigma}(p)+\Omega_{q'\sigma'}(p))t}\times \\ &\times b^\dagger_{q\sigma}b^\dagger_{q'\sigma'}|p\nu\rangle|\omega_p(t)\rangle\Big]\,, \quad (4.1.40)\end{aligned}$$

We also introduced

$$\tilde{B}_{p\mu}(t) = B_{p\mu}(t) - \sum_{q\neq 0,\sigma}\sigma\frac{W^2_{q\sigma}}{4L}\chi^*_t(\Omega^{+\mu}_{q\sigma}(p))\chi_t(\Omega_{q\sigma}(p))\,. \quad (4.1.41)$$

This function has a logarithmic divergence in the TLL cutoff, but it is vanishing if the two baths share identical properties (v_σ, K_σ, g_σ). This is an indication that the properties in the asymmetric scenario will depend explicitly on the UV cutoff, i.e. are sensitive to the microscopic model underlying the effective TLL Hamiltonian, just as the LCE Green's function did. For this reason, we will mostly focus on the symmetric case, where we can discard this term and obtain universal results.

In general, we will be interested to calculate observables at the leading perturbative order, and this means that for most of the times the first-order approximation to the state will suffice, namely equations (4.1.39) and (4.1.40) with As and Bs set to zero.

Equations (4.1.39) and (4.1.40) suggest a clear physical picture of the evolution of the system. As we have seen in 2.3 for a static impurity, in the bosonic language the OC corresponds to the bath state becoming a coherent state with a diverging number of boson excited (either in time or in system size). In the present theory we see the same description of the phenomenon in the "zeroth" order solution [equations (4.1.14) and (4.1.15)], thanks to the choice of $\mathcal{H}_0$ and to the LLP transformation. In this basis, each momentum state p of the impurity becomes "dressed" with its own coherent state

of the baths, $|\omega_p(t)\rangle$, causing a momentum-dependent OC. These states describe how the baths slowly relax to the sudden injection of the impurity into the system. The parameters $f_{q\sigma}(t) \equiv -W_{q\sigma}/(2L)\,\chi_t(\Omega_{q\sigma}(p))$ that describe the state $|\omega_p(t)\rangle$ [equation (4.1.12)] are formally analogous to the ones in the static case, the only difference is the substitution of the bath dispersion $\varepsilon_q = v|q|$ with $\Omega_{q\sigma}(p) = v_\sigma|q| - pq/M + q^2/2M$, which incorporates the effect of the finite impurity speed ($-pq/M$) and of the recoil energy ($q^2/2M$) caused by the finite mass. In the limit $M \to \infty$, the case of a static impurity is recovered.

In our model, the OC does not exhaust the physics, as there is also the emission of phonons from the deexcitation $|po\rangle \to |pe\rangle$. In our perturbative solution, equations (4.1.39) and (4.1.40), this process is described by the first order correction (4.1.28) and by the $J_\perp$-dependent terms in the second-order one [equations (4.1.37), (4.1.38)]. Both these terms feature phonons added on top of the coherent-state background. This is in accord with our splitting of the impurity-bath interaction in intra- and inter-band processes. The $J_\perp$-independent terms in equations (4.1.37) and (4.1.38) account for the correlation effects of the recoil energy $: P_b^2/2M :$.

The time evolution of a wave packet $|\Psi(0)\rangle = \sum_{p\mu} c_{p\mu}\,|p\mu,\omega\rangle$ is simply reconstructed by the superposition of equation (4.1.39) or (4.1.40):

$$\begin{aligned}|\Psi(t)\rangle = \sum_{p\mu} e^{-i\lambda_{p\mu}t}\,|p\mu\rangle\, e^{-ih_0(p)t}\Bigg[&(c_{p\mu}a_{p\mu} + c_{p\bar\mu}a_{p\bar\mu}B_{p\bar\mu}(t))\,|\omega\rangle + \\ &+ c_{p\bar\mu}a_{p\bar\mu}\sum_{q\sigma}\sigma\tfrac{W_{q\sigma}}{2L^{1/2}}\tfrac{1-e^{i\Omega^{-\mu}_{q\sigma}t}}{\Omega^{-\mu}_{q\sigma}}b^\dagger_{q\sigma}\,|\omega\rangle + \\ &+ \sum_{q\sigma,q'\sigma'}\left(c_{p\mu}a_{p\mu}A^{\mu\mu}_{q\sigma,q'\sigma'}(p,t) + c_{p\bar\mu}a_{p\bar\mu}A^{\bar\mu\mu}_{q\sigma,q'\sigma'}(p,t)\right)b^\dagger_{q\sigma}b^\dagger_{q'\sigma'}\,|\omega\rangle\Bigg]\,,\end{aligned} \tag{4.1.42}$$

or

$$\begin{aligned}|\Psi(t)\rangle = \sum_{p\mu} e^{-i\lambda_{p\mu}t}\,|p\mu\rangle\Bigg[&(c_{p\mu}a_{p\mu} + c_{p\bar\mu}a_{p\bar\mu}\tilde B_{p\bar\mu}(t))\,|\omega_p(t)\rangle \\ &+ c_{p\bar\mu}a_{p\bar\mu}e^{-2i\mu J_\perp t}\sum_{q\sigma}\sigma\tfrac{W_{q\sigma}}{2L^{1/2}}\tfrac{1-e^{-i\Omega^{-\mu}_{q\sigma}t}}{\Omega^{-\mu}_{q\sigma}}b^\dagger_{q\sigma}\,|\omega_p(t)\rangle + \\ &+ \sum_{q\sigma,q'\sigma'}\left(c_{p\mu}a_{p\mu}A^{\mu\mu}_{q\sigma,q'\sigma'}(p,t) + c_{p\bar\mu}a_{p\bar\mu}A^{\bar\mu\mu}_{q\sigma,q'\sigma'}(p,t)\right)\times \\ &\times e^{-i(\Omega_{q\sigma}(p)+\Omega_{q'\sigma'}(p))t}b^\dagger_{q\sigma}b^\dagger_{q'\sigma'}\,|\omega_p(t)\rangle\Bigg]\end{aligned} \tag{4.1.43}$$

The calculation and characterisation of the normalisation factors $a_{p\mu}(t)$ follows from the discussion of the $F_p(J,t)$ functions in the previous chapter. To be clear, we just recall the asymptotic behaviours

$$a_{pe}(t) \sim e^{z_{pe} - i\Delta\lambda_{pe}t + \mathcal{O}(1/t)} \tag{4.1.44a}$$

$$a_{po}(t) \sim e^{z_{po} - i\Delta\lambda_{po}t - 2\gamma_p t + \mathcal{O}(1/t)}\,, \tag{4.1.44b}$$

where $z_{p\mu}$ are two complex constants ($z_{p\,e,o} = c_A(p,t_0) \pm c_B(p)$ in the notation of chapter 3).

The main limitation of the present perturbative solution is that the normalisation is perturbative as well. For instance, for the first-order result

$$\begin{aligned}\langle\Psi_{p\mu}(t)|\Psi_{p\mu}(t)\rangle = |a_{p\mu}|^2\left(1+2\sum_{q\neq 0,\sigma}\frac{W_{q\sigma}^2}{4L}\frac{1-\cos\Omega_{q\sigma}(p)^{+\mu}t}{(\Omega_{q\sigma}(p)^{+\mu})^2}+\mathcal{O}\left(\frac{\tilde{g}^4}{\nu^4}\right)\right) = \\ = e^{2\,\mathrm{Re}\,F_p(-\mu J_\perp,t)}[1-2\,\mathrm{Re}\,F_p(-\mu J_\perp,t)+\mathcal{O}\left(\frac{\tilde{g}^4}{\nu^4}\right)] \sim \\ \sim 1+\mathcal{O}\left(\left[\mathrm{Re}\,F_p(-\mu J_\perp,t)\right]^2\right) = 1+\mathcal{O}\left(\frac{\tilde{g}^4}{\nu^4}\right)\,. \quad (4.1.45)\end{aligned}$$

The deviation from the unit norm is formally of the fourth order. However, the amount of norm loss $\langle\Psi_{p\mu}(t)|\Psi_{p\mu}(t)\rangle - 1$ depends on time, and there is no guarantee that the higher perturbative order implies that the norm loss remains small for all times. This turns out to be the case for the even mode, for which $\mathrm{Re}\,F_p(-J_\perp,t)$ is asymptotically constant. For the odd mode, $\mathrm{Re}\,F_p(J_\perp,t) \sim 2\gamma_p t$, and eventually the norm will decrease to 0. This means that as time goes on the states with more than one phonon added to $|\omega_p\rangle$ become important. The timescale for the decrease is set by the decay time $\tau_p^{dec} \equiv (2\gamma_p)^{-1}$: the norm decreases to 0.9 in a time of about $0.25\tau_p^{dec}$, and to 0.5 in about $0.8\tau_p^{dec}$. This is usually not a very stringent limitation, because the decay time is of order $\mathcal{O}(\nu^2/\tilde{g}^2)$ and so it can be rather long in the perturbative regime of small coupling. Therefore, we will always consider the evolution for times not beyond $0.5\tau_p^{dec}$. There will be observables for which the norm loss will cause evidently wrong behaviours at long times, whereas the qualitative behaviour of some other observables will not be affected by the loss of normalisation.

As a check of the reliability of this solution, we can calculate the Green's function $G_{\parallel}(p,t) = -i\langle p\sigma,\omega|e^{-i\mathcal{H}t}|p\sigma,\omega\rangle$ in this approach and compare it with the one from the LCE from the previous chapter. In general

$$G_{\sigma\sigma}(p,t) = -i\langle p\sigma|e^{-i\mathcal{H}t}|p\sigma\rangle = \frac{1}{2}\sum_{\mu}\left[G_{\mu\mu}(p,t)+\sigma G_{\bar{\mu}\mu}(p,t)\right]\,, \quad (4.1.46a)$$

$$G_{\bar{\sigma}\sigma}(p,t) = -i\langle p\bar{\sigma}|e^{-i\mathcal{H}t}|p\sigma\rangle = \frac{1}{2}\sum_{\mu}\left[G_{\mu\mu}(p,t)-\sigma G_{\bar{\mu}\mu}(p,t)\right]\,, \quad (4.1.46b)$$

where

$$G_{\mu\nu}(p,t) \equiv -i\langle p\mu,\omega|e^{-i\mathcal{H}t}|p\nu,\omega\rangle\,. \quad (4.1.47)$$

In our perturbative approximation $e^{-i\mathcal{H}t}|p\mu,\omega\rangle \approx |\psi_{p\mu}\rangle$, and using either equation (4.1.39) or (4.1.40) we obtain

$$G_{\mu\mu}(p,t) = -ia_{p\mu}(t)e^{-i\lambda_{p\mu}t}\langle\omega|\omega_p(t)\rangle\,, \quad (4.1.48a)$$

$$G_{\bar{\mu}\mu}(p,t) = -ia_{p\mu}(t)e^{-i\lambda_{p\bar{\mu}}t}\langle\omega|\omega_p(t)\rangle\,\tilde{B}_{p\mu}(t)\,. \quad (4.1.48b)$$

We have already recognised that $a_{p\mu}(t) = e^{F(-\mu J_\perp,t)}$, and calculated that $\langle\omega|\omega_p(t)\rangle = e^{F(0,t)}$ [equation (4.1.15)]. Therefore, in the symmetric case when $\tilde{B}_{p\mu}(t) = 0$, we recover exactly equation (3.0.25). Therefore, we can say that the "improved" perturbative treatment we have just developed should be equivalent to the LCE.

The comparison with the LCE Green's function in the asymmetric case is less clear, because both in the LCE and in the perturbative technique of this work the corresponding function depends explicitly on the cutoff Λ.

For some purposes, it may be useful to have an expression for the time-evolving state in the laboratory frame, namely before the LLP transformation. This state can be easily obtained by applying $U_{LLP} = e^{-iXP_b}$ to equation (4.1.43). The transformation is simpler to perform in the position basis for the impurity:

$$\begin{aligned}|\Psi_{lab}(t)\rangle \equiv e^{-iXP_b}|\Psi_{LLP}(t)\rangle = e^{-iXP_b}\sum_{p\mu}|p\mu\rangle_d|\psi_{p\mu}(t)\rangle_b = \\ = \frac{1}{N^{1/2}}e^{-iqXP_b}\sum_{jp\mu}e^{ipaj}|j\mu\rangle_d|\psi_{p\mu}(t)\rangle_b = \\ = \frac{1}{N^{1/2}}\sum_{jp\mu}e^{ipaj}|j\mu\rangle_d e^{-iajP_b}|\psi_{p\mu}(t)\rangle_b \ .\end{aligned}$$

Using the properties of the coherent states, we find

$$\begin{aligned}|\Psi_{lab}(t)\rangle =& \frac{1}{N^{1/2}}\sum_{jp\mu}e^{i(paj-\lambda_{p\mu}t)}|j\mu\rangle_d\Big[c_{p\mu}a_{p\mu}+ \\ &-c_{p\bar{\mu}}a_{p\bar{\mu}}e^{-2\mu i J_\perp t}\sum_{q\sigma}\sigma\frac{W_{q\sigma}}{2\sqrt{L}}\frac{1-e^{-i\Omega^{-\mu}_{q\sigma}(p)t}}{\Omega^{-\mu}_{q\sigma}(p)}e^{-iqaj}b^\dagger_{q\sigma}+\mathcal{O}(g^2)\Big]|\omega_p(j,t)\rangle \ ,\end{aligned} \tag{4.1.49}$$

where

$$\begin{aligned}\left|\omega^0_p(j,t)\right\rangle \equiv e^{-iqajP_b}|\omega_p(t)\rangle = \\ = e^{i\,\mathrm{Im}\,F_p(0,t)}\left|\mathrm{coh}\left[-\frac{W_{q\sigma}}{2L^{1/2}}\chi_t(\Omega_{q\sigma}(p))e^{-iqaj}\right]\right\rangle \ .\end{aligned} \tag{4.1.50}$$

WAVE PACKETS In the following paragraphs we will show the numerical results for the evolution of the impurity probability density, the bath density and bath momentum density when the impurity is initialised in a wave packet within the $\uparrow$ bath. The present perturbative method allows for virtually arbitrary wave packets, compatibly with the low-momentum conditions for the validity of the long-wavelength model. We will usually choose a Gaussian profile in momentum space:

$$c_{p\mu} = 2^{-1/2}N(p_0,\delta p)e^{-\frac{(p-p_0)^2}{4\delta p^2}-ix_0p} \ , \tag{4.1.51}$$

where p_0 is the average momentum, δp is the width of the distribution, x_0 is the average initial position and $N(p_0,\delta p)$ is chosen to ensure that $\sum_{p\mu}|c_{p\mu}|^2 = 1$. Notice that the above momentum profile corresponds to a wave function that is factorised between space and bath index, but more general states can be equally considered. The relation $c_{pe} = c_{po}$ ensures that the impurity is injected in the $\uparrow$ bath. We work in a finite-size system of length L ($L = 1000(Mv)^{-1}$, unless noted otherwise), with periodic boundary conditions. Momenta are then quantized according to $p_n = 2\pi/L\cdot n, \quad n\in\mathbb{Z}$, and we take a wave packet composed of N_p momenta, distributed symmetrically around p_0. More specifically, we define $n_{p_0}\in\mathbb{Z}$ such that $p_0 = 2\pi/L\,n_{p_0}$, then we take $p_n = 2\pi/L(n_{p_0}+n)$ where $n = -N_p/2+1,\dots,N_p/2$ when N_p is even, and $n = -(N_p-1)/2,\dots,(N_p-1)/2$ when N_p is odd. In our calculations, the number of momenta ranged from $N_p = 16$ up to $N_p = 128$. We also played with non-Gaussian profiles.

4.1.3 Results for impurity observables

In the following paragraphs, we will present both analytical and numerical results for the dynamics of various impurity observables. We will see that the present perturbative approach shows its limits when describing the properties of the impurity.

Impurity oscillations

The simplest observable is the probability that the impurity is found in the bath σ, which is the expectation value of the operator

$$n_\sigma \equiv \sum_j d^\dagger_{j\sigma} d_{j\sigma} \,. \tag{4.1.52}$$

After the LLP transformation and the mapping to pseudo-spins, it reads [compare with equation (4.0.3) and equation (4.0.5)]

$$n_\sigma = \frac{1}{2}(1 + \sigma\sigma_3) \,. \tag{4.1.53}$$

Using the notation

$$|\Psi(t)\rangle = \sum_{p\mu} |p\mu\rangle_d \, |\psi_{p\mu}(t)\rangle_b \tag{4.1.54}$$

for the evolved state (notice that the bath states are not normalised to one), we find[9]

$$\langle n_\sigma \rangle_t = \frac{1}{2} + \frac{\sigma}{2} \sum_{p\mu} \langle \psi_{p\mu}(t) | \psi_{p\bar{\mu}}(t) \rangle \,. \tag{4.1.55}$$

In the following, we will use the shorthand

$$\langle \mathcal{O} \rangle_t \equiv \langle \Psi(t) | \mathcal{O} | \Psi(t) \rangle \tag{4.1.56}$$

for indicating the expectation value of an observable $\mathcal{O}$ at time t. The overlaps in equation (4.1.55) are easily calculated to be

$$\begin{aligned}
\langle \psi_{p\mu}(t) | \psi_{p\bar{\mu}}(t) \rangle = e^{-2i\mu J_\perp t} \big[& (c_{p\mu} a_{p\mu})^* c_{p\bar{\mu}} a_{p\bar{\mu}} + \\
& + |c_{p\bar{\mu}} a_{p\bar{\mu}}|^2 \tilde{B}^*_{p\bar{\mu}}(t) + |c_{p\mu} a_{p\mu}|^2 \tilde{B}_{p\mu}(t) \big] + \\
& + |c_{p\mu} a_{p\mu}|^2 \sum_{q\neq 0,\sigma} \sigma \frac{W^2_{q\sigma}}{4L} \frac{1 - e^{i\Omega_{q\sigma}(p)t}}{\Omega_{q\sigma}(p)} \frac{1 - e^{-i\Omega^{+\mu}_{q\sigma}(p)t}}{\Omega^{+\mu}_{q\sigma}(p)} + \\
& + |c_{p\bar{\mu}} a_{p\bar{\mu}}|^2 \sum_{q\neq 0,\sigma} \sigma \frac{W^2_{q\sigma}}{4L} \frac{1 - e^{i\Omega^{-\mu}_{q\sigma}(p)t}}{\Omega^{-\mu}_{q\sigma}(p)} \frac{1 - e^{-i\Omega_{q\sigma}(p)t}}{\Omega_{q\sigma}(p)} + \\
& + e^{2i\mu J_\perp t} (c_{p\bar{\mu}} a_{p\bar{\mu}})^* c_{p\mu} a_{p\mu} \sum_{q\neq 0,\sigma} \frac{W^2_{q\sigma}}{4L} \frac{1 - e^{i\Omega^{-\mu}_{q\sigma}(p)t}}{\Omega^{-\mu}_{q\sigma}(p)} \frac{1 - e^{-i\Omega^{+\mu}_{q\sigma}(p)t}}{\Omega^{+\mu}_{q\sigma}(p)} + \\
& + \mathcal{O}\Big((gK^{1/2}/v)^3 \Big)
\end{aligned} \tag{4.1.57}$$

9 Notice that we are setting explicitly $\langle \Psi(t) | \Psi(t) \rangle \equiv 1$. However, this is true only for short times with respect to $\min_p (2\gamma_p)^{-1}$, because of the perturbative normalisation. If we were to take this into account, we would have $\sum_\sigma \langle n_\sigma \rangle$ decreasing from 1 in time.

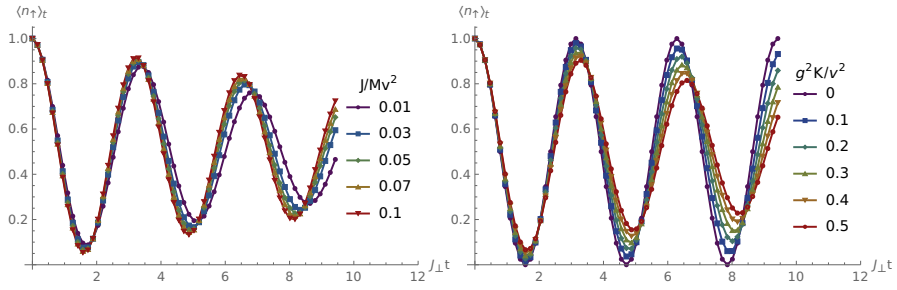

Figure 4.1: Time evolution of $\langle n_\uparrow \rangle$ for the wave packet equation (4.1.51), with $p_0 = 0.1Mv$, $\delta p = 0.02$, and $N_p = 32$. In plot (a) the coupling is kept fixed to $g^2K = 0.5v^2$, while $J_\perp$ is varied, while in plot (b) we vary the coupling while keeping a constant $J_\perp = 0.05Mv^2$. Notice that in (a) the time is expressed in units of $J_\perp^{-1}$, which is different for different plots.

at second order. We can express the equation above in terms of simpler function. For instance, in the symmetric case, it reads

$$\begin{aligned}\langle \psi_{p\mu}(t)|\psi_{p\bar{\mu}}(t)\rangle = e^{-2i\mu J_\perp t}(c_{p\mu}a_{p\mu})^* c_{p\bar{\mu}}a_{p\bar{\mu}} + \\ - \tfrac{\mu}{2J_\perp} e^{2i\mu J_\perp t}(c_{p\bar{\mu}}a_{p\bar{\mu}})^* c_{p\mu}a_{p\mu}\big\{(H_p^S(\mu J_\perp,t))^* - H_p^S(-\mu J_\perp,t) + \\ + e^{-2i\mu J_\perp t}\big[H_p^S(\mu J_\perp,t) - (H_p^S(-\mu J_\perp,t))^*\big]\big\}\,, \end{aligned} \tag{4.1.58}$$

where we introduced the function

$$H_p^S(J,t) \equiv -\sum_{q\neq 0,\sigma} \frac{W_{q\sigma}^2}{8L}\frac{1-e^{-i\Omega_{q\sigma}^{-\mu}(p)t}}{\Omega_{q\sigma}^{-\mu}(p)} = \frac{i}{2}\frac{\partial}{\partial t}F_p(J,t)\,. \tag{4.1.59}$$

In figures 4.1a and 4.1b we show the time evolution of $\langle n_\uparrow \rangle_t$, namely the probability of finding the impurity in bath $\uparrow$ at time t (the probability for the other bath is simply $\langle n_\downarrow \rangle_t = 1 - \langle n_\uparrow \rangle_t$). We can observe that the interaction with the baths has two effects. First, the amplitude of the oscillations around the average value $1/2$ becomes a decreasing function of time. This decay is more pronounced for larger coupling (figure 4.1b) and larger $J_\perp$ (figure 4.1a, once the time is measured in $J_\perp$-independent units). Second, the frequency of the oscillations is decreased, by an amount that is larger for increasing coupling (figure 4.1b) and decreasing $J_\perp$ (figure 4.1a).

We can have an analytic insight on these observations by examining the expression equation (4.1.55) for $\langle n_\uparrow \rangle_t$. In particular, if we keep only the first term in the bath states overlap equation (4.1.57), which gives the leading contribution, and we use the asymptotic relations equations (4.1.44) for $a_{p\mu}$, we find

$$\langle n_\sigma \rangle_t \sim \tfrac{1}{2} + \sigma\,\mathrm{Re}\sum_p e^{z_{pe}^* + z_{po}} c_{pe}^* c_{po} e^{-2i\tilde{J}_{\perp,p}t - 2\gamma_p t}\,, \tag{4.1.60}$$

where $\tilde{J}_{\perp,p}$ is the renormalised inter-bath hopping amplitude. In particular, if the impurity is initially in bath σ_0, then $\sigma_3|\Psi(0)\rangle = \sigma_0|\Psi(0)\rangle$ implies that $c_{p\bar{\mu}} = \sigma_0 c_{p\mu}$ (and therefore $\sum_p |c_{p\mu}|^2 = 1/2$ from normalisation). Substituting in the equation above we obtain

$$\langle n_\sigma \rangle_t \sim \tfrac{1}{2} + \sigma\sigma_0 \sum_p |c_{pe}|^2 e^{-2\gamma_p t} e^{\mathrm{Re}(z_{pe}+z_{po})}\cos[2\tilde{J}_{\perp,p}t + \mathrm{Im}(z_{pe} - z_{po})]\,,$$

From this expression we can see that $\langle n_\sigma \rangle_t - 1/2$ is given by a superposition of damped oscillating contributions, one for each momentum in the wave packet. For comparison, in the non-interacting case we would have

$$\langle n_\sigma \rangle_t^{(0)} = \tfrac{1}{2} + \sigma \operatorname{Re} \sum_p c_{pe}^\dagger c_{po} e^{-2iJ_\perp t} \,, \tag{4.1.61}$$

and for the usual initial condition within bath σ_0

$$\langle n_\sigma \rangle_t^{(0)} = \tfrac{1}{2} + \sigma\sigma_0 \sum_p |c_{pe}|^2 \cos 2J_\perp t \,,$$

which shows that the impurity periodically switches from one bath to the other. In the weak-coupling regime we are examining, the interaction with the baths decreases the hopping frequency ($\tilde{J}_{\perp,p} < J_\perp$), while the amplitude of the oscillations decreases exponentially with a decay time of $1/(2\gamma_p)$. While our solution ceases to be accurate beyond this decay time, it hints at the property that $\langle n_\sigma \rangle_t \to 1/2$ eventually. This limiting behaviour is what we would expect from physical intuition: in a sufficiently long time, the impurity put in contact with a thermal bath at zero temperature should reach its ground state, $|p_f, e\rangle_d$, in which it is equally likely to be found in any of the baths.

We write the asymptotic momentum as p_f because there is no guarantee that it may vanish. Indeed, as we have already noticed, at zero temperature intra-band scattering with emission of phonons is forbidden by energy and momentum conservation, and the only phonons emitted, capable to carry away the impurity momentum, come from the deexcitation of the odd band to the even one. The amount of energy available to these phonons is therefore limited to about $2J_\perp$ (this is a rough estimate, neglecting the recoil of the impurity), and as each emitted phonon of momentum q contributes with an energy $v_\sigma|q|$ we see that there must be a limit to the amount of momentum that is possible to transfer to the baths. On the other hand, there is no (classical) kinematic constraint that would forbid a complete decoherence of the odd mode. Although these considerations concern a timescale which is not attainable in our present formalism, we can say on a nonperturbative ground that for a sufficiently large momentum or small inter-bath hopping we expect the impurity to retain a finite asymptotic speed. Similar phenomena have been already observed in the single-bath case [28, 68].

Impurity momentum

In problems concerning mobile impurities, a natural observable to be considered is the impurity momentum. In the LLP basis, it reads $P_d = P - P_b$, so,

as P is a constant of motion, all that is required to compute is the momentum carried by the baths. The latter is given by

$$\begin{aligned}\langle P_b\rangle_t &= \sum_{q\neq 0,\sigma} q\left\langle b^\dagger_{q\sigma}b_{q\sigma}\right\rangle_t = \\ &= 2\sum_{p\mu}|c_{p\mu}a_{p\mu}|^2\sum_{q\neq 0,\sigma} q\frac{W^2_{q\sigma}}{4L}\frac{1-\cos\Omega^{+\mu}_{q\sigma}(p)t}{(\Omega^{+\mu}_{q\sigma}(p))^2}+ \\ &+2\,\mathrm{Re}\left[\sum_{p\mu}(c_{p\mu}a_{p\mu})^* c_{p\bar{\mu}}a_{p\bar{\mu}}\sum_{q\neq 0,\sigma}\sigma q\frac{W^2_{q\sigma}}{4L}\frac{1-e^{-i\Omega_{q\sigma}(p)t}}{\Omega_{q\sigma}(p)}\frac{1-e^{i\Omega^{-\mu}_{q\sigma}(p)t}}{\Omega^{-\mu}_{q\sigma}(p)}\right]+ \\ &+2\sum_{p\mu}|c_{p\mu}|^2\sum_{q\neq 0,\sigma} q\frac{W^2_{q\sigma}}{4L}\frac{1-\cos\Omega_{q\sigma}(p)t}{(\Omega_{q\sigma}(p))^2}\end{aligned} \tag{4.1.62}$$

The sums over the momenta can be converted into energy integrals by introducing the appropriate density of states

$$\begin{aligned}\tfrac{1}{L}\sum_{q\neq 0} qW^2_{q\sigma}f(\Omega_{q\sigma}(p)) &= \int d\varepsilon\, R^\sigma_1(\varepsilon;p)f(\varepsilon)\,, \\ R^\sigma_1(\varepsilon;p) &\equiv \tfrac{1}{L}\sum_{q\neq 0} qW^2_{q\sigma}\delta(\varepsilon-\Omega_{q\sigma}(p))\,,\end{aligned}$$

which in the continuum limit is given by

$$\begin{aligned}R^\sigma_1(\varepsilon;p) &= \tfrac{M^2\tilde{g}^2_\sigma}{(2\pi)^2}\theta(\varepsilon)e^{-\varepsilon/\Lambda}\times \\ &\times\sum_{s=\pm 1}\left[-s\left(v_\sigma+s\tfrac{p}{M}\right)\right]\left[\left(1+\tfrac{\varepsilon}{k_{s\sigma}(p)}\right)^{1/2}-2+\left(1+\tfrac{\varepsilon}{k_{s\sigma}(p)}\right)^{-1/2}\right].\end{aligned} \tag{4.1.63}$$

Unlike the previously used $R_\sigma(\varepsilon)$, this density of states behaves as ε^2 for $\varepsilon\to 0$.

The expression (4.1.62) is composed of three contributions. The first two are contributions coming from the deexcitation of the odd mode, as signalled by their explicit dependence on $J_\perp$. The second of these two accounts for the asymmetries in the bath index, as it is vanishes if the baths are symmetric or if the impurity is initialised in one of its noninteracting eigenstates. The last part of equation (4.1.62) comes from the coherent background $|\omega_p(t)\rangle$ term of the baths state, and is independent of the initial bath index of the impurity. It quantifies the momentum adsorbed by the baths as they adjust to the injection of the impurity.

We will see that it is possible to define a different measure of the impurity speed, using a definition of average position that is appropriate with the pbc. The properties of this alternative speed are in accord with the ones of the true impurity momentum defined above.

The time evolution of the impurity momentum is displayed in figures 4.2 and 4.3, as function of the various parameters of the model. In all plots, the impurity is initialised in the $\uparrow$ bath with a definite momentum[10] p_0. We

10 As we did with $\langle n_\sigma\rangle_t$, writing it as $1/2+\sigma\langle\sigma_3\rangle_t/2$, we take $\langle P\rangle_t = \langle P\rangle_{t=0} = p_0$, i.e. we ignore the effect of the loss of normalisation on the conserved total momentum.

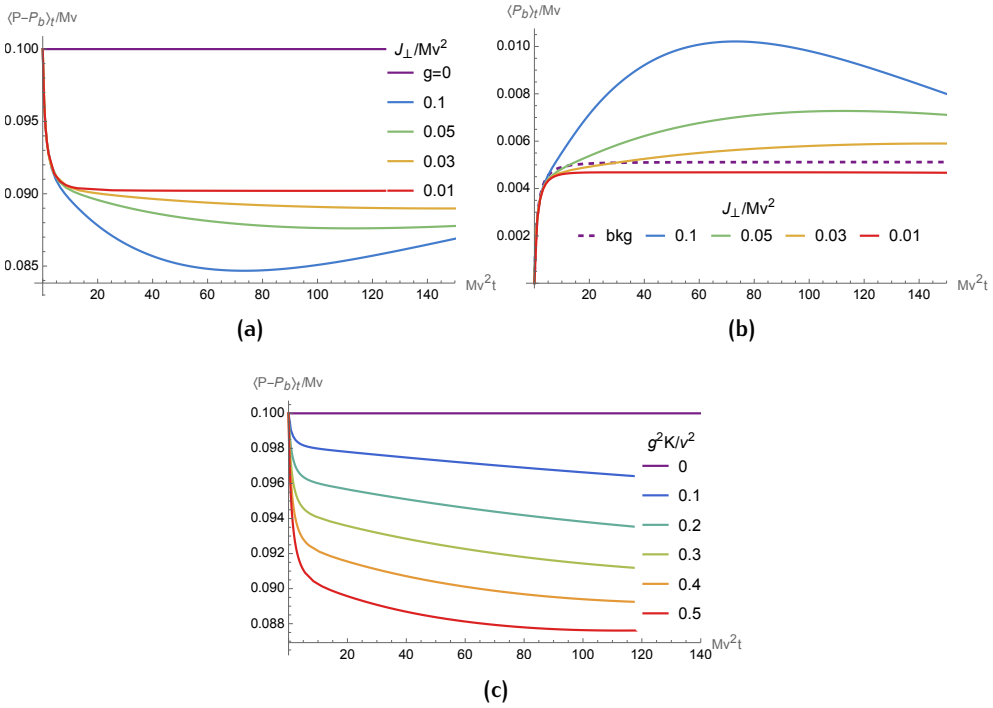

Figure 4.2: Time evolution of the impurity momentum for the initial state $|p_0 \uparrow\rangle_d$, and symmetric baths. Plots (a) and (b) are for $p_0 = 0.1Mv$, $g^2K = 0.5v^2$ and show the effect of increasing $J_\perp$. Plot (b) shows the decomposition of the bath momentum in (a) in a background component (dashed line) and a decay component. Plot (c) has $p_0 = 0.1Mv$, $J_\perp = 0.05Mv^2$ and shows the effect of increasing the coupling.

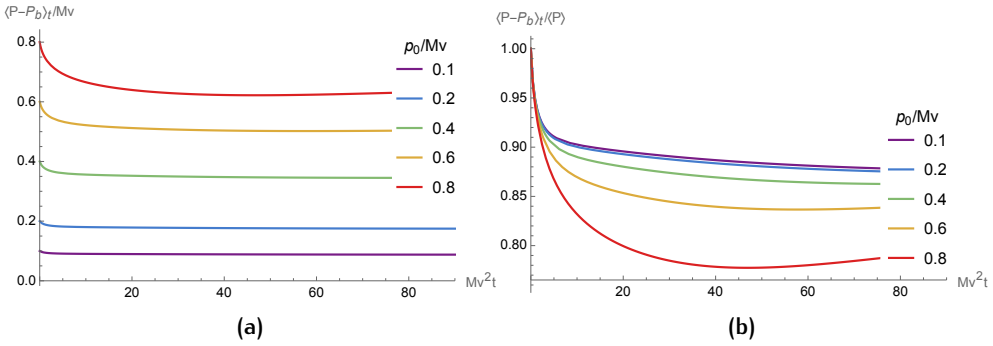

Figure 4.3: Time evolution of the impurity momentum for the initial state $|p_0 \uparrow\rangle_d$, symmetric baths, and increasing p_0. The other parameters are $g^2K = 0.5v^2$ and $J_\perp = 0.05Mv^2$. In (b) we show the ratio $\langle P - P_b\rangle_t / \langle P\rangle = 1 - \langle P_b\rangle_t / p_0$.

observe that the momentum decay can be divided in two phases: an initial abrupt drop followed by a decrease at a milder rate. At later times, some curves tend to bend upward. This increase is likely not physical, because it can be attributed to the loss of state normalisation, that causes $\langle P_b \rangle_t$ to shrink in magnitude. Figure 4.2a shows the effect of the inter-bath hopping on the momentum. We can see that the initial rapid decrease is basically unaffected by $J_\perp$, while the subsequent decay is faster for larger hopping. This suggests that the two phases of the decay originate from two different processes. To have a clearer picture of this separation, in figure 4.2b we display the decomposition of the baths momentum reported in 4.2a. The dashed line is the third term of equation (4.1.62), which is $J_\perp$-independent, while the other lines give the first term of the equation (the second contribution is absent in the symmetric case). With the aid of this plot, we interpret the two phases of momentum decay in the following way. The first, fast-decreasing region is caused by the baths relaxing to the injection of the impurity, while in the second phase the impurity momentum is carried away by the phonons generated from the deexcitation of the odd mode.

Indeed, this first phase occurs on a timescale that appears to be independent of $J_\perp$, and well before the impurity starts oscillating into the $\downarrow$ bath.[11] From figure 4.2b we see that the first and last terms of equation (4.1.62) contribute equally to the bath momentum during this initial phase. After the initial transient, the background contribution saturates to a constant value, while the first term of equation (4.1.62) continues to grow, albeit at a slower rate (except for the unphysical decrease at late times). The timescale of this growth is shorter the larger is $J_\perp$, which is what we expect from the fact that the odd mode decay constant $2\gamma(p_0)$ is an increasing function of $J_\perp$. At the lowest inter-bath hopping we considered, $J_\perp = 0.01 M v^2$, the timescale is so long that the contribution to $\langle P_b \rangle_t$ from the odd mode decay appears to converge to a value slightly below that of the background.

The dependence of the impurity momentum on the coupling is shown in figure 4.2c. As expected, the decrease is more marked for stronger coupling, while the two-phase structure is kept unaltered. A larger $gK^{1/2}/v$ increases the fraction of momentum that is lost in the initial transient, but not the timescale in which it occurs.

The following figures 4.3 show the slowdown of the impurity momentum at different initial momenta. We can recognise the initial transient and the subsequent slower decay, with the former being faster and lasting longer for larger momenta. The entity of the decrease may be also traced back to the increase of the decay rate $2\gamma(p)$ with p_0, which implies that the production of phonons caused by the odd mode deexcitation occurs earlier and more rapidly. It is useful to compare the various graphs by taking the ratio with the initial momentum (i.e. the total one), as is reported in figure 4.2b. In this figure, we can observe that the initial transient actually follows a common shape for all momenta at small times. After the transient, we see that for increasing p_0 not only the absolute value of momentum that is transferred to the baths becomes larger, but also the relative amount of it. Instead, at smaller momenta $|p| \lesssim 0.2 M v$ the ratio $\langle P_d \rangle_t / p_0$ tends to a common profile,

11 We suspect that the timescale of the first phase is comparable with that of the dimensional crossover we highlighted in chapter 3.

independent of p_0. This is explained by noticing that $R_1^\sigma(\varepsilon; p_0)$ is linear in p_0 for small momentum $|p_0| \ll M v_\sigma$, hence for a single momentum component $\langle P_b \rangle(t) = v(t) p_0/(Mv) + \mathcal{O}\big(p_0^2/(Mv)^2\big)$, with $v(t)$ independent of p_0.

Impurity density

Our perturbative solution allows us to directly access the probability of finding the impurity at the site j and in the bath σ, namely the expectation value of the number operator $d^\dagger_{j\sigma} d_{j\sigma}$. This is invariant under the LLP transformation [see equation (4.0.2)]. Using $d^\dagger_{j\sigma} d_{j\sigma} = N^{-1} \sum_p e^{ipaj} \sum_k d^\dagger_{k-p\sigma} d_{k\sigma}$ and $d_{p\sigma} = (d_{pe} + \sigma d_{po})/\sqrt{2}$ we find

$$\left\langle d^\dagger_{j\sigma} d_{j\sigma} \right\rangle_t = \tfrac{1}{2N} \sum_p e^{ipja} \sum_{k,\mu} \left(\langle \psi_{k-p\mu} | \psi_{k\mu} \rangle + \sigma \langle \psi_{k-p\mu} | \psi_{k\bar{\mu}} \rangle \right). \quad (4.1.64)$$

Notice that equation (4.1.64) correctly reproduces equation (4.1.55) when summed on all sites. The fundamental ingredients of the above equation are the overlaps of the bath states, which read

$$\begin{aligned}
\langle \psi_{p\mu}(t) | \psi_{k\mu}(t) \rangle = e^{i(E_p - E_k)t} \langle \omega_p(t) | \omega_k(t) \rangle \Bigg[& (c_{p\mu} a_{p\mu})^* c_{k\mu} a_{k\mu} + \\
& + (c_{p\bar{\mu}} a_{p\bar{\mu}})^* c_{k\mu} a_{k\mu} \tilde{B}^*_{p\bar{\mu}} + (c_{p\mu} a_{p\mu})^* c_{k\bar{\mu}} a_{k\bar{\mu}} \tilde{B}_{k\bar{\mu}} + \\
& + e^{-i\mu 2 J_\perp t} (c_{p\mu} a_{p\mu})^* c_{k\bar{\mu}} a_{k\bar{\mu}} \sum_{q\neq 0,\sigma} \sigma \frac{W^2_{q\sigma}}{4L} \frac{1 - e^{i\Omega_{q\sigma}(p)t}}{\Omega_{q\sigma}(p)} \frac{1 - e^{-i\Omega^{-\mu}_{q\sigma}(k)t}}{\Omega^{-\mu}_{q\sigma}(k)} + \\
& + e^{i\mu 2 J_\perp t} (c_{p\bar{\mu}} a_{p\bar{\mu}})^* c_{k\mu} a_{k\mu} \sum_{q\neq 0,\sigma} \sigma \frac{W^2_{q\sigma}}{4L} \frac{1 - e^{i\Omega^{-\mu}_{q\sigma}(p)t}}{\Omega^{-\mu}_{q\sigma}(p)} \frac{1 - e^{-i\Omega_{q\sigma}(k)t}}{\Omega_{q\sigma}(k)} + \\
& + (c_{p\bar{\mu}} a_{p\bar{\mu}})^* c_{k\bar{\mu}} a_{k\bar{\mu}} \sum_{q\neq 0,\sigma} \frac{W^2_{q\sigma}}{4L} \frac{1 - e^{i\Omega^{-\mu}_{q\sigma}(p)t}}{\Omega^{-\mu}_{q\sigma}(p)} \frac{1 - e^{-i\Omega^{-\mu}_{q\sigma}(k)t}}{\Omega^{-\mu}_{q\sigma}(k)} + \mathcal{O}\Big((gK^{1/2}/v)^3 \Big) \Bigg],
\end{aligned} \quad (4.1.65a)$$

$$\begin{aligned}
\langle \psi_{p\mu} | \psi_{k\bar{\mu}} \rangle = e^{i(E_p - E_k - 2\mu J_\perp)t} \langle \omega_p(t) | \omega_k(t) \rangle \Bigg[& (c_{p\mu} a_{p\mu})^* c_{k\bar{\mu}} a_{k\bar{\mu}} + \\
& + (c_{p\bar{\mu}} a_{p\bar{\mu}})^* c_{k\bar{\mu}} a_{k\bar{\mu}} \tilde{B}^*_{p\bar{\mu}} + (c_{p\mu} a_{p\mu})^* c_{k\mu} a_{k\mu} \tilde{B}_{k\mu} + \\
& + e^{i\mu 2 J_\perp t} (c_{p\mu} a_{p\mu})^* c_{k\mu} a_{k\mu} \sum_{q\neq 0,\sigma} \sigma \frac{W^2_{q\sigma}}{4L} \frac{1 - e^{i\Omega_{q\sigma}(p)t}}{\Omega_{q\sigma}(p)} \frac{1 - e^{-i\Omega^{+\mu}_{q\sigma}(k)t}}{\Omega^{+\mu}_{q\sigma}(k)} + \\
& + e^{i\mu 2 J_\perp t} (c_{p\bar{\mu}} a_{p\bar{\mu}})^* c_{k\bar{\mu}} a_{k\bar{\mu}} \sum_{q\neq 0,\sigma} \sigma \frac{W^2_{q\sigma}}{4L} \frac{1 - e^{i\Omega^{-\mu}_{q\sigma}(p)t}}{\Omega^{-\mu}_{q\sigma}(p)} \frac{1 - e^{-i\Omega_{q\sigma}(k)t}}{\Omega_{q\sigma}(k)} + \\
& + e^{i4\mu J_\perp t} (c_{p\bar{\mu}} a_{p\bar{\mu}})^* c_{k\mu} a_{k\mu} \sum_{q\neq 0,\sigma} \frac{W^2_{q\sigma}}{4L} \frac{1 - e^{i\Omega^{-\mu}_{q\sigma}(p)t}}{\Omega^{-\mu}_{q\sigma}(p)} \frac{1 - e^{-i\Omega^{+\mu}_{q\sigma}(k)t}}{\Omega^{+\mu}_{q\sigma}(k)} + \\
& + \mathcal{O}\Big((gK^{1/2}/v)^3 \Big) \Bigg].
\end{aligned} \quad (4.1.65b)$$

The overlap of the coherent states is given by

$$\ln\langle\omega_p(t)|\omega_k(t)\rangle = -\frac{1}{4L}\sum_{q\sigma} W_{q\sigma}^2 \left[\frac{1+i\Omega_{q\sigma}(p)t-e^{i\Omega_{q\sigma}(p)t}}{(\Omega_{q\sigma}(p))^2}+\right.$$
$$\left.+\frac{1-i\Omega_{q\sigma}(k)t-e^{-i\Omega_{q\sigma}(k)t}}{(\Omega_{q\sigma}(k))^2}-\frac{1-e^{i\Omega_{q\sigma}(p)t}}{\Omega_{q\sigma}(p)}\frac{1-e^{-i\Omega_{q\sigma}(k)t}}{\Omega_{q\sigma}(k)}\right] =$$
$$= F_p^*(0,t)+F_k(0,t)+\frac{1}{4L}\sum_{q\sigma} W_{q\sigma}^2\frac{1-e^{i\Omega_{q\sigma}(p)t}}{\Omega_{q\sigma}(p)}\frac{1-e^{-i\Omega_{q\sigma}(k)t}}{\Omega_{q\sigma}(k)}\,. \quad (4.1.66)$$

For any $p \neq k$ it has a slow, power-law decrease in time and it is a non-analytic function of the momenta in $p = k$. Of course, for $p = k$ it is identically equal to 1 (as $|\omega_p(t)\rangle$ is normalised), which is also its maximum absolute value.

We wish to briefly comment on the numerical effort required to compute the impurity density (4.1.64), using equation (4.1.57). Equation (4.1.64) implies that if we have N_p momenta in the initial impurity wave packet, we have to compute $2\cdot N_p(N_p+1)/2$ overlaps $\langle\psi_{p\mu}(t)|\psi_{k\nu}(t)\rangle$, and each one of these requires the evaluation of a few sums over bath momenta q. Therefore, if we cutoff the sums to N_q bath momenta, the total number of function evaluations scales as $N_p(N_p+1)N_q$. The sum over the p momentum in equation (4.1.64) is easily recognised as a Fourier Transform, and so it can be performed by means of any Fast-Fourier Transform algorithm, which is inexpensive for the low number of impurity momenta considered in this work (at most of the order of $N_p \sim 10^2$). Also the evaluation of the $a_{p\mu}(t) = \exp F_p(-\mu J_\perp, t)$ factors is rather fast, if the optimised approach for $\exp F_p(-\mu J_\perp, t)$ presented in the previous chapter is employed. In general, we have tried to express the various sums over bath momenta as integrals over appropriate densities of states, and then to relate these to the $F_p(J,t)$ and $H_p(J,t)$ functions introduced in chapter 3. When this is possible, the resulting expressions can be computed in a fast way in the continuum limit. However, we have not been able to perform this procedure in all sums involving $\Omega_{q\sigma}(p)$ evaluated at two different impurity momenta p [indicated as p and k in equation (4.1.57)], so that these terms have to be explicitly summed or integrated in q. Moreover, we could not find a complex integration path for q that removes the oscillating behaviour of the integrands, implying that the convergence of the integrals (or sums) is slowed down. Therefore, these terms that are "off-diagonal" in the impurity momentum are the slowest part of the computation of the impurity density, and of many of the observables that we will analyse in the following paragraphs. As a consequence, the computation of these terms sets the speed of the whole numerical calculations.

In figures 4.4 and 4.5 we compare the time evolution of the probability density of the impurity in the free and interacting cases. The baths are symmetric, as usual, and the two figures refer to two different values of $J_\perp$. Varying g_σ produces analogous results. The two figures show that the motion of the wave packet interacting with the baths is qualitatively similar to the free one: the whole probability distribution oscillates between the two baths with a frequency of about $2J_\perp$, while moving to the right at a speed of around p_0/M. In fact, in the perturbative regime the absolute effect of the baths on

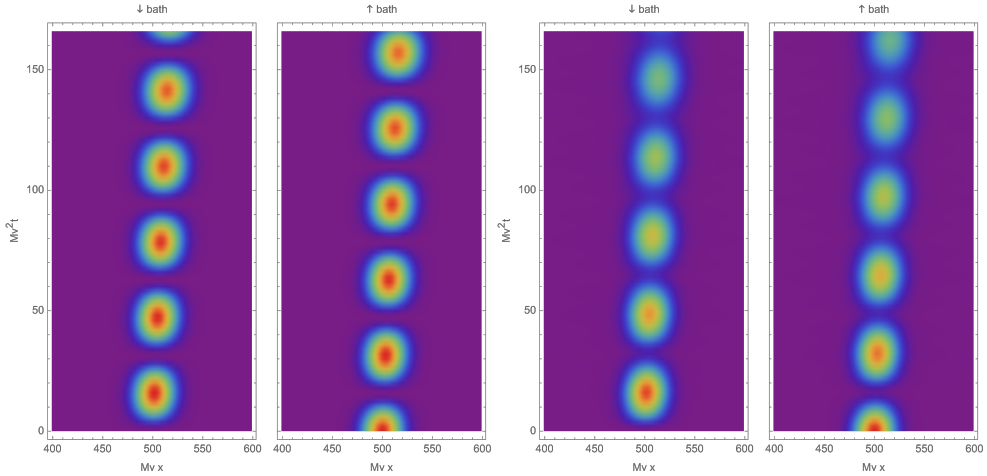

(a) $g^2K = 0$ **(b)** $g^2K = 0.5v^2$

Figure 4.4: Comparison of the time evolution of probability density for (a) the free and (b) the interacting impurity with $g^2K = 0.5v^2$. In both figures the wave packet is initialised with the Gaussian distribution (4.1.51) of 64 momenta around $p_0 = 0.1Mv$, with standard deviation $\delta p = 0.04Mv$. The baths are symmetric, and $J_\perp = 0.1Mv^2$. The total length of the system is $L = 1000\,(Mv)^{-1}$, but only its central part is depicted. The colour scale for the two figures is the same.

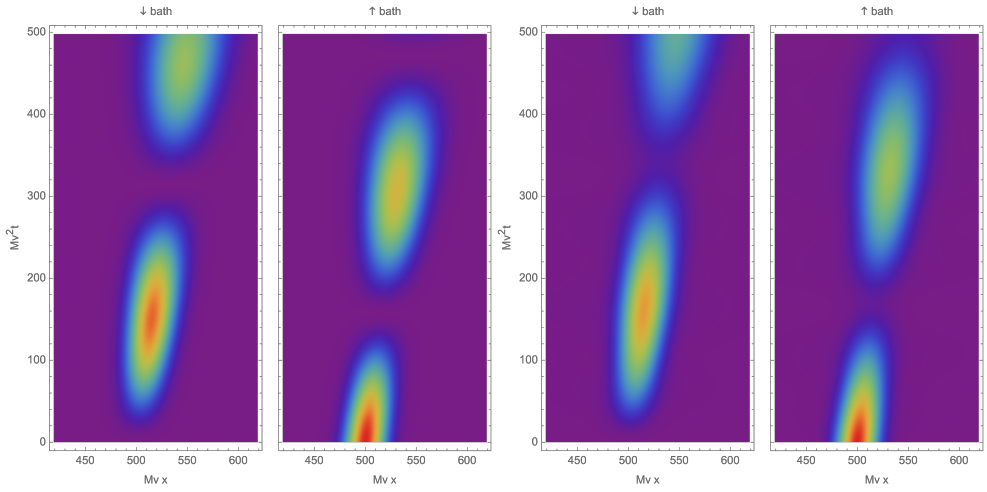

(a) $g^2K = 0$ **(b)** $g^2K = 0.5v^2$

Figure 4.5: Comparison of the time evolution of probability density for (a) the free and (b) the interacting impurity with $g^2K = 0.5v^2$. In both figures the wave packet is initialised with the Gaussian distribution (4.1.51) of 64 momenta around $p_0 = 0.1Mv$, with standard deviation $\delta p = 0.04Mv$. The baths are symmetric, and $J_\perp = 0.01Mv^2$. The total length of the system is $L = 1000\,(Mv)^{-1}$, but only its central part is depicted. The colour scale for the two figures is the same.

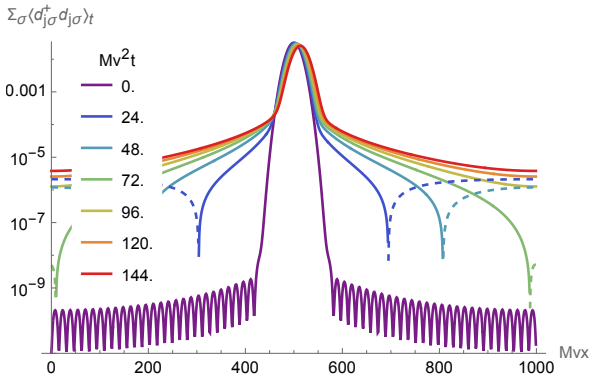

Figure 4.6: Logarithmic plot of the impurity probability density at different times, showing the rapid flow of the distribution weight towards the tails. The dashed portions of the graphs correspond to regions of (unphysical) negative probability density. The parameters are the same as figures 4.4 and 4.5, except for $J_\perp = 0.03Mv^2$.

the impurity momentum and frequency of oscillation is rather small. The most prominent differences in the time evolution of the wave packet are two, namely the larger spread in the "time direction" and the visible decay of the amplitude. The former can be traced back to the property that the renormalised inter-bath hopping $\tilde{J}_{\perp p}$ depends on the system momentum p, implying that each momentum component in the wave packet oscillates at its own rhythm. This explains at least partially the increased "fuzziness" of the probability density. The loss of synchronisation might not be the full reason for this effect, because the momentum variance of the wave packet is rather small, and the $\tilde{J}_{\perp p}$s are very close to $J_\perp$ in the perturbative regime. Moreover, the dependence of the various renormalised parameters on p is rather small if p is far from Mv (see 3.1.3 and 3.2). A second reason for the phenomenon is decoherence, namely the decay of the odd component of the impurity state, so that eventually any oscillation should disappear. In this perspective, the spread in the time direction is the initial evidence of this process, as the distinction between successive oscillations tends to fade out.

The other most visible difference between the interacting and the free density evolution is the enhanced rate of decrease of the height of the wave packet. This arises partly from the progressive loss of normalisation, and partly from the rapid flowing of probability towards the the tails of the distribution. This is not visible on the scale of figures 4.4 and 4.5, and it is better appreciated in logarithmic scale, as depicted in figure 4.6. This figure shows that the tails are much "fatter" than the noninteracting case (which would correspond to a translated version of the $t = 0$ plot, with a slight widening of the central part), and that this extra weight is established faster than the sound speed. Moreover, up to a certain time the far edges of the distribution are not even positive, which is clearly unphysical. While these tails could signal an actual tendency of the impurity to spread, their unrealistic features (faster-than-sound build-up and partially negative sign) lead us to conclude that this behaviour is likely to be an artefact of the perturbative method. Therefore, the approach we developed in the present chapter is not particularly suited to the quantitative description of the impurity density.

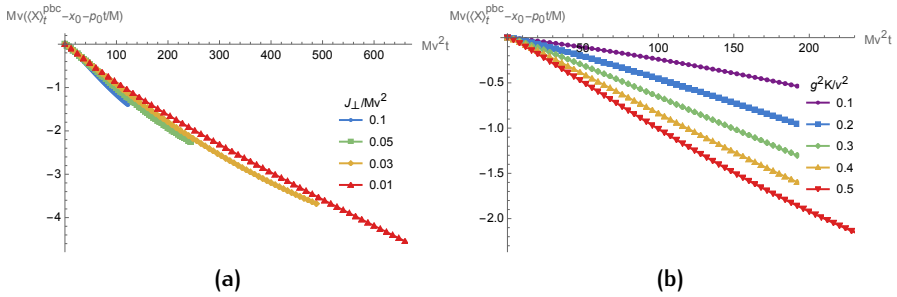

Figure 4.7: Deviation of the average impurity position from the noninteracting trajectory $x(t) = x_0 + \langle P\rangle\, t/M$. A nonlinear slowdown is found, more marked for (a) large $J_\perp$ and (b) large g. The wave packet is Gaussian with $p_0 = 0.1Mv$, $x_0 = 0$, $\delta p = 0.02Mv$ and $N_p = 32$. The parameters are $g^2K = 0.5v^2$ for (a), and $J_\perp = 0.05Mv^2$ for (b).

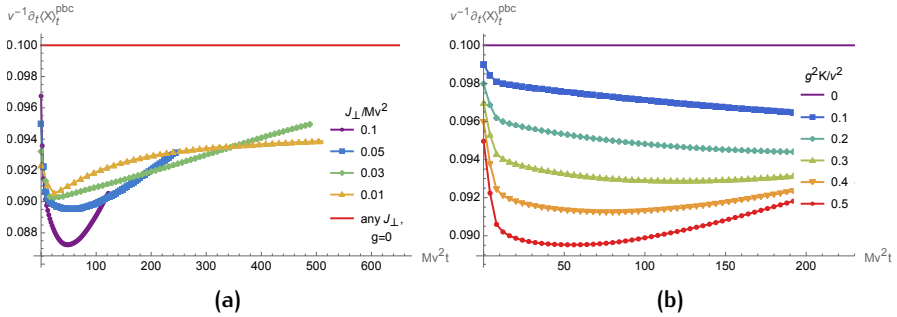

Figure 4.8: Time evolution of the average impurity speed computed as a numerical derivative of the average position defined in equations (4.1.67). The parameters for the two plots are the same as figures 4.7.

On the other hand, it could still be useful at a qualitative level. For instance, from figure 4.6 we can see the shape of the packet around its centre remains Gaussian with good approximation.

We can further characterise the effect of the baths on the impurity by measuring other observables, but keeping in mind the possibility that the tails of the distribution might affect the final results.

In 4.1.3, we have measured the impurity speed by a direct calculation of the momentum carried by the baths (remember that $\langle P_d\rangle_t = \langle P\rangle_0 - \langle P_b\rangle_t$). A different definition of the speed can be obtained by measuring the time evolution of the impurity position. In periodic boundary conditions, the position operator is ill-defined, therefore we measure the average position and variance of the position as

$$\langle X\rangle_t^{pbc} \equiv \frac{L}{2\pi}\,\mathrm{Im}\ln\left\langle e^{i2\pi X/L}\right\rangle_t \tag{4.1.67a}$$

$$\mathrm{Var}^{pbc}(X,t) \equiv -2\frac{L^2}{(2\pi)^2}\,\mathrm{Re}\ln\left\langle e^{i2\pi X/L}\right\rangle_t . \tag{4.1.67b}$$

These equations reduce to the trivial expressions of position mean and variance in the $L \to +\infty$ limit. The average $\langle X\rangle_t^{pbc}$ introduced above is defined

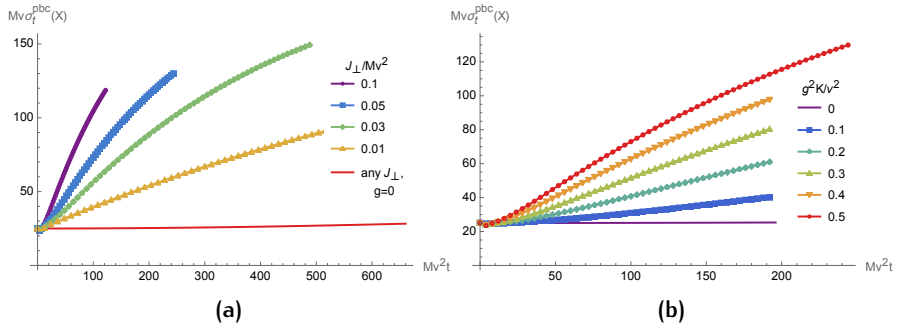

Figure 4.9: Time evolution of the standard deviation of the impurity position calculated from equations (4.1.67). The parameters for the two plots are the same as figures 4.7.

only modulo L, as it should be in pbc. In particular, in the single-impurity subspace we have

$$e^{iqX} = \sum_{j\sigma} e^{iqaj} d^\dagger_{j\sigma} d_{j\sigma} \,, \tag{4.1.68}$$

hence we can compute $\langle e^{iqX} \rangle$ simply by weighting e^{iqaj} with $\left\langle d^\dagger_{j\sigma} d_{j\sigma} \right\rangle$. The results of these calculations are shown in figures 4.7. These plots show the deviation of the average impurity position from the trajectory $x(t) = x_0 + \langle P \rangle_0 \, t/M$ that the impurity would follow in the absence of the baths. The first plot, figure 4.7a, compares different values of $J_\perp$, while the second, figure 4.7b, displays a varying coupling. Both plots clearly indicate that the interaction with the baths slows down the impurity motion, an effect that is more pronounced for larger coupling or larger inter-bath hopping. Of course, this behaviour is expected, because both the relaxation of the baths to the injection of the impurity, and the phonon emission from the odd mode decay transfer the impurity momentum to the baths. This transfer is obviously faster for larger coupling, and its enhancement with $J_\perp$ is explained by the increase of the odd mode decay rate ($2\gamma(p)$ is an increasing function of $J_\perp$).

The plots figures 4.7 also show that the slowing down of the impurity occurs in a nonlinear fashion. We can investigate this aspect further by taking a numerical derivative of the average position, which yields a possible estimate of the impurity speed. The time evolution of this observable is displayed in figures 4.8. We can recognise the same behaviour that we noticed above, namely that the speed diminution is more severe for larger inter-bath hopping figure 4.8a and larger coupling figure 4.8b. But the most interesting feature that these figures reveal is how the speed changes with time: it decreases very rapidly in the very first instants of the time evolution, then it tends to settle or increase again. While the increase at late times can be attributed to the loss of normalisation, the rapid initial decrease is presumably a genuine physical prediction. It shows that a significant fraction of the momentum is lost in a time much shorter than the odd mode decay time $(2\gamma(p))^{-1}$, and therefore it cannot be attributed to the emission of phonons from decoherence. Then, it must be associated with the baths relaxation to the presence of the impurity, which has to occur on a quite short timescale.

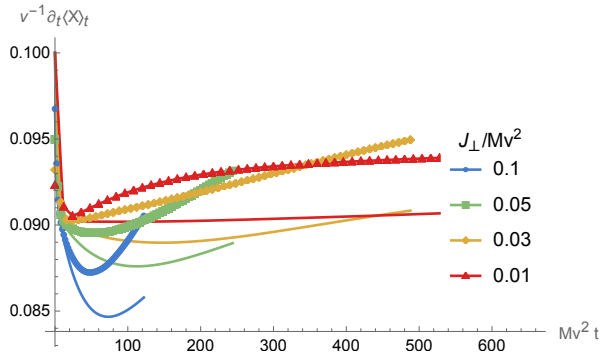

Figure 4.10: Comparison of the impurity speed calculated from the pbc average (4.1.67) (lines with markers) with the one calculated from the bath momentum (4.1.62) (thin lines), for various values of $J_\perp$. The former overestimates the latter, but has the same qualitative behaviour. The system parameters are the same as figure 4.7a

Indeed, we have already observed this two-step behaviour of the impurity speed in 4.1.3. We compare the two definitions of impurity speed in figure 4.10. We can see that the speed calculated from the pbc average position (4.1.67) is generally higher than the one calculated from $\langle P_d\rangle_t = \langle P\rangle_0 - \langle P_b\rangle_t$. Indeed, there is no reason for the two definitions to yield coinciding results. However, they follow the same pattern, namely a steep decrease at short times, followed by a milder decay.[12]

For completeness, in figures 4.9 we report the time evolution of the standard deviation $\sigma_t^{pbc} = [\mathrm{Var}^{pbc}(X,t)]^{1/2}$ of the impurity position. We observe that, after a slight decrease at short times, the standard deviation rapidly rises well above its noninteracting value. This growth is faster for larger $J_\perp$ (figure 4.9a) and for stronger coupling (figure 4.9b). What these plots are measuring is nothing but the build-up of probability in the tail regions of the impurity distribution function (see figure 4.6), a feature that we already discussed as being probably non-physical.

4.1.4 Results for bath observables

In models of mobile impurities, most often the main focus is on the properties of the interacting impurity. Here, we take a complementary view, investigating the time evolution of observables which characterise the baths. This possibility is offered by the perturbative technique we developed, as it gives an approximation of the state describing the whole impurity-bath system. Besides yielding useful insights on the dynamics of the system, observables such as the bath density can be actually accessed in ultracold atom experiments (see [74], for instance).

12 It is evident that the tendency of the speed to increase at later times is stronger for the pbc average. This might due to the loss of normalisation or to the unphysical properties of the tail regions of the impurity density.

NUMBER OF EXCITED PHONONS We will first look at a very simple observable, the number of excited phonons in a given bath σ:

$$\begin{aligned}
N^{ph}_{\sigma}(t) &\equiv \sum_{q\neq 0} \left\langle b^{\dagger}_{q\sigma} b_{q\sigma} \right\rangle_t = \\
&= \sum_{p\mu} |c_{p\mu} a_{p\mu}|^2 \sum_{q\neq 0} \frac{W^2_{q\sigma}}{4L} 2 \frac{1-\cos \Omega^{+\mu}_{q\sigma}(p)t}{(\Omega^{+\mu}_{q\sigma}(p))^2} + \\
&+ 2\sigma \,\mathrm{Re} \left[\sum_{p\mu} (c_{p\mu} a_{p\mu})^* c_{p\bar{\mu}} a_{p\bar{\mu}} \sum_{q\neq 0} \frac{W^2_{q\sigma}}{4L} \frac{1-e^{-i\Omega_{q\sigma}(p)t}}{\Omega_{q\sigma}(p)} \frac{1-e^{i\Omega^{-\mu}_{q\sigma}(p)t}}{\Omega^{-\mu}_{q\sigma}(p)} \right] + \\
&+ \sum_{p\mu} |c_{p\mu}|^2 \sum_{q} \frac{W^2_{q\sigma}}{4L} 2 \frac{1-\cos \Omega_{q\sigma}(p)t}{(\Omega_{q\sigma}(p))^2} = \\
&= -2\,\mathrm{Re} \sum_{p\mu} \left\{ |c_{p\mu} a_{p\mu}|^2 F_{p\sigma}(-\mu J_{\perp}, t) - (c_{p\mu} a_{p\mu})^* c_{p\bar{\mu}} a_{p\bar{\mu}} \mathcal{A}^{\mu}_{p\sigma}(t) \right\} + \\
&- 2\,\mathrm{Re} \sum_{p} \sum_{\mu} |c_{p\mu}|^2 F_{p\sigma}(0, t) \,,
\end{aligned} \tag{4.1.69}$$

where

$$\begin{aligned}
\mathcal{A}^{\mu}_{p\sigma}(t) &\equiv \sum_{q\neq 0} \frac{W^2_{q\sigma}}{4L} \frac{1-e^{-i\Omega_{q\sigma}(p)t}}{\Omega_{q\sigma}(p)} \frac{1-e^{i\Omega^{-\mu}_{q\sigma}(p)t}}{\Omega^{-\mu}_{q\sigma}(p)} = \\
&= \frac{1}{2\mu J_{\perp}} \left[H^*_{p\sigma}(-\mu J_{\perp}, t) - H_{p\sigma}(0, t) + e^{-2\mu i J_{\perp} t} (H_{p\sigma}(\mu J_{\perp}, t) - H^*_{p\sigma}(0, t)) \right] .
\end{aligned} \tag{4.1.70}$$

The number of phonons in each bath can be clearly divided into three contributions. The first is proportional to $-2\,\mathrm{Re}\, F_{p\sigma}(-\mu J_{\perp}, t)$, which for $\mu = o$ gives a factor of $2\gamma(p)t$. This is the rapid increase of phonons caused by the spontaneous emission from the odd impurity mode, and represents the leading term. The second contribution has a sign depending on the bath index σ, and it is essentially an oscillating term. This part takes into account the differences between the evolution of the two baths that are caused by the initialisation of the impurity, namely in which bath it is first injected (in fact, it vanishes if only one parity band is occupied). On the contrary, the third term does not care about the initial bath of the impurity, only its very presence in the system, and at late times it shows a slow, logarithmic growth:

$$-2\,\mathrm{Re} \sum_{p} \sum_{\mu} |c_{p\mu}|^2 F_{p\sigma}(0, t) \sim \sum_{p} \sum_{\mu} |c_{p\mu}|^2 \frac{\beta^{sb}_{\sigma}(p)}{2} \ln t + \mathcal{O}(t^0) \,.$$

This behaviour is strongly reminiscent of the one encountered in section 2.3, namely equation (2.3.16), and can be seen as the signature of the OC. We show the behaviour of equation (4.1.69) in figures 4.11 and 4.12. The first two figures compare the time evolution of the number of phonons in the $\uparrow$ (thick lines) and $\downarrow$ baths (dashed lines), for two different values of the inter-bath hopping. In both plots we can see that $N^{ph}_{\uparrow}$ and $N^{ph}_{\downarrow}$ oscillate out of phase around a mean value that has a steep increase at very short times and then slows down its growth as time goes on. As the impurity is initialised in the $\uparrow$ bath, $N^{ph}_{\uparrow}$ has the fastest growth, initially. The slight tendency to decrease at later times is caused by the loss of state normalisation beyond the odd mode decay time. The difference between the plots (a) and (b) is that the first refers

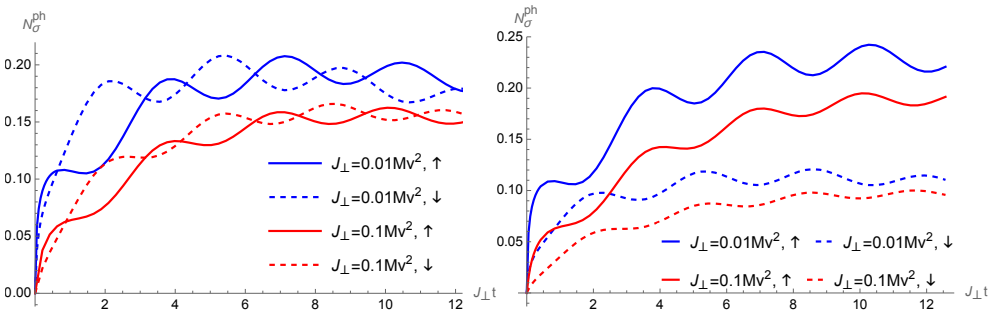

(a) Symmetric **(b)** Asymmetric

Figure 4.11: Number of phonons in the ↑ (thick lines) and ↓ (dashed lines) baths, for an impurity initialised in bath ↑ at zero momentum. Plot (a) refers to a symmetric scenario with $g^2K = 0.5v^2$, while (b) is for asymmetric couplings $g_\uparrow^2 K = 0.5v^2$ and $g_\downarrow^2 K = 0.25v^2$. Notice that the time is measured in units of $J_\perp^{-1}$.

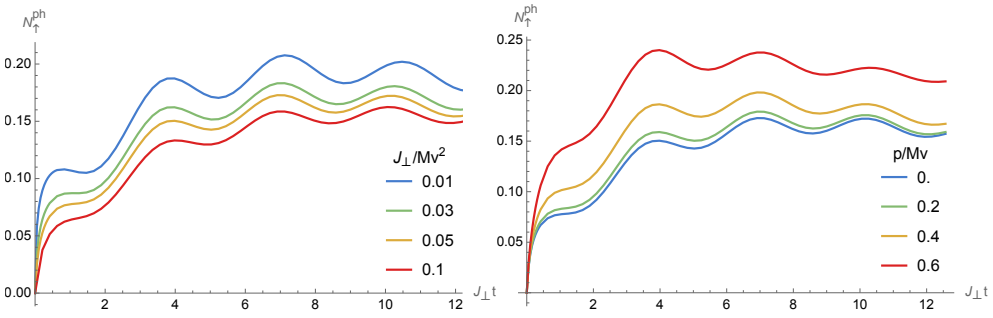

(a) **(b)**

Figure 4.12: Number of phonons generated in the ↑ bath for various values of $J_\perp$ (a) and p, showing that the growth is more pronounced for larger momenta and smaller inter-bath hopping. The baths are symmetric, with couplings $g^2K = 0.5v^2$ and $p = 0$ for (a), while $J_\perp = 0.05Mv^2$ for (b). Notice that the time is measured in units of $J_\perp^{-1}$.

to a symmetric situation, whereas in the second the impurity-bath coupling to the ↑ bath is larger than the one to the ↓ bath. As a consequence, $N^{ph}_{\uparrow}$ increases to higher values than[13] $N^{ph}_{\downarrow}$. In both settings, the plots show that lower values of $J_\perp$ cause a larger number of phonons to be excited, albeit on a slower timescale (as the whole dynamics slows down when $J_\perp$ is decreased).

The next figures 4.12 show the number of excited phonons in the ↑ bath for different inter-bath hopping (a) and for increasing momentum (b). The first one expands the observation made above, namely that when the time evolution of N^{ph}_{σ} is compared measuring time in the appropriate unit $J_\perp^{-1}$ (i.e the bare oscillation period), the number of phonons grows monotonically as $J_\perp$ is lowered. The second plot proves that the same monotonic growth occurs upon increasing the initial impurity momentum (the re-scaling of time in units of the period is not necessary in this case). As a last observation, we remark that the number of phonons in each bath does not always grows in time, as it actually decreases a bit during each oscillation (the total number of phonons, $\sum_\sigma N^{ph}_{\sigma}(t)$ is monotonically increasing in time, though). We are not sure if this is a consequence of the approximation, the loss of normalisation or if it is a genuine physical feature. If the latter case were true, it would mean that whenever the impurity changes bath, it adsorbs some of the previously emitted phonons.

CORRELATION FUNCTIONS We now turn to more complex observables, namely averages and correlation functions of the bath densities $\rho_\sigma(x)$ and conjugate momenta [31] $\Pi_\sigma(x)$,

$$\rho_\sigma(x) = -\frac{1}{\pi}\frac{d}{dx}\phi_\sigma(x) = \frac{K_\sigma^{1/2}}{L^{1/2}}\sum_{q\neq 0} V_q(e^{iqx}b_{q\sigma} + e^{-iqx}b^\dagger_{q\sigma}) \tag{4.1.71a}$$

$$\Pi_\sigma(x) = \frac{1}{\pi}\frac{d}{dx}\theta_\sigma(x) = \frac{1}{K_\sigma^{1/2}L^{1/2}}\sum_{q\neq 0} \mathrm{sgn}(q)V_q(e^{iqx}b_{q\sigma} + e^{-iqx}b^\dagger_{q\sigma})\,, \tag{4.1.71b}$$

where $\mathrm{sgn}(q)$ is the sign function. We remark that we understand $\rho_\sigma(x)$ as the fluctuation part of the density, that is, we already subtracted the average density $\rho^{(0)}_\sigma$ from it. While the physical meaning of $\rho_\sigma(x)$ is obvious, it may be less so for the momentum density $\Pi_\sigma(x)$. The equation of motion for the density (i.e. the continuity equation) shows that, within our long-wavelength approximation, $\Pi_\sigma(x)$ is proportional to the particle current of the baths: $j_\sigma(x) = v_\sigma K_\sigma \Pi_\sigma(x)$.

To use the perturbative solution we found, we must first perform a LLP transformation [equation (4.0.2)], which replaces $b_{q\sigma} \to b_{q\sigma}e^{-iqX}$. Therefore, we have

$$\langle\rho_\sigma(x)\rangle_t = 2\,\mathrm{Re}\left[\frac{K_\sigma^{1/2}}{L^{1/2}}\sum_{q\neq 0} V_q e^{iqx}\left\langle e^{-iqX}b_{q\sigma}\right\rangle_t\right], \tag{4.1.72a}$$

$$\langle\Pi_\sigma(x)\rangle_t = 2\,\mathrm{Re}\left[\frac{1}{K_\sigma^{1/2}L^{1/2}}\sum_{q\neq 0} \mathrm{sgn}(q)V_q e^{iqx}\left\langle e^{-iqX}b_{q\sigma}\right\rangle_t\right]. \tag{4.1.72b}$$

13 The choice of initialising the impurity in the strongest-interacting bath is irrelevant at late times. We have verified that if it were prepared in the ↓ bath, $N^{ph}_{\downarrow}$ would increase above $N^{ph}_{\uparrow}$ only at very early times.

Using expression (4.1.42) [or (4.1.43)] and the property that $e^{-iqx}|p\mu\rangle = |p-q\mu\rangle$, we find

$$\begin{aligned}\left\langle e^{-iqx} b_{q\sigma}\right\rangle_t = -\frac{W_{q\sigma}}{2L^{1/2}} \sum_{p\mu} e^{i(E_{p-q}-E_p)t} \langle \omega_{p-q}(t)|\omega_p(t)\rangle \times \\ \times (c_{p-q,\mu} a_{p-q,\mu}(t))^* \left[c_{p\mu} a_{p\mu}(t) \chi_t(\Omega_{q\sigma}(p)) + \right. \\ \left. + \sigma e^{-i\mu 2 J_\perp t} c_{p\bar{\mu}} a_{p\bar{\mu}}(t) \chi_t(\Omega^{-\mu}_{q\sigma}(p))\right] + \mathcal{O}\left((gK^{1/2}/v)^3\right), \quad (4.1.73)\end{aligned}$$

at the lowest order. It can immediately be seen that the two densities $\langle \rho_\sigma(x)\rangle_t$ and $\langle \Pi_\sigma(x)\rangle_t$ vanish unless the initial impurity state contains more than one momentum. This is physically consistent with the intuition that the impurity in a well-defined momentum state is uniformly distributed along the bath(s).

We would like to remark that the higher-order harmonics in the bosonised bath density equation (2.2.13) yield only a finite-size correction to the equations (4.1.72). For instance, let us take the first correction to the bath density, that reads

$$\begin{aligned}\langle \delta_2 \rho_\sigma(x)\rangle^{lab}_t &= 2A_2 \bar{\rho}_\sigma \langle \cos(2\bar{\rho}_\sigma x - 2\phi_\sigma(x))\rangle^{lab}_t = \\ &= 2A_2 \bar{\rho}_\sigma \operatorname{Re}\left[e^{2i\bar{\rho}_\sigma x}\left\langle e^{-2i\phi_\sigma(x)}\right\rangle^{lab}_t\right], \end{aligned} \quad (4.1.74)$$

where A_2 is a non-universal, dimensionless amplitude and $\langle\cdot\rangle^{lab}_t$ means that the average is taken over the state in the laboratory frame, equation (4.1.49). Let us start with the "zeroth-order" approximation to the state, i.e. keeping only the coherent state contributions.

$$\begin{aligned}\left\langle e^{-2i\phi_\sigma(x)}\right\rangle^{lab}_t &= \frac{1}{N} \sum_{\substack{j,p,\mu \\ j',p',\mu'}} e^{i(p'aj'-paj)-i(\lambda_{p'\mu'}-\lambda_{p\mu})t} c^*_{p\mu} a^*_{p\mu} c_{p'\mu'} a_{p'\mu'} \times \\ &\times \langle j'\mu'|j\mu\rangle \left\langle \omega_p(j,t)\middle|e^{-2i\phi_\sigma(x)}\middle|\omega_{p'}(j',t)\right\rangle + \mathcal{O}(g) = \\ &= \frac{1}{N} \sum_{p,p',\mu,j} e^{i(p'-p)aj - i(\lambda_{p'\mu}-\lambda_{p\mu})t} \times \\ &\times c^*_{p\mu} a^*_{p\mu} c_{p'\mu'} a_{p'\mu'} \left\langle \omega_p(j,t)\middle|e^{-2i\phi_\sigma(x)}\middle|\omega_{p'}(j,t)\right\rangle + \mathcal{O}(g)\end{aligned}$$

The matrix element between the coherent bath states can be computed by first expressing $e^{-2i\phi_\sigma(x)}$ in normal-ordered form [see equation (2.2.15)]:

$$e^{-2i\phi_\sigma(x)} = e^{-2\pi^2 \frac{K_\sigma}{L} \sum_{q\neq 0} \frac{V_q^2}{q^2}} e^{-2\pi \frac{K_\sigma^{1/2}}{L^{1/2}} \sum_{q\neq 0} \frac{V_q}{q} e^{-iqx} b^\dagger_q} e^{2\pi \frac{K_\sigma^{1/2}}{L^{1/2}} \sum_{q\neq 0} \frac{V_q}{q} e^{iqx} b_q}, \quad (4.1.75)$$

which is obtained using the Baker-Campbell-Hausdorff formula $e^A e^B = e^{A+B} e^{1/2[A,B]}$ truncated for the present case in which $[A,B] \propto \mathbb{1}$. Then

$$\begin{aligned}\left\langle \omega_p(j,t)\middle|e^{-2i\phi_\sigma(x)}\middle|\omega_{p'}(j,t)\right\rangle = \left\langle \omega_p(j,t)\middle|\omega_{p'}(j,t)\right\rangle e^{-2\pi^2 \frac{K_\sigma}{L} \sum_{q\neq 0} \frac{V_q^2}{q^2}} \times \\ \times e^{2\pi \frac{K_\sigma^{1/2}}{2L} \sum_{q\neq 0} \frac{V_q}{q} W_{q\sigma} [e^{-iq(x-aj)} \chi^*_t(\Omega_{q\sigma}(p)) - e^{iq(x-aj)} \chi_t(\Omega_{q\sigma}(p'))]}. \quad (4.1.76)\end{aligned}$$

The overlap $\left\langle \omega_p(j,t)\middle|\omega_{p'}(j,t)\right\rangle$ turns out to coincide with $\left\langle \omega_p(t)\middle|\omega_{p'}(t)\right\rangle$, which is given by equation (4.1.15) and is a finite quantity. Analogously, the

last exponential in the above equation gives a finite contribution, because the summed function behaves like $V_q W_{q\sigma}/q \sim V_q^2/q \sim |q|/q$ for small momentum. On the contrary, the first exponential (coming from the normal ordering of $e^{-2i\phi_\sigma(x)}$) turns out to be decreasing as a power-law in the system length L. In fact, approximating the momentum sum in the exponent with an integral in the continuum limit, we obtain

$$2\pi^2 \tfrac{K_\sigma}{L} \sum_{q\neq 0} \tfrac{V_q^2}{q^2} \approx 2\pi^2 K_\sigma \int_{-\infty}^{+\infty} \tfrac{dq}{2\pi} \tfrac{V_q^2}{q^2} = K_\sigma \int_0^{+\infty} dq\, \tfrac{q}{q^2} e^{-\alpha q} \,,$$

which is divergent at small momenta. Since in pbc momentum is quantised in units of $2\pi/L$ and the original sum excludes $q = 0$, we cut off the integral as

$$2\pi^2 \tfrac{K_\sigma}{L} \sum_{q\neq 0} \tfrac{V_q^2}{q^2} \approx K_\sigma \int_{2\pi/L}^{+\infty} dq\, \tfrac{1}{q} e^{-\alpha q} = -K_\sigma E_1(\tfrac{2\pi\alpha}{L}) \,.$$

Since $E_1(z) \sim -\gamma - \ln z + \mathcal{O}(z)$ for $z \to 0$ [23], the equation above means that the density correction is suppressed by a factor

$$e^{\gamma K_\sigma} \left(\tfrac{L}{2\pi\alpha}\right)^{-K_\sigma} \,. \tag{4.1.77}$$

The extension of the above calculations to the first-order contribution to the state yields again only finite terms in the large-size limit, except for the above suppression factor that is carried around by the $e^{-2i\phi_\sigma(x)}$ operator. Therefore, unless A_2 compensates for (4.1.77)[14], we conclude that the correction to the bath density coming from the first harmonics in the bosonised density (2.2.13) (and, analogously, for all higher harmonics) is only a finite-size effect, which is smaller the larger is the Luttinger parameter K_σ. Notice that the suppression factor does not depend on any of the impurity properties. Albeit encouraging with regard to the accuracy of the approximations of our model, the observation that the correction to the density is small does not imply that the cosine term in the density is always irrelevant for the physics, because we are not including it in the interaction term in the Hamiltonian. Rather, it implies that there is some kind of self-consistency in the approximation, as a term neglected in the Hamiltonian does not resurface in an observable.

As the impurity is exchanged between the baths, these will become correlated. We will measure the amount of inter-bath correlation by computing the equal-time connected correlation functions

$$\langle \rho_\sigma(x)\rho_{\bar\sigma}(y)\rangle_t^c \equiv \langle \rho_\sigma(x)\rho_{\bar\sigma}(y)\rangle_t - \langle \rho_\sigma(x)\rangle_t \langle \rho_{\bar\sigma}(y)\rangle_t \tag{4.1.78a}$$

$$\langle \Pi_\sigma(x)\Pi_{\bar\sigma}(y)\rangle_t^c \equiv \langle \Pi_\sigma(x)\Pi_{\bar\sigma}(y)\rangle_t - \langle \Pi_\sigma(x)\rangle_t \langle \Pi_{\bar\sigma}(y)\rangle_t \,, \tag{4.1.78b}$$

14 This depends on the model underlying the TLL effective field theory. However, the A_2 non-universality means that it is a UV-sensitive quantity, so we do not expect a IR divergence like the one needed to compensate equation (4.1.77).

whose expressions are

$$\langle \rho_\sigma(x)\rho_{\bar\sigma}(y)\rangle_t = (K_\sigma K_{\bar\sigma})^{1/2} 2\,\mathrm{Re}\left\{ \frac{1}{L}\sum_{q,\bar q\neq 0} V_q V_{\bar q} \times \right.$$
$$\left. \times\left[\left\langle b_{q\sigma} b_{\bar q\bar\sigma} e^{-i(q+\bar q)X}\right\rangle_t e^{i(qx+\bar q y)} + \left\langle b^\dagger_{q\sigma} b_{\bar q\bar\sigma} e^{i(q-\bar q)X}\right\rangle_t e^{-i(qx-\bar q y)}\right]\right\}, \tag{4.1.79a}$$

$$\langle \Pi_\sigma(x)\Pi_{\bar\sigma}(y)\rangle_t = (K_\sigma K_{\bar\sigma})^{-1/2} 2\,\mathrm{Re}\left\{ \frac{1}{L}\sum_{q,\bar q\neq 0} V_q V_{\bar q}\,\mathrm{sgn}(q\bar q) \times \right.$$
$$\left. \times\left[\left\langle b_{q\sigma} b_{\bar q\bar\sigma} e^{-i(q+\bar q)X}\right\rangle_t e^{i(qx+\bar q y)} + \left\langle b^\dagger_{q\sigma} b_{\bar q\bar\sigma} e^{i(q-\bar q)X}\right\rangle_t e^{-i(qx-\bar q y)}\right]\right\}. \tag{4.1.79b}$$

The relevant averages are given by

$$\begin{aligned}
&\left\langle b_{q\sigma} b_{\bar q\bar\sigma} e^{-i(q+\bar q)X}\right\rangle_t = \\
&= \sum_{p,\bar p,\mu} \delta_{\bar p - p, q+\bar q} e^{i(E_p - E_{\bar p})t} \langle \omega_p(t)|\omega_{\bar p}(t)\rangle \\
&\times \left\{ \frac{W_{q\sigma}W_{\bar q\bar\sigma}}{4L}\left[(c_{p\mu}a_{p\mu})^* c_{\bar p\mu} a_{\bar p\mu} \chi_t(\Omega_{q\sigma}(\bar p))\chi_t(\Omega_{\bar q\bar\sigma}(\bar p)) + \right.\right. \\
&+ \sigma e^{-i\mu 2J_\perp t}(c_{p\mu}a_{p\mu})^* c_{\bar p\bar\mu} a_{\bar p\bar\mu}\big(\chi_t(\Omega^{-\mu}_{q\sigma}(\bar p))\chi_t(\Omega_{\bar p\bar\sigma}(\bar p)) + \\
&\left.\left. - \chi_t(\Omega_{q\sigma}(\bar p))\chi_t(\Omega^{-\mu}_{\bar p\bar\sigma}(\bar p))\big)\right] + \right. \\
&\left. + 2(c_{p\mu}a_{p\mu})^*\left[c_{\bar p\mu}a_{\bar p\mu} A^{\mu\mu}_{q\sigma,\bar q\bar\sigma}(\bar p, t) + c_{\bar p\bar\mu}a_{\bar p\bar\mu} A^{\bar\mu\mu}_{q\sigma,\bar q\bar\sigma}(\bar p, t)\right]\right\} + \\
&+ \mathcal{O}\Big((gK^{1/2}/v)^3\Big)
\end{aligned} \tag{4.1.80a}$$

and

$$\begin{aligned}
&\left\langle b^\dagger_{q\sigma} b_{\bar q\bar\sigma} e^{i(q-\bar q)X}\right\rangle_t = \\
&= \frac{W_{q\sigma}W_{\bar q\bar\sigma}}{4L} \sum_{p,\bar p,\mu} \delta_{\bar p - p, -q+\bar q} e^{i(E_p - E_{\bar p})t} \langle \omega_p(t)|\omega_{\bar p}(t)\rangle \\
&\times \big[(c_{p\mu}a_{p\mu})^* c_{\bar p\mu} a_{\bar p\mu}\big(\chi^*_t(\Omega_{q\sigma}(p))\chi_t(\Omega_{\bar q\bar\sigma}(\bar p)) + \\
&- \chi^*_t(\Omega^{+\mu}_{q\sigma}(p))\chi_t(\Omega^{+\mu}_{\bar q\bar\sigma}(\bar p))\big) \\
&+ \sigma e^{-i\mu 2J_\perp t}(c_{p\mu}a_{p\mu})^* c_{\bar p\bar\mu} a_{\bar p\bar\mu}\big(\chi^*_t(\Omega^{+\mu}_{q\sigma}(p))\chi_t(\Omega_{\bar p\bar\sigma}(\bar p)) + \\
&- \chi^*_t(\Omega_{q\sigma}(p))\chi_t(\Omega^{-\mu}_{\bar p\bar\sigma}(\bar p))\big)\big] + \mathcal{O}\Big((gK^{1/2}/v)^3\Big).
\end{aligned} \tag{4.1.80b}$$

As we can see, these averages depend on the amplitudes $A^{\mu\nu}$ of the two-phonon terms in the state evolution. We point out that in the limit $J_\perp \to 0$ the baths become decoupled from each other, so we expect that inter-bath correlations factorise as $\langle \rho_\sigma(x)\rho_{\bar\sigma}(y)\rangle_t\big|_{J_\perp=0} = \langle \rho_\sigma(x)\rangle_t\big|_{J_\perp=0}\langle \rho_{\bar\sigma}(y)\rangle_t\big|_{J_\perp=0}$ (and analogously for momentum). However, this is not true for the perturbative expressions equations (4.1.80) given above. This is explained by noticing that in our perturbative solution we broke up the interaction in two terms, treating one exactly while expanding in the second one. When $J_\perp = 0$, this separation is unjustified, and it actually gives rise to a spurious (yet small) inter-bath correlation.[15] On the other hand, observables such as $\langle \rho_\sigma(x)\rangle_t$ and

15 This behaviour can be understood as follows: at $J_\perp = 0$, and neglecting recoil, the time evolution operator for the baths is $e^{-i(h_0(p)+\sigma_3 V)}$. The correct solution is to set σ_3 to

$\langle \Pi_\sigma(x) \rangle_t$ converge to the right limit for $J_\perp \to 0$. Among the observables we have analysed, it seems that only the inter-bath correlation functions has a problematic $J_\perp \to 0$ limit. To avoid analysing the resulting unphysical correlations, we choose to work with the correlation functions with their $J_\perp = 0$ values subtracted.

Before illustrating the results of the numerical evaluation of densities and correlation functions, it is worth to comment on the algorithmic complexity for their computation. The densities equations (4.1.72) are quite cheap to compute, as they require to evaluate equation (4.1.73) ($2 \cdot N_p$ terms for the N_p momentum components of the wave packet) for each of the N_q bath momenta. The slowest part of the terms that have to be summed is the overlap $\langle \omega_{p-q}(t) | \omega_p(t) \rangle$, because it contains a term "off-diagonal" in momentum [see equation (4.1.15)] that has to be integrated without optimisation strategies, as we discussed for the impurity density. Still, there is only one non-optimised term, and as a result the computation is rather fast.[16]

On the contrary, the inter-bath correlation functions are much more expensive to compute. From equations (4.1.79) and (4.1.80) it is evident that one needs to sum $\mathcal{O}\left(N_q^2 N_p^2\right)$ oscillating terms.

Numerical results: bath density evolution

In figure 4.13 we show the bath density evolution for increasing values of $J_\perp$, keeping all other parameters constant. The baths have identical properties. The initial impurity wave packet starts in the $\uparrow$ bath, with an average position $x_0 = L/2$ and a momentum distribution that is centred around $p_0 = 0.1Mv$, with a width (standard deviation) of $\delta p = 0.04Mv$ (correspondingly, the spatial width of the wave packet is about $\delta x \sim 1/(2\delta p) = 12.5(Mv)^{-1}$). These figures show that the density evolution has a common structure: a trough that follows the impurity (notice how it is inclined to the right, owing to the nonzero average momentum p_0), flanked by two wave fronts that "radiate" in opposite directions at the speed of sound (which is $v = 1$ in our units). As time goes on, the region between these features (the "light-cone" $|x| \leqslant vt$) becomes filled with density ripples, which can be seen as a manifestation of the emission of real phonons because of the deexcitation from the odd to the even mode. This interpretation follows from the observation that these ripples ultimately come from the $b^\dagger_{q\sigma} |\omega_p(t)\rangle$ terms (i.e. from the the last term of equation (4.1.73)), which we interpreted as representing spontaneous emission. On the other hand, the trough and the wave front are all contained in the coherent states $|\omega_p(t)\rangle$. More physically, the ripples have a wavelength that is inversely proportional to $J_\perp$, corresponding roughly to the wave vectors $q_\pm$ that solve $\Omega_{q_\pm \sigma}(p_0) = 2J_\perp$ (the negative and positive solutions of this equation apply to backward and forward emission, respec-

one of its eigenvalues (depending on the initial bath index of the impurity), and then to diagonalise the resulting Hamiltonian. Our interaction-splitting procedure is roughly equivalent to insisting on treating $\sigma_3 V$ as a perturbation, obtaining $e^{-i(h_0(p)+\sigma_3 V)} \approx e^{-ih_0(p)t}[1 - i\sigma_3 \int_0^t dt_1\, V(t_1) - \int_0^t dt_1 \int_0^{t_1} dt_2\, V(t_1)V(t_2)]$, which is a rather poor approximation to the exact dynamics. The $V(t_1)V(t_2)$ term is the one responsible for the spurious correlations.

16 It takes only a few minutes to generate the time evolution of the density for $N_p = 32$ momenta on the author's laptop, without need for parallelisation.

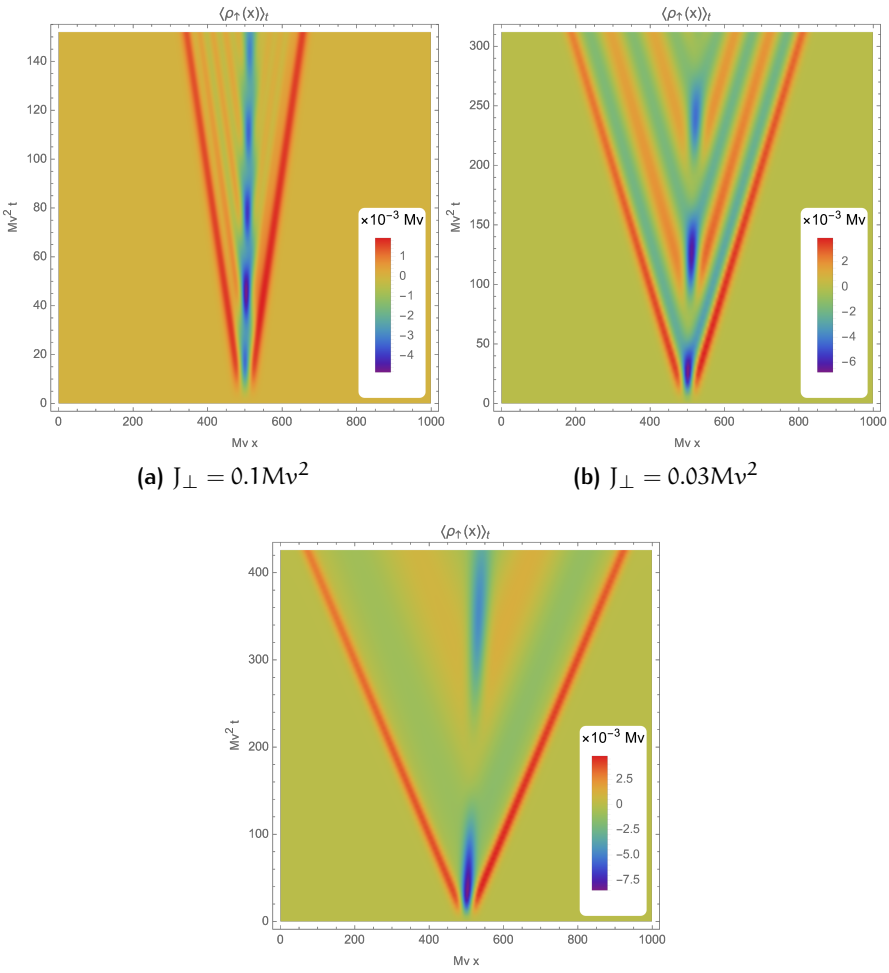

(a) $J_\perp = 0.1Mv^2$ **(b)** $J_\perp = 0.03Mv^2$

(c) $J_\perp = 0.01Mv^2$

Figure 4.13: Dynamics of the density perturbation of bath ↑ caused by the introduction of an impurity wave packet. The parameters are $g^2K = 0.5v^2$, $K = 2$ for both baths (we take $M = 1$, $v = 1$). The wave packet has the form (4.1.51) with $N_p = 64$ and $\delta p = 0.04Mv$. The cutoffs are $Mv\alpha = 0.5$ and $\Lambda = 10Mv^2$. Plots (a) to (c) differ in the inter-bath hopping $J_\perp$.

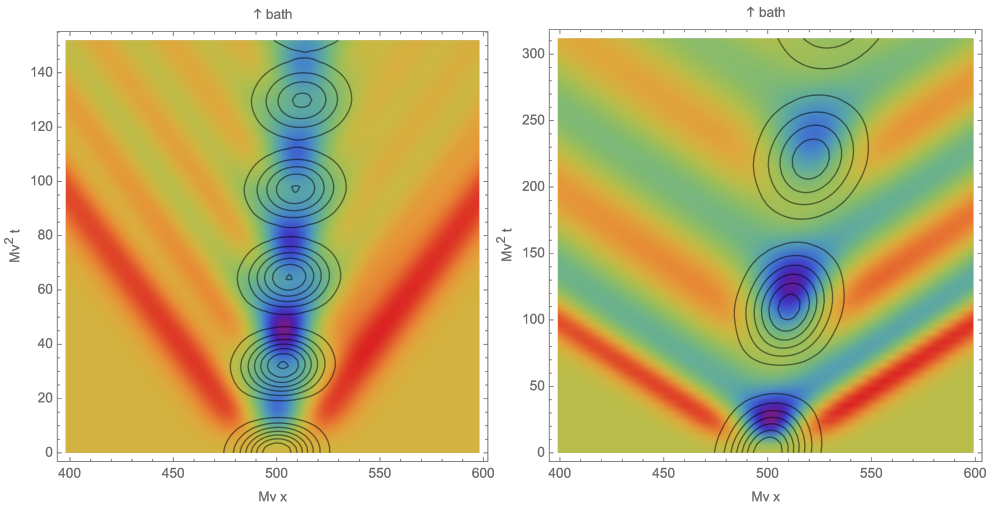

(a) $J_\perp = 0.1Mv^2$ **(b)** $J_\perp = 0.03Mv^2$

Figure 4.14: Comparison of the dynamics of the density fluctuation in the baths (colour scale) and of the impurity density (black contours). The oscillations are nearly out of phase for (a) large $J_\perp$ while they synchronise at (b) lower $J_\perp$. The parameters are the same as figure 4.13.

tively). These observations support our view of the perturbative solution as being decomposed into a "bath relaxation" (trough and wave fronts) and spontaneous emission.

As $J_\perp$ becomes smaller, the ripples become higher and of longer wavelength, and the whole density profile becomes wider. Ad the same time, the depth of the minimum oscillates more and more evidently, as the impurity oscillation becomes slower. This agrees with the intuition that at $J_\perp = 0$ the single-bath situation should be recovered, in which the impurity remains in its initial bath.

We observe that the ripples are emitted when the trough reaches its maximal depth, which we can interpret as the moment when the impurity transits in the bath. This observation suggests an alternative, semiclassical way of looking at the phonon emission: as the impurity leaves a bath for the other, the original one tends to relax back to equilibrium (i.e., zero average density), but then the impurity oscillates back into the bath, and so another pair of wave fronts is emitted. Overall, the result is a series of ripples, as observed in figures 4.13. This interpretation is supported by comparing the bath density evolution with the one of the impurity density, as depicted in figures 4.14. Indeed, we observe that the oscillations in the depth of the central dip in the bath density do follow the position and bath oscillations of the impurity wave packet. However, as the baths relax rather slowly, in general the time at which the trough reaches its maximal depth lags behind the moment of maximal height of the impurity density. This delay is particularly relevant for the larger values of $J_\perp$ (figure 4.14a), whereas for lower inter-bath hopping the oscillations are almost synchronised (figure 4.14b).

The bath are identical in their properties and initial state, the only source of asymmetry in their behaviour is the initial position of the impurity, which we chose to be the ↑ bath. This causes the ↓ bath to interact with the impurity

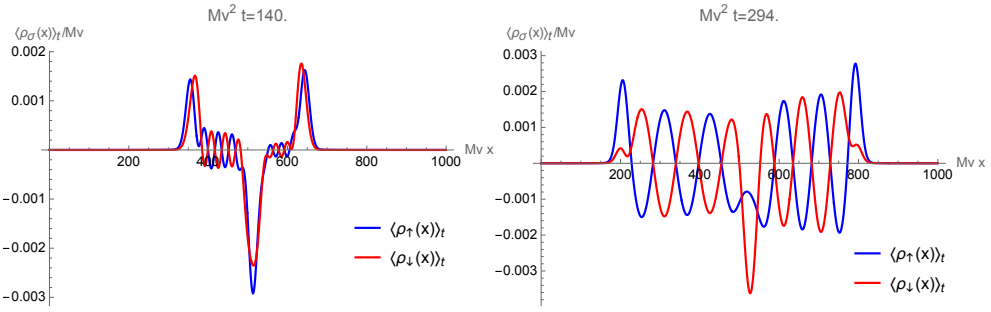

(a) $J_\perp = 0.1Mv^2$ **(b)** $J_\perp = 0.03Mv^2$

Figure 4.15: Density profile in both baths at a given instant of time. The parameters are the same as figure 4.13.

a little later than the $\uparrow$ one (roughly after a fraction of the bare oscillation period $2\pi/J_\perp$). Because of this, the density profile of the $\downarrow$ bath is qualitatively similar to the $\uparrow$ one, but it is "delayed" by the time it takes the impurity to change its initial bath. This is shown in figure 4.15, in which the $\uparrow$ bath density is shown in blue and the $\downarrow$ one in red. At large $J_\perp$, the impurity is rapidly exchanged, and therefore the density profiles of the baths are "synchronised", almost coinciding with each other (except from the ripples), and with very little relative lag. As $J_\perp$ is decreased, the oscillations in the trough depth become wider and wider and thus can be clearly seen to be out of phase, while the wave fronts are always in phase, but show a visible lag. Moreover, the wave fronts in the $\downarrow$ bath decrease in height with respect to their $\uparrow$ counterparts when $J_\perp$ assumes smaller values. The ripples are rigorously out of phase. In fact, we have already remarked that the ripples come from the second term in the square brackets in equation (4.1.73), which is multiplied by $\sigma = \pm 1$.

From figures 4.13 and especially from 4.15 it is immediate to notice that the density profile is not symmetric around $x = L/2$. The reason is, of course, that we endowed the impurity with a finite average momentum, so that the forward and backward direction are not equivalent. Indeed, not only the position of the central trough moves to the right, away from $x = L/2$, but also the profiles of the wave fronts and ripples on the right of the impurity differ from those on the left. The wave fronts emitted in the forward directions are always taller than the ones emitted backwards. The height of the ripples does not follow the same scheme (indeed, we will see that it depends also on other factors), but their wavelength is smaller in the forward direction. As we mentioned before, this wavelength corresponds to the wave vectors $q_\pm$ that solve[17] $\Omega_{q_\pm\sigma}(p_0) = 2J_\perp$, which is nothing but the equation imposing energy conservation in the emission of a phonon during a transition from the odd to the even impurity mode. The relation $q_+(p_0) > |q_-(p_0)|$ is simply the Doppler shift of the wavelength caused by the motion of the source, albeit the magnitude of the shift does not follow the usual classical formula

17 There is one such pair of phonon momenta for each impurity momentum contributing to the wave packet, but the differences are rather small and so we keep only the central momentum, for clarity.

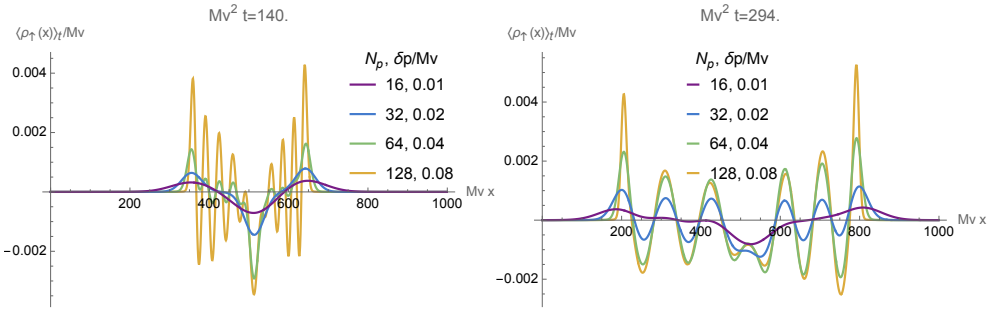

(a) $J_\perp = 0.1Mv^2$ **(b)** $J_\perp = 0.03Mv^2$

Figure 4.16: Density profile in the ↑ baths at a given instant of time, for decreasing width $1/(2\delta p)$ of the initial wave packets. The system parameters are the same as figure 4.13.

$q_\pm(p_0) = q_\pm(p_0 = 0)/(1 \mp p_0/Mv)$ because of the finite recoil energy of the impurity.

Another feature that can be clearly seen in figure 4.15 is that the trough and wave fronts have a distinct shape from that of the ripples. This is also evident from the observation that the wavelength of the ripples depends on $J_\perp$, whereas the width of the other two does not. Indeed, it is not hard to guess that trough and wave fronts are essentially "images" of the Gaussian profile of the impurity wave packet, albeit slightly distorted. The shape of the ripples is instead more or less sinusoidal, and this suggests that their behaviour is governed by the intrinsic dynamics of the baths, rather than by the details of the shape of the wave packet.

These observations are substantiated by investigating the effect of the initial wave packet width on the bath density profile. This is shown in figures 4.16, in which the density profile of the ↑ bath at a given time is compared for decreasing widths $\delta x \sim 1/(2\delta p)$, for two values of the inter-bath hopping. To keep the wave packet shape unaltered while decreasing its standard deviation, we have kept the ratio $\delta p/N_p$ constant.[18] The main effect of a smaller width is that the magnitude of the density fluctuations is increased. This is easily understood for the wave fronts and the central trough if we trust the observation that they have the same shape as the wave packet, as a narrower Gaussian is also taller. On the other hand, the influence on the height of the ripples can be partially understood by observing that wave packets with maximal width (equal to the length of the system) are made of only one momentum, and therefore (compare with equations (4.1.72)) produce no density perturbation in the baths. Then, a continuity argument suggests that wider wave packets should give rise to smaller density fluctuations, including the ripples. We will return to this point in a few paragraphs.

We also notice that the dependence of the density fluctuation amplitude is more prominent for the ripples than for the through and wave fronts, to the point that a wide enough wave packet is able to effectively suppress the ripples altogether. This effect is more noticeable for larger inter-bath hopping

18 A large δp with a small N_p means that the Fourier components of the initial wave packet vanish more or less abruptly at larger momenta, and the impurity density would then show oscillations according to Gibbs' phenomenon [23]

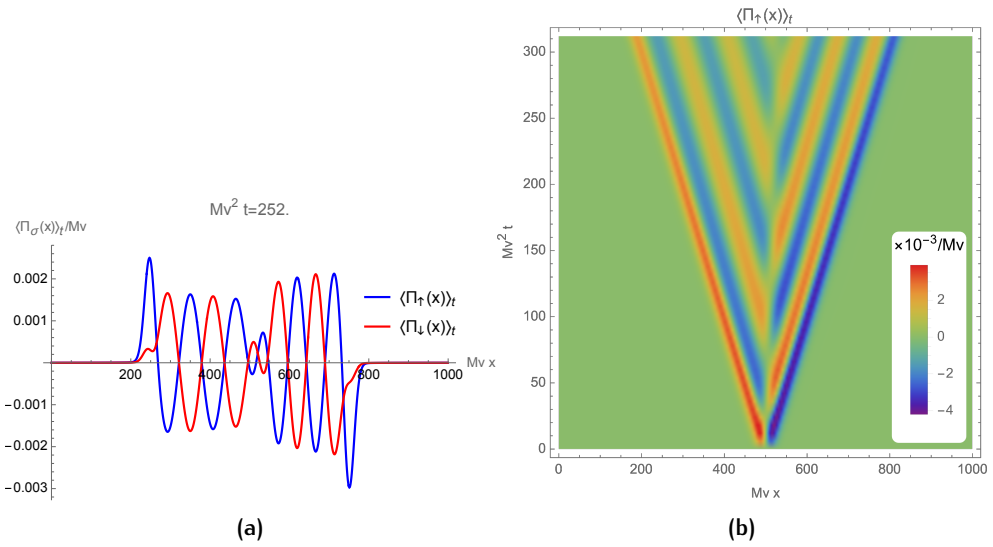

Figure 4.17: Momentum density evolution. Figure (a) shows a snapshot of the momentum density profiles for both baths, while figure (b) shows the full evolution of the ↑ bath momentum density. The parameter settings are $g^2K = 0.5v^2$, $K = 2$ for both baths, and $J_\perp = 0.03Mv^2$

$J_\perp$, as from figures 4.16 we can see that $\delta p = 0.02Mv$ is sufficient to cancel the ripples at $J_\perp = 0.1Mv^2$, whereas at $J_\perp = 0.03Mv^2$ it is not. On the contrary, the wavelength of the ripples is not affected by the wave packet width, whereas the central dip and the wave fronts change their shape, becoming narrower and more peaked as δp is increased. This is in accord with our observation that they should be shifted images of the initial wave packet.

We have also computed the momentum density $\langle \Pi_\sigma(x) \rangle_t$, whose typical behaviour is illustrated in figures 4.17. The time evolution of the momentum density shares many qualitative features with the density. There is a central part that follows the motion of the impurity, made of a relative minimum and a maximum that oscillate in time, cyclically exchanging their roles. From them, two trains of ripples expand in opposite directions, up to two wave fronts. Contrary to the density, these wave fronts are out of phase: the left-moving one is positive, while the right-moving one is negative. This does not seem to be related to the sign of the momenta in the wave packet. As in the case of the density, the central part and the wave fronts are always present for any $J_\perp$, whereas the ripples increase their amplitude as $J_\perp$ becomes smaller. Moreover, all features except from the wave fronts are out of phase between the two baths.

We want to briefly comment upon the scaling of the densities with Luttinger parameters K_σ. In the long-wavelength effective Hamiltonian (2.2.16), K_σ enters only through the combination $\tilde{g}_\sigma \equiv g_\sigma K_\sigma^{1/2}$, hence the expectation value equation (4.1.73) of $\langle e^{-iqX} b_{q\sigma} \rangle$ only depend on $\tilde{g}_\sigma$. On the other hand, the densities equation (4.1.73) explicitly contain K_σ, and we can express their scaling as

$$\langle \rho_\sigma(x) \rangle_t = K_\sigma^{1/2} f_\rho(g_\uparrow^2 K_\uparrow, g_\downarrow^2 K_\downarrow) \,, \tag{4.1.81a}$$

$$\langle \Pi_\sigma(x) \rangle_t = K_\sigma^{-1/2} f_\Pi(g_\uparrow^2 K_\uparrow, g_\downarrow^2 K_\downarrow) \,, \tag{4.1.81b}$$

where f_ρ and f_Π are two appropriate functions that we do not need to specify here. From the equations above, we can deduce that the *shape* of the density profiles is controlled only by the effective coupling $\tilde{g}_\sigma$, while if one varies K_σ while keeping $\tilde{g}_\sigma = g_\sigma K_\sigma^{1/2}$ fixed the density or momentum profile only gets rescaled. Thus, each of the figures shown above can be taken to represent a family of density profiles.

Insights from the equations of motion

The results presented thus far can be interpreted in the light of the linear relation between the bath density and the impurity density. In fact, the Heisenberg equations of motion for $\rho_\sigma(x,t)$ and $\Pi_\sigma(x,t)$ read

$$\partial_t \rho(x,t) = -\partial_x[v_\sigma K_\sigma \Pi_\sigma(x,t)] \tag{4.1.82a}$$

$$\partial_t \Pi_\sigma(x,t) = -v_\sigma \partial_x \left[\tfrac{1}{K_\sigma}\rho_\sigma(x) + \tfrac{g_\sigma}{\pi v_\sigma} d_\sigma^\dagger(x,t) d_\sigma(x,t)\right] . \tag{4.1.82b}$$

We are taking the continuum limit $a \to 0$ for the impurity, to keep the notation simple.[19] The equation of motion for the density alone can be derived by combining the above equations:

$$\left(\tfrac{1}{v_\sigma^2}\partial_t^2 - \partial_x^2\right)\rho_\sigma(x,t) = \tfrac{g_\sigma K_\sigma}{\pi v_\sigma}\partial_x^2[d_\sigma^\dagger(x,t)d_\sigma(x,t)] . \tag{4.1.83}$$

Albeit we can explicitly solve this equation for $\rho_\sigma(x,t)$ using the Green's function for the d'Alembert operator $v_\sigma^{-2}\partial_t^2 - \partial_x^2$, we can easily guess the solution by recognising that we can use the results from linear response theory. In fact, if the impurity density were a classical field we would obtain the same equation. But the equation is linear in both the density and the source, so linear response theory yields the exact result, and the operator nature of the "external field" $g_\sigma d_\sigma^\dagger(x,t)d_\sigma(x,t)$ never comes up. Therefore, we obtain

$$\begin{aligned}\rho_\sigma(x,t) = \rho_\sigma(x,0) + \\ + g_\sigma \int_{\mathbb{R}} dx' \int_0^t dt' \, \chi_\sigma(x-x',t-t') d_\sigma^\dagger(x',t') d_\sigma(x',t') ,\end{aligned} \tag{4.1.84}$$

where $\rho_\sigma(x,0)$ is the noninteracting density, equation (4.1.71). We remark that, unlike linear response theory that deals with expectation values, the above equation is a relation between operators. This difference will show up in the next paragraphs. The above equation is valid within the approximation that the bosonised density retains only the longest-wavelength contribution $-1/\pi\partial_x\phi_\sigma(x)$, which guarantees that the equations of motion for the densities are linear. The kernel $\chi_\sigma(x,t)$ is the retarded density-density linear response function for the baths,

$$\begin{aligned}\chi_\sigma(x,t) \equiv -i\theta(t)\,\langle\omega|[\rho_\sigma(x,t),\rho_\sigma(0,0)]|\omega\rangle = \\ = \theta(t)\tfrac{K_\sigma}{2\pi}\left[\delta'_\alpha(x+v_\sigma t) - \delta'_\alpha(x-v_\sigma t)\right] ,\end{aligned} \tag{4.1.85}$$

19 These results are easily translated to the lattice case with the substitution $d_\sigma^\dagger(x,t)d_\sigma(x,t) \to \sum_j \delta(x-aj) d_{j\sigma}^\dagger(t) d_{j\sigma}(t)$.

where the prime indicates a derivative with respect to the argument of the function

$$\delta_\alpha(x) \equiv \frac{1}{\pi}\frac{\alpha}{x^2+\alpha^2} \,. \tag{4.1.86}$$

This is a smeared representation of the Dirac delta function, whose smearing parameter α is the length that serves as a UV cutoff for the TLL.

If we take the average of equation(4.1.84) over the initial state, we obtain the relation

$$\langle \rho_\sigma(x)\rangle_t = g_\sigma \int_{\mathbb{R}} dx' \int_0^t dt'\, \chi_\sigma(x-x', t-t') \left\langle d^\dagger_\sigma(x') d_\sigma(x')\right\rangle_{t'} \tag{4.1.87}$$

between the bath and impurity density. If we compare equations (4.1.72), (4.1.73) and (4.1.64) we see that the above relation can be satisfied only approximately by our perturbative solution, but it can still provide a guide to the interpretation of the numerical results. For instance, it gives a foundation to the "semi-classical" behaviour of $\langle \rho_\sigma(x)\rangle_t$. In fact, substituting the expression for the retarded response function with $\alpha \to 0$ we get

$$\begin{aligned}\langle \rho_\sigma(x)\rangle_t = \tfrac{g_\sigma K_\sigma}{2\pi} \int_0^t dt' \Big[\partial_{x'} \left\langle d^\dagger_\sigma(x') d_\sigma(x')\right\rangle_{t'} \Big|_{x'=x+v_\sigma(t-t')} + \\ - \partial_{x'} \left\langle d^\dagger_\sigma(x') d_\sigma(x')\right\rangle_{t'} \Big|_{x'=x-v_\sigma(t-t')} \Big] \,,\end{aligned} \tag{4.1.88}$$

where the spatial arguments $x \pm v_\sigma(t-t')$ have to be interpreted modulo translation by the length of the system, L, because of the pbc. This equation helps us to understand the features of the time evolution of the bath density that we highlighted in the previous paragraphs. Indeed, it shows that the density a coordinates (x,t) is a *superposition* of the all the values of the (gradients of the) impurity density on the light-cone of the given space-time point. Besides showing that the baths have rather long "memory", the superposition of the various images of the non-positive-definite gradient of the impurity density paves the way to interference effects. Indeed, it is possible to show that the behaviour of the ripples amplitude (i.e. their suppression for sufficiently large $J_\perp$ or small δx) can be explained as an interference effect, in which there is a cancellation between opposite-sign terms at different times in the past. In appendix A we show that this destructive interference occurs only if the initial wave packet is large enough, according to the relation

$$\delta x \gtrsim \delta x^\pm_{c,\sigma}(p_0, J_\perp), \qquad \delta x^\pm_{c,\sigma}(p_0, J_\perp) \equiv \left(v_\sigma \pm \tfrac{p_0}{M}\right) \frac{\pi}{2\tilde{J}_{\perp,p_0}} \,, \tag{4.1.89}$$

or, equivalently, if the momentum distribution is sufficiently narrow:

$$\delta p \lesssim \delta p^\pm_{c,\sigma}(p_0, J_\perp), \qquad \delta p^\pm_{c,\sigma}(p_0, J_\perp) \equiv \frac{\tilde{J}_{\perp,p_0}}{\pi\left(v_\sigma \pm \tfrac{p_0}{M}\right)} \,, \tag{4.1.90}$$

Ignoring for a moment the dependence on p_0, we see that $\delta p^\pm_{c,\sigma}(p_0, J_\perp)$ is about $0.03Mv$ for $J_\perp = 0.1Mv^2$ and $0.01Mv$ for $J_\perp = 0.03Mv^2$. Indeed, looking at figures 4.16, we see that all three plots showing no sign of ripples (two for $J_\perp = 0.1Mv^2$ and one for $J_\perp = 0.03Mv^2$) occur precisely if the above inequality is satisfied at the respective value of $J_\perp$. The positive or negative

sign in equations (4.1.89) and (4.1.90) refer to the ripples emitted backward or forward, respectively. This directional dependence allows us to justify the asymmetric height of the ripples, as the critical width for backward emission is larger than the one for the forward emission, which implies that the cancellation effect is less effective in the backward direction, resulting in the larger ripple amplitude that we observed.

As the equations of motion (4.1.82) are also linear for the momentum density $\Pi_\sigma(x,t)$, we can use linear response theory to relate this quantity to the impurity density, in analogy with equation (4.1.84):

$$\begin{aligned}\Pi_\sigma(x,t) &= \Pi_\sigma(x,0)+ \\ &+ g_\sigma \int_{\mathbb{R}} dx' \int_0^t dt'\, \chi_\sigma^{\Pi\rho}(x-x',t-t') d_\sigma^\dagger(x',t') d_\sigma(x',t') \,, \end{aligned} \tag{4.1.91}$$

where $\chi_\sigma^{\Pi\rho}(x,t)$ is the momentum-density retarded response function:

$$\begin{aligned}\chi_\sigma^{\Pi\rho}(x,t) &\equiv -i\theta(t) \langle\omega|[\Pi_\sigma(x,t),\rho_\sigma(0,0)]|\omega\rangle = \\ &= -\theta(t)\tfrac{1}{2\pi}\left[\delta'_\alpha(x+v_\sigma t)+\delta'_\alpha(x-v_\sigma t)\right] \,. \end{aligned} \tag{4.1.92}$$

The same arguments for the interpretation of $\langle\rho_\sigma(x)\rangle_t$ can be repeated for $\langle\Pi_\sigma(x)\rangle_t$.

We notice en passant that equations (4.1.82) imply a proportionality relation between the densities in a stationary state (including thermal equilibrium). In fact, in such a state $\partial_t \langle\Pi_\sigma(x)\rangle_{ss} = 0$, so that

$$\langle\rho_\sigma(x)\rangle_{ss} = \text{const.} - \tfrac{g_\sigma K_\sigma}{v_\sigma \pi} \left\langle d_\sigma^\dagger(x) d_\sigma(x)\right\rangle_{ss} \,.$$

The arbitrary constant is fixed by requiring that $\int dx\, \rho_\sigma(x) = 0$:

$$\langle\rho_\sigma(x)\rangle_{ss} = \tfrac{g_\sigma K_\sigma}{v_\sigma \pi}\left[\tfrac{1}{L} n_\sigma^{ss} - \left\langle d_\sigma^\dagger(x) d_\sigma(x)\right\rangle_{ss}\right] \,, \tag{4.1.93}$$

where $n_\sigma^{ss} \equiv \int dx \left\langle d_\sigma^\dagger(x) d_\sigma(x)\right\rangle_{ss}$ is the total probability that the impurity is in bath σ.

Numerical results: correlation functions

The typical behaviour of the equal-time correlation function is shown in figures 4.18, 4.19 and 4.20. The initial impurity wave packet is a similar to the one of the previous paragraphs, namely a Gaussian made up of $N_p = 32$ momenta, centred around $p_0 = 0.1Mv$, with standard deviation $\delta p = 0.02Mv$. All plots refer to the same g_σ, while we vary $J_\perp$.

Figures 4.18a and 4.18b show a sequence of "snapshots" of the full spatial behaviour of the correlation function at various moments of time. These show that the correlations are concentrated within two "lobes", with a series of ripples between them. As time advances, the lobes move apart from each other, while both their amplitude and spatial width increase. The expansion is roughly ballistic, that is, all distances increase linearly in time, albeit with a larger speed in the relative $r = x - y$ direction than in the "centre-of-mass" $R = (x+y)/2$ one. As this expansion takes place, in the region between the lobes a series of ripples is formed, whose amplitude increases in time.

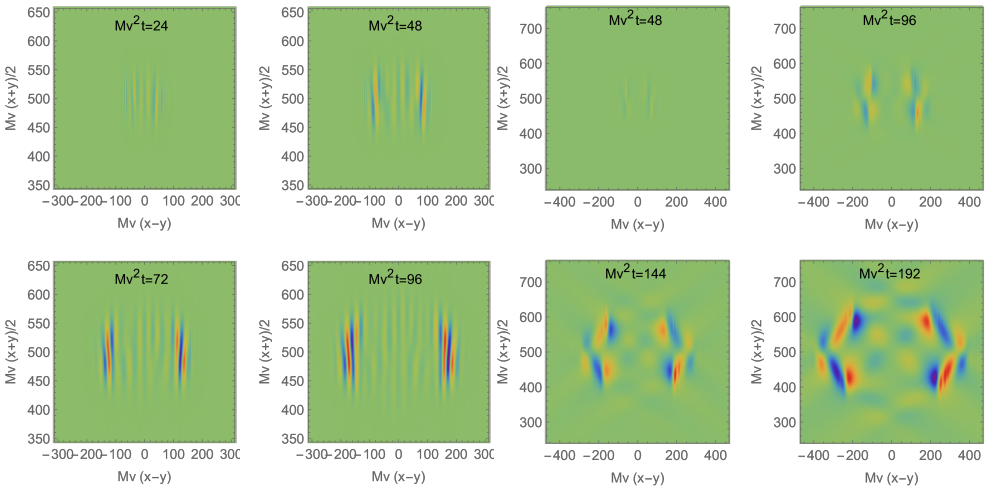

(a) $J_\perp = 0.1Mv^2$ **(b)** $J_\perp = 0.01Mv^2$

Figure 4.18: Time evolution of the connected density-density correlation function. The baths are identical, with parameters $g^2K = 0.5v^2$ and $K = 2$. The wave packet is Gaussian, with $p_0 = 0.1Mv$, $\delta p = 0.02Mv$ and $N_p = 32$. The colour scale is normalised to the last "snapshot" of each set of plots.

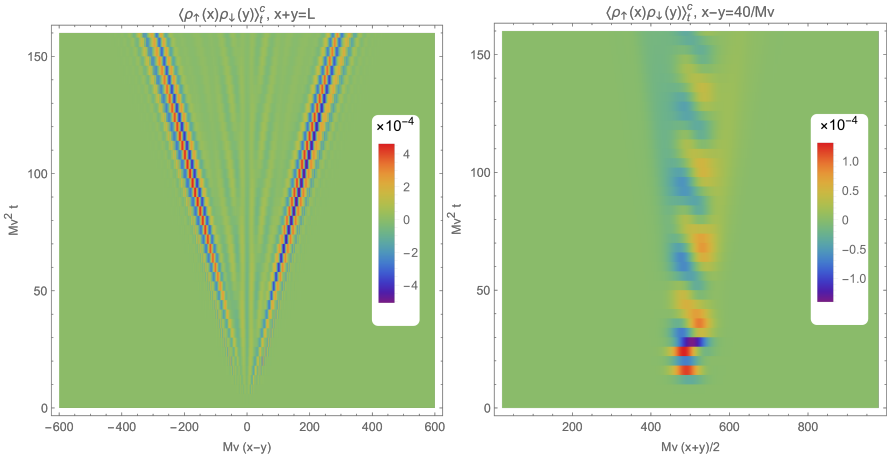

(a) **(b)**

Figure 4.19: Two "slices" of the density correlation function evolution at $J_\perp = 0.1Mv^2$ (figure 4.18a). The parameters are the same as figure 4.18. Figure (a) shows it as a function of the relative coordinate $r = x - y$, while (b) uses the centre of mass coordinate $R = (x + y)/2$.

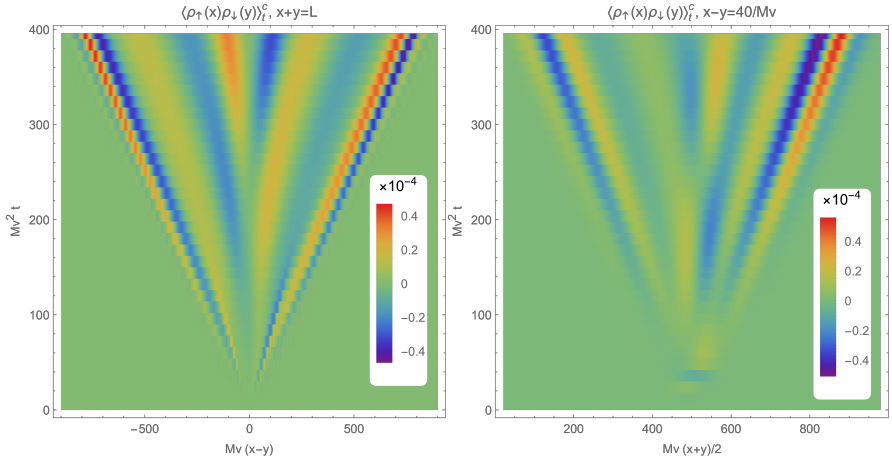

Figure 4.20: Two "slices" of the density correlation function evolution at $J_\perp = 0.01Mv^2$ (figure 4.18b). The parameters are the same as figure 4.18. Figure (a) shows it as a function of the relative coordinate $r = x - y$, while (b) uses the centre of mass coordinate $R = (x + y)/2$

We remark that we have stopped all calculations before the light cone get too close to the edges of the system[20], in order to avoid finite-size effects (besides the discretisation of momenta). Therefore, the observed features should be a result of the intrinsic dynamics of the system under investigation, rather than an effect of interference through the boundaries.

These inter-bath density (or momentum) correlation functions are not symmetric under exchange of x and y, despite the fact that $\rho_\uparrow(x)$ (or $\Pi_\uparrow(x)$) and $\rho_\downarrow(y)$ ($\Pi_\downarrow(y)$) commute and that the baths have identical properties. This is because the evolution is made asymmetric by the initial conditions, namely the impurity starting in bath $\uparrow$, with an average nonzero momentum. However, from figure 4.18 it is easy to notice an approximate anti-symmetry with respect to the lines $r = 0$ and $R = L/2$.

Analogously to the case of the density averages, the correlation functions obey a specific scaling with respect to the Luttinger parameters K_σ:

$$\left\langle \rho_\uparrow(x)\rho_\downarrow(y)\right\rangle_t = (K_\uparrow K_\downarrow)^{1/2} f_{\rho\rho}(g_\uparrow^2 K_\uparrow, g_\downarrow^2 K_\downarrow)\ , \tag{4.1.94a}$$

$$\left\langle \Pi_\uparrow(x)\Pi_\downarrow(y)\right\rangle_t = (K_\uparrow K_\downarrow)^{-1/2} f_{\Pi\Pi}(g_\uparrow^2 K_\uparrow, g_\downarrow^2 K_\downarrow)\ . \tag{4.1.94b}$$

The scaling of the densities, equation (4.1.81), ensures that the same relation holds for the connected correlation functions. We have verified numerically that changing $g_\sigma K_\sigma^{1/2}$ only causes minor changes in the shape of the correlation functions, apart from an obvious change in the amplitude. The most relevant shape modifications are those induced by a change in $J_\perp$. At large $J_\perp$ (figure 4.18a), the correlation function oscillates basically only in the relative r direction, whereas the profile along R shows less features. As $J_\perp$ is lowered (figure 4.18b), the shape of the lobes becomes more complex, mainly because the correlation function oscillates also in the R direction. Moreover, the ripples "leak out" of the inter-lobe region.

20 For instance, notice that the "snapshots" in figure 4.18 cover an area in (r, R) space which is rather smaller than the whole allowed rectangle $[-L, L] \times [0, L]$.

Since the relative $r = x - y$ and centre-of-mass coordinate $R = (x + y)/2$ clearly have different roles, it is useful to look at them one at a time, as we display in the next figures.

In the time evolution of $\langle \rho_\uparrow(x)\rho_\downarrow(y)\rangle_t^c$ as a function of the coordinate difference, as shown in figures 4.19a and 4.20a, correlations appear only within a "light-cone" $|x - y| \leqslant vt$. The maximal amplitude occurs around the light-cone itself ($|x - y| \approx vt$), while within the interior there are waves that appear to be radiated from $x = y$. A comparison with figure 4.18 leads to identify the light-cone region with the lobes, while the waves in the interior are the ripples. The wavelength of the latter roughly corresponds to that of the phonons emitted during the deexcitation of the odd impurity mode. This identification, as in the case of the density, comes from the analytical expressions [equations (4.1.80)], and from the observation that the wavelength is essentially independent of g_σ and K_σ, while it is inversely correlated with $J_\perp$, as can be appreciated by comparing figure 4.19 and figure 4.20. As in the case of the average densities, the amplitude of these "ripples" relative to the light-cone lobes increases for smaller $J_\perp$.

Summing up, the behaviour of the correlation function along the relative coordinate basically reflects the "relativistic" nature of TLL bath dynamics, namely the property that inter-bath correlations are generated and propagated as linearly dispersing sound modes.

The situation looks different if seen in the centre-of-mass coordinate R, as figures 4.19b and 4.20b show. Here, we can distinguish a central area in which two trains of ripples oscillate out of phase, and an outer area formed of waves that radiate at the speed of sound from the central area. This distinction is sharp for higher $J_\perp$ (figure 4.19b), as the relative amplitude of the emitted waves increase with decreasing $J_\perp$. The inner ripples occupy an area that spreads very slowly in space, and is centred along the trajectory $R = L/2 + p_0 t/M$. Moreover, their oscillations in time occur with a period of about $\pi/J_\perp$, that is, half of the impurity oscillation period. These clues leads us to identify this "section" of the correlation function as the one more closely reflecting the motion of the impurity and the profile of its wave packet. In order to plot figures 4.19b and 4.20b, we chose a value for r. Changing it causes two main effects: first, the correlation function is zero up to a time that increases with r (an effect of the finite sound speed, presumably). Second, as r is decreased the oscillations in time get washed away by a featureless background contribution, until at $r = 0$, i.e. $x = y$, there are no more visible oscillations. In all our numerical computations, $\langle \rho_\uparrow(x)\rho_\downarrow(x)\rangle_t^c$ is always negative.

These properties of the correlation functions can be rationalised using equation (4.1.84). Here we can see that this equation implies a whole hi-

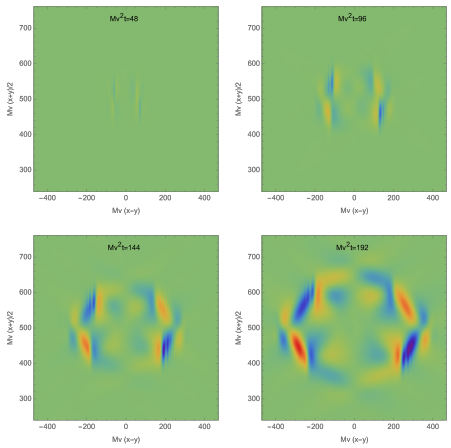

Figure 4.21: Time evolution of the connected momentum density correlation function. The baths are identical, with parameters $g^2K = 0.5v^2$, $K = 2$ and $J_\perp = 0.01Mv^2$. The colour scale is normalised to the last "snapshot" of each set of plots.

erarchy of relations that go beyond linear response theory. Indeed, we can compute

$$\begin{aligned}\langle \rho_\sigma(x)\rho_{\bar\sigma}(y)\rangle_t^c = \\ = g_\sigma \int dx_1\, dt_1\, \chi_\sigma(x-x_1,t-t_1)\left\langle d_\sigma^\dagger(x_1,t_1)d_\sigma(x_1,t_1)\rho_{\bar\sigma}(y,0)\right\rangle + \\ + g_{\bar\sigma}\int dx_2\, dt_2\, \chi_{\bar\sigma}(x-x_2,t-t_2)\left\langle \rho_\sigma(x,0)d_{\bar\sigma}^\dagger(x_2,t_2)d_{\bar\sigma}(x_2,t_2)\right\rangle + \\ + g_\uparrow g_\downarrow \int dx_1\, dt_1\, dx_2\, dt_2\, \chi_\sigma(x-x_1,t-t_1)\chi_{\bar\sigma}(x-x_2,t-t_2)\times \\ \times \left\langle d_\sigma^\dagger(x_1,t_1)d_\sigma(x_1,t_1)d_{\bar\sigma}^\dagger(x_2,t_2)d_{\bar\sigma}(x_2,t_2)\right\rangle^c , \quad (4.1.95)\end{aligned}$$

where we see that the bath density correlation function is related to the connected impurity density correlation function

$$\begin{aligned}\left\langle d_\sigma^\dagger(x_1,t_1)d_\sigma(x_1,t_1)d_{\bar\sigma}^\dagger(x_2,t_2)d_{\bar\sigma}(x_2,t_2)\right\rangle^c \equiv \\ \equiv \left\langle d_\sigma^\dagger(x_1,t_1)d_\sigma(x_1,t_1)d_{\bar\sigma}^\dagger(x_2,t_2)d_{\bar\sigma}(x_2,t_2)\right\rangle + \\ - \left\langle d_\sigma^\dagger(x_1,t_1)d_\sigma(x_1,t_1)\right\rangle\left\langle d_{\bar\sigma}^\dagger(x_2,t_2)d_{\bar\sigma}(x_2,t_2)\right\rangle , \quad (4.1.96)\end{aligned}$$

which, unlike $\langle \rho_\sigma(x)\rho_{\bar\sigma}(y)\rangle_t^c$, correlates the densities at different times, and so it cannot be calculated from the knowledge of $|\Psi(t)\rangle$ only. Thus, in principle we could use equation (4.1.95) to compute this impurity density correlation function. For now, we can just point out that thanks to this formula we have a hint on why $\langle \rho_\sigma(x)\rho_{\bar\sigma}(y)\rangle_t^c$ as a function of $(x+y)/2$ seems to mirror the time evolution of the impurity wave packet—indeed, we can now understand that it is keeping track of the impurity density (and impurity-bath density) correlation function.

We conclude this section by briefly discussing the connected momentum correlation function, $\langle \Pi_\uparrow(x)\Pi_\downarrow(y)\rangle_t^c$. An example is shown in 4.21. It has the same qualitative features of the density correlation function, namely a

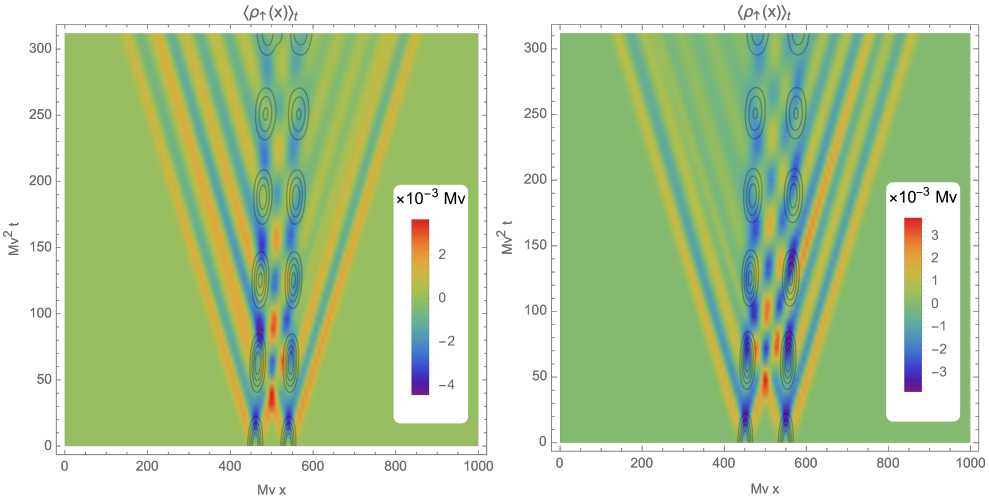

Figure 4.22: The colour plot shows the time evolution of the perturbation in the ↑ bath density produced by an impurity wave packet in the form (4.1.97). The contours depict the time evolution of the noninteracting wave packet. The system parameters are $g^2K = 0.5v^2$ (symmetric baths), $J_\perp = 0.05Mv^2$, $N_p = 64$, $\delta p = 0.05Mv$ and $d = 80(Mv)^{-1}$ for (a), while $d = 99(Mv)^{-1}$ for (b).

pair of expanding lobes enclosing a region of smaller oscillations. It is distinguishable from the density correlation from the more complex pattern of the ripples, and from the observation that we found that the $x = y$ correlation is always positive (while it is negative for the density).

Playing with wave packets

We have experimented with a few wave packets with a non-Gaussian initial momentum distribution. We show two interesting examples in figures 4.22 and 4.23. The first one, 4.22, shows the time evolution of the bath density when the impurity is initialised with a wave packet defined as

$$c_{p\mu} \propto e^{-\frac{(p-p_0)^2}{4\delta p^2} - ix_0 p} \cos\left(\frac{pd}{2}\right), \tag{4.1.97}$$

which in real space translates to a superposition of two Gaussian peaks of width $\approx 1/(2\delta p)$, separated by a distance d. The time evolution of the noninteracting impurity density is shown as a contour plot for ease of comparison. We can understand the bath density evolution as the superposition of two copies of the behaviour we have analysed in the previous paragraphs for a single Gaussian peak. We can recognise the oscillating central dips that follow the motion of the two impurity density peaks, each one emitting its own pair of wave fronts and its trains of ripples. Moreover, the two sets of perturbations superimpose and give rise to interference effects, such as the visible time delay between the times of maximum depth of the two troughs, and the enhanced peak that forms in the middle. These interference effects are governed by the interplay of the distance between the two peaks and the period of the impurity oscillations. Indeed, for $d = 80(Mv)^{-1}$ (figure 4.22a)

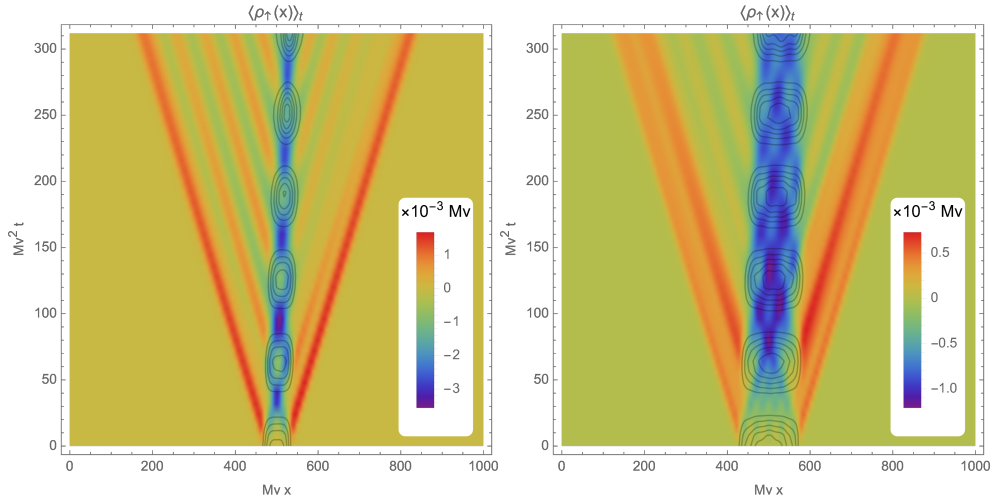

Figure 4.23: The colour plot shows the time evolution of the perturbation in the ↑ bath density produced by an impurity wave packet in the form (4.1.98). The contours depict the time evolution of the noninteracting wave packet. The system parameters are $g^2K = 0.5v^2$ (symmetric baths), $J_\perp = 0.05Mv^2$, $N_p = 64$ and $R = 40(Mv)^{-1}$ for (a), $R = 80(Mv)^{-1}$ for (b).

the forward emission is suppressed, while for $d = 99(Mv)^{-1}$ the backward emission is the one subjected to destructive interference.

Figures 4.23 shows the bath density perturbation that is obtained with the wave packet

$$c_{p\mu} \propto e^{-ix_0 p} \frac{J_1\left((p-p_0)R\right)}{p-p_0}\,, \tag{4.1.98}$$

where $J_1(z)$ is the first-order Bessel function of the first kind [23]. In the continuum limit, this wave packet would yield a parabolic initial impurity density $\left[1-(x-x_0)^2/R^2\right]\theta(x-x_0+R)\theta(R-x+x_0)$. The actual shape of the finite-length, finite-N_p situation is a peak with steep sides and a somewhat flattened top (except for some extra oscillations emerging at larger R). These features can be observed in the contour lines depicting the time evolution of the noninteracting wave packet in both figures 4.23. These plots exhibit some remarkable interference effects. For the one at a smaller radius $R = 40(Mv)^{-1}$ (figure 4.23a), these appear to involve only the central trough, which cyclically splits in two shallower halves that subsequently fuse back together. For a larger radius $R = 80(Mv)^{-1}$ (figure 4.23b) we observe that the central trough takes almost a whole bare oscillation period to deepen, and in the meanwhile its size is paradoxically shrinking. After this initial transient, its shape evolves through an intricate pattern, sequentially splitting in two twin minima or one dip and two satellite ones on its sides. This peculiar behaviour is probably linked to the motion of the small peaks on the top of the impurity density. For this wave packet, we also observe some unusually thick and structured wave fronts, which support the idea that they represent (possibly distorted) travelling images of the initial impurity density. On the other hand, ripples have a small amplitude, in comparison. This agrees with

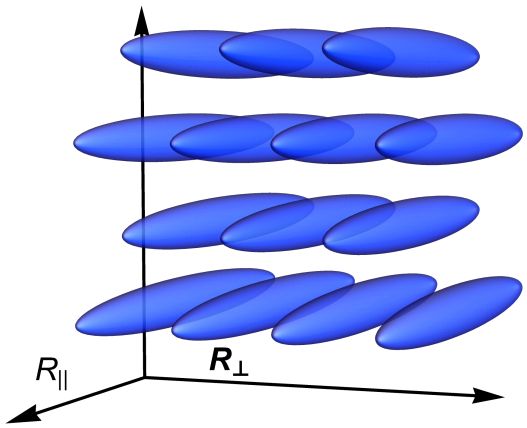

Figure 4.24: A representation of a two-dimensional lattice of baths. The coordinate $R_{\parallel}$ runs parallel to the long dimension of the baths, while $\mathbf{R}_{\perp}$ spans the plane (or line) perpendicular to them.

the observation we made in the previous paragraphs, that more spread wave packets suppress the ripples.

4.2 MORE THAN TWO BATHS

In this section we extend the present "improved" perturbative treatment to the case in which the impurity has access to many baths, and we observe the evolution of the orthogonality catastrophe exponent with the number of baths.

4.2.1 Definition of the model and LLP transformation

We shall assume that the baths are arranged in a periodic lattice in one or two dimensions, parallel to each other, so that the impurity moves in two (2D) or three dimensions (3D), respectively. For clarity, we will refer to these two setups as $1+1$D and $2+1$D, respectively. A $2+1$D example is shown in figure 4.24. For computational simplicity, we assume that the lattice of baths is simple (i.e. each site corresponds to one bath only—the extension to non-simple lattices is straightforward) and that it obeys periodic boundary conditions. The latter requirement is realistic for a 1D lattice of baths, that in pbc becomes a ring, while it can not be easily realised for a 2D lattice. As in many different contexts, the choice of pbc is motivated by the advantage of having translational symmetry, which simplifies the theoretical description. We will see that the structure of the results we will obtain do not rely on the choice of boundary conditions for the lattice of baths, and that they can be easily generalised to open boundary conditions.

We adopt a tight-binding description for the impurity, whose position is specified by a 2D or 3D vector $\mathbf{R}$, running on the sites of the lattice. We divide this vector as $\mathbf{R} \equiv (R_{\parallel}, \mathbf{R}_{\perp})$, with $R_{\parallel}$ being the longitudinal direction along the baths and $\mathbf{R}_{\perp}$ that labels the sites in the lattice of baths. The latter

defines the transverse direction, analogously to the index σ in the two-bath scenario, and it is a number or a 2D vector if the baths form a row or a 2D lattice, respectively. We assume that each bath has $N_\parallel$ lattice sites, and that there are N_b baths. We recover the two-bath scenario analysed before if we take a row of $N_b = 2$ baths. As in the latter setup, we assume $N_\parallel \gg N_b$, so that we can adopt a continuum description for the intra-bath (longitudinal) motion of the impurity, while the inter-bath motion is quantised.

The Hamiltonian has the usual form $\mathcal{H} = \mathcal{H}_{\text{imp}} + \mathcal{H}_{\text{bath}} + \mathcal{H}_c$, where

$$\mathcal{H}_{\text{imp}} \equiv -J_\parallel \sum_{R_\parallel, \mathbf{R}_\perp} \left(d^\dagger_{R_\parallel + a_\parallel, \mathbf{R}_\perp} d_{R_\parallel, \mathbf{R}_\perp} + \text{h.c.} - 2 d^\dagger_{R_\parallel, \mathbf{R}_\perp} d_{R_\parallel, \mathbf{R}_\perp} \right) + - \sum_{R_\parallel, \mathbf{R}_\perp, \boldsymbol{e}_\perp} J_{\boldsymbol{e}_\perp} \left(d^\dagger_{R_\parallel, \mathbf{R}_\perp + \boldsymbol{e}_\perp} d_{R_\parallel, \mathbf{R}_\perp} + \text{h.c.} \right) , \tag{4.2.1a}$$

$$\mathcal{H}_{\text{bath}} \equiv \sum_{q \neq 0 \mathbf{R}_\perp} \nu_{\mathbf{R}_\perp}(|q|) b^\dagger_{q \mathbf{R}_\perp} b_{q \mathbf{R}_\perp} , \tag{4.2.1b}$$

$$\mathcal{H}_c \equiv \sum_{R_\parallel, \mathbf{R}_\perp} g_{\mathbf{R}_\perp} d^\dagger_{R_\parallel, \mathbf{R}_\perp} d_{R_\parallel, \mathbf{R}_\perp} \rho_{\mathbf{R}_\perp}(R_\parallel) = = \sum_{q \neq 0, R_\parallel, \mathbf{R}_\perp} \frac{g_{\mathbf{R}_\perp} K^{1/2}_{\mathbf{R}_\perp} V_q}{L^{1/2}} d^\dagger_{R_\parallel, \mathbf{R}_\perp} d_{R_\parallel, \mathbf{R}_\perp} e^{-iq R_\parallel} \left(b^\dagger_{q \mathbf{R}_\perp} + b_{q \mathbf{R}_\perp} \right) , \tag{4.2.1c}$$

In the above equations, we defined $a_\parallel$ to be the lattice spacing in the longitudinal direction, $\boldsymbol{e}_\perp$ runs on the nearest-neighbours in the transverse lattice. The inter-bath hopping in the direction $\boldsymbol{e}_\perp$ has been denoted as $J_{\boldsymbol{e}_\perp}$. Notice that for $N_b = 2$ the correspondence is $J_{\boldsymbol{e}_\perp} = J_\perp/2$. The baths are exactly as in the two-bath case, namely they have length $L = N_\parallel a_\parallel$ and obey pbc in the longitudinal direction, so that q is their quantised longitudinal momentum. Hence, $b^\dagger_{q \mathbf{R}_\perp}$ creates a phonon of momentum q in the bath residing at lattice point $\mathbf{R}_\perp$.

The free impurity Hamiltonian is diagonalised by building the Bloch sums

$$d_{\mathbf{p}} \equiv \tfrac{1}{N_s^{1/2}} \sum_{\mathbf{R}} e^{-i \mathbf{p} \mathbf{R}} d_{\mathbf{R}} , \tag{4.2.2}$$

where $N_s = N_\parallel N_b$ is the total number of sites. The diagonalised Hamiltonian reads $\mathcal{H}_{\text{imp}} = \sum_{\mathbf{p}} \lambda(\mathbf{p}) d^\dagger_{\mathbf{p}} d_{\mathbf{p}}$, where

$$\lambda(\mathbf{p}) \equiv 2J_\parallel (1 - \cos(p_\parallel a_\parallel)) - 2 \sum_{\boldsymbol{e}_\perp} J_{\boldsymbol{e}_\perp} \cos(\mathbf{p}_\perp \boldsymbol{e}_\perp) . \tag{4.2.3}$$

In analogy with $\mathbf{R}$, we split the momentum $\mathbf{p}$ in longitudinal ($p_\parallel$) and transverse ($\mathbf{p}_\perp$) components. The transverse components generalise the parity index μ of the two-bath case. As usual, we assume that the longitudinal momentum is small, $|p_\parallel| a_\parallel \ll 1$, so that we can approximate[21] $2J_\parallel (1 - \cos(p_\parallel a_\parallel)) \approx p_\parallel^2/(2M) \equiv E(p)$, and we call

$$\Delta(\mathbf{p}_\perp) \equiv -2 \sum_{\boldsymbol{e}_\perp} J_{\boldsymbol{e}_\perp} \cos(\mathbf{p}_\perp \boldsymbol{e}_\perp) , \tag{4.2.4}$$

21 Notice that we are defining the mass M to be the one associated with the longitudinal motion. This is because we are setting ourselves in a situation in which the longitudinal motion is almost in the continuum limit, whereas the transverse motion is strongly quantised because the number of baths, N_b, is finite.

so that $\lambda(\mathbf{p}) = E(p_\parallel) + \Delta(\mathbf{p}_\perp)$. The picture we have in mind is that $N_\parallel \gg N_b$, so that we have a collection of N_b parabolic bands labelled by the transverse momentum $\mathbf{p}_\perp$.

Now we adopt the same strategy we applied before, namely we use an appropriate LLP transformation to move to a basis in which the total momentum conservation is evident. The 1D nature of the baths implies that they can only carry longitudinal momentum, therefore the LLP transformation involves only the longitudinal degrees of freedom:

$$U_{LLP} \equiv e^{-i\sum_R R_\parallel d^\dagger_R d_R P_b}\,, \begin{cases} U^\dagger_{LLP} d_R U_{LLP} = e^{-iR_\parallel P_b} d_R \\ U^\dagger_{LLP} b_{q\mathbf{R}_\perp} U_{LLP} = e^{-iq\sum_R R_\parallel d^\dagger_R d_R} b_{q\mathbf{R}_\perp} \end{cases}, \tag{4.2.5}$$

where $P_b \equiv \sum_{q\neq 0,\mathbf{R}_\perp} q b^\dagger_{q\mathbf{R}_\perp} b_{q\mathbf{R}_\perp}$ is the (longitudinal) baths momentum. In the LLP basis, the Hamiltonian reads $\mathcal{H}_{LLP} \equiv U^\dagger_{LLP}\mathcal{H}U_{LLP} = \mathcal{H}^{LLP}_{imp} + \mathcal{H}_{bath} + \mathcal{H}^{LLP}_c$, where

$$\mathcal{H}^{LLP}_{imp} = \sum_{\mathbf{p}} \left[E(p_\parallel - P_b) + \Delta(\mathbf{p}_\perp)\right] d^\dagger_{\mathbf{p}} d_{\mathbf{p}}\,, \tag{4.2.6a}$$

$$\mathcal{H}^{LLP}_c = \sum_{q\neq 0,\mathbf{R}_\perp} \frac{g_{\mathbf{R}_\perp} K^{1/2}_{\mathbf{R}_\perp} V_q}{L^{1/2}} \sum_{R_\parallel,} d^\dagger_{R_\parallel,\mathbf{R}_\perp} d_{R_\parallel,\mathbf{R}_\perp} \left(b^\dagger_{q\mathbf{R}_\perp} + b_{q\mathbf{R}_\perp}\right)\,. \tag{4.2.6b}$$

In this basis, the phonons interact with the impurity only through the combination

$$\begin{aligned} n_{\mathbf{R}_\perp} &\equiv \sum_{R_\parallel,} d^\dagger_{R_\parallel,\mathbf{R}_\perp} d_{R_\parallel,\mathbf{R}_\perp} = \\ &= \frac{1}{N_b} \sum_{p_\parallel,\mathbf{p}_\perp,\mathbf{p}'_\perp} e^{i(\mathbf{p}'_\perp - \mathbf{p}_\perp)} d^\dagger_{p_\parallel \mathbf{p}_\perp} d_{p_\parallel \mathbf{p}'_\perp} = \\ &= \frac{1}{N_b}\mathbb{1} + \frac{1}{N_b}\sum_{p_\parallel} \sum_{\mathbf{p}_\perp \neq \mathbf{p}'_\perp} e^{i(\mathbf{p}'_\perp - \mathbf{p}_\perp)} d^\dagger_{p_\parallel \mathbf{p}_\perp} d_{p_\parallel \mathbf{p}'_\perp}\,, \end{aligned} \tag{4.2.7}$$

which is invariant under translations along the baths, as it is diagonal in the longitudinal momentum $p_\parallel$. Therefore, as in the two-baths case, the whole Hamiltonian becomes a sum over different total longitudinal momentum sectors, $\mathcal{H}_{LLP}(p_\parallel)$. Then, we can work within one of such sectors, with a fixed value of $p_\parallel$.

4.2.2 Perturbative solution

We follow the steps of the two-bath case, so we split the LLP Hamiltonian in an unperturbed part and a perturbation, $\mathcal{H}_{\mathrm{LLP}}(p_\parallel) = \mathcal{H}_0(p_\parallel) + \Delta\mathcal{H}(p_\parallel)$, where

$$\mathcal{H}_0(p_\parallel) = \frac{p_\parallel^2}{2M} + \sum_{\mathbf{p}_\perp} \Delta(\mathbf{p}_\perp) d^\dagger_{p_\parallel \mathbf{p}_\perp} d_{p_\parallel \mathbf{p}_\perp} + \\ + \sum_{q\neq 0, \mathbf{R}_\perp} \left[\Omega_{q\mathbf{R}_\perp}(p_\parallel) b^\dagger_{q\mathbf{R}_\perp} b_{q\mathbf{R}_\perp} + \frac{W_{q\mathbf{R}_\perp}}{N_b L^{1/2}} (b^\dagger_{q\mathbf{R}_\perp} + b_{q\mathbf{R}_\perp}) \right] , \tag{4.2.8a}$$

$$\Delta\mathcal{H}(p_\parallel) = \sum_{\mathbf{R}_\perp} \sum_{\mathbf{p}_\perp \neq \mathbf{p}'_\perp} \frac{W_{q\mathbf{R}_\perp}}{N_b L^{1/2}} e^{i(\mathbf{p}_\perp - \mathbf{p}'_\perp)\mathbf{R}_\perp} d^\dagger_{p_\parallel \mathbf{p}'_\perp} d_{p_\parallel \mathbf{p}_\perp} (b^\dagger_{q\mathbf{R}_\perp} + b_{q\mathbf{R}_\perp}) + \frac{:P_b^2:}{2M} . \tag{4.2.8b}$$

We introduced the quantities

$$\Omega_{q\mathbf{R}_\perp}(p_\parallel) \equiv v_{\mathbf{R}_\perp}|q| - \frac{p_\parallel}{M} q + \frac{q^2}{2M} , \tag{4.2.9}$$

and

$$W_{q\mathbf{R}_\perp} \equiv g_{\mathbf{R}_\perp} K^{1/2}_{\mathbf{R}_\perp} V_q , \tag{4.2.10}$$

that generalise $\Omega_{q\sigma}(p)$ and $W_{q\sigma}$, for two baths.

We assume that the initial state is $|\Psi(0)_{\mathbf{p}}\rangle = |p_\parallel, \mathbf{p}_\perp\rangle_d |\omega\rangle_b \equiv |p_\parallel, \mathbf{p}_\perp, \omega\rangle$ (which is invariant under the LLP transformation). Then we make the Ansatz

$$|\Psi_{\mathbf{p}}(t)\rangle = a_{\mathbf{p}}(t) e^{-i\mathcal{H}_0(p_\parallel)t} \left[|p_\parallel, \mathbf{p}_\perp, \omega\rangle + \left|\phi^{(1)}_{\mathbf{p}}(t)\right\rangle + \mathcal{O}(g^2) \right] , \tag{4.2.11}$$

and we introduce it in the opportunely adapted version of equations (4.1.19), i.e. with $p\mu \to p_\parallel, \mathbf{p}_\perp$. We obtain[22]

$$\left|\phi^{(1)}_{\mathbf{p}}(t)\right\rangle = \sum_{\substack{q\neq 0, \mathbf{R}_\perp \\ \mathbf{k}_\perp (\neq \mathbf{p}_\perp)}} \frac{W_{q\mathbf{R}_\perp}}{N_b L^{1/2}} e^{i(\mathbf{p}_\perp - \mathbf{k}_\perp)\mathbf{R}_\perp} \chi^*_t(\Omega_{q\mathbf{R}_\perp}(p_\parallel) + \Delta_{\mathbf{k}_\perp \mathbf{p}_\perp}) \times \\ \times b^\dagger_{q\mathbf{R}_\perp} |p_\parallel \mathbf{k}_\perp, \omega\rangle \tag{4.2.12}$$

and

$$a_{\mathbf{p}}(t) = \exp\left[\frac{1}{N_b^2} \sum_{\mathbf{R}_\perp} \sum_{\mathbf{k}_\perp (\neq \mathbf{p}_\perp)} F^{\mathrm{sb}}_{p_\parallel \mathbf{R}_\perp}(-\Delta_{\mathbf{k}_\perp \mathbf{p}_\perp}, t) \right] , \tag{4.2.13}$$

with

$$\Delta_{\mathbf{k}_\perp \mathbf{p}_\perp} \equiv \Delta(\mathbf{k}_\perp) - \Delta(\mathbf{p}_\perp) = \lambda(p_\parallel, \mathbf{k}_\perp) - \lambda(p_\parallel, \mathbf{p}_\perp) \tag{4.2.14}$$

and we defined the single-bath F-function

$$F^{\mathrm{sb}}_{p_\parallel \mathbf{R}_\perp}(\Delta, t) \equiv -\frac{1}{L} \sum_{q\neq 0} W^2_{q\mathbf{R}_\perp} \frac{1 - i(\Omega_{q\mathbf{R}_\perp}(p_\parallel) - \Delta)t - e^{-i(\Omega_{q\mathbf{R}_\perp}(p_\parallel) - \Delta)t}}{(\Omega_{q\mathbf{R}_\perp}(p_\parallel) - \Delta)^2} . \tag{4.2.15}$$

22 We use the notation $\sum_{\mathbf{k}_\perp (\neq \mathbf{p}_\perp)}$ to indicate a sum over all $\mathbf{k}_\perp$ that are different from a given $\mathbf{p}_\perp$.

A comparison with equations (3.0.16) and (4.1.29) shows that it is equal to $4F_{p\sigma}(J,t)$, with $p = p_\parallel$, $\mathbf{R}_\perp$ playing the role of σ and $\Delta = 2J$. We also define

$$F^{sb}_{p_\parallel}(\Delta,t) \equiv \sum_{\mathbf{R}_\perp} F^{sb}_{p_\parallel \mathbf{R}_\perp}(\Delta,t)\ . \tag{4.2.16}$$

As usual, we can re-write the perturbative expansion by letting $e^{-i\mathcal{H}_0(p_\parallel)t}$ act on the states:

$$\begin{aligned}|\Psi_{\mathbf{p}}(t)\rangle = a_{\mathbf{p}}(t)e^{-i\lambda(\mathbf{p})t}\Big[\,|p_\parallel,\mathbf{p}_\perp\rangle\,\Big|\omega_{p_\parallel}(t)\Big\rangle + \\ -\sum_{\substack{q\neq 0,\mathbf{R}_\perp\\ \mathbf{k}_\perp(\neq\mathbf{p}_\perp)}} \frac{W_{q\mathbf{R}_\perp}}{N_b L^{1/2}} e^{i(\mathbf{p}_\perp-\mathbf{k}_\perp)\mathbf{R}_\perp}\chi_t(\Omega_{q\mathbf{R}_\perp}(p_\parallel)+\Delta_{\mathbf{k}_\perp\mathbf{p}_\perp})\times \\ \times\,|p_\parallel\mathbf{k}_\perp\rangle\, b^\dagger_{q\mathbf{R}_\perp}\Big|\omega_{p_\parallel}(t)\Big\rangle\Big]\ ,\end{aligned} \tag{4.2.17}$$

where $\Big|\omega_{p_\parallel}(t)\Big\rangle$ is the analogous to $|\omega_p(t)\rangle$ for two baths, namely the time evolution of the boson vacuum under the unperturbed Hamiltonian, and it has a similar expression:

$$\Big|\omega_{p_\parallel}(t)\Big\rangle \equiv e^{i\frac{1}{N_b^2}\,\mathrm{Im}\,F^{sb}_{p_\parallel}(0,t)}\left|\mathrm{coh}\left[-\frac{W_{q\mathbf{R}_\perp}}{N_b L^{1/2}}\frac{1-e^{-i\Omega_{q\mathbf{R}_\perp}(p_\parallel)t}}{\Omega_{q\mathbf{R}_\perp}(p_\parallel)}\right]\right\rangle\ . \tag{4.2.18}$$

For a generic initial condition $|\Psi(0)\rangle = \sum_{\mathbf{p}} c_{\mathbf{p}}\,|\mathbf{p},\omega\rangle$, we get its time evolution by superimposing the single-momentum solutions.

We want to remark that the perturbative procedure presented thus far does not rely on the pbc assumed in the transverse direction(s), except for the explicit form of the free impurity bands. The results obtained thus far can be easily adapted to other boundary conditions by simply changing the expression for $\lambda(p_\parallel,\mathbf{p}_\perp)$, namely

$$\lambda(p_\parallel,\mathbf{p}_\perp) = E(p_\parallel)+\Delta(\mathbf{p}_\perp) \to \lambda(p_\parallel,\alpha) = E(p_\parallel)+\Delta(\alpha)\ , \tag{4.2.19}$$

where α is the set of quantum numbers that enumerates the free impurity bands in the chosen boundary conditions. Accordingly, in all formulae the transverse momentum indices $\mathbf{p}_\perp$ should be substituted with the new indices α. The use of pbc in the longitudinal direction can be thought of as a mere technical choice of momentum discretisation, as we always assume that we work close enough to the continuum limit $a_\parallel \to 0$ that the differences associated to the boundary conditions in the longitudinal direction are expected to be irrelevant.

4.2.3 The impurity Green's function

In the following paragraphs, we will calculate the impurity Green's function and discuss its properties. We will show that the many-baths scenario displays new qualitative features that are not present in the two-baths setup.

The impurity Green's function for $t > 0$ is given by

$$iG(\mathbf{p},t) \equiv \langle\Omega|d_{\mathbf{p}}(t)d^\dagger_{\mathbf{p}}|\Omega\rangle = \langle\mathbf{p},\omega|e^{-i\mathcal{H}t}|\mathbf{p},\omega\rangle = \langle\Psi_{\mathbf{p}}(0)|\Psi_{\mathbf{p}}(t)\rangle\ . \tag{4.2.20}$$

We are considering only the "diagonal" components in the transverse momenta (the Green's function is already diagonal in the longitudinal momentum), so that the above quantity is also the return probability amplitude and the Loschmidt echo. In the symmetric case, which corresponds to a uniform 1+1D or 2+1D system, these components turn out to be the only nonvanishing ones of the Green's function. Using equation (4.2.17), we obtain

$$\begin{aligned} iG(\mathbf{p},t) &= a_{\mathbf{p}}(t)e^{-i\lambda_{\mathbf{p}}t}\left\langle \omega \middle| \omega_{p_\parallel}(t)\right\rangle = \\ &= a_{\mathbf{p}}(t)e^{-i\lambda_{\mathbf{p}}t}e^{i\frac{1}{N_b^2}\operatorname{Im}F^{sb}_{p_\parallel}(0,t)-\frac{1}{2}\sum_{q\neq 0,\mathbf{R}_\perp}\frac{W^2_{q\mathbf{R}_\perp}}{N_b^2 L}|\chi_t(\Omega_{q\mathbf{R}_\perp}(p_\parallel))|^2} = \\ &= a_{\mathbf{p}}(t)e^{-i\lambda_{\mathbf{p}}t}e^{\frac{1}{N_b^2}F^{sb}_{p_\parallel}(0,t)}, \end{aligned}$$

and finally

$$G(\mathbf{p},t) = -ie^{-i\lambda_{\mathbf{p}}t+\frac{1}{N_b^2}\sum_{\mathbf{R}_\perp}\sum_{\mathbf{k}_\perp}F^{sb}_{p_\parallel\mathbf{R}_\perp}(-\Delta_{\mathbf{k}_\perp\mathbf{p}_\perp},t)}. \tag{4.2.21}$$

This is expression is once again strongly reminiscent of the one we found in the two-bath scenario, namely the second of equations (3.0.25), which is in fact a special case of equation (4.2.21). In the $N_b = 2$ case, $F_p(-\mu J_\perp, t)$ encoded most of the "quasiparticle" effects, including decoherence, while $F_p(0,t)$ quantified the OC, giving rise to the power-law behaviour. In particular, we already noticed that the power law is the same for both bands. However, in the multi-bath case there is room for some significant differences. In equation (4.2.21), every factor $F^{sb}_{p_\parallel\mathbf{R}_\perp}(-\Delta_{\mathbf{k}_\perp\mathbf{p}_\perp},t)$ brings about either a renormalisation ($\Delta_{\mathbf{k}_\perp\mathbf{p}_\perp} > 0$) or a decay ($\Delta_{\mathbf{k}_\perp\mathbf{p}_\perp} < 0$) if $\Delta_{\mathbf{k}_\perp\mathbf{p}_\perp} \neq 0$, while every time that $\Delta_{\mathbf{k}_\perp\mathbf{p}_\perp} = 0$ in the sum there is a corresponding power law, as $F^{sb}_{p_\parallel\mathbf{R}_\perp}(0,t) \sim -\beta^{sb}_{\mathbf{R}_\perp}(p_\parallel)\ln t + \text{const}$. We recall that (see 3.1.3 and refs. [46, 50]) the single-bath OC exponent is

$$\beta^{sb}_{\mathbf{R}_\perp}(p_\parallel) = \frac{g^2_{\mathbf{R}_\perp}K_{\mathbf{R}_\perp}}{2\pi^2 v^2_{\mathbf{R}_\perp}}\frac{1+\left(\frac{p}{Mv_{\mathbf{R}_\perp}}\right)^2}{\left[1-\left(\frac{p}{Mv_{\mathbf{R}_\perp}}\right)^2\right]^2}. \tag{4.2.22}$$

The important point is that for generic baths lattices $\Delta_{\mathbf{k}_\perp\mathbf{p}_\perp} = 0$ is satisfied for *sets* of $\mathbf{k}_\perp$ that include more than $\mathbf{k}_\perp = \mathbf{p}_\perp$ only, as in the case $N_b = 2$. In other words, as $\Delta_{\mathbf{k}_\perp\mathbf{p}_\perp} = 0$ implies that $\lambda(p_\parallel, \mathbf{k}_\perp) = \lambda(p_\parallel, \mathbf{p}_\perp)$, in a generic lattice we find that the OC exponent *depends on the band* considered (labelled by $\mathbf{p}_\perp$) and it is proportional to the energy degeneracy of $\lambda(p_\parallel, \mathbf{p}_\perp)$, $\deg(\mathbf{p}_\perp)$. In formulae,

$$\beta^{N_b}(\mathbf{p}) = \frac{\deg(\mathbf{p}_\perp)}{N_b^2}\sum_{\mathbf{R}_\perp}\beta^{sb}_{\mathbf{R}_\perp}(p_\parallel) \tag{4.2.23}$$

This is the central result of this section. The above equation has many interesting consequences.

The first one regards the scaling of β^{N_b} with N_b. Of course, it is always bounded by

$$\beta^{N_b}(\mathbf{p}) \leqslant \frac{\deg(\mathbf{p}_\perp)}{N_b}\max_{\mathbf{R}_\perp}\beta^{sb}_{\mathbf{R}_\perp}(p_\parallel), \tag{4.2.24}$$

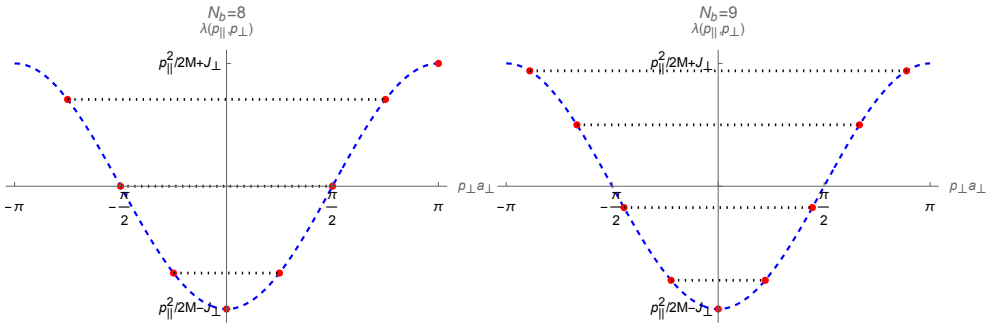

(a) $N_b = 8$ **(b)** $N_b = 9$

Figure 4.25: Energies of the free impurity bands for a row of (a) 8 and (b) 9 baths, relative to $p_\parallel^2/(2M)$. The red points indicate the actual impurity levels, whereas the dashed blue line gives the nearest-neighbour dispersion in the $N_b \to \infty$ limit. Degenerate levels are joined by dotted black lines. Notice that we took $J_{e_\perp} = J_\perp/2$.

where the inequality is saturated in the "symmetric case" in which all baths have identical properties ($g_{\mathbf{R}_\perp}$,$K_{\mathbf{R}_\perp}$ and $\nu_{\mathbf{R}_\perp}$):

$$\beta^{N_b}(\mathbf{p}) = \frac{\deg(\mathbf{p}_\perp)}{N_b}\beta^{sb}(p_\parallel) \, . \tag{4.2.25}$$

This confirms the hand-waving discussion presented in 3.1.3, namely that in the perturbative regime the baths effectively "see" only a fraction $1/N_b$ of the impurity, and the coupling constant relevant for the OC becomes $g_{\mathbf{R}_\perp}/N_b$ [this is evident in the interaction piece included in $\mathcal{H}_0$, see equation (4.2.8)]. At the quadratic order in the coupling this reasoning leads to equation (4.2.23) and to the scaling above, but it misses the degeneracy factor. We see that if $\deg(\mathbf{p}_\perp)$ does not grow proportionally to N_b, $\beta^{N_b}(p_\parallel)$ is a decreasing function of the number of baths, and ultimately goes to zero for an infinite lattice:

$$\lim_{N_b \to +\infty} \beta^{N_b}(p_\parallel) = 0 \, . \tag{4.2.26}$$

This behaviour is consistent with one expected for an impurity in a 2D or 3D phonon bath because, contrary to the 1D case, higher-dimensional mobile impurities usually retain their quasiparticle properties [79]. Notice that the $N_b \to +\infty$ limit leads to a 2D or 3D *bosonic* bath, not a fermionic one, because to obtain the latter case one should add the higher harmonics (i.e, the backscattering terms) in the bosonised density [31]. Nevertheless, the conclusion would not change, as mobile impurities in dimension 2 or higher have a finite quasiparticle residue[23], i.e. a finite limit $\lim_{t\to+\infty}|G(\mathbf{p},t)|$ [79, 88]. The second consequence of equation (4.2.23) concerns the role of the level degeneracy factor $\deg(\mathbf{p}_\perp)$, and therefore the band dependence of the OC exponent.

For instance, let us take a row of baths with lattice spacing $a_\perp$. The bands structure is given by

$$\Delta(p_\perp) = -J_\perp \cos(p_\perp a_\perp) \, ,$$

23 There are, of course, exceptions, such as Bose polarons immersed in an ideal Bose gas [40] or at unitarity (i.e. infinite scattering length. Both these scenarios lie outside of the region of applicability of our approximations.) [88].

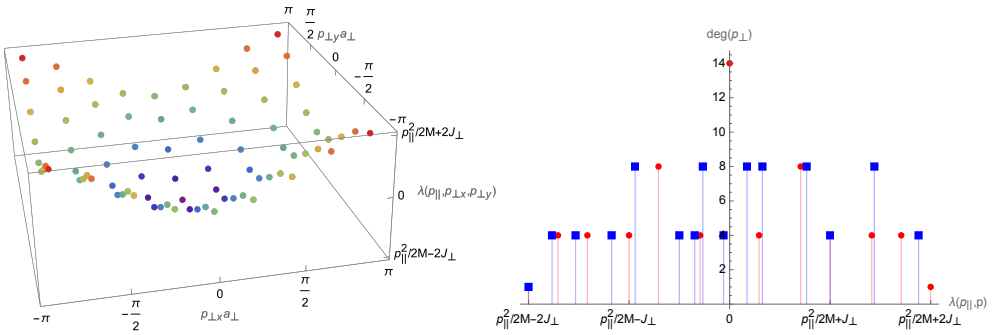

Figure 4.26: (a) Energy levels of the bands of a 9×9 baths lattice. (b) The band degeneracies for square lattices with 8×8 (red circles) and 9×9 (blue squares) sites. We took $J_{e_\perp} = J_\perp/2$ in all nearest-neighbour directions.

where we took $J_{e_\perp} = J_\perp/2$. We show the band structure in figure 4.25 at a given $p_\parallel$, for $N_b = 8$ and $N_b = 9$. We see that the band bottom $p_\perp = 0$ is always non-degenerate, hence $\beta^{N_b}(p_\parallel, 0) = \beta^{sb}(p_\parallel)/N_b$. Going up in energy, we find a series of doubly degenerate states with opposite $p_\perp$, for which $\beta^{N_b}(p_\parallel, \pm p_\perp) = 2\beta^{N_b}(p_\parallel, 0)$. Here we find a difference between odd and even numbers of baths: in the former case, the topmost levels are still doubly degenerate, whereas in the latter there is a state at the very edge of the Brillouin zone (either at $p_\perp a_\perp = \pi$ or $-\pi$, depending on the chosen convention) which is again nondegenerate. Thus, we see an example of band dependence of the OC exponent, and we see that the sequence of the different exponents is sensitive to the parity of the number of baths. Moreover, this is a scenario in which all exponents vanish in the limit of infinite baths, because the maximum degeneracy of any level is 2. Now we see that our usual $N_b = 2$ case is a little special in having the same OC exponent for all bands, because the two bands turn out to be the $p_\perp = 0$ (that we called even) and $p_\perp a_\perp = \pi$ (odd), which are the only two without degeneracy.

We can observe a larger variety of behaviours if we take the baths to be arranged in a $N_\perp \times N_\perp$ square lattice. In this case we have

$$\Delta(p_{\perp,x}, p_{\perp,y}) = -J_\perp[\cos(p_{\perp,x} a_\perp) + \cos(p_{\perp,y} a_\perp)] \, .$$

An example of the bands energy structure is depicted in figure 4.26a for a 9×9 lattice. The degeneracies of the various band levels is depicted in figure 4.26b, for $N_\perp = 8$ (red circles) and $N_\perp = 9$ (blue squares). Once more, the lowest-energy (and the highest one, for even $N_\perp$) band is not degenerate, while (almost all) the other levels are 4- or 8-fold degenerate. These degeneracies come from the symmetry of $\Delta(p_{\perp,x}, p_{\perp,y})$ under exchange of $p_{\perp,x}$ and $p_{\perp,y}$ (if they are different) and under change of sign $p_{\perp,x/y} \to -p_{\perp,x/y}$, the two different degeneracy values depending on the independence of these two sets of transformations. So, we can observe OC exponents that are 4 or 8 times the one of the fundamental band $\mathbf{p}_\perp = 0$. Also in this 2D case, we observe a strong dependence of the degeneracies on the parity of N_b: while in the odd N_b case only the $\mathbf{p}_\perp = 0$ band is nondegenerate (the others having degeneracy 4 or 8), in the even N_b case there is the state of maximal energy residing at one corner of the Brillouin zone (e.g. $\mathbf{p}_\perp a_\perp = (\pi, \pi)$),

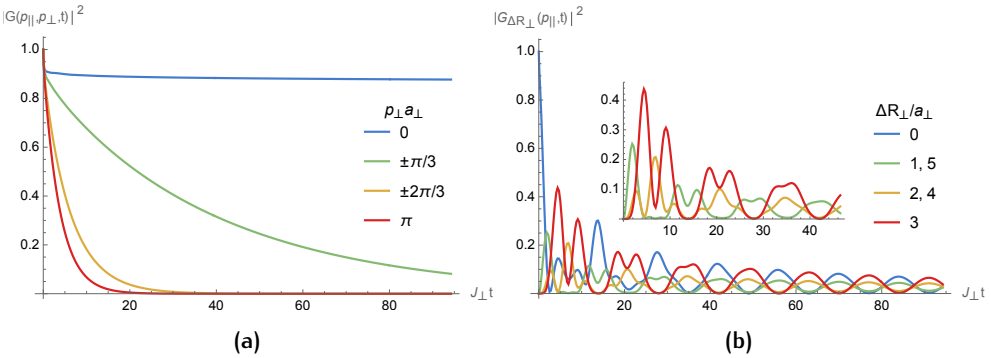

Figure 4.27: Numerical evaluation of the Green's function for a row of 6 identical baths, for $g^2K = 0.5v^2$, $2J_{e_\perp} = J_\perp = 0.05Mv^2$ and $p_\parallel = 0$. Plot (a) shows the return probability for the various transverse momenta, while (b) displays the Green's function at various transverse distances. The inset in (b) magnifies the smaller components.

that is nondegenerate and, most importantly, there is a largely degenerate level at the middle of the spectrum, that is, $\Delta(p_{\perp,x}, p_{\perp,y}) = 0$. These states are the ones connected by the well-known nesting symmetry[24] of the square lattice [66], which yield a degeneracy of $2N_\perp - 2$. This scaling of the degeneracy means that its OC exponent would have a unusually slow decay $\beta^{N_b}(p_\parallel) = \mathcal{O}\left(N_b^{-1/2}\right)$ in the $N_b \to +\infty$ limit, in which the level becomes the energy at which lies the well-known van Hove singularity of the square lattice [66]. Using a rectangular set of baths, i.e. of the type $N_x \times N_y$, brings further freedom in the possible degeneracies of the spectrum. Playing with the numbers of sites (N_x, N_y) and their parity, one can obtain a various patterns of degeneracy, including ones that are "intermediate" with respect to the two described above for $N_x = N_y$.

It is important to notice that the expression for the OC exponent (4.2.23) does not rely on the choice of the boundary conditions. Indeed, we have already remarked that the present formalism applies for any boundary conditions, with the requirement that we have to trade the transverse momentum label for the quantum numbers that are appropriate to the noninteracting impurity bands. However, the numerical relations between the various exponents that we presented in the previous paragraphs do depend on the choice of the pbc, because the degeneracy factors are sensitive to the boundary conditions.

We end this theoretical discussion by showing two examples of the Green's function equation (4.2.21) calculated numerically in figures 4.27 and 4.28. The first pair of plots is from a row of $N_b = 6$ baths, while the second one is from a square lattice of 4×4 baths. The first plot of each pair shows the full set of distinct return probabilities $|G(\mathbf{p}, t)|^2$ for various transverse momenta $\mathbf{p}_\perp$. Because of the symmetries of the spectrum in the Brillouin zone, there are subset of momenta that give the same $|G(\mathbf{p}, t)|^2$. One can appreciate that there is always the lowest-energy state $\mathbf{p}_\perp = 0$ whose Green's function only has a very slow power-law decay, whereas the other excited states decay

24 These states lie on the square with vertices $(0,0)$, $(\pi,0)$, (π,π) and (π,π), whose parallel edges differ by the vectors $(\pi,0)$, (π,π).

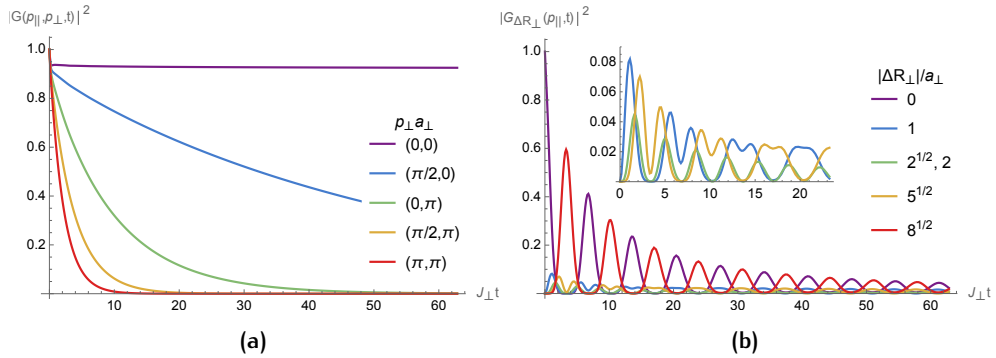

Figure 4.28: Numerical evaluation of the Green's function for a plaquette of 4×4 identical baths, for $g^2K = 0.5v^2$, $2J_{e_\perp} = J_\perp = 0.05Mv^2$ and $p_\parallel = 0$. Plot (a) shows the five possible return probabilities as functions of the transverse momentum, while (b) displays the Green's function for different shells of neighbouring baths in transverse distances. The inset in (b) magnifies the smaller components.

exponentially, the decay being faster for higher energy. The dimensional crossover at short times is readily observable as a very steep decrease of $|G(\mathbf{p}, t)|^2$ from 1, especially for $\mathbf{p}_\perp = 0$.

The second plot in each pair shows the Green's function in transverse direction:

$$\begin{aligned} G_{\mathbf{R}'_\perp, \mathbf{R}_\perp}(p_\parallel, t) &\equiv -i \langle \Omega | d_{p_\parallel \mathbf{R}'_\perp}(t) d^\dagger_{p_\parallel \mathbf{R}_\perp} | \Omega \rangle = \\ &= \frac{1}{N_b} \sum_{\mathbf{p}_\perp} e^{i\mathbf{p}_\perp (\mathbf{R}'_\perp - \mathbf{R}_\perp)} G(p_\parallel, \mathbf{p}_\perp, t) \, , \end{aligned} \tag{4.2.27}$$

where the second equality refers to the symmetric case, when the Green's function is diagonal in momentum. The pbc assumed for the lattice of baths imply that $G_{\mathbf{R}'_\perp, \mathbf{R}_\perp}(p_\parallel, t)$ is a function only of the distance $\Delta\mathbf{R}_\perp = \mathbf{R}'_\perp - \mathbf{R}_\perp$, modulo the periodicity of the lattice. This periodic nature of the lattice plays an important role in determining the interference patterns that shape the Green's function for such small "plaquettes". From figures 4.27b and 4.28b we can observe that the interference strongly influences the initial behaviour of the various components, which is complex and rather unpredictable. After a few oscillations, the shape of the oscillations tends to settle to a more regular one. Interference is responsible also for the fact that in both figures the second-largest component of the Green's function is the one in which $|\Delta\mathbf{R}_\perp|$ maximal, i.e. $|\Delta\mathbf{R}_\perp| = 3$ and $|\Delta\mathbf{R}_\perp| = 8^{1/2}$ in the $1+1$D and $2+1$D scenarios, respectively. This effect is particularly prominent in the latter case. Nonetheless, the off-diagonal components (i.e. the ones for $\Delta\mathbf{R}_\perp \neq 0$) still follow the naive expectation that their rising from zero takes longer the larger is $|\Delta\mathbf{R}_\perp|$.

TUNABLE OC EXPONENT An interesting feature of the many-baths exponent (4.2.23) is that it can be modified by manipulating the degeneracy of the states. The first and most obvious way to do it is by choosing a different lattice of baths. We have already given some examples of this possibility in the case of a row or a square lattice of baths, but we may envisage more

exotic situations. For instance, the Lieb [63] and kagome [93] lattices both feature a dispersionless band, whose degeneracy scales as the number of sites. This extensive degeneracy implies the possibility to reach a rather large $\beta^{N_b}(\mathbf{p})$, which moreover would be constant as N_b grows. The existence of such finite limit for $\beta^{N_b}(\mathbf{p})$ suggests that the continuum limit of the present model would feature a finite OC exponent in a bosonic system. Of course, this argument is highly hand-waving, as lattices yielding a flat band such as the two mentioned above are necessarily non-simple, and thus they would need a generalisation of the formulae presented in this section. Moreover, the presence of a dispersionless band would probably require a method able to tackle a strong impurity-bath coupling. We are not aware of any work dealing with the OC of impurities with flat bands.

A second way to alter the degeneracy factors is to use external fields acting on the impurity. This has the advantage of being far more flexible than changing the lattice, as external fields can be easily modified, even in real time, so that the OC exponent could actually become tunable in the course of an experiment.[25] Another important advantage of external fields is that they can be used to alter the degeneracy of the lowest band. This is relevant for experiments, as the power-law contribution to the decay of higher-lying bands may be difficult to observe because of the simultaneous exponential decay (see figures 4.27a and 4.28a). On the other hand, the decay of the Green's function for the band of lowest energy is purely power-law (at zero temperature, at least).

We illustrate the above ideas with the example of a row of baths in pbc, namely N_b baths arranged at the vertices of a regular polygon of N_b sides. Let us suppose that the impurity has a charge q and it is subjected to a homogeneous magnetic field[26] $\mathbf{B}$. By the Peierls substitution [65], the effect of this magnetic field can be well approximated by adding a phase to the hopping parameters $J_{e_\perp} \to J_{e_\perp} e^{i\theta_{e_\perp}}$ and $J_\parallel \to J_\parallel e^{i\theta_\parallel}$ in the terms of $\mathcal{H}_d$ that connect different sites, namely

$$\begin{aligned}\mathcal{H}_{\text{imp}}(\theta_\parallel, \theta_\perp) \equiv -J_\parallel \sum_{\mathbf{R}} \left(e^{i\theta_\parallel} d^\dagger_{R_\parallel + a_\parallel, R_\perp} d_{R_\parallel, R_\perp} + \text{h.c.} - 2 d^\dagger_{\mathbf{R}} d_{\mathbf{R}} \right) + \\ - \sum_{\mathbf{R}} J_{e_\perp} \left(e^{i\theta_\perp} d^\dagger_{R_\parallel, R_\perp + a_\perp} d_{R_\parallel, R_\perp} + \text{h.c.} \right) \ .\end{aligned} \tag{4.2.28}$$

In particular, the phases have the expressions

$$\theta_\parallel = q \int_{(R_\parallel, R_\perp)}^{(R_\parallel + a_\parallel, R_\perp)} d\mathbf{x} \cdot \mathbf{A}(\mathbf{x}) \ , \tag{4.2.29a}$$

$$\theta_\perp = q \int_{(R_\parallel, R_\perp)}^{(R_\parallel, R_\perp + a_\perp)} d\mathbf{x} \cdot \mathbf{A}(\mathbf{x}) \ , \tag{4.2.29b}$$

where $\mathbf{A}(\mathbf{x})$ is the vector potential in a chosen gauge, and the line integrals run on any path that joins the two extreme points.

25 Of course, with ultracold atoms is already possible to change the OC exponent by modifying the coupling constant with the aid of external magnetic fields, exploiting the Feschbach resonances of the atomic species involved.

26 We neglect the effect of the impurity spin. We can imagine that the field is sufficiently strong to hinder spin flips, so that the impurity spin is conserved, or that the impurity is charged, but spinless.

Going to the momentum basis we find that the new energy bands are obtained from the old ones by shifting the momenta $p_{\parallel,\perp} \to p_{\parallel,\perp} - \theta_{\parallel,\perp}/a_{\parallel,\perp}$, i.e.

$$\lambda_{\theta_\parallel,\theta_\perp}(p_\parallel, p_\perp) = \lambda\left(p_\parallel - \frac{\theta_\parallel}{a_\parallel}, p_\perp - \frac{\theta_\perp}{a_\perp}\right) = \\ = 2J_\parallel\left[1 - \cos\left(p_\parallel a_\parallel - \theta_\parallel\right)\right] - 2J_{e_\perp}\cos(p_\perp a_\perp - \theta_\perp) \quad (4.2.30)$$

Let us take the simple setting in which the magnetic field points parallel to the baths, a direction that we take to be z. In the symmetric gauge the vector potential is $\mathbf{A} = \mathbf{B} \times \mathbf{x}/2$ and therefore equations (4.2.29) imply $\theta_\parallel = 0$. Thus, we can focus on the effect of $\theta_\perp$. A generic real value of $\theta_\perp$ lifts all degeneracies of the spectrum. However, there is a subset of rational values of $\theta_\perp/\pi$ that entail a nontrivial behaviour. If the phase is an even multiple of π/N_b the spectrum is unchanged, only shifted by $\theta_\perp/a_\perp$ with respect to the transverse Brillouin zone. On the contrary, if $\theta_\perp$ is an odd multiple of π/N_b then the lowest-energy band is doubly degenerate. In this case, if N_b is even all energy levels are doubly degenerate, whereas for odd N_b the pattern of degeneracies is inverted with respect to the zero-field case, namely the energy levels are doubly degenerate except for the highest one, which is nondegenerate. To sum up, if we focus on the lowest level, we see that it is nondegenerate for all values of the external field except for $\theta_\perp = (2k+1)\pi/N_b$, $k \in \mathbb{Z}$. This means that its OC exponent can be doubled by tuning the magnetic field such that $\theta_\perp = (2k+1)\pi/N_b$.

LIMITATIONS There are two main limitations to the possibility of observing the various behaviours of the OC discussed above.

The first one is that in all our examples,the existence and extent of the levels degeneracy strongly relied on the symmetries of the lattice. For instance, if the square lattice is deformed to a rectangular one by making the hoppings $J_{e_\perp}$ different for the two possible directions $\boldsymbol{e}_\perp$, the degeneracies are reduced to 2 or 4 (as only the inversion symmetry $\mathbf{p}_\perp \to -\mathbf{p}_\perp$ remains), unless the two Js are in some special ratio. And if the lattice is not perfect, not even this degeneracy survives in general. This is the same strong sensitivity to the details of the lattice of baths that allowed us to tune the degeneracy factors by means of boundary conditions and/or external fields.

A second point is that, unless one tunes the ground state degeneracy by means of external fields, to observe the variety of OC exponents one has to measure the power-law decay of excited states, which are, however, prone to decoherence. In equation (4.2.21), every factor of $F^{sb}_{p_\parallel \mathbf{R}_\perp}(-\Delta_{\mathbf{k}_\perp \mathbf{p}_\perp}, t)$ with $\Delta_{\mathbf{k}_\perp \mathbf{p}_\perp} < 0$ (i.e. whenever there is a decay channel with $\lambda(p_\parallel, \mathbf{k}_\perp) < \lambda(p_\parallel, \mathbf{p}_\perp)$ for the $\mathbf{p}$ state) increases the overall decay constant of the state with by $2\gamma_{p_\parallel}(J_\perp = -\Delta_{\mathbf{k}_\perp \mathbf{p}_\perp}/2)$. Therefore, the higher the energy of the state, the larger its decay constant, both because the number of decay channel increases and both because $2\gamma_{p_\parallel}(J_\perp)$ is an increasing function of $J_\perp = -\Delta_{\mathbf{k}_\perp \mathbf{p}_\perp}/2$. This means that excited states may become rapidly depopulated, and their power-law decay at long times may become hard to observe. A finite temperature of the baths would increase this decay further. However, given the large number of possibilities on choosing the lattice and the parameters, we believe that it should be feasible to observe the effect of the level

degeneracy on $\beta^{N_b}(\mathbf{p})$ on the lowest-lying bands in the spectrum. And, of course, the ground state is always immune from decoherence, except from the effect of temperature.

As a final warning, we point out that the exact scaling of the OC exponent $\beta^{N_b}(\mathbf{p})$ with N_b may be different from N_b^{-2}, because the latter directly comes from keeping only the second order in perturbation theory. Every factor of $g_{\mathbf{R}_\perp}$ in higher-order terms would always be accompanied by a corresponding factor of N_b^{-1}. Part of these factors can probably be cancelled by intermediate transverse momentum summations, and we do not know if there could be terms that would turn out to have the same overall order as the second in N_b^{-1}. Such a "large-N" discussion is highly nontrivial on the technical side, because as we have already seen the unperturbed Hamiltonian already contains the coupling constant, while the recoil term $:P_b^2:/(2M)$ does not, so that the actual number of $g_{\mathbf{R}_\perp}/N_b$ is difficult to guess in advance. Moreover, embarking in such an analysis would be probably meaningless without including also the backscattering terms in the bosonised density equation (2.2.13). However, at present we do not have any intuition on the influence of such terms on the OC exponent, not even at the lowest perturbative order. The above reasoning equally applies to the exact scaling of $\beta^{N_b}(\mathbf{p})$ with the degeneracy of the level. The prediction (4.2.23) would still represent the exact leading behaviour in the large-N_b limit if every higher-order term is proportional to powers of N_b^{-1} higher than 2. Even if some subset of these higher-order terms would contribute to $\beta^{N_b}(\mathbf{p})$ with a factor of order $\mathcal{O}(N_b^{-2})$, this would still be suppressed by a power of $g_{\mathbf{R}_\perp}$ larger than the leading one at weak coupling. This means that there is a chance that equation (4.2.23) should be a reasonable prediction in the weak-coupling regime. However, even if it were not valid at a quantitative level, the overall message of this section would still be valid qualitatively: the OC exponent depends on the number of baths and on the degeneracy of the impurity bands, and the latter can be tuned by exploiting lattice symmetries and external fields.

5 CONCLUSIONS AND FURTHER PERSPECTIVES

In this thesis, we have explored various aspects of the dynamics of an impurity moving in more than one 1D bath. A recurring theme has been the investigation of the orthogonality catastrophe (OC) that follows the injection of the impurity in the system. This phenomenon has been studied by calculating the Green's function of the impurity, which also described the time evolution and spectral features of the latter. The distinctive signature of the OC is that the Green's function shows a power-law tail at long times. This function has been calculated using suitable perturbative expansions in the impurity-bath coupling, namely the Linked Cluster Expansion (LCE) and a time-dependent perturbation theory around a nontrivial dynamics. All of our results are nonperturbative in the inter-bath hopping, $J_\perp$.

In the two-bath scenario we have performed a detailed asymptotic expansion of the LCE Green's function at long times, which turned out to be very accurate in comparison with its numerical evaluation. The expansion has allowed us to obtain the renormalisation of the dispersion of the impurity bands, as well as the exponent of the power-law decay and the lifetime of the odd mode. One of our main results is that the OC, leading to the breakdown of the quasiparticle picture, survives the inclusion of a second 1D bath and dominates the long-time behaviour of all the components of the Green's function. In particular, the exponent characterising the long-time behaviour of the Green's function is given by half of the average of the exponents of the individual baths and, notably, is the same for the intra-bath Green's functions and for that connecting the two baths, demonstrating that the behaviour of the system at long times is dominated by the interactions within each bath. This implies that, for this system, the motion inside each bath and the inter-bath motion can not be decoupled.

In the case of two asymmetric baths, the Green's function is nonuniversal, acquiring a high-frequency component at short times and exhibiting persistent oscillations at longer times. Only at asymptotically large times the symmetric Green's function is recovered.

In real experiments, the temperature of the baths is always finite, so we have extended the LCE treatment to this scenario. The effect of the temperature is to suppress the Green's function, limiting the possibility to observe its coherent oscillations and the power-law tail. At sufficiently long times, we found analytically that this suppression is exponential in time, with a different decay constant for the even and odd modes. For low temperatures, the two decay constants are approximately coinciding, and are proportional to the temperature, in accord with the literature [84]. On the other hand, we also found that the OC exponent is not altered by the finite temperature (within our second-order approximation, at least). We analysed the visibility conditions of the coherent oscillations of the Green's function, reaching the intuitive conclusion that they can be best observed by keeping the tempera-

ture smaller than the inter-bath hopping $J_\perp$. The overall exponential decay hides the power-law tail of the zero-temperature results. Yet, the knowledge of the analytical behaviour of the thermal decay would allow to extract the power-law exponent from a numerical fit of the experimental data. This fit should yield cleaner results if the thermal decay is small, which requires large $J_\perp$ and small temperature (namely, the same conditions suggested for the coherent oscillations).

Using a perturbation theory in the inter-band part of the interaction we have been able to reproduce the LCE Green's function and the OC with a method which also allows us to access the evolution of the whole impurity-bath system. The advantage of this approach is that it provides an analytic expression for the time evolution of the state of the whole impurity-baths system. This has allowed us to compute the time evolution of observables beyond the impurity Green's function, including the often-neglected properties of the baths. Moreover, the numerical effort required by the approach is sufficiently low so that we have been able to treat the case in which the impurity is initialised in a wave packet of an (almost) arbitrary shape. A limit of the technique is that it cannot be extended to arbitrary large times, because the norm of the state decays from one on the time scale of the odd mode decay time, $(2\gamma(p))^{-1}$.

On the impurity side, we have analysed the time evolution of its population within each bath, observing how the persistent oscillations of the free impurity are damped and slowed down by the interaction with the baths. This (expected) phenomenon hints at the eventual thermalisation of the bath degree of freedom. On the contrary, the impurity momentum does not appear to converge to zero: within the time scale of validity of the approximation, it actually shows a tendency to converge to a constant value. Indeed, at zero temperature there is no friction in a conventional sense in our system. We have observed that momentum is transferred to the baths in two steps: a short transient, connected to the bath relaxation and independent of $J_\perp$, and a much slower decay caused by the emission of phonons during the deexcitation of the odd mode. Finally, we have also examined the time evolution of the probability density of finding the impurity in a given position and bath, for various Gaussian wave packets.

We have studied the time evolution of observables describing the dynamics of the baths, which are rarely discussed in the literature on mobile impurities, but are nonetheless accessible to experiments. We have looked at the number of excited phonons, which shows a slow logarithmic divergence in time, related to the OC, superimposed with the faster growth caused by the emission of phonons from the odd mode decay.

The most interesting results have been obtained for the time evolution of the expectation values and correlation functions of the particle and momentum (current) densities of the baths. The particle density shows a semiclassical behaviour, intuitively similar to that of a pond in which a stone has been thrown. After the impurity has been injected into one of the baths, a localised density depletion forms and follows its motion (with a certain time lag depending on $J_\perp$). At the same time, two wave fronts are generated and propagate away (as the "rings" on the water surface in the pond analogy). Moreover, each time the impurity oscillates between the baths, a new pair of

ripples is emitted. Varying the width of the initial Gaussian wave packet of the impurity and its inter-bath hopping amplitude $J_\perp$, we have found that the wave fronts and the trough are approximate images of the wave packet itself, and that the emission of ripples can be suppressed by employing wider wave packets. We have also found that the bath momentum density displays a behaviour analogous to that of the density. When the initial impurity wave packet has a markedly non-Gaussian shape, we find complex interference phenomena, both in the ripples and within the central trough.

The inter-bath, equal-times connected density and momentum density correlations revealed a rich structure in real space. The correlation is non-vanishing only in an area in (x, y) space, which expands ballistically. Two features can be distinguished, a pair of lobes and a series of ripples between them. Along the relative direction, $r = x - y$, the correlation function mainly shows the "relativistic" dynamics of the bath, with a clear light-cone as the phonons generated by the impurity spread the correlations. Along the centre-of-mass direction $R = (x + y)/2$, instead, besides the light-cone of emitted phonons there is a part of the correlations that follows the impurity wave packet in its motion.

Lastly, we have made the first steps towards a many-baths system, in which the impurity moves in a 1D or 2D lattice of 1D baths. We have obtained the time evolution of the state of the system with the perturbative technique developed before. The impurity Green's function has revealed qualitative differences from the two-baths setup. First of all, the Green's function shows a complex short-time behaviour, caused by interference effects between the various paths of propagation within the lattice of baths. More importantly, we have found that each band of the noninteracting impurity is characterised by its own OC exponent, which is proportional to the degeneracy of the band. We have then speculated that it may be possible to tune the OC exponent either by properly designing the lattice of baths, or by changing the degeneracies by means of external magnetic fields. We also shown that for generic lattices of baths, the OC exponents vanish in the limit of an infinite number of lattice sites.

Finally, we discuss some perspectives for future extensions of this work. The first aspect that requires further investigations is the effect of backscattering terms of the impurity-bath coupling (i.e. the higher harmonics of the bosonised density (2.2.13), that we have neglected at small momentum) on the system dynamics. These terms would allow us to treat higher impurity momenta, a regime in which qualitatively new features, such as pseudo-Bloch oscillations, are expected [70, 82]. The perturbative technique that we developed can be extended to include these interaction terms. Backscattering can be introduced within the LCE straightforwardly, albeit likely at the expense of the analytical tractability of the resulting integrals. We are not aware of works in which the latter calculation has been performed, in any impurity model.

The weakest spot of the perturbative approach is the loss of normalisation. This limitation should be cured by adding successive orders in perturbation theory. However, this would yield excessively cumbersome terms that would cause the method to loose its analytic attractiveness. A possible way to get over the limitations of the perturbative approach (and, possibly, to reach a

stronger coupling regime) is to promote the perturbative solution (4.1.40) to a variational Ansatz, in which the amplitude of the various terms and the coefficients of the coherent background state $|\omega_p(t)\rangle$ are the variational parameters. This Ansatz would be strongly reminiscent of a popular Ansatz for higher-dimensional Fermi polarons, in which the impurity state is expanded in terms with an increasing number of particle-hole pairs excited from the Fermi sphere [20, 67].

A line of research which we deem promising is based on the Generalised Fulton-Gouterman (GFG) transformation, that we introduced in appendix B. Besides the advantage of treating the impurity-baths entanglement exactly, it may help to provide some nonperturbative statements on the system properties, both dynamic and thermodynamic. The approaches based on the mean-field Ansätze introduced in appendix B are already under development. Moreover, the GFG transformation can be easily adapted to incorporate the backscattering terms, and it does not even require the bosonisation of the baths—indeed, it is based on a symmetry that is agnostic on how the degrees of freedom of the theory are represented. With these extensions, we may envisage a path to the strong-coupling regime of the model (which necessarily has to include backscattering).

The regime of strong impurity-baths interaction is an obvious direction that is worth investigating. In this regime, already the ground-state properties can be challenging to determine. Indeed, the most important question for the physics of strong-coupling polarons is the existence of a localisation transition, namely if the tendency to decrease the energy of the system by creating a depletion of the bath density surrounding the impurity (acting as a potential well on it) can actually lead to a spontaneous breaking of translational symmetry and endow the impurity with a finite position variance. In our model we have two different possible motions, transverse and longitudinal, that can become localised in principle, thus we could ask ourselves if one of the two could localise before the other. It is difficult to determine the occurrence of a localisation transition, as commonly used variational methods may yield misleading results [19, 89]. For the bath degree of freedom, the related spin-boson model is predicted to feature localised phases for ohmic baths [61]. On the other hand, to the best of our knowledge there are no definitive proofs of localisation for impurities interacting with acoustic phonons [25, 30, 90]. These arguments imply that the problem of strong-coupling localisation will have to be tackled with proper theoretical techniques.

Finally, we find the many-baths scenario of section 4.2 particularly fascinating, and deserving a deeper analysis. A first motivation is that this setup is already within the reach of present experiments—indeed, they are performed on lattices of 1D subsystems, as we have described in section 2.1. From a more theoretical point of view, already the calculation of the Green's function has shown that the OC in this system has nontrivial features that cannot be found in other popular impurity models. We find especially intriguing the possibility to tune the OC exponents by altering the degeneracies of the impurity spectrum. Beyond the phenomenon of the OC, it seems promising to study the dynamics of the various observables that characterise

the system. The perturbative solution that we found can be used for this purpose, and hopefully it will help to unveil some new and interesting physics.

A BATH DENSITY EVOLUTION FROM LINEAR RESPONSE

In this appendix, we use equation (4.1.88) of section 4.1.4 to obtain a qualitative and quantitative understanding of the observed behaviour of the time evolution of the bath density profiles.

We repeat here the equation, for clarity:

$$\langle \rho_\sigma(x) \rangle_t = \frac{g_\sigma K_\sigma}{2\pi} \int_0^t dt' \left[\partial_{x'} \left\langle d_\sigma^\dagger(x') d_\sigma(x') \right\rangle_{t'} \Big|_{x'=x+v_\sigma(t-t')} + \right.$$
$$\left. - \partial_{x'} \left\langle d_\sigma^\dagger(x') d_\sigma(x') \right\rangle_{t'} \Big|_{x'=x-v_\sigma(t-t')} \right] .$$

In figures A.1 we show the integrand of equation (4.1.88), using a numerical lattice derivative of the interacting impurity density we computed in 4.1.3 for $g^2K = 0.5v^2$, in the $\uparrow$ bath and for two different values of the inter-bath hopping. The wave packets are composed of $N_p = 32$ momenta, and are initially Gaussian with standard deviation $\delta p = 0.02Mv$ in momentum, which translates to a spatial width of $\delta x = 1/(2\delta p) = 25(Mv)^{-1}$. In the notation of equation (4.1.88), the time t at which we want to calculate the bath density is fixed in each plot (and coincides with the maximum time shown), while the horizontal and vertical axes of the figures run along the desired position x and the integration time t', respectively. Therefore, the bath density at a given position is obtained by integration along a vertical line, as the red dotted-dashed lines shown as examples. To highlight the periodicity of the oscillations, we measure time in the renormalised period of density oscillations, $\tilde{T}_{p_0} \equiv \pi/\tilde{J}_{\perp,p_0}$. As the impurity density is essentially a Gaussian, its derivative has both a positive and a negative part, depicted in warm and cold colours, respectively, and this two-lobe structure is repeated along the lines $t' = t + (x - x_0 - p_0 t/M)/v_{-\sigma}$ and $t' = t + (x - x_0 - p_0 t/M)/v_{+\sigma}$, as dictated by the causality structure of equation (4.1.88) (we are ignoring the small slowdown of the impurity momentum) and by the periodic oscillations from one bath to the other. Recall that $v_{\pm\sigma} \equiv v_\sigma \pm p_0/M$. The four tilted lines show the approximate locus of the maxima and minima: $t' = t + (x - x_0 - p_0 t/M \pm \delta x)/v_{-\sigma}$ for the black lines and $t' = t - (x - x_0 - p_0 t/M \pm \delta x)/v_{-\sigma}$ for the white ones. Notice that we are neglecting the increase in width of the wave packet during its dynamics. It can be seen in the figures that it does not seem to play a relevant role, so we take δx to be the initial standard deviation.

If we compare the bath densities in figures 4.16, we see that figure A.1a corresponds to a situation in which there are no ripples, while figure A.1b gives rise to ripples. Now it is easy to understand how this situation emerges from equation (4.1.88). Let us take the position corresponding to the red line in figure A.1a. We see that during the time integration we encounter a positive contribution and part of two negative lobes belonging to the previous two impurity oscillations. The results will thus be close to zero. On the other

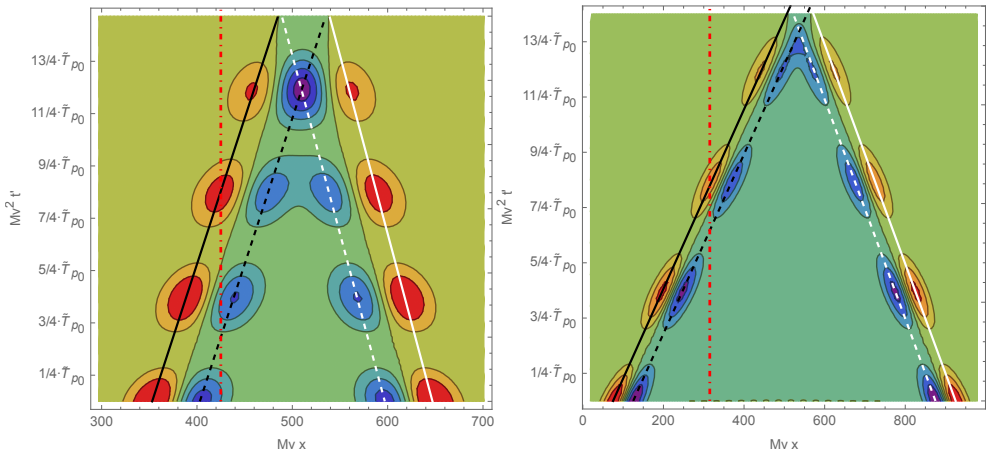

(a) $J_\perp = 0.1Mv^2$ **(b)** $J_\perp = 0.03Mv^2$

Figure A.1: Contour plot of the integrand of equation (4.1.88), computed with the impurity density obtained numerically. Warm colours correspond to positive values, while cold colours indicate negative values. The coupling is $g^2K = 0.5v^2$ (symmetric baths), with a Gaussian wave packet composed of $N_p = 32$ momenta with standard deviation $\delta p = 0.02Mv$. Time is measured in units of the interacting density oscillation period $\tilde{T}_{p_0} = \pi/\tilde{J}_{\perp,p_0}$ (the absolute timescales of the two plots are therefore different). For the meaning of the various lines, see the text.

hand, the integration path in figure A.1b only encounters a positive lobe, and therefore it will give rise to the positive part of a ripple. If we change position, the same situation occurs: for $J_\perp = 0.1Mv^2$, any vertical line will always cross regions of both signs, with the result that it will always close to zero, while for $J_\perp = 0.03Mv^2$ it will alternatively cross positive and negative regions, resulting in oscillations of the density, i.e. the ripples. Thus, we see that the ripples emerge from an interference effect between subsequent oscillations of the impurity. The extent of this interference is regulated the interplay between the periodic impurity oscillations, the sound speed and the width of the wave packet. We can make a quantitative estimate of the parameters needed for a destructive interference: it happens whenever the oscillation period is such that the position of a positive lobe overlaps with the position of the negative lobe of the previous oscillation. With the help of figures A.1, this translates to

$$v_{\pm\sigma}\tilde{T}_{p_0} \lesssim 2\delta x\,, \tag{A.0.1}$$

which directly leads to equations (4.1.89) and (4.1.90) in the main text.

The only regions that are exempted from this interference mechanism are the farthest positions reachable by causality, $|x - x_0| \approx vt$, and the ones around the centre $x \approx x_0 + p_0 t/M$, which are easily identified with the wave fronts and the central dip of the bath density, respectively. Indeed, from figures A.1 we can see that for $|x - x_0| \approx v_\sigma t$ the time integral intersects only positive lobes, while around $x = x_0 + p_0 t/M$ there is a region with only negative contributions. Therefore, we obtain the features we observed in section 4.1.4, namely that the wave fronts are always positive, while the trough is always negative. These arguments also show that the wave-fronts

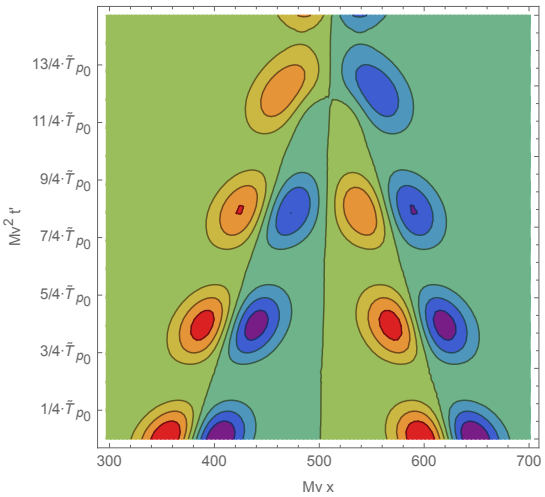

Figure A.2: Same as figure A.1a (i.e for $J_\perp = 0.1Mv^2$), but for the bath momentum density.

are images of the impurity density at the initial time, whereas the trough is sensitive only to the density in the near past. In the main text, we claimed that the wave fronts and the central dip were images of the impurity density. This would be exactly true if the density evolution were given simply by a translation: $\left\langle d^\dagger_\sigma(x')d_\sigma(x')\right\rangle_{t'} = N_0(x - x_0 - p_0t'/M)$, where $N_0(x - x_0)$ is the initial profile shape:

$$\langle \rho_\sigma(x,t)\rangle_t = \frac{g_\sigma K_\sigma}{2\pi}\left[\frac{1}{v_{+\sigma}}N_0(x - x_0 + vt) + \right.$$
$$\left. - \left(\frac{1}{v_{+\sigma}} - \frac{1}{v_{-\sigma}}\right)N_0(x - x_0 + p_0t/M) + \frac{1}{v_{-\sigma}}N_0(x - x_0 - vt)\right].$$

We can easily recognise the first and the last terms as the two counter-propagating wave fronts, which are translated images of the wave packet, and a negative trough that follows the impurity. We also see that the heights of the wave fronts are different from each other, with the backward being shorter than the forward one, the difference being larger the faster is the impurity. The equation above is valid only in a highly idealised situation, in which there is only one bath ($J_\perp = 0$) and the wave packet does not spread. In our situation, both hypotheses are false, but we can guess that the most relevant phenomena are caused by the retardation effects given by the density oscillations[1]. For instance, the ratio of the wave fronts heights of the bath density we computed numerically tends to $v_{+\sigma}/v_{-\sigma}$ at long times.

As a final remark, we point out that the same arguments given above can be repeated for the bath momentum density, as the momentum-density response function equation (4.1.92) has the same structure as the density-density one. In particular, we would obtain the analogous of equation (4.1.88), but with the two translated density gradients added to each other instead of being subtracted. We would then obtain an integrand depicted in figure A.2,

1 Indeed, it is possible to obtain an analytic expression of the bath density if we take $\left\langle d^\dagger_\sigma(x')d_\sigma(x')\right\rangle_{t'} = N_0(x - x_0 - p_0t'/M)(\cos J_\perp t')^2$, that is, if we again discard the wave packet spreading. In the solution, we can still recognise the presence of the wave fronts and the trough.

which clearly shows the characteristic feature of the bath momentum density that we observed in the main text, namely that the fluctuations emitted forward and backward are approximately inverted images of each other, instead of being approximately mirror images as in the case of the density.

B MORE UNITARY TRANSFORMATIONS

In this appendix, we present a unitary transformation that diagonalises the impurity's bath degree of freedom. We also sketch two mean-field approaches that rely on this transformation for approximating its ground-state and dynamical properties. The exposition will have a preliminary character, because this line of research is still ongoing. We choose to include this topic because of the conceptual relevance of the transformation.

B.1 THE GENERALISED FULTON–GOUTERMAN TRANSFORMATION

When the baths are identical, it is possible to find a basis in which the impurity is completely decoupled from the baths. In fact, in this case the system enjoys an additional symmetry, namely the invariance under exchange of the baths, and this corresponds to a extra conserved quantity. We start from equation (4.1.4), that we report here for clarity:

$$\mathcal{H}_{\mathrm{LLP}}(p) = \tfrac{(p-P_b)^2}{2M} - J_\perp \sigma_1 + \sum_{q\neq 0,\mu} v|q| b^\dagger_{q\mu} b_{q\mu} + \\ + \sum_{q\neq 0} \tfrac{W_q}{(2L)^{1/2}} (b^\dagger_{qe} + b_{qe}) + \sigma_3 \sum_{q\neq 0} \tfrac{W_q}{(2L)^{1/2}} (b^\dagger_{qo} + b_{qo}) \,. \quad \text{(B.1.1)}$$

We rewrite the above Hamiltonian as a matrix in the bath index pseudo-spin space:

$$\mathcal{H}_{\mathrm{LLP}}(p) = \begin{pmatrix} \mathcal{H}_b(p) + V & -J_\perp \\ -J_\perp & \mathcal{H}_b(p) - V \end{pmatrix} , \quad \text{(B.1.2)}$$

where

$$\mathcal{H}_b(p) \equiv \tfrac{(p-P_b)^2}{2M} + \sum_{q\neq 0,\mu} v|q| b^\dagger_{q\mu} b_{q\mu} + \sum_{q\neq 0} \tfrac{W_q}{\sqrt{2L}} (b^\dagger_{qe} + b_{qe}) \,, \\ V \equiv \sum_{q\neq 0} \tfrac{W_q}{\sqrt{2L}} (b^\dagger_{qo} + b_{qo}) \,.$$

Now we apply the unitary transformation[1] [78, 89]

$$U_{\mathrm{GFG}} \equiv \frac{1}{\sqrt{2}} \begin{pmatrix} 1 & 1 \\ R & -R \end{pmatrix} = \tfrac{\mathbb{1}-R}{2} \tfrac{\mathbb{1}+i\sigma_2}{\sqrt{2}} + \tfrac{\mathbb{1}+R}{2} \tfrac{\sigma_1+\sigma_3}{\sqrt{2}} \,. \quad \text{(B.1.3)}$$

Following [78], we will refer to this as the Generalised Fulton-Gouterman (GFG) transformation. In the equation above,

$$R \equiv e^{i\pi \sum_{q\neq 0} b^\dagger_{qo} b_{qo}} = (-1)^{N_o} = R^{-1} = R^\dagger \quad \text{(B.1.4)}$$

1 Although the original Fulton-Gouterman transformation [27] dates back to 1961, and was later generalised [78], it has been recently re-discovered in [5] and [6] as a useful tool to treat impurity problems.

counts the parity of the number $N_o \equiv \sum_{q\neq 0} b^\dagger_{qo} b_{qo}$ of odd phonons, and acts by changing the sign of b_{qo}: $R^\dagger b_{qo} R = -b_{qo}$. Hence, $R^\dagger V R = -V$, while $\mathcal{H}_b$ remains unchanged. The remarkable result is that the spin is diagonalised:

$$\begin{aligned}
\mathcal{H}_{GFG}(p) &\equiv U^\dagger_{GFG}\mathcal{H}_{LLP}(p)U_{GFG} = \mathcal{H}_b + V - J_\perp R\sigma_3 = \\
&= \tfrac{(p-P_e-P_o)^2}{2M} + \sum_{q\neq 0,\mu}\left[v|q|b^\dagger_{q\mu}b_{q\mu} + \tfrac{W_q}{\sqrt{2L}}(b^\dagger_{q\mu}+b_{q\mu})\right] + \\
&- \sigma_3 J_\perp e^{i\pi\sum_{q\neq 0} b^\dagger_{qo}b_{qo}} = \\
&= \tfrac{p^2}{2M} + \tfrac{P_e P_o}{M} + \sum_\mu \tfrac{:P^2_\mu:}{2M} + \\
&+ \sum_{q\neq 0,\mu}\left[\Omega_q(p) b^\dagger_{q\mu}b_{q\mu} + \tfrac{W_q}{\sqrt{2L}}(b^\dagger_{q\mu}+b_{q\mu})\right] - \sigma_3 J_\perp e^{i\pi\sum_{q\neq 0} b^\dagger_{qo}b_{qo}} .
\end{aligned} \tag{B.1.5}$$

Therefore, the dynamics in the GFG frame decomposes into independent spin components: if $|\psi_{LLP}(0)\rangle = \sum_{p\mu} c_{p\mu}|p\mu\rangle|\omega\rangle$, then

$$|\psi_{GFG}(t)\rangle \equiv U^\dagger_{GFG} e^{-i\mathcal{H}_{LLP}t}|\psi_{LLP}(0)\rangle = \sum_{p\sigma} c_{p,\mu=\sigma}|p\sigma\rangle_d |\varphi_{p\sigma}(t)\rangle_b , \tag{B.1.6a}$$

where

$$|\varphi_{p\sigma}(t)\rangle \equiv e^{-i\mathcal{H}^\sigma_{GFG}(p)t}|\omega\rangle , \tag{B.1.6b}$$

$$i\frac{d}{dt}|\varphi_{p\sigma}(t)\rangle = \mathcal{H}^\sigma_{GFG}(p)|\varphi_\sigma(t)\rangle \equiv (\mathcal{H}_b(p) + V - \sigma J_\perp R)|\varphi_{p\sigma}(t)\rangle . \tag{B.1.6c}$$

The notation $c_{p,\mu=\sigma}$ means c_{pe} if $\sigma = \uparrow$, and c_{po} if $\sigma = \downarrow$. From the solutions above, we can go back to the LLP basis

$$\begin{aligned}
|\psi_{LLP}(t)\rangle &= U_{GFG}|\psi_{GFG}(t)\rangle = \\
&= \tfrac{1}{\sqrt{2}}\sum_p \Big[|p\uparrow\rangle\left(c_{pe}|\varphi_{p\uparrow}(t)\rangle + c_{po}|\varphi_{p\downarrow}(t)\rangle\right) + \\
&\quad + |p\downarrow\rangle R\left(c_{pe}|\varphi_{p\uparrow}(t)\rangle - c_{po}|\varphi_{p\downarrow}(t)\rangle\right)\Big] = \\
&= \sum_p \Big[|pe\rangle\left(c_{pe}\tfrac{\mathbb{1}+R}{2}|\varphi_{p\uparrow}(t)\rangle + c_{po}\tfrac{\mathbb{1}-R}{2}|\varphi_{p\downarrow}(t)\rangle\right) + \\
&\quad + |po\rangle\left(c_{pe}\tfrac{\mathbb{1}-R}{2}|\varphi_{p\uparrow}(t)\rangle + c_{po}\tfrac{\mathbb{1}+R}{2}|\varphi_{p\downarrow}(t)\rangle\right)\Big] .
\end{aligned} \tag{B.1.7}$$

Notice that $Q_\pm \equiv (\mathbb{1}\pm R)/2$ are two orthogonal projectors: $Q_+ + Q_- = \mathbb{1}$, $Q^2_\pm = Q_\pm$, $Q_+Q_- = 0$. In particular, if $|\psi(0)\rangle = |pe\rangle|\omega\rangle$ ($|po\rangle|\omega\rangle$), the time-evolved state is $|\psi_{LLP}(t)\rangle = |pe\rangle Q_+|\varphi_{p\uparrow}(t)\rangle + |po\rangle Q_-|\varphi_{p\downarrow}(t)\rangle$ ($|\psi_{LLP}(t)\rangle = |pe\rangle Q_-|\varphi_{p\uparrow}(t)\rangle + |po\rangle Q_+|\varphi_{p\downarrow}(t)\rangle$). By taking the projection of the latter with the states $|p\mu\rangle|\omega\rangle$, and using $Q_+|\omega\rangle = |\omega\rangle$, $Q_-|\omega\rangle = 0$, we find the Green's functions:

$$G_{ee}(p,t) = -i\theta(t)\langle\omega|\varphi_{p\uparrow}(t)\rangle , \tag{B.1.8a}$$

$$G_{oo}(p,t) = -i\theta(t)\langle\omega|\varphi_{p\downarrow}(t)\rangle , \tag{B.1.8b}$$

$$G_{\bar\mu\mu}(p,t) = 0 . \tag{B.1.8c}$$

When translating these relations to the bath index basis, we find that

$$G_{\sigma'\sigma}(p,t) = \tfrac{1}{2}(G_{ee}(p,t) + \sigma'\sigma G_{oo}(p,t)) \,.$$

Thus, we have proven that the off-diagonal components of $G_{\sigma'\sigma}(p,t)$ are exactly equal, confirming that what we had observed in chapter 3 in the LCE approximation is actually true to all orders in perturbation theory.

The advantage of having found a basis where baths and impurity are decoupled is that we can focus on finding good approximations for the baths state, while the entanglement with the impurity—which is often hard to take care of—is perfectly accounted for by the combination of LLP and GFG transformations. For this reason, in the following paragraphs we describe how we could use a minimalist mean-field theory for describing the both the static and dynamical properties of the system

B.2 MEAN-FIELD THEORY FOR THE GROUND STATE

As simple application of the GFG transformation we can try to find the ground state of the system, and its properties. In the GFG basis we have a family of Hamiltonians $\mathcal{H}^{\sigma}_{GFG}(p)$, so we should find for which momentum p and spin σ the ground-state energy has its minimum.

In a given (p,σ) sector, we seek a variational approximation to the ground state in the form of a coherent state[2],

$$|\varphi_{p\sigma}\rangle = |\mathrm{coh}[f_{q\mu}]\rangle \,, \tag{B.2.1}$$

where the complex coefficients[3] $f_{q\mu}$ have to be found minimising the energy

$$\mathcal{E}[f_{q\mu}, f^*_{q\mu}] \equiv \langle \mathrm{coh}[f_{q\mu}]|\mathcal{H}^{\sigma}_{GFG}(p)|\mathrm{coh}[f_{q\mu}]\rangle = \tfrac{p^2}{2M} + \sum_{q\neq 0,\mu} \Omega_q(p)|f_{q\mu}|^2 + \\ + \sum_{q\neq 0,\mu} \tfrac{W_q}{(2L)^{1/2}}(f_{q\mu} + f^*_{q\mu}) + \tfrac{1}{2M}\Big[\sum_{q\neq 0,\mu} q|f_{q\mu}|^2\Big]^2 - \sigma J_\perp e^{-2\sum_{q\neq 0}|f_{q0}|^2} \,. \tag{B.2.2}$$

This minimisation yields

$$f_{q\mu} = -\frac{W_q}{(2L)^{1/2}(\Omega_q(p-P_b) + 2\delta_{\mu,o}\sigma J_\perp e^{-2N_o})} \,. \tag{B.2.3}$$

where we defined the total bath momentum P_b and the number of odd phonons N_o

$$P_b \equiv \sum_{q\neq 0,\mu} q|f_{q\mu}|^2 \,, \tag{B.2.4a}$$

$$N_o \equiv \sum_{q\neq 0} |f_{q0}|^2 \,. \tag{B.2.4b}$$

2 Similar Ansätze have been already used in related models of mobile impurities [87].

3 There is a different set of these coefficients for each σ, but we omit the bath index for brevity.

It is easy to see that equation (B.2.3) coincides with the static saddle-point condition for the action $\mathcal{S}$ when calculating the finite-temperature partition function as a coherent state path integral [1]

$$Z_{p\sigma} = \int D(\bar{b}_{q\mu}(\tau) b_{q\mu}(\tau)) e^{-S[\bar{b}_{q\mu}(\tau), b_{q\mu}(\tau)]} \,. \tag{B.2.5}$$

This equivalence occurs because the variational energy (B.2.2) is proportional to the action evaluated on a constant trajectory $b_{q\mu}(\tau) = f_{q\mu}$.

We observe from equation (B.2.3) that in our mean-field Ansatz, the correlations between the phonon modes are included via P_b and N_o. The former acts by renormalising the impurity momentum in $\Omega_q(p - P_b)$, while the second one describes the reduction of the inter-bath hopping amplitude $J_\perp \to J_\perp e^{-2N_o}$. As our Ansatz does not contain any true correlation between the phonon states, we expect that it will provide a reasonable approximation to the ground state of the system only for small couplings.

The formal solution equation (B.2.3) depends on two unknown parameters N_o and P_b, that have to be found by requiring self-consistency:

$$P_b = \sum_{q\neq 0} q \frac{W_q^2}{2L} \left[\frac{1}{(\Omega_q(p-P_b))^2} + \frac{1}{(\Omega_q(p-P_b)+\sigma 2 J_\perp e^{-2N_o})^2} \right] , \tag{B.2.6a}$$

$$N_o = \sum_{q\neq 0} \frac{W_q^2}{2L} \frac{1}{\left[\Omega_q(p-P_b)+\sigma 2 J_\perp e^{-2N_o}\right]^2} \,. \tag{B.2.6b}$$

It is possible to go to the thermodynamic limit by introducing the usual densities of states

$$R(\varepsilon; p) \equiv \frac{1}{L} \sum_{q\neq 0} W_q^2 \delta(\varepsilon - \Omega_q(p)) \,, \tag{B.2.7a}$$

$$R_1(\varepsilon; p) \equiv \frac{1}{L} \sum_{q\neq 0} q W_q^2 \delta(\varepsilon - \Omega_q(p)) \tag{B.2.7b}$$

to write

$$P_b = \int_0^{+\infty} d\varepsilon \, R_1(\varepsilon; p - P_b) \left[\frac{1}{\varepsilon^2} + \frac{1}{(\varepsilon + \sigma 2 J_\perp e^{-2N_o})^2} \right] , \tag{B.2.8a}$$

$$N_o = \int_0^{+\infty} d\varepsilon \, R(\varepsilon; p - P_b) \frac{1}{(\varepsilon + \sigma 2 J_\perp e^{-2N_o})^2} \,. \tag{B.2.8b}$$

We already encountered the first density of states $R(\varepsilon, p - P_b)$ in chapter 3, while found the second in 4.1.3. We recall here its expression:

$$\begin{aligned} R_1(\varepsilon; p) = {} & \frac{M^2 \tilde{g}^2}{(2\pi)^2} \theta(\varepsilon) e^{-\varepsilon/\Lambda} \times \\ & \times \sum_{s=\pm 1} \left[-s\left(v + s\tfrac{p}{M}\right) \right] \left[\left(1 + \tfrac{\varepsilon}{k_s(p)}\right)^{1/2} - 2 + \left(1 + \tfrac{\varepsilon}{k_s(p)}\right)^{-1/2} \right] , \end{aligned} \tag{B.2.9}$$

where $k_s(p) \equiv (Mv + sp)^2/(2M)$. It is of order $\mathcal{O}(\varepsilon^2)$ for $\varepsilon \to 0$. Of course, we have to distinguish the $\sigma = \uparrow = 1$ from the $\sigma = \downarrow = -1$ case in equations (B.2.8). While the former scenario does not pose any difficulty, we see that in the latter the equation for N_o involves a divergent integral for any $N_o \geqslant 0$. This implies that $N_o^\downarrow$ must be infinite, because in this case

$$N_o^\downarrow = \int_0^{+\infty} d\varepsilon \, R(\varepsilon; p - P_b^\downarrow) \frac{1}{\varepsilon^2} \sim \int_0^{+\infty} d\varepsilon \, \frac{\varepsilon e^{-\varepsilon/\Lambda}}{\varepsilon^2} = +\infty \tag{B.2.10}$$

and so the self-consistency is guaranteed. In particular, if we approximate the finite-size situation by introducing an infrared cutoff $\varepsilon_{\min} = 2\pi v/L$ for the integral, we obtain that $N_o^{\downarrow} \sim \ln L$, which shows that this divergence is an instance of the OC. Therefore, in the $\sigma = \downarrow$ case, the saddle-point solution depends on one parameter only, $P_b^{\downarrow}$, which is determined by the equation

$$P_b^{\downarrow} = \int_0^{+\infty} d\varepsilon \, R_1(\varepsilon; p - P_b^{\downarrow}) \frac{2}{\varepsilon^2} \, . \tag{B.2.11}$$

It is possible to find explicit expressions for the integrals in equations (B.2.8). Using

$$\int_0^{+\infty} d\varepsilon \, \frac{1}{(\varepsilon+\Delta)^2} \frac{1}{(1+\varepsilon/k)^{1/2}} = \frac{k}{\Delta(k-\Delta)} \left[1 - \frac{\Delta}{k} \frac{\operatorname{arccosh}(k/\Delta)^{1/2}}{(1-\Delta/k)^{1/2}} \right] , \tag{B.2.12a}$$

$$\int_0^{+\infty} d\varepsilon \, \frac{1}{(\varepsilon+\Delta)^2} \left(1 + \frac{\varepsilon}{k}\right)^{1/2} = \frac{1}{\Delta} - \frac{\Delta}{k} \frac{\operatorname{arccosh}(k/\Delta)^{1/2}}{k(1-\Delta/k)^{1/2}} \, , \tag{B.2.12b}$$

we obtain

$$P_b = \frac{M^2 \tilde{g}^2}{2(2\pi)^2} \sum_{s=\pm 1} \frac{-s(v + s(p-P_b)/M)}{k_s(p-P_b)} f_P\left(\frac{2J_\perp e^{-2N_o}}{k_s(p-P_b)}\right) , \tag{B.2.13a}$$

$$N_o = \frac{M\tilde{g}^2}{2(2\pi)^2} \sum_{s=\pm 1} \frac{1}{k_s(p-P_b)} f_N\left(\frac{2J_\perp e^{-2N_o}}{k_s(p-P_b)}\right) , \tag{B.2.13b}$$

where

$$f_P(x) \equiv 1 + \frac{1}{1-x}\left[1 - x\frac{\operatorname{arccosh}(x^{-1/2})}{(1-x)^{1/2}}\right] , \tag{B.2.14a}$$

$$f_N(x) \equiv \frac{1}{1-x}\left[\frac{\operatorname{arccosh}(x^{-1/2})}{(1-x)^{1/2}} - 1\right] \tag{B.2.14b}$$

with the usual understanding that $\operatorname{arccosh}(x) = i \arccos(x)$ when $|x| < 1$. The above functions (B.2.14) are both monotonically decreasing in x, but they have different limiting behaviours:

$$\lim_{x\to 0} f_P(x) = f_P(0) = 2, \quad \lim_{x\to 0} f_N(x) = +\infty \, , \tag{B.2.15a}$$

$$\lim_{x\to +\infty} f_P(x) = 1, \quad \lim_{x\to +\infty} f_N(x) = 0 \, , \tag{B.2.15b}$$

The variational estimate of the energy can be written in function of the two parameters N_o, P_b:

$$E_{gs}^{\sigma} = \frac{p^2}{2M} + \sum_{q\neq 0,\mu} \frac{W_q}{(2L)^{1/2}} f_{q\mu}^{\sigma} - \frac{(P_b^{\sigma})^2}{2M} - \sigma J_\perp (2N_o^{\sigma} + 1) e^{-2N_o^{\sigma}} \, , \tag{B.2.16}$$

where

$$\sum_{q\neq 0,\mu}\frac{W_q}{(2L)^{1/2}}f^{\sigma}_{q\mu}=-\sum_{q\neq 0,\mu}\frac{W_q^2}{2L}\frac{1}{\Omega_q(p-P^{\sigma}_b)+\sigma\delta_{\mu,0}2J_\perp e^{-2N^{\sigma}_o}}=$$

$$=-\frac{1}{2}\int_0^{+\infty}d\varepsilon\,R(\varepsilon,p-P^{\sigma}_b)\left[\frac{1}{\varepsilon}+\frac{1}{\varepsilon+\sigma 2J_\perp e^{-2N^{\sigma}_o}}\right]=$$

$$=\begin{cases}-\frac{M\tilde{g}^2}{2(2\pi)^2}\sum_{s=\pm 1}\left\{-\gamma-\ln\frac{4k_s(p-P^{\uparrow}_b)}{\Lambda}+e^{\frac{2J_\perp e^{-2N^{\uparrow}_o}}{\Lambda}}E_1\left(\frac{2J_\perp e^{-2N^{\uparrow}_o}}{\Lambda}\right)+\right.\\ \left.-2\frac{\operatorname{arccosh}\left[\frac{k_s(p-P^{\uparrow}_b)}{2J_\perp e^{-2N^{\uparrow}_o}}\right]}{\left[1-\frac{2J_\perp e^{-2N^{\uparrow}_o}}{k_s(p-P^{\uparrow}_b)}\right]^{1/2}}\right\}, \quad \sigma=\uparrow,\\ -\frac{M\tilde{g}^2}{(2\pi)^2}\sum_{s=\pm 1}\left[-\gamma-\ln\frac{4k_s(p-P^{\downarrow}_b)}{\Lambda}\right], \quad \sigma=\downarrow\end{cases} \tag{B.2.17}$$

where we recall that γ is Euler-Mascheroni constant and $E_1(x)$ is the exponential integral function [23]. We notice that, unlike P_b and N_o, the contribution equation (B.2.17) to the variational energy depends explicitly on the UV cutoff Λ for the baths.

B.3 MEAN-FIELD THEORY FOR THE TIME EVOLUTION

We can extend the coherent state Ansatz to approximate the dynamics:

$$|\varphi_{p\sigma}(t)\rangle=e^{-i\zeta_{p\sigma}(t)}\,|\mathrm{coh}[f_{q\mu}(t)]\rangle\ , \tag{B.3.1}$$

with the initial conditions $\zeta_{p\sigma}(0)=0$, $f_{q\mu}(0)=0$ when the initial state is the boson vacuum. The best approximation of the state evolution on the manifold defined by the equation above can be found by looking for the extremum of the functional [58]

$$\mathcal{L}[\zeta_{p\sigma}(t),f_{q\mu}(t),f^*_{q\mu}(t)]=\frac{i}{2}\left(\left\langle\varphi_{p\sigma}(t)\middle|\frac{d}{dt}\varphi_{p\sigma}(t)\right\rangle+\right.$$

$$\left.-\left\langle\frac{d}{dt}\varphi_{p\sigma}(t)\middle|\varphi_{p\sigma}(t)\right\rangle\right)-\langle\varphi_{p\sigma}(t)|\mathcal{H}^{\sigma}_{\mathrm{GFG}}(p)|\varphi_{p\sigma}(t)\rangle=$$

$$=\frac{d}{dt}\zeta_{p\sigma}(t)+\frac{i}{2}\sum_{q\neq 0,\mu}\left(f^*_{q\mu}\frac{d}{dt}f_{q\mu}-\frac{d}{dt}f^*_{q\mu}f_{q\mu}\right)-\mathcal{E}[f_{q\mu},f^*_{q\mu}]\ , \tag{B.3.2}$$

where $\mathcal{E}[f_{q\mu},f^*_{q\mu}]$ is the same energy functional (B.2.2). The equation of motion for $f_{q\mu}(t)$ is

$$i\frac{d}{dt}f_{q\mu}(t)=\left[\Omega_q(p-P_b(t))+2\delta_{\mu,0}\sigma J_\perp e^{-2N_o(t)}\right]f_{q\mu}(t)-\frac{W_q}{(2L)^{1/2}}\ , \tag{B.3.3}$$

where $P_b(t)$ and $N_o(t)$ are defined by equations (B.2.4), as functions of the time-dependent variational parameters $f_{q\sigma}(t)$. The phase $\zeta_{p\sigma}(t)$ enters in the above Lagrangian function through a total time derivative, so it cannot

be fixed by the equations of motion. A possible choice to determine it is to require that $\langle \varphi_{p\sigma}(t)|i\frac{d}{dt} - \mathcal{H}^{\sigma}_{GFG}(p)|\varphi_{p\sigma}(t)\rangle = 0$, which yields

$$\frac{d}{dt}\zeta_{p\sigma}(t) = \mathcal{E}[f_{q\mu}, f^*_{q\mu}] - \frac{i}{2}\sum_{q\neq 0,\mu}\left(f^*_{q\mu}\frac{d}{dt}f_{q\mu} - \frac{d}{dt}f^*_{q\mu}f_{q\mu}\right) . \tag{B.3.4}$$

Equation (B.3.3) is similar to the one for the ground state, equation (B.2.3), and just like the latter it can be formally solved in terms of the unknown *functions* $N_o(t)$ and $P_b(t)$:

$$\begin{aligned} f_{q\mu}(t) = f_{q\mu}(0)e^{i\int_0^t dt'[\Omega_q(p-P_b(t'))+2\delta_{\mu,o}\sigma J_\perp e^{-2N_o(t')}]} + \\ - i\frac{W_q}{2L^{1/2}}\int_0^t dt'\, e^{-i\int_{t'}^t dt_1[\Omega_q(p-P_b(t_1))+2\delta_{\mu,o}\sigma J_\perp e^{-2N_o(t_1)}]} . \end{aligned} \tag{B.3.5}$$

Setting $f_{q\mu}(0) = 0$, we can write down two self-consistency equations

$$\begin{aligned} P_b(t) &= \sum_{q\neq 0,\mu} q\frac{W_q^2}{2L}\left|\int_0^t dt'\, e^{-i\int_{t'}^t dt_1[\Omega_q(p-P_b(t_1))+2\delta_{\mu,o}\sigma J_\perp e^{-2N_o(t_1)}]}\right|^2 = \\ &= \frac{1}{2}\sum_{\mu}\int_0^t dt_1\int_0^t dt_2\int d\varepsilon\, R_1\left(\varepsilon; p - \frac{1}{t_1-t_2}\int_{t_2}^{t_1} dt'\, P_b(t')\right)\times \\ &\quad \times e^{i\varepsilon(t_1-t_2)+2i\sigma J_\perp\delta_{\mu,o}\int_{t_2}^{t_1}dt' e^{-2N_o(t')}} , \end{aligned} \tag{B.3.6a}$$

$$\begin{aligned} N_o(t) &= \sum_{q\neq 0}\frac{W_q^2}{2L}\left|\int_0^t dt'\, e^{-i\int_{t'}^t dt_1[\Omega_q(p-P_b(t_1))+2\sigma J_\perp e^{-2N_o(t_1)}]}\right|^2 = \\ &= \frac{1}{2}\int_0^t dt_1\int_0^t dt_2\int d\varepsilon\, R\left(\varepsilon; p - \frac{1}{t_1-t_2}\int_{t_2}^{t_1} dt'\, P_b(t')\right)\times \\ &\quad \times e^{i\varepsilon(t_1-t_2)+2i\sigma J_\perp\int_{t_2}^{t_1}dt' e^{-2N_o(t')}} . \end{aligned} \tag{B.3.6b}$$

The second form of these equations could be useful to access the continuum limit in their numerical solution. Otherwise, we should simply integrate the equations of motion (B.3.3) numerically.

From equations (B.1.8), we can find the Green's functions

$$G_{ee}(p,t) = -i\theta(t)e^{-i\zeta_{p\uparrow}(t)-\frac{1}{2}\sum_\mu N^{\uparrow}_\mu(t)} , \tag{B.3.7a}$$

$$G_{oo}(p,t) = -i\theta(t)e^{-i\zeta_{p\downarrow}(t)-\frac{1}{2}\sum_\mu N^{\downarrow}_\mu(t)} \tag{B.3.7b}$$

Notice the similarity with equation (2.3.17) for the static impurity. This analogy ultimately comes from the fact that in both cases the bath is in a coherent state.

BIBLIOGRAPHY

[1] Alexander Altland and Benjamin B. Simons. *Condensed Matter Field Theory*. 2nd ed. Cambdridge University Press, 2010.

[2] P W Anderson. "A poor man's derivation of scaling laws for the Kondo problem". In: *Journal of Physics C: Solid State Physics* 3.12 (Dec. 1970), pp. 2436–2441. DOI: 10.1088/0022-3719/3/12/008.

[3] P. W. Anderson. "Infrared Catastrophe in Fermi Gases with Local Scattering Potentials". In: *Phys. Rev. Lett.* 18 (24 June 1967), pp. 1049–1051. DOI: 10.1103/PhysRevLett.18.1049.

[4] M. Arzamasovs, F. Bovo, and D. M. Gangardt. "Kinetics of Mobile Impurities and Correlation Functions in One-Dimensional Superfluids at Finite Temperature". In: *Phys. Rev. Lett.* 112 (17 Apr. 2014), p. 170602. DOI: 10.1103/PhysRevLett.112.170602.

[5] Yuto Ashida et al. "Solving Quantum Impurity Problems in and out of Equilibrium with the Variational Approach". In: *Phys. Rev. Lett.* 121 (2 July 2018), p. 026805. DOI: 10.1103/PhysRevLett.121.026805.

[6] Yuto Ashida et al. "Variational principle for quantum impurity systems in and out of equilibrium: Application to Kondo problems". In: *Phys. Rev. B* 98 (2 July 2018), p. 024103. DOI: 10.1103/PhysRevB.98.024103.

[7] Assa Auerbach. *Interacting Electrons and Quantum Magnetism*. 1st ed. Springer-Verlag, 1994.

[8] Carl M. Bender and Steven A. Orsag. *Advanced Mathematical Methods for Scientists and Engineers I*. 1st. Springer, 1999.

[9] Immanuel Bloch, Jean Dalibard, and Wilhelm Zwerger. "Many-body physics with ultracold gases". In: *Rev. Mod. Phys.* 80 (3 July 2008), pp. 885–964. DOI: 10.1103/RevModPhys.80.885.

[10] Julius Bonart and Leticia F. Cugliandolo. "Effective potential and polaronic mass shift in a trapped dynamical impurity–Luttinger liquid system". In: *EPL (Europhysics Letters)* 101.1 (Jan. 2013), p. 16003. DOI: 10.1209/0295-5075/101/16003.

[11] Julius Bonart and Leticia F. Cugliandolo. "From nonequilibrium quantum Brownian motion to impurity dynamics in one-dimensional quantum liquids". In: *Phys. Rev. A* 86 (2 Aug. 2012), p. 023636. DOI: 10.1103/PhysRevA.86.023636.

[12] Filippo Bovo. *Nonlinear Bosonization and Refermionization in One Dimension with the Keldysh Functional Integral*. Oct. 2016. arXiv: 1610.08110 [cond-mat.quant-gas].

[13] A. H. Castro Neto and A. O. Caldeira. "Alternative approach to the dynamics of polarons in one dimension". In: *Phys. Rev. B* 46 (14 Oct. 1992), pp. 8858–8876. DOI: 10.1103/PhysRevB.46.8858.

[14] A. H. Castro Neto and A. O. Caldeira. "Mobility and diffusion of a particle coupled to a Luttinger liquid". In: *Phys. Rev. B* 50 (7 Aug. 1994), pp. 4863–4866. DOI: 10.1103/PhysRevB.50.4863.

[15] A. H. Castro Neto and A. O. Caldeira. "New model for dissipation in quantum mechanics". In: *Phys. Rev. Lett.* 67 (15 Oct. 1991), pp. 1960–1963. DOI: 10.1103/PhysRevLett.67.1960.

[16] A. H. Castro Neto and Matthew P. A. Fisher. "Dynamics of a heavy particle in a Luttinger liquid". In: *Phys. Rev. B* 53 (15 Apr. 1996), pp. 9713–9718. DOI: 10.1103/PhysRevB.53.9713.

[17] J. Catani et al. "Quantum dynamics of impurities in a one-dimensional Bose gas". In: *Phys. Rev. A* 85 (2 Feb. 2012), p. 023623. DOI: 10.1103/PhysRevA.85.023623.

[18] Marko Cetina et al. "Ultrafast many-body interferometry of impurities coupled to a Fermi sea". In: *Science* 354.6308 (2016), pp. 96–99. DOI: 10.1126/science.aaf5134.

[19] Zhi-De Chen and Hang Wong. "Artifact of phonon-induced localization by the existing variational calculations used in the spin-boson model". In: *Phys. Rev. B* 78 (6 Aug. 2008), p. 064308. DOI: 10.1103/PhysRevB.78.064308.

[20] F. Chevy. "Universal phase diagram of a strongly interacting Fermi gas with unbalanced spin populations". In: *Phys. Rev. A* 74 (6 Dec. 2006), p. 063628. DOI: 10.1103/PhysRevA.74.063628.

[21] Cheng Chin et al. "Feshbach resonances in ultracold gases". In: *Rev. Mod. Phys.* 82 (2 Apr. 2010), pp. 1225–1286. DOI: 10.1103/RevModPhys.82.1225.

[22] Jozef T. L. Devreese. "Fröhlich Polarons Lecture course including detailed theoretical derivations". In: *arXiv:1012.4576 [cond-mat.other]* (Nov. 2015). DOI: https://doi.org/10.48550/arXiv.1012.4576.

[23] *NIST Digital Library of Mathematical Functions*. https://dlmf.nist.gov/, Release 1.0.25 of 2019-12-15. F. W. J. Olver, A. B. Olde Daalhuis, D. W. Lozier, B. I. Schneider, R. F. Boisvert, C. W. Clark, B. R. Miller, B. V. Saunders, H. S. Cohl, and M. A. McClain, eds. URL: https://dlmf.nist.gov/.

[24] Moritz Drescher, Manfred Salmhofer, and Tilman Enss. "Quench Dynamics of the Ideal Bose Polaron at Zero and Nonzero Temperatures". In: *Phys. Rev. A* 103 (3 Mar. 2021), p. 033317. DOI: 10.1103/PhysRevA.103.033317.

[25] Matthew P. A. Fisher and Wilhelm Zwerger. "Ground-state symmetry of a generalized polaron". In: *Phys. Rev. B* 34 (8 Oct. 1986), pp. 5912–5915. DOI: 10.1103/PhysRevB.34.5912.

[26] Takeshi Fukuhara et al. "Quantum dynamics of a mobile spin impurity". In: *Nature Physics* 9.4 (Apr. 1, 2013), pp. 235–241. ISSN: 1745-2481. DOI: 10.1038/nphys2561.

[27] Robert L. Fulton and Martin Gouterman. "Vibronic Coupling. I. Mathematical Treatment for Two Electronic States". In: *The Journal of Chemical Physics* 35.3 (1961), pp. 1059–1071. DOI: 10.1063/1.1701181.

[28] O. Gamayun. "Quantum Boltzmann equation for a mobile impurity in a degenerate Tonks-Girardeau gas". In: *Phys. Rev. A* 89 (6 June 2014), p. 063627. DOI: 10.1103/PhysRevA.89.063627.

[29] M. Gaudin. "Un systeme a une dimension de fermions en interaction". In: *Physics Letters A* 24.1 (1967), pp. 55–56. ISSN: 0375-9601. DOI: https://doi.org/10.1016/0375-9601(67)90193-4.

[30] B. Gerlach and H. Löwen. "Analytical properties of polaron systems or: Do polaronic phase transitions exist or not?" In: *Rev. Mod. Phys.* 63 (1 Jan. 1991), pp. 63–90. DOI: 10.1103/RevModPhys.63.63.

[31] Thierry Giamarchi. *Quantum Physics in One Dimension*. 1st ed. Oxford: Clarendon Press, 2003.

[32] Gabriele Giuliani and Giovanni Vignale. *Quantum Theory of the Electron Liquid*. Cambridge University Press, 2005.

[33] Alexander O. Gogolin, Alexander A. Nersesyan, and Alexei M. Tsvelik. *Bosonization and Strongly Correlated Systems*. Cambridge University Press, 1998.

[34] J. Goold et al. "Orthogonality catastrophe as a consequence of qubit embedding in an ultracold Fermi gas". In: *Phys. Rev. A* 84 (6 Dec. 2011), p. 063632. DOI: 10.1103/PhysRevA.84.063632.

[35] A. Goussev et al. "Loschmidt echo". In: *Scholarpedia* 7.8 (2012). revision #127578, p. 11687. DOI: 10.4249/scholarpedia.11687.

[36] Hermann Grabert, Peter Schramm, and Gert-Ludwig Ingold. "Quantum Brownian Motion - The Functional Integral Approach". In: *Physics Reports-Review section of Pysics Letters* 168.3 (Oct. 1988), pp. 115–207. ISSN: 0370-1573. DOI: 10.1016/0370-1573(88)90023-3.

[37] M. Gring et al. "Relaxation and Prethermalization in an Isolated Quantum System". In: *Science* 337.6100 (2012), pp. 1318–1322. DOI: 10.1126/science.1224953.

[38] Fabian Grusdt, Gregory E Astrakharchik, and Eugene Demler. "Bose polarons in ultracold atoms in one dimension: beyond the Fröhlich paradigm". In: *New Journal of Physics* 19.10 (Oct. 2017), p. 103035. DOI: 10.1088/1367-2630/aa8a2e.

[39] Fabian Grusdt and Eugene Demler. *New theoretical approaches to Bose polarons*. 2015. arXiv: 1510.04934 [cond-mat.quant-gas].

[40] Nils-Eric Guenther et al. "Mobile impurity in a Bose-Einstein condensate and the orthogonality catastrophe". In: *Phys. Rev. A* 103 (1 Jan. 2021), p. 013317. DOI: 10.1103/PhysRevA.103.013317.

[41] D. B. Gutman, Yuval Gefen, and A. D. Mirlin. "Bosonization of one-dimensional fermions out of equilibrium". In: *Phys. Rev. B* 81 (8 Feb. 2010), p. 085436. DOI: 10.1103/PhysRevB.81.085436.

[42] Hartmut Haug and Antti-Pekka Jauho. *Quantum Kinetics in Transport and Optics of Semiconductors*. Ed. by M. Cardona. 1st ed. Vol. 123. Solid-State Sciences. Springer, Berlin, Heidelberg, 1996.

[43] Alexander Cyril Hewson. *The Kondo Problem to Heavy Fermions*. Cambridge Studies in Magnetism. Cambridge University Press, 1993. DOI: 10.1017/CBO9780511470752.

[44] S. Hofferberth et al. "Radiofrequency-dressed-state potentials for neutral atoms". In: *Nature Physics* 2.10 (Oct. 2006), pp. 710–716. ISSN: 1745-2481. DOI: 10.1038/nphys420.

[45] Adilet Imambekov, Thomas L. Schmidt, and Leonid I. Glazman. "One-dimensional quantum liquids: Beyond the Luttinger liquid paradigm". In: *Rev. Mod. Phys.* 84 (3 Sept. 2012), pp. 1253–1306. DOI: 10.1103/RevModPhys.84.1253.

[46] N.A. Kamar. "Quantum dynamics in one-dimensional and two-leg ladder systems". PhD thesis. University of Geneva, 2019. URL: https://archive-ouverte.unige.ch/unige:128219.

[47] Naushad Ahmad Kamar, Adrian Kantian, and Thierry Giamarchi. "Dynamics of a mobile impurity in a two-leg bosonic ladder". In: *Phys. Rev. A* 100 (2 Aug. 2019), p. 023614. DOI: 10.1103/PhysRevA.100.023614.

[48] C. L. Kane and Matthew P. A. Fisher. "Transmission through barriers and resonant tunneling in an interacting one-dimensional electron gas". In: *Phys. Rev. B* 46 (23 Dec. 1992), pp. 15233–15262. DOI: 10.1103/PhysRevB.46.15233.

[49] C. L. Kane and Matthew P. A. Fisher. "Transport in a one-channel Luttinger liquid". In: *Phys. Rev. Lett.* 68 (8 Feb. 1992), pp. 1220–1223. DOI: 10.1103/PhysRevLett.68.1220.

[50] A. Kantian, U. Schollwöck, and T. Giamarchi. "Competing Regimes of Motion of 1D Mobile Impurities". In: *Phys. Rev. Lett.* 113 (7 Aug. 2014), p. 070601. DOI: 10.1103/PhysRevLett.113.070601.

[51] Michael Knap et al. "Time-Dependent Impurity in Ultracold Fermions: Orthogonality Catastrophe and Beyond". In: *Phys. Rev. X* 2 (4 Dec. 2012), p. 041020. DOI: 10.1103/PhysRevX.2.041020.

[52] Jun Kondo. "Resistance Minimum in Dilute Magnetic Alloys". In: *Prog. Theor. Phys.* 32.1 (July 1964), pp. 37–49. ISSN: 0033-068X. DOI: 10.1143/PTP.32.37.

[53] Petr Král. "Nonequilibrium linked cluster expansion for steady-state quantum transport". In: *Phys. Rev. B* 56 (12 Sept. 1997), pp. 7293–7303. DOI: 10.1103/PhysRevB.56.7293.

[54] Austen Lamacraft. "Dispersion relation and spectral function of an impurity in a one-dimensional quantum liquid". In: *Phys. Rev. B* 79 (24 June 2009), p. 241105. DOI: 10.1103/PhysRevB.79.241105.

[55] Austen Lamacraft. "Kondo Polarons in a One-Dimensional Fermi Gas". In: *Phys. Rev. Lett.* 101 (22 Nov. 2008), p. 225301. DOI: 10.1103/PhysRevLett.101.225301.

[56] L. D. Landau and S. I. Pekar. "Effective mass of a polaron". In: *Zh. Eksp. Teor. Fiz.* 5 (1948), pp. 419–423.

[57] L.D. Landau. "On the motion of electrons in a crystal lattice". In: *Phys. Z. Sowietunion* 3 (1933), p. 664.

[58] W. T. Langhoff, S. T. Epstein, and M. Karplus. "Aspects of Time-Dependent Perturbation Theory". In: *Rev. Mod. Phys.* 44 (3 July 1972), pp. 602–644. DOI: 10.1103/RevModPhys.44.602.

[59] D. K. K. Lee and Y. Chen. "X-ray response of the Luttinger model". In: *Phys. Rev. Lett.* 69 (9 Aug. 1992), pp. 1399–1402. DOI: 10.1103/PhysRevLett.69.1399.

[60] T. D. Lee, F. E. Low, and D. Pines. "The Motion of Slow Electrons in a Polar Crystal". In: *Phys. Rev.* 90.2 (Apr. 1953), pp. 297–302. DOI: 10.1103/PhysRev.90.297.

[61] A. J. Leggett et al. "Dynamics of the dissipative two-state system". In: *Rev. Mod. Phys.* 59 (1 Jan. 1987), pp. 1–85. DOI: 10.1103/RevModPhys.59.1.

[62] Maciej Lewenstein, Anna Sanpera, and Verònica Ahufinger. *Ultracold Atoms in Optical Lattices: Simulating quantum many-body systems*. 1st. Oxford University Press, 2012.

[63] Elliott H. Lieb. "Two theorems on the Hubbard model". In: *Phys. Rev. Lett.* 62 (10 Mar. 1989), pp. 1201–1204. DOI: 10.1103/PhysRevLett.62.1201.

[64] Elliott H. Lieb and Werner Liniger. "Exact Analysis of an Interacting Bose Gas. I. The General Solution and the Ground State". In: *Phys. Rev.* 130 (4 May 1963), pp. 1605–1616. DOI: 10.1103/PhysRev.130.1605.

[65] J. M. Luttinger. "The Effect of a Magnetic Field on Electrons in a Periodic Potential". In: *Phys. Rev.* 84 (4 Nov. 1951), pp. 814–817. DOI: 10.1103/PhysRev.84.814.

[66] Gerald D. Mahan. *Many-Particle Physics*. 2nd ed. New York: Plenum press, 1993. ISBN: 0306434237.

[67] Pietro Massignan, Matteo Zaccanti, and Georg M Bruun. "Polarons, dressed molecules and itinerant ferromagnetism in ultracold Fermi gases". In: *Reports on Progress in Physics* 77.3 (Feb. 2014), p. 034401. DOI: 10.1088/0034-4885/77/3/034401.

[68] Charles J. M. Mathy, Mikhail B. Zvonarev, and Eugene Demler. "Quantum flutter of supersonic particles in one-dimensional quantum liquids". In: *Nature Physics* 8.12 (2012), pp. 881–886. ISSN: 1745-2481. DOI: 10.1038/nphys2455.

[69] V. Meden et al. "Hot-electron relaxation: An exactly solvable model and improved quantum kinetic equations". In: *Phys. Rev. B* 52 (8 Aug. 1995), pp. 5624–5636. DOI: 10.1103/PhysRevB.52.5624.

[70] Florian Meinert et al. "Bloch oscillations in the absence of a lattice". In: *Science* 356.6341 (2017), pp. 945–948. ISSN: 0036-8075. DOI: 10.1126/science.aah6616.

[71] Lena Nicolin and Dvira Segal. "Non-equilibrium spin-boson model: Counting statistics and the heat exchange fluctuation theorem". In: *The Journal of Chemical Physics* 135.16 (2011), p. 164106. DOI: 10.1063/1.3655674.

[72] Tetsuo Ogawa, Akira Furusaki, and Naoto Nagaosa. "Fermi-edge singularity in one-dimensional systems". In: *Phys. Rev. Lett.* 68 (24 June 1992), pp. 3638–3641. DOI: 10.1103/PhysRevLett.68.3638.

[73] Sebastian Paeckel et al. "Time-evolution methods for matrix-product states". In: *Annals of Physics* 411 (2019), p. 167998. ISSN: 0003-4916. DOI: https://doi.org/10.1016/j.aop.2019.167998.

[74] Stefan Palzer et al. "Quantum Transport through a Tonks-Girardeau Gas". In: *Phys. Rev. Lett.* 103 (15 Oct. 2009), p. 150601. DOI: 10.1103/PhysRevLett.103.150601.

[75] L. Parisi and S. Giorgini. "Quantum Monte Carlo study of the Bose-polaron problem in a one-dimensional gas with contact interactions". In: *Phys. Rev. A* 95 (2 Feb. 2017), p. 023619. DOI: 10.1103/PhysRevA.95.023619.

[76] Rudolf Peierls. *Surprises in Theoretical Physics*. 1st ed. Princeton Series in Physics. Princeton, New Jersey: Princeton University Press, 1979.

[77] Christopher J. Pethick and Henrik Smith. *Bose–Einstein Condensation in Dilute Gases*. 2nd ed. Cambridge University Press, 2008. DOI: 10.1017/CBO9780511802850.

[78] Matthias Rapp and Max Wagner. "Multiband Fulton - Gouterman transformation and its application to electron - phonon systems". In: *Journal of Physics A: Mathematical and General* 30.8 (Apr. 1997), pp. 2811–2823. DOI: 10.1088/0305-4470/30/8/025.

[79] Achim Rosch. "Quantum-coherent transport of a heavy particle in a fermionic bath". In: *Adv. Phys.* 48.3 (1999), pp. 295–394. DOI: https://doi.org/10.1080/000187399243446.

[80] Achim Rosch and Thilo Kopp. "Heavy Particle in a d-Dimensional Fermionic Bath: A Strong Coupling Approach". In: *Phys. Rev. Lett.* 75 (10 Sept. 1995), pp. 1988–1991. DOI: 10.1103/PhysRevLett.75.1988.

[81] Francesco Scazza et al. *Repulsive Fermi and Bose Polarons in Quantum Gases*. 2022. arXiv: 2204.06984.

[82] M. Schecter, D.M. Gangardt, and A. Kamenev. "Dynamics and Bloch oscillations of mobile impurities in one-dimensional quantum liquids". In: *Annals of Physics* 327.3 (2012), pp. 639–670. ISSN: 0003-4916. DOI: https://doi.org/10.1016/j.aop.2011.10.001.

[83] André Schirotzek et al. "Observation of Fermi Polarons in a Tunable Fermi Liquid of Ultracold Atoms". In: *Phys. Rev. Lett.* 102 (23 June 2009), p. 230402. DOI: 10.1103/PhysRevLett.102.230402.

[84] Richard Schmidt et al. "Universal many-body response of heavy impurities coupled to a Fermi sea: a review of recent progress". In: *Reports on Progress in Physics* 81.2 (Jan. 2018), p. 024401. DOI: 10.1088/1361-6633/aa9593.

[85] Ulrich Schollwöck. "The density-matrix renormalization group in the age of matrix product states". In: *Annals of Physics* 326.1 (2011). January 2011 Special Issue, pp. 96–192. ISSN: 0003-4916. DOI: https://doi.org/10.1016/j.aop.2010.09.012.

[86] K. D. Schotte and U. Schotte. "Tomonaga's Model and the Threshold Singularity of X-Ray Spectra of Metals". In: *Phys. Rev.* 182 (2 June 1969), pp. 479–482. DOI: 10.1103/PhysRev.182.479.

[87] Aditya Shashi et al. "Radio-frequency spectroscopy of polarons in ultracold Bose gases". In: *Phys. Rev. A* 89 (5 May 2014), p. 053617. DOI: 10.1103/PhysRevA.89.053617.

[88] Yulia E. Shchadilova et al. "Quantum Dynamics of Ultracold Bose Polarons". In: *Phys. Rev. Lett.* 117 (11 Sept. 2016), p. 113002. DOI: 10.1103/PhysRevLett.117.113002.

[89] Herbert B. Shore and Leonard M. Sander. "Ground State of the Exciton-Phonon System". In: *Phys. Rev. B* 7 (10 May 1973), pp. 4537–4546. DOI: 10.1103/PhysRevB.7.4537.

[90] H Spohn. "Roughening and pinning transitions for the polaron". In: *Journal of Physics A: Mathematical and General* 19.4 (Mar. 1986), pp. 533–545. DOI: 10.1088/0305-4470/19/4/014.

[91] Martino Stefanini, Massimo Capone, and Alessandro Silva. *A full view on the dynamics of an impurity coupled to two one-dimensional fermionic baths*. 2022. arXiv: 2206.13478.

[92] Martino Stefanini, Massimo Capone, and Alessandro Silva. "Motion of an impurity in a two-leg ladder". In: *Phys. Rev. B* 103 (9 Mar. 2021), p. 094310. DOI: 10.1103/PhysRevB.103.094310.

[93] Itiro Syôzi. "Statistics of Kagomé Lattice". In: *Prog. Theor. Phys.* 6.3 (June 1951), pp. 306–308. ISSN: 0033-068X. DOI: 10.1143/ptp/6.3.306.

[94] A. N. Wenz et al. "From Few to Many: Observing the Formation of a Fermi Sea One Atom at a Time". In: *Science* 342.6157 (2013), pp. 457–460. DOI: 10.1126/science.1240516.

[95] M. B. Zvonarev, V. V. Cheianov, and T. Giamarchi. "Edge exponent in the dynamic spin structure factor of the Yang-Gaudin model". In: *Phys. Rev. B* 80 (20 Nov. 2009), p. 201102. DOI: 10.1103/PhysRevB.80.201102.